Citation: Rees-Crockford, Thomas (2020) Magnetohydrodynamic Instabilities in Solar Prominences. Doctoral thesis, Northumbria University.

Magnetohydrodynamic Instabilities in Solar Prominences

T Rees-Crockford, MPhys

PhD

February 2020

Magnetohydrodynamic Instabilities in Solar Prominences

Thomas Rees-Crockford, MPhys

A thesis submitted in partial fulfilment of the requirements of the University of Northumbria at Newcastle for the degree of Doctor of Philosophy

Research undertaken in the Faculty of Engineering and Environment in the Department of Maths, Physics, and Electrical Engineering

Abstract

This work aims to understand of the nature of the magnetic environment which guides the evolution of solar prominences on both large and small scales, of which little is known. By understanding the large-scale evolution of prominences through investigation of eruptive instabilities we can gain insight into how to observationally recover in 3D key features of the torus instability. Through the small-scale evolution we gain knowledge of the fundamental nature of a rarely observed phenomena, the magnetic Rayleigh-Taylor instability, and its manifestation within the prominence substructure. This insight has allowed us to determine the likely magnetic properties of the prominence plasma. We have used imaging and spectropolarimetric data from both satellites and ground-based telescopes. Using stereoscopic techniques we reconstructed features of a solar prominence in 3D utilising pairs of satellites with large seperation angles. By developing novel edge-detection techniques, and iterating upon parametric fitting techniques we conducted a detailed kinematic analysis of an erupting prominence. We have measured the fundamental properties of large numbers of falling plumes within prominences and explained their origins through the RTI. We then supported these observations with ideal-MHD code MANCHA. We have confirmed the role of the TI in an prominence eruption. We have measured fundamental properties of plume with a large number of events. By understanding the TI we allow for the advancement of space-weather prediction. By understanding the RTI we gain insight into the magnetic environment of a prominence.

Acknowledgements

I would like to thank my girlfriend, office mates, friends, family, and supervisors, and all those who have made it possible for me to complete this through their kindness and support.

I would also like to thank my examiners for their help in improving the clarity and quality of this work.

Declaration

I declare that the work contained in this thesis has not been submitted for any other award and that it is all my own work. I also confirm that this work fully acknowledges opinions, ideas and contributions from the work of others.

Any ethical clearance for the research presented in this thesis has been approved. Approval has been sought and granted by the Ethics Online system, submission reference 1076 on 25/09/2017.

I declare that the word count of this thesis is 42462 words.

Name: Thomas Rees-Crockford
Signature:
Date: 26/02/2020

Contents

Chapter 1

An Introduction to Prominences and Their Instabilities

To begin at the beginning

Dylan Thomas, *Under Milk Wood*

Parts of this chapter form the basis of content of a paper entitled "2D and 3D Analysis of a Torus-Unstable Quiet-Sun Prominence Eruption" that has been submitted to The Astrophysical Journal in collaboration with my supervisors, Drs. E. Scullion and D.S. Bloomfield.

1.1 An overview of Prominences

Solar prominences are long, cool, dense features of the solar atmosphere (Engvold, 2015, and references therein) that consist of a spine, a footpoint at each end, and sometimes barbs along its length (Lin et al., 2008). As their temperature is often on the order of $10^3 - 10^4$ kelvin they are significantly colder than the mega-Kelvin coronal atmosphere that surrounds them. Due to this they appear in absorption when contrasted against the disk, as can be seen in Fig. 1.1, where they are known as filaments. This has a major impact on observing them when on-disk, since they largely appear in absorption, though there exists a surrounding Prominence-Corona Transition Region (PCTR) (Parenti, 2014, and references therein) which does appear in emission. This will be discussed in more detail in Sec. 1.1.1. However, due to the density of the plasma, $10^9 - 10^{11}$ cm^{-3} (Parenti, 2014), much of the prominence structure can still be seen in absorption wavelengths. Against the background of space they can appear in emission in certain wavelengths, but both on- and off-disk structures will be referred to hereafter as prominences. This limit in the choice of wavelengths to observe with nonetheless allows important features of the structure to be determined, with different wavelengths offering different characteristic temperatures. For instance two popular spectral lines, Hα (6582.8 Å) and He II (304 Å) are both high intensity chromospheric lines and optically thick. In contrast, the plasma is optically thin in Fe IX(171Å) but emits with low intensity. These lines, and others, will be discussed further in Sec. 1.1.1.

In terms of their magnetic nature, the magnetic field is known to generally dominate over plasma effects, though localised reversals of this have been reported (Heinzel et al., 2010). Statistical studies, such as those completed by Wang et al. (2010) and Bernasconi et al. (2005) show that most prominences are located between the equator and ± 60° in heliographic latitude, have lengths between 30-110 Mm, heights of up to 200 Mm above the surface, and have widths of around 1 to 10 Mm. Prominences are also highly variable in lifespan, with some lasting up to a few hours whilst others can last for months (Parenti, 2014).

This variation in lifespan, and in other parameters, is mostly due to their environments; active region prominences are both shorter (in length and height), and shorter-lived than quiescent prominences. Due to these variations several classification systems have been created over the decades of prominence studies, some of which even include features of the solar atmosphere which would no longer be considered prominences such as coronal loops, and spicules. We adopt here the classification system suggested by Engvold (2015), wherein more information of the history of prominence classification may also be found. This system suggests three main classes of prominence based upon their host environment; active region, intermediate (found somewhere between an active region and a region of quiet-sun), and quiescent. As noted by Engvold, this system has been adapted from earlier works to suit the large and varied continuum of observations.

Regardless of their host environment, prominences exist suspended over a polarity inversion line (PIL) with each footpoint connecting to the opposite magnetic polarities. This PIL itself sits along the prominence channel, an area filled with field-aligned chromospheric fibrils (Gaizauskas, 1998). This field alignment allowed the assignment of chirality to the prominence channel, with Martin et al. (1992) defining a channel to be dextral or sinistral dependent on the direction of the axial magnetic field as seen by an observer on the positive-polarity side of the channel. The chirality of prominences has also been observed (Martin, 1998), with dextral flux ropes dominating in the northern hemisphere, and sinistral in the southern. As quiescent prominences can have long lifespans they must have stable magnetic structures. Furthermore, prominence barbs have been found to directly match the handedness of their host, though the nature of the barbs themselves is still an area of debate. What can be said is that the barbs are protrusions of threads out from the prominence and into, at least, the chromosphere below (Lin et al., 2008). As the magnetic structure itself is difficult to observe under the atmospheric conditions of non-local thermal equilibirum (non-LTE, discussed further in Sec. 1.1.1) it must be interpreted through the properties of the plasma it suspends. Therefore it can be difficult to ascertain its exact nature. However, there are considered to be two leading magnetic configurations of prominences – sheared arcades (Antiochos et al., 1994) or stable magnetic flux ropes (MFRs) (Kuperus & Raadu, 1974). In either case, historically, the mass of the prominence

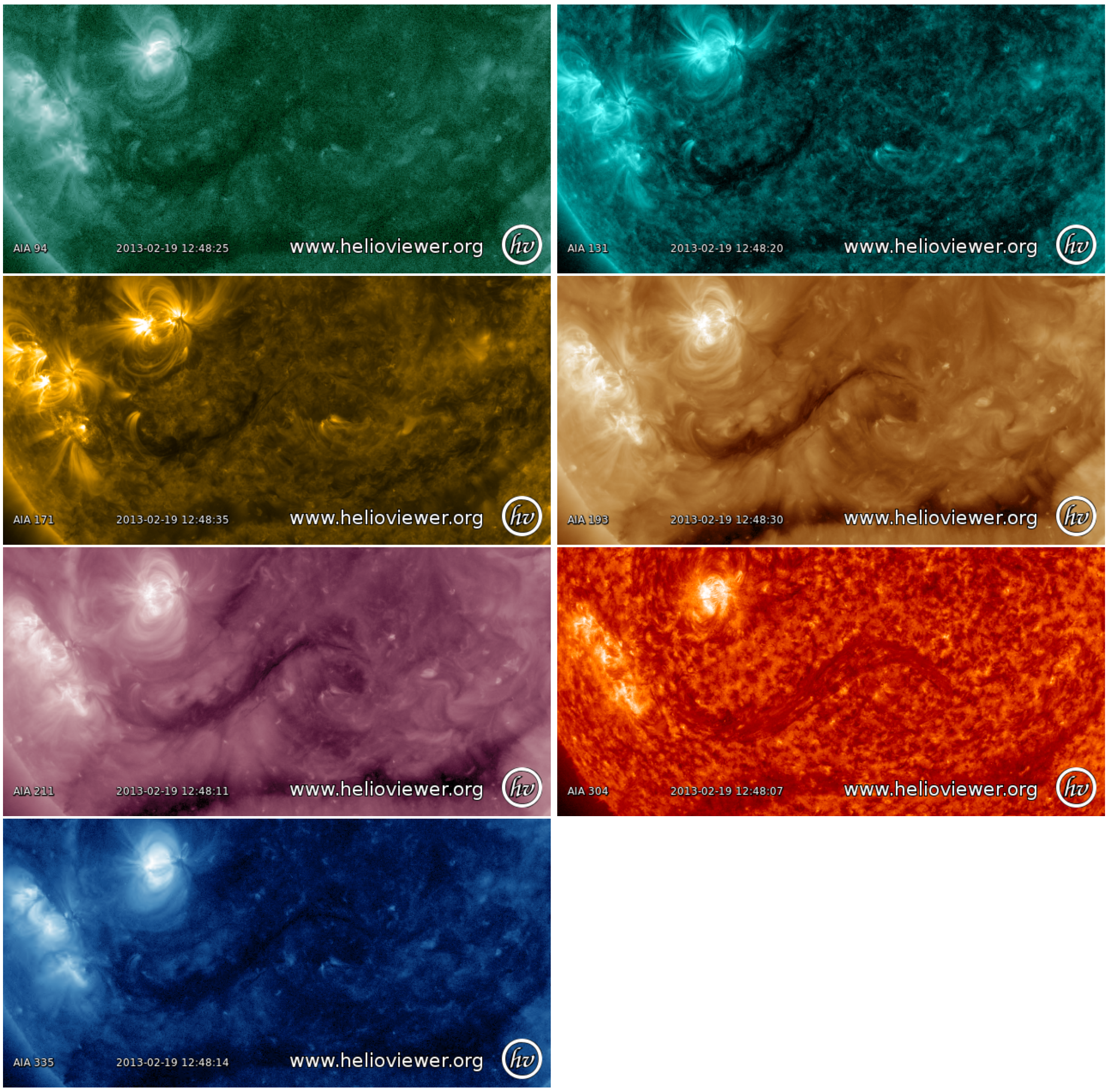

Figure 1.1: The prominence, studied later in Chapter 4, a week before its eruption in the 7 EUV wavelengths of SDO/AIA. The sigmoidal structure of the prominence is present on disk in absorption in all wavelengths, only appearing in emission when on the limb (not shown here) in 304 Å (bottom of right column) and weakly in 171 Å (left column, 2nd from top). Images created using quick-look data from `www.helioviewer.org`

could be considered to settle within the structure from the overlying corona to fill "dips" in the magnetic structure (Gibson, 2018). In the case of sheared arcades, plasma accumulates near the apices of the sheared loops. In the flux rope model, the mass collects in the "dips" of the poloidal field. In both models the dips form a continuous stream of plasma through the structure, which is then observed as the prominence. It was later shown by Karpen et al. (2001) that this continuous stream can actually allow the prominence to form without dips, though it was also noted that this was very likely to happen. Furthmore, Aulanier & Demoulin (1998); Aulanier et al. (1998, 1999) study the effects of multiple possible magnetic configurations of prominences, and concluded that a flux rope was the most likely configuration, but also noting that there is no guarantee that the mass will fill the dips. The two models cannot be entirely separated, as sheared-arcades can form MFRs as part of an eruptive process, though it is the onset of instability in MFRs that provides one preferential aspect in favour of the stable MFR model. Where relevant for this work, we will consider the prominence to exist as a MFR. The evolution of an MFR, whether pre-existing or newly formed, is highly dependent upon its relation to the background magnetic field, as will be discussed in Sec. 1.2.

1.1.1 Prominence Spectra

As mentioned previously, there are a few wavelengths one can use to observe the prominence in emission. However, with sufficient spatial, spectral, and temporal resolution it is possible to determine many properties of the prominence and its plasma. For instance: plasma temperature, non-thermal velocities, electron density, gas pressure, the ionisation ratio, and the flow velocity. We focus here on the direct inversion of spectra for the cool core plasma and optically thin hot PCTR plasma. There is an alternative semi-empirical method that uses iterative non-LTE radiative transfer functions but this is beyond the scope of this work. For a more detailed review of both see Labrosse et al. (2010), whose lead we follow here. In the simplest case one can recover the temperature and non-thermal velocities of a Gaussian-shaped line profile from the Doppler-width.

$$\Delta\lambda_D = \frac{\lambda_0}{c}\left(\frac{2kT}{m} + \xi^2\right)^{1/2} \quad , \tag{1.1}$$

where λ_0 is the rest wavelength, T the ion temperature, m the ion mass, and ξ represents the (usually Maxwellian distributed) non-thermal velocity that accounts for additional unresolved motions in optically thin plasma. In most works ξ describes the averaged line-of-sight value, and is affected by uncertainties in both the line-width measurement and T. As noted by Baudin et al. (2007), this is especially true for lines where it is difficult to establish the formation temperature, such as those produced by neutral and singly-ionised ions.

An upper limit may be placed on electron density from the Stark effect on Balmer lines (Inglis & Teller, 1939). Some alternative methods rely on the Hanle effect, which is a depolarisation due to the magnetic field (Bommier et al., 1986, and references therein). These methods utilise the additional collisional depolarisation that is proportional to density in certain lines, but not in others. Another alternative method relies on Thompson scattering, but can often only provide a lower estimate of the density (Jejčič & Heinzel, 2009, and references therein). Across these methods are found similar values ($10^9 - 10^{11}$ cm^{-3}), with the range coming not just from differences in technique but event, and positions within the event.

The ionisation degree. This can be most simply defined as the ratio of the proton density, n_p, (approximately equal to the electron density, n_e) to the neutral hydrogen density (which can be approximated to the population density of the ground state, kn_g). This plays an important part in determining the momentum balance. As this requires a simultaneous measurement of both $n_p(\approx n_e)$ and n_g few studies have been dedicated to this. Common reference values are found between $0.2 - 0.9$.

The gas pressure is important due to its role in determining β, the ratio of gas pressure to magnetic pressure, which is given by Whilst this tends to be fairly small for prominences where magnetic fields dominate, it is more directly observable. A common method for doing this is by taking the ratio of Hβ to Ca II, as originally suggested by Heasley & Milkey (1976). This value varies slightly over a prominence, but more so between prominences.

1.2 Field Instabilities

There are two principle classes of MFR eruptive instabilities; those that are based on resistive processes (i.e. rapid magnetic field reconfiguration) and those based on ideal MHD instabilities (i.e. magnetic pressure balancing). In all cases, however, the magnetic field plays an extremely important role in governing the onset and development of the eruption. Specifically, gradients in the magnetic field play a key role in whether an eruption will "succeed", i.e., whether the eruption will eject material into space. In some cases, such as Török & Kliem (2005), the eruptive mechanism cannot overcome the overlying magnetic field and the eruption will result in a "failed" or "partial" eruption. This is especially important when considering the torus instability as that mechanism is directly related to the magnetic field gradient, as will be discussed further in Sec. 1.2.2.2.

1.2.1 Resistive Eruptions

There are two primary models that rely on resistive processes; "tether-cutting" models (Moore et al., 2001), and "breakout" models (Antiochos, 1998; Lynch et al., 2008, 2D and 3D respectively)

1.2.1.1 Tether-Cutting Models

Tether-cutting models rely on the formation of an instability and reconnection below a prominence in a bipolar sheared system. This reconnection causes the eruption of the prominence, with a near-simultaneous flare also being possible. Moore et al. (2001) showed that a tether-cutting eruption would proceed, for sigmoidal systems, as follows and as illustrated in Fig. 1.2.

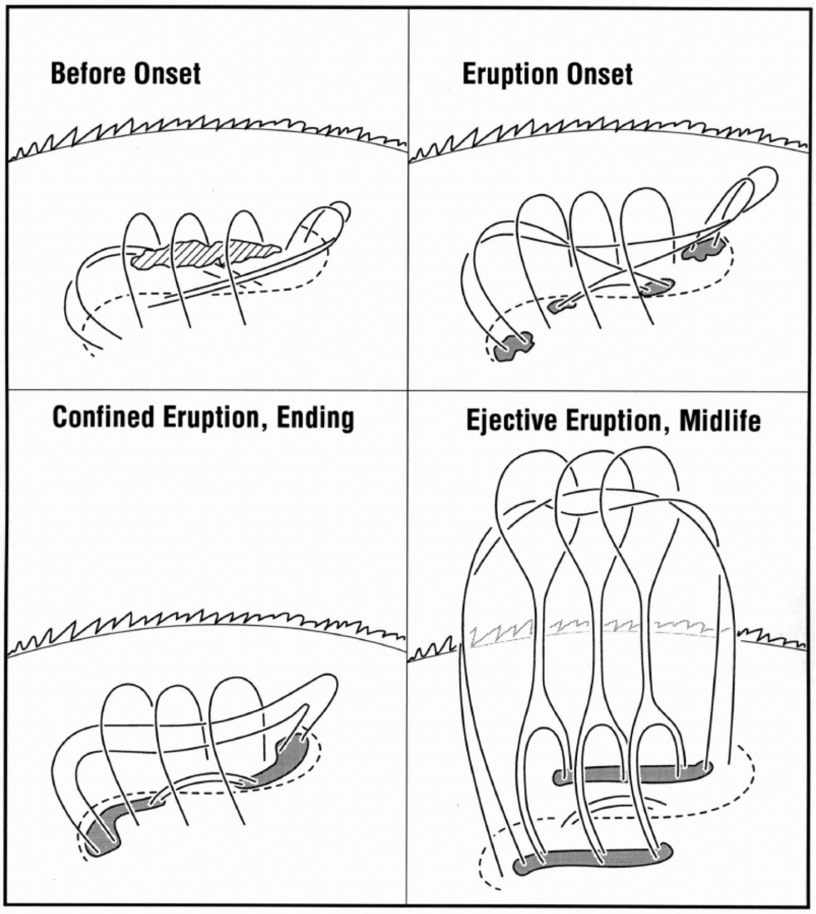

Figure 1.2: This cartoon shows the proposed evolution of an eruption under the tether-cutting mechanism, as shown by Moore et al. (2001). The basic configuration of the magnetic field are shown throughout the development of the instability, with the dashed line showing the polarity inversion line. The grey dashed area shows an example of mass that is sometimes present, and the solid grey areas show regions of flare emission caused by the reconnection.

First, Moore creates an arbitrary separation in the magnetic field between the inner “core” field, and the outer “envelope” field. The core field is rooted close to the PIL, with the envelope field covering the rest of the bipole that is rooted elsewhere. Before the eruption the sheared field is comprised of two oppositely curved “elbows”. The low-lying parts of the elbow, reach under the envelope field. The envelope field pushes the core field down, forcing the elbows to become almost horizontal and capable of carrying a prominence. These two elbows then shear past each other along the section of the PIL that separates them. The opposite elbows will then reconnect if they come into contact. This has also been labelled “J to S” reconnection by some authors. Thus, reconnection occurs due to the flux cancellation at the PIL below the prominence, i.e. the ‘tethers’ will be ‘cut’.

1.2.1.2 Breakout Models

Breakout models differ slightly in their mechanism of eruption between 2.5D and full 3D. However, they rely on largely the same physics, with 3D models actually being slightly simpler mechanically than the 2.5D models. Only a description of 3D models will be expanded upon here. As modelled by Lynch et al. (2008), the initial system consists of two distinct flux systems, with the boundary between forming a dome-like separatrix that encompasses the flux covering the active region’s (AR’s) PIL. There are also two spine field lines, as shown in figure 1.3, one connecting the separatrix surface to an AR of opposite polarity. The other originates in the opposite hemisphere and also connects to the separatrix surface.

A coronal null point is formed where the two lines meet. In a breakout eruption, reconnection occurs at a current sheet located at the null point, i.e between the inner-arcade field and overlying field. This transfers some of the overlying unsheared field from one side of the AR flux system to the other, and also from the outer background flux to the inner background flux. This additional flux

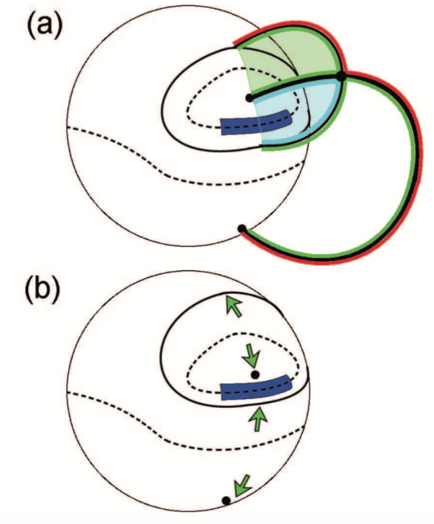

Figure 1.3: (a) shows the connection of the two spine fields. (b) shows the surface evolution of the AR separatrix dome and spine field during the breakout reconnection process. Image taken from Lynch et al. (2008).

being deposited over the PIL shifts the separatrix dome in one direction, and the spine fields the other. The system thus minimises the amount of unsheared flux that it is required to open when the low-lying sheared flux is ejected. The positive feedback between expansion of the stressed inner-arcade and rate of breakout reconnection at the null point eventually leads to the explosive eruption and flare reconnection process. In 3D, the eruption requires that the entire separatrix surface must open to eject the stressed, sheared field.

1.2.2 Ideal MHD Eruptions

Here we consider two ideal MHD instabilities: the kink instability (KI) (Török et al., 2004) and the torus instability (TI) (Kliem & Török, 2006).

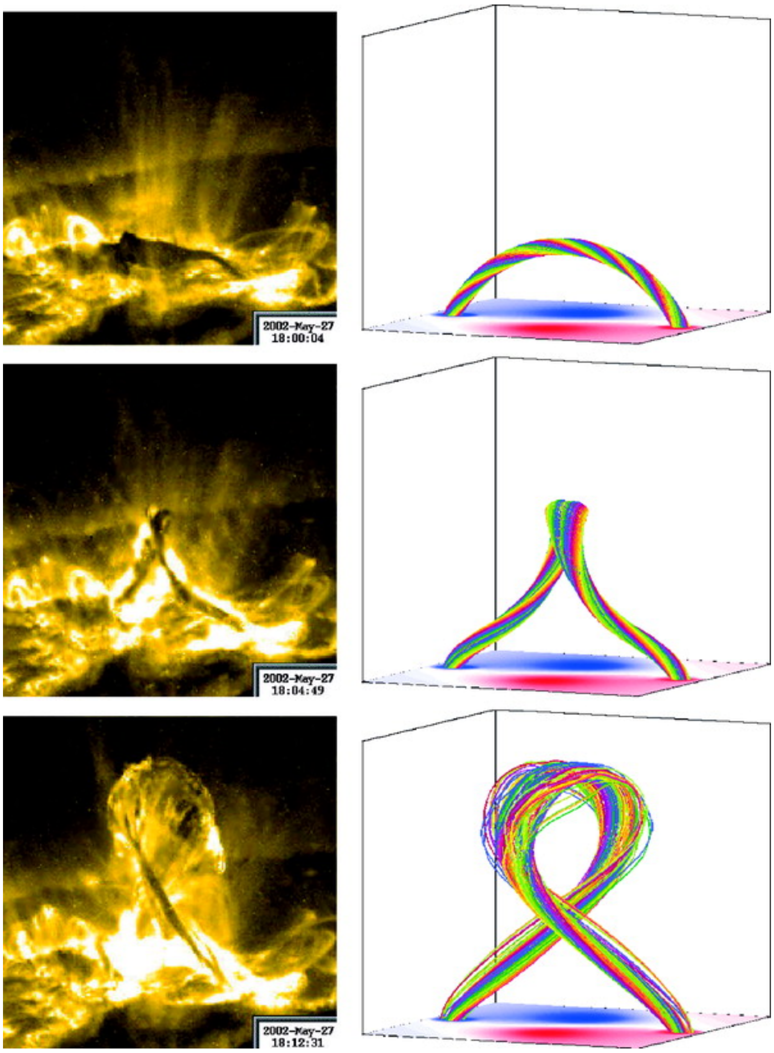

Figure 1.4: An example of the kink instability and its characteristic helical deformation from Török & Kliem (2005)

1.2.2.1 The Kink Instability

The kink instability, first suggested as an eruptive mechanism by Sakurai (1976), is one based upon the twisted nature of a flux rope supporting the prominence plasma. It can be imagined as twisting both ends of a string until it deforms on itself, or becomes "kinked". As shown by Török et al. (2004) the stability of a flux rope is controlled by the total twist, i.e. how much the field lines wind about the rope axis, and is given by

$$\Phi = \frac{lB_\phi(r)}{rB_z(r)} \tag{1.2}$$

where l is the length of the current-carrying flux system, r is the minor (toroidal) radius, and B_ϕ and B_z are the azimuthal and axial field components, respectively. Additionally, they note the importance towards stability of the radial profile of the twist, the effect of line-tying, the ratio of radius to twist scale length, and the effect of localising the current that results from magnetic twist to within a certain radius.

The instability is thought to occur once the twist exceeds a critical value. Hood & Priest (1979) showed that this critical value would be $\Phi_{crit} \geq 2\pi$ for a large aspect ratio coronal loop. Further numerical work on this topic performed by Galsgaard & Nordlund (1997) has shown this value to vary as a function of several properties, such as field strength, tube diameter, and magnetic resistivity to be in the range $4 \leq \Phi_{crit} \leq 8$. In some cases, such as shown in figure 1.4, once this threshold is reached the flux rope can erupt due to a vertical current sheet forming under the rising flux rope. In other cases it is thought that the kink instability may trigger the torus instability, which then causes the eruption. In either case, Fan & Gibson (2007) showed that the resulting eruption seemed to "rupture" the overlying arcade field by pushing it aside. Although it was previously thought that this model could only result in a confined, or "failed" eruption, Török & Kliem (2005) showed that the model could also account for ejective, "successful", eruptions. The actual mechanism for the instability is the conversion of the twist of the magnetic structure, Φ, to the dimensionless quantity of writhe, W. Writhe was defined by Calugareanu (1959) as a measurement of the helical deformation of the loop about the loop axis. This conversion lowers the magnetic energy by reducing the tension of the twisted field, and allows the conservation of helicity, defined as $H = (W + \Phi)F^2$, where F is the flux of the flux tube (Török et al., 2010). Though it has been suggested that this conversion is not a 1:1 process (Török et al., 2014). It was instead suggested that the amount of twist converted would be dependent on the number of helical turns that would develop along the axis of the flux rope during the evolution of the instability. This, in turn, would also depend on two things. Firstly, the wavelength of the most unstable mode, and secondly the range of the unstable modes that could be reached due to the finite length of the rope axis. For a full discussion of the conversion see Sec. 3.2 in Török et al. (2014). This would subsequently result in an exponential increase in the writhe during the linear phase of the instability, with writhe becoming saturated during the nonlinear phase. Recent modelling of the kink instability has shown that it is possible for it to be triggered by mass drainage (Fan, 2017; Fan et al., 2018; Jenkins et al., 2018). Figure 1 of Török & Kliem (2005), shown here as Fig. 1.4, reveals something important about the kink instability. Its development is dependent on the overlying field. In an active region, the overlying field gradient would be greater than over the quiet sun and would therefore be more likely to confine the development of the instability. Török & Kliem (2005) stated that this would be a major contributor in whether the instability would be able to saturate, or whether other processes, such as the torus instability, would begin to act on the flux rope.

1.2.2.2 The Torus Instability

The Torus instability can be thought of as a lateral kink instability distributed uniformly over the entire loop. Unlike the kink instability, however, it cannot be stabilised by the presence of a toroidal magnetic field component within the torus. It is perhaps better thought of as loss of equilibrium between a radially outward force of the flux rope (also known as the hoop force) and a radially inward force due to the pre-existing overlying field. This force balance was first described by Shafranov (1966), who considered it as a toroidal Lorentz force (the hoop force) and the net pressure gradient of a curved channel being balanced by an external poloidal magnetic field, B_{ex}, that is also generated by a Lorentz force. A possible cause for the loss of equilibrium was considered by Bateman (1978) who found that the torus would expand, after being perturbed, against an external poloidal field that decreased at a critical rate in the direction of the major radius, R. This dimensionless rate is called the decay index, n, and was derived by Bateman as

$$n = -\frac{d\ln(B_{ex})}{d\ln(R)} \ , \tag{1.3}$$

with a critical value at $n > 1.5$ if an overlying field gradient of $B_{ex} \propto R^{-n}$ is assumed. The torus instability for low beta plasma in a uniform magnetic field was investigated by Kliem & Török (2006). They concluded that the torus instability was a feasible mechanism for coronal mass ejections (CMEs), with the instability guiding their medium-scale expansion. Aulanier et al. (2010) presented simulations of such, showing rapid acceleration of a flux rope as it exceeded the critical decay index necessary for the instability to occur.

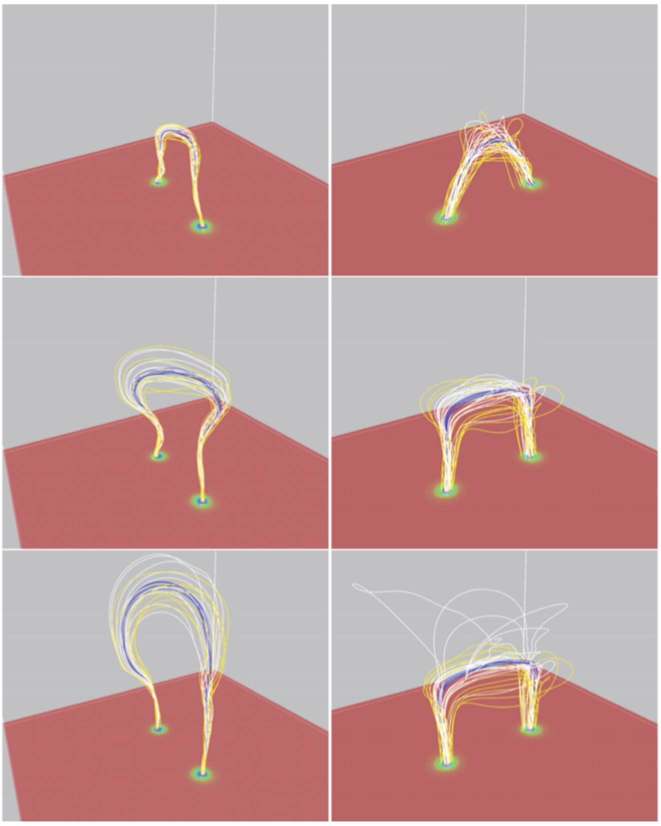

Figure 1.5: An example of a toroidal loop expanding as it rises. (Hood et al., 2009)

Given the importance of the critical value of the decay index in determining the role of the torus instability in an eruption, much work has been done on confining the possible range of values it can take. Table 1.1 presents measurements of the critical value, derived from both observations and simulations for events within both active and quiet Sun environments, across a range of studies. Here we group critical values based upon the location where it is determined. Note that papers in which the decay index has been defined beforehand (i.e. the authors have just applied a theoretical value of n), rather than recovered from the work itself have been excluded. As can be seen in Table 1.1, the critical value is generally found to be lower when measured at the top of the prominence mass

Table 1.1. Decay index values

Vertical Location Through Prominence/FR Structure	Critical Decay Index	Study Type	Source Region	References
Prominence mass	1.74, 2.04[a]	Obs.	AR	Liu (2008)
Prominence mass	> 2.5[b]	Obs.	AR	Liu et al. (2010)
Prominence mass	$0.98 - 1.68$[c]	Obs.	QS	Xu et al. (2012)
Prominence mass	≥ 1	Obs.	AR	Zuccarello et al. (2014a,b)
Prominence mass	1.20 ± 0.29[d]	Obs.	QS	McCauley et al. (2015)
Prominence mass	$0.9 - 1.1$	Obs.	AR	Lee et al. (2016)
Prominence mass (magnetic dips below FR axis)	1.1 ± 0.1	Sim.	AR	Zuccarello et al. (2016)
Prominence mass	$0 - 2$[e]	Obs.	QS	Aggarwal et al. (2018)
Prominence mass	1.2 ± 0.1	Obs.	QS	Sarkar et al. (2019)
Prominence mass	$0.8 - 1.3$	Obs.	AR	Vasantharaju et al. (2019)
FR axis	≥ 1.5	Ana.	...	Bateman (1978)
FR axis	≈ 1.5	Ana.	QS	Kliem & Török (2006)
FR axis	> 1.5	Ana.	AR	Kliem & Török (2006)
FR axis	~ 2	Sim.	QS	Fan & Gibson (2007)
FR axis (location of thin current channel)	1.1[f], 1.3[g]	Ana.	AR	Démoulin & Aulanier (2010)
FR axis	$1.5 - 1.75$	Sim.	AR	Kliem et al. (2013)
FR axis	1.5	Obs.	AR	Jiang et al. (2016)
FR axis	1.4 ± 0.1	Sim.	AR	Zuccarello et al. (2016)
FR axis (highest-lying NLFFF lines over PIL)	> 0.8[h]	Obs.	AR	Jing et al. (2018)
FR axis (cavity centroid)	1.3 ± 0.1	Obs.	QS	Sarkar et al. (2019)

Note. — a,b) Averaged over 42 – 105 Mm. c) For the five QS events averaged over 42 – 105 Mm. d) See Table. 5 in reference. e) Many events, each averaged over 42 – 105 Mm. See Fig. 5e in reference. f,g) For straight and curved current channels respectively. h) In the sample studied, all events showing decay indices >0.8 were ejective (i.e., all of the confined events had <0.8) although ejective events did span this threshold.

than at the location of the flux rope axis.

However, there are a few important points to consider when calculating the decay index. Firstly, as shown by Démoulin & Aulanier (2010), is the shape of the flux rope itself. Further to this point, the work of Garren & Chen (1994); Olmedo & Zhang (2010); Olmedo et al. (2013) consider the changes to the Lorentz self-force that are caused by deviations from axisymmetry. For the most part they find that small to moderate deviations do not have a significant impact. Therefore, for a mostly axisymmetric flux rope we should not expect any significant difference in the derived decay index. This will be discussed further in Sections 1.2.2.3 and 4.2.3. Secondly, Zuccarello et al. (2016) show there is a significant difference in regards to where it is measured. It was shown that changing the point from the flux rope's axis to the estimated top of the prominence changed the value from $n_{crit} \approx 1.4 \pm 0.1$ to $n_{crit} \approx 1.1 \pm 0.1$. The conclusion was therefore drawn that the apparent difference between theoretical and observational values of the decay index may arise from the difference in the point of measurement. This was lent further credence observationally by Sarkar et al. (2019), who compared the top of the prominence mass to the centre of the cavity centroid (assumed to be the location of the FR axis), and found differing values.

1.2.2.3 Observational signatures

KI – The most clear signature of the KI is the evolution of the shape of the prominence as it writhes. However, the writhe that causes this change in shape can also develop from shear-field-driven writhing, reconnection with the surrounding field, or the straightening of the sigmoid. Kliem et al. (2012) state that unambiguous signatures of the KI would be flux rope legs approaching each other, an apex rotation of over 130°, and multiple helical turns developing over the structure. However, the level to which these are visible is dependent on how far the instability develops which itself is dependent on the confinement of the structure. For an unconfined event we should not necessarily expect to see total saturation.

We should instead expect to see the structure show the development of writhe as it evolves, whilst at the same time being able to rule out or quantify the other sources of writhe. Accurate calculation of the writhe will require careful determination of the 3D structure.

TI – In the axisymmetric case, or in the case of small deviations from it, one should expect to recover the decay index measured from the centre of the torus, as shown by Eq. (1.3). However, a question remains open: what happens when the deviation from axisymmetry is significant? This can happen for several reasons, though we focus only on three. Firstly, the presence of mass in a flux rope can cause dips. Secondly, the footpoints of the flux rope can be so widely separated (e.g. in the case of quiet-sun or trans-equatorial prominences) requiring modelling as an ellipse section, and possibly one with a significant eccentricity (see Garren & Chen (1994)). Thirdly, the prominence may be sigmoidal. In reality it can be any combination of the above. We resolve this by relying on a simple feature; the direction of force balance. In the case of a sufficiently long, dipped flux rope, this is vertical rather than radial. Thus, we choose instead to define the decay index based on the vertical separation between the solar surface and the flux rope. This keeps the equation of the same form as Eq. (1.3), instead just requiring a change in definition in the direction of R. As the MFR itself may not be observed, we instead consider the prominence-mass leading edge (though the following statements are true for both). Assuming only minor variations on height and field gradient between any two neighbouring points along the prominence leading edge results in two observational signatures. Firstly, if the onset height can be determined the decay index should be smoothly varying if measured over neighbouring points along the prominence, but varying slowly over the length of the prominence and potentially over the course of the eruption. A slowly varying decay index should, in principle, allow us to rule out break-out and tether-cutting (i.e. non-ideal) eruption scenarios, that would otherwise lead to more abrupt decay index variation as, initially at least, it would only impact on part of the structure. As a result of this, one must be very careful about using a single critical value to define an event because the derived critical decay index may only be valid for a small section of the structure. Therefore the decay index should be evaluated along a significant portion of the structure. In addition, it should not be inferred that the observed height of the prominence leading edge at the time of eruption is necessarily the height at which the eruption has begun. This is due to the difference between the position of the prominence mass and the flux rope axis. The second signature is that the onset of acceleration of the eruption should be proportionally later in time for points measured along the structure that are further away from the structure's apex.

1.2.3 Prominence Eruptions and CMEs

At the end of a prominence's life it may erupt due to any of the mechanisms laid out in the previous sections. Though these eruptions are often considered symmetrical in theoretical works for ease, there is no condition that requires it. Their spatial configuration is instead dependent upon the symmetry of the host environment. In the case of flares, one can easily follow the EUV brightenings to determine symmetry (Tripathi et al., 2006). For eruptions without reconnection, or at least obvious reconnection, one must instead observe the prominence itself. In the symmetric case, the eruption will move outwards from its initiation point in both directions equally. In the asymmetric case, the eruption may begin at one footpoint and propagate to the other. Liu et al. (2009) separate the asymmetric case further into 'whipping' and 'zipping' sub-categories. 'Whipping' denotes one leg whipping outwards if the eruption initiates at the point at which it is anchored. 'Zipping' denotes the eruption 'zipping' away from the visible initiation point to the ‘invisible’ leg, which becomes visible as mass begins to drain from it. For visual examples of this see Figs. 14 and 16 in Liu et al. (2009). In a statistical study of erupting prominences McCauley et al. (2015) found that in the case of QS events 52% were symmetric, 39% were asymmetric, with the rest being indeterminable.

Some prominence eruptions will become a CME. This association is strong ($>$ 70%), but not one-to-one (Munro et al., 1979; Gopalswamy et al., 2003; McCauley et al., 2015). However, several works state that this is likely due to limitations in both the observations and their processing (Gopalswamy et al., 2003; Alzate & Morgan, 2017). CMEs are predominantly observed in Thomson-scattered white-light, and not in the collisional emission lines of the low corona. CMEs can usually be found to exhibit a three-part structure: the bright core, a cavity, and the leading edge, as can be seen in Fig. 1.6. In the case of prominence eruptions, this core is the expelled flux rope (House et al., 1981; Illing & Hundhausen, 1985; Webb & Howard, 2012; Hutton & Morgan, 2015). The transformation from flux rope to bright core was studied by Aulanier et al. (2010). Though they studied the evolution of a sheared system undergoing flux-cancellation and tether-cutting, they found that neither was actually capable of causing an eruption. Instead, the two could cause the creation of a flux rope and then drive it to the unstable regime of the torus instability. This view was expanded further by Aulanier (2014), who essentially reduced the currently proposed mechanisms of eruptions down to two real classes: drivers and triggers. Drivers are the mechanisms capable of driving the eruption to an eruptive regime, but cannot in of themselves cause an eruption. Triggers are the actual mechanisms of eruption; in that work either breakout or the TI. In the case of the work presented in Chapter 4, we investigate the role of the KI as a driver, and the TI as the trigger.

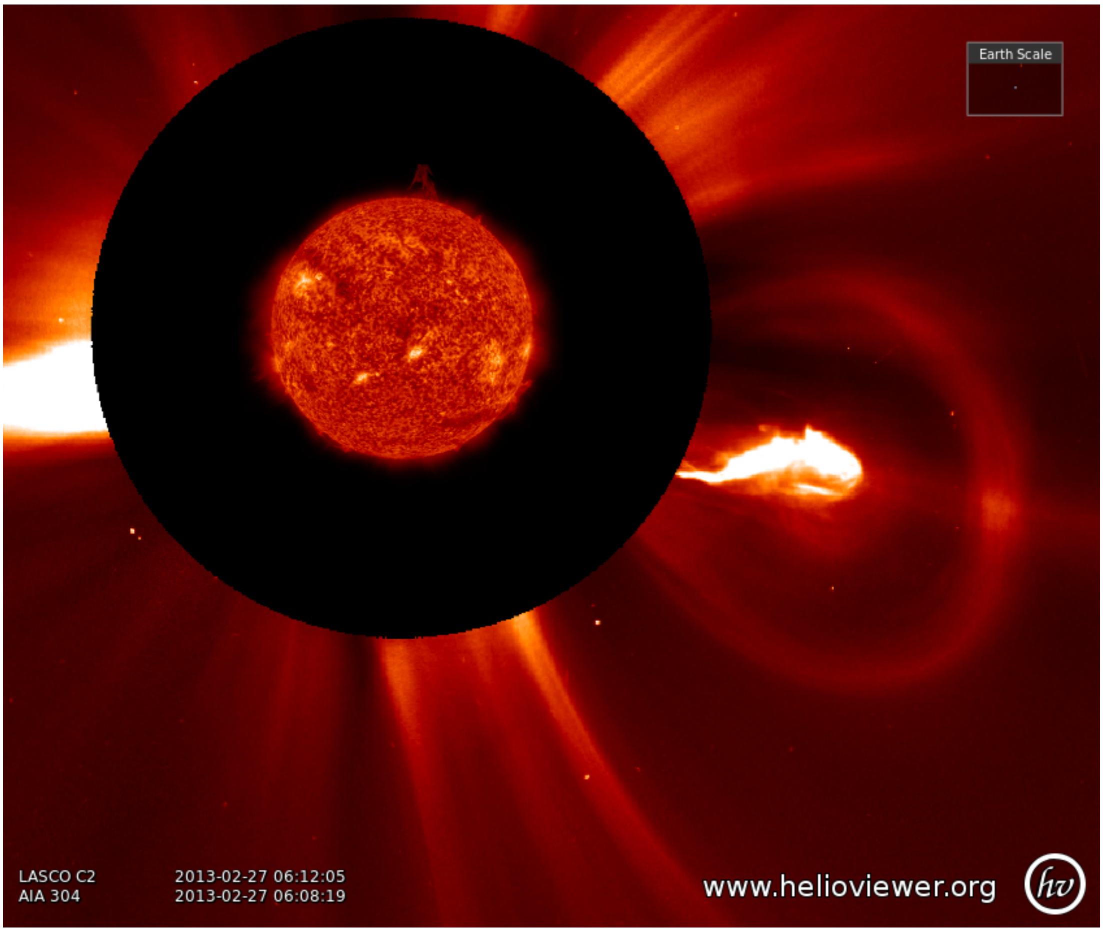

Figure 1.6: An example of a CME's three part structure: the leading edge, cavity and bright core. This is the CME related to the event studied in Chapters 3 and 4. Image generated using quick-look data from `www.helioviewer.org`

1.3 Fluid Instabilities

Despite much being known about the plasma of a prominence, less is known about the magnetic fields that comprise its structure. In addition to eruptive instabilities there are many small-scale instabilities, such as the interchange instability, and the Richtmyer-Meshkov instability that are associated primarily with fluid motion. Here we consider two; the Kelvin-Helmholtz instability (KHI) and the Rayleigh-Taylor instability (RTI).

1.3.1 The Kelvin-Helmholtz Instability (KHI)

The KHI is caused by the relative motion of two heterogeneous fluids along a boundary layer with sufficient shear force to overcome the surface tension. For instance, air moving over water will create water waves and crests. However, in the case of a magnetic plasma, the instability can be suppressed through several effects associated with compressibility and/or magnetic tension (Chandrasekhar, 1961). In the case of the Sun, one would expect to see the instability develop at the edges of dense coronal structures, such as prominences, and has been observed on multiple occasions, using both SDO/AIA and Hinode/SOT.

The first observation of the KHI in prominences was presented by Ryutova et al. (2010), who investigated an especially energetic branch of the instability. In particular, they studied the non-linear "explosive" branch for which they derived several properties. A key factor in this branch is the conversion of energy loss into an amplitude growth, effectively turning linear perturbations into non-linear growths. However, under specific conditions this explosive growth rate triggers stabilising nonlinear effects that compete to form a characteristic "mushroom cap" in the resulting plume. They concluded that this particular branch of the KHI would be characterised by a single plume moving through the prominence, rather than the series of plumes as would be seen with the RTI. This is given credence by a similar set of observational analysis by Berger et al. (2010). Whilst published earlier than Ryutova et al. (2010), they made no attempt to interpret the results as the KHI. However, in their Sec. 3.5 they note that:

"Plume formation in all prominences is highly intermittent, showing no clear spatial regularity or temporal periodicity. However, we find that when a certain location beneath a plume-forming quiescent prominence initiates a plume, that plume is often followed by several more at somewhat regular intervals". This would certainly match the interpretation of Ryutova et al., though one must ask what long-term periodicity one can expect from a highly turbulent medium.

Foullon et al. (2011) reported further evidence of the KHI in the solar atmosphere. Investigating a post-flare CME using AIA, though speculated to have involved a prominence eruption by Druckmüller et al. (2014), they found what they interpreted to be the linear phase of the instability on one side of the ejecting plasma, though whether the instability is observed at later times is debatable. The authors claim it is seen only in one wavelength (131Å, corresponding to 11MK) due to the enhanced emission against the corona. They note that their interpretation of the group speed of the instability versus, the speed of the ejecting plasma, is at the limit of the linear phase. If this was the case, then the sudden development of the non-linear phase provides an additional explanation to the sudden disappearance of the linear phase, beyond just the proposed rotation. They note that the extreme temperature may reduce the threshold for instability due to the enhancements to viscosity and thermal dissipation. Möstl et al. (2013) claimed to observe the KHI and performed subsequent simulations, albeit in 2.5D. Whilst their claim to an observation is entirely tenuous, the simulations they performed would certainly suggest it to be feasible. They also note the importance of a strong parallel **B**-field providing a stabilising effect on the prominence, thereby suggesting a reason as to why the instability would only be viewed on a single side of a prominence. The instability criteria for the KHI has been derived (Zaqarashvili et al., 2015) for twisted and rotating solar jets, and found to be at the point at which the kinetic energy of rotation becomes greater than the magnetic energy of twist. However, this derivation utilised linear and incompressible MHD equations, something that may not be strictly physical over longer time-frames. A further theoretical investigation by Martínez-Gómez et al. (2015) showed that turbulent flows in prominences with sub-Alfvénic flow velocities may be evidence for the instability in partially-ionised plasmas (See also

Khomenko, 2017). One of the main reasons that visual confirmation of the KHI is so difficult is due to the necessity of multiple peaks to be present to confirm the characteristic wavelength. Ideally, one would find enough peaks to confirm the characteristic wavelength, and also be able to show the evolution of the instability across multiple time-steps. There is observational evidence to support this scenario as reported by Berger et al. (2017a), but their use of Hinode/SOT's 25 second cadence may exclude the possibility of observing its evolution. The Kelvin-Helmholtz can also be found at the edge of plasma that is itself guided by the Rayleigh-Taylor Instability.

1.3.2 The Rayleigh-Taylor Instability (RTI)

The RTI is classically thought of as a more dense fluid falling through a less dense fluid, resulting in characteristic rising bubbles and falling plumes. For a pair of incompressible fluids of uniform density the growth rate can be calculated simply as

$$\sigma^2 = gk\left(\frac{\rho_h - \rho_l}{\rho_h + \rho_l}\right) \ , \tag{1.4}$$

where σ is the growth rate, g the constant acceleration due to gravity, k the wavenumber of the perturbation, and ρ the density subscripted with 'h'igher and 'l'ower. The term in brackets, $(\rho_h - \rho_l)/(\rho_h + \rho_l)$ is also known as the Atwood number, A (Chandrasekhar, 1961). In this case, as the wavenumber grows so too does the growth rate. Trivially one can see that due to the inverse relationship of wavenumber to wavelength, smaller scales will result in higher growth rates. It can also be easily seen that in any case where $\rho_h > \rho_l, \ \ \sigma > 1$ and the plasma is unstable. This can be extended into the magnetohydrodynamic case, into the Magnetic Rayleigh-Taylor Instability (MRTI), most simply through incompressible ideal-MHD to include the effect of a magnetic field (Chandrasekhar, 1961).

In this case, the magnetic field acts to suppress the growth of the instability as:

$$\sigma^2 = gAk - \left(\frac{(\mathbf{k} \cdot \mathbf{B})^2}{2\pi(\rho_h + \rho_l)} \right) \ , \tag{1.5}$$

where $\mathbf{B}$ is the magnetic field along an axis parallel to the interface, as seen in Fig. 1.7.

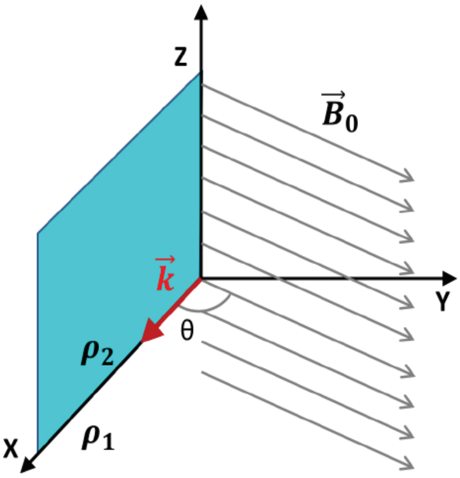

Figure 1.7: Schematic of the magnetic field orientation within the numerical domain, as shown in (Khomenko et al., 2014). Here B_0 is the magnetic field vector, and θ is the angle of the magnetic field to the interface.

The field acts to suppress the instability through magnetic tension, and takes the form of an Alfvén wave along the surface. Thus, when the magnetic field is present, the rate of growth becomes a competition between the force of gravity and the restoring force of magnetic tension. Due to the form of the numerator, we may consider two extreme cases. First we consider a magnetic field perpendicular to the plane of the plasma, i.e. $\mathbf{k} \cdot \mathbf{B} = 0$. In such a case the instability reduces back to eq. (1.4), i.e. the hydrodynamic case. Secondly, we consider a magnetic field parallel to the plane of the plasma, i.e. $\mathbf{k} \cdot \mathbf{B} = \mathbf{k} \parallel \mathbf{B}$. In this case the instability is most effected by the magnetic field. Furthermore, we can exploit the co-directionality of the wave vector and the magnetic field to derive the most unstable mode through the differentiation of eq. (1.5) with respect to k. This leads to

$$k_c = \frac{\pi g(\rho_h - \rho_l)}{B^2} \ , \tag{1.6}$$

where the subscript c denotes critical. As mentioned previously this can be exploited to find the critical wavelength of the most unstable mode

$$\lambda_c = \frac{2B^2}{g(\rho_h - \rho_l)} \ . \tag{1.7}$$

Generalising this to a magnetic field of any angle from the parallel, and taking a form more similar to that as presented in Khomenko et al. (2014), for reasons that will become apparent in Chapter. 5, we find:

$$\lambda_c = \frac{4\pi B^2 \cos^2\theta}{g\mu(\rho_h - \rho_l)} \ . \tag{1.8}$$

where θ is the angle between the magnetic field and the interface, and μ is the magnetic permeability.

However, in the solar context, and especially in the context of prominences the role of this wavelength is somewhat diminished. This is due to the partially ionised nature of the plasma. This means that although the ions will experience the magnetic field, and thus be appropriately suppressed, the neutrals will remain predominantly in the hydrodynamic regime, i.e. they will experience eq. (1.4) not eq. (1.5), and instead be influenced by the collisional frequency between species.

The observation and modelling of this instability in prominences, of which we will now give a brief overview has, up to this point, mostly focussed on bubbles rising from the seemingly evacuated voids (also confusingly called bubbles by many authors) that accompany them.

The first modelling of the MRTI on the Sun was performed by Isobe et al. (2005), who focussed on flux emergence. They found that it resulted in the spontaneous creation of prominence structures, and in patchy reconnection which they claimed was able to explain the intermittent nature of heating within the prominence structure.

The first observation of a bubble within a quiescent prominence was presented by Stellmacher & Wiehr (1973), and determined the properties of the rising bubbles in both Hα and Ca$^+$ (8542 Å). Stellmacher & Wiehr showed that the bubbles rose at $\sim$ 12 km s^{-1}. From the Ca$^+$, they were also able to determine that the bubble was not void of all material, but instead void of cool material.

The next observation of a rising bubble was presented in Berger et al. (2008). Using both Ca II H and Hα, Berger et al. were able to recover bubbles widths of 170-700 km, rise speeds of $\sim$ 20 km s^{-1}, and maximum heights of 10-20 Mm. They also hypothesised as to the exact mechanism of bubble formation. They first suggested that the bubble could be a result of thermal buoyancy, and performed some basic calculations that would put it at around 60,000 kelvin. Whilst this would certainly put the bubble outside the passband of the SOT, it fails to describes their magnetic fields. They further discount any explanation that would require a high β to exist within the bubbles, citing the fact that prominences are low β phenomena.

An alternative suggestion was presented by de Toma et al. (2008), who alongside presenting two sets of their own observations from the Mauna Lea Solar Observatory (MLSO), suggested the rising bubbles to be magnetically-closed low-density structures which become unstable and rise buoyantly through the prominence plasma. However, care must be taken when comparing these observation to others. This is due to the observed bright central core (in Hα) of these bubbles as they rise. This is not observed in any other observation of the MRTI, and as such may be a somewhat separate phenomena. This may be due to instrumental differences in bandpasses etc, as most observations are with Hinode/SOT.

Image sequences event clearly show that for the 2007-11 event, the bright core emerges from close to, if not, the surface of the Sun and disrupt the void from below which then causes the rising bubble. The authors also note an almost simultaneous bubble forms along the northern edge of the prominence, which they interpret to also have a bright core. de Toma et al. no found evidence of the bubbles in SOHO/EIT 304 Å, suggesting the bubble is devoid of matter between 10,000-80,000 K. This would disagree with the interpretation of the bubbles as regions of ~60,000 K plasma, though this is perhaps due to them being a different phenomena.

Chae et al. (2008) studied the flow patterns of prominence matter using Hinode/SOT. Whilst they do not claim to observe the RTI, they find a region from which plasma consistently flows firstly horizontally, and then vertically downwards. Their inclusion here will become obvious shortly. Due to the length that the plasma travels along the horizontal direction it is likely that the field lines themselves are horizontal. They conjecture that the sudden change in direction is due to the formation of dips in the magnetic field, where the plasma is able to accumulate and ultimately fall. They remark that the horizontal width of the falling blob may be indicative of the ratio of the horizontal component of the magnetic field to the vertical i.e. $w \propto B_x/B_z$ (see Sec 4 in reference for a full discussion).

Next we look at the work of Chae (2010). These "knots" are from the same event, and therefore identical to the downward plumes studied previously by the author. In this work they look more closely at the kinematics of the plumes, finding downward velocities in the range of 10-30 km s^{-1} with an average of 16 km s^{-1}, and accelerations of -0.1 to 0.1 km s^{-2} averaging around 0 km s^{-2}. They posited that occasionally the plumes would undergo impulsive acceleration, something they interpreted as evidence of the dips they form from reconnecting.

They also infer several other general properties of the acceleration of the plumes, which may miss more simple explanations. For instance, they state the plumes are constantly interacting with the horizontal field lines they are falling through, but do not state how this will effect the determined acceleration. They instead infer that the plumes are not constantly falling under gravity but are rather sequentially impulsively accelerated. This misses the fact that if the plumes are interacting with the field lines, they will be constantly deflected. This means that the recovered plane-of-sky displacement will vary dependent on the strength of the deflection, and thus the apparent acceleration will change. For instance, if a plume is moving almost entirely perpendicularly to the plane-of-sky is deflected such that its direction is now entirely downward in the plane-of-sky the recovered acceleration will appear to increase. Furthermore, if a field line has just undergone reconnection and is returning to an "un-dipped" configuration (most likely through a damped oscillation), it will impart an upwards acceleration to any plume.

The reason we have included these works is due to the conjecture of van Ballegooijen & Cranmer (2010), who looked at how the prominence structure may be the result of heavily tangled field lines, and that these downflows are in fact RT unstable.

The MRTI in quiescent prominences was expanded upon by Ryutova et al. (2010). They determine that the observational growth rate of the plumes can be determined simply through their kinematics, and related to the theoretical growth rate as

$$\sigma_{\text{obs}} = \frac{1}{t_2 - t_1} \ln\left(\frac{h_2}{h_1}\right) \ , \tag{1.9}$$

where t is time, h is height, the subscripts 1 and 2 refer to two separate time frames, and the theoretical growth rate is

$$\sigma_{\text{th}} = \sqrt{\frac{2\pi g}{\lambda} A \left[1 - \frac{B^2 \cos^2 \theta}{(\rho_h - \rho_l) g \lambda}\right]}\,, \tag{1.10}$$

which will be used and expanded upon later in Chapter 5.

The evolution of the downflows was studied further by Haerendel & Berger (2011). They describe these plumes as finite plasma packets forming through vertical structures that disconnect them from their inflow field lines under the force of gravity. They further describe how the plumes are acted upon and decelerated by the excitation of waves in the field lines they are falling through. Furthermore, and a further reason they are included here, is how to relate the observed widths and speeds of the plasma to their density, temperature, and magnetic field strength. This will be expanded upon in Chapter 5.

The first direct simulations of the upflowing bubbles were presented by Hillier et al. (2011, 2012) in the context of the the Kippenhahn–Schlüter model of a prominence. They determined the relative importance of several initial conditions that the development of the bubbles are dependent on. For instance, the ratio of the bubble width to the current sheet width plays a greater role than β in the determination of the bubble velocity.

Díaz et al. (2012) studied the RTI in a partially-ionised plasma consisting of two fluids. They found that the critical threshold of instability is unaffected by the compressibility and ion-neutral collision rate. However, the inclusion of ion-neutral collisions was found to be essential in order the describe the evolution of the instability in prominences.

Terradas et al. (2012) investigated the potential relationship between the RTI and a thread's lifetime in the context of an infinitely long slab. They report that for threads in quiescent prominences, one should expect short lifetimes.

Further numerical modelling of this instability has been attempted by Khomenko et al. (2014) using the MANCHA [1] code for a partially-ionised plasma consisting of one fluid. They found that the inclusion of an ambipolar diffusion term increases the growth rate of small-scale nodes in the non-linear regime by up to a half, and an increase in temperatures of up to almost a third.

They also found a small, but not necessarily meaningful increase in velocities. However, these simulations are done only in 2.5D, which would therefore neglect the superposition of the modes formed in a 3D system. These modes would take perturbation components that are both parallel and perpendicular to the applied magnetic field, as noted by Hillier (2016). Hillier also suggests that the magnetic field does not stabilise small scale perturbations, but rather plays a role in determining the ratio between parallel and perpendicular components.

The interplay of the rising bubbles and falling plumes was investigated numerically by Keppens et al. (2015), who found particularly good agreement between their low field case and observations.

This modelling work was expanded by Xia & Keppens (2016) for a twin-layer prominence, where it was suggested that the horizontal and vertical threads of previous observations and models were actually the same structure viewed from two different angles.

As mentioned previously, Hillier (2016) showed the effects of mode superposition. However, other important features were also introduced. For instance, it was shown that the non-linear regime begins once the boundary between the two fluids had deformed more than $1/k$ in the z-direction. It was also shown that the growth rate of the most unstable mode for a given magnetic field angle, θ, is given by

$$\sigma^2 = \frac{Agk}{2} \, , \tag{1.11}$$

which makes it independent of the magnetic field strength. Perhaps most impor-

---

[1] `http://www.iac.es/proyecto/spia/pages/codes.php`

tantly however if the instability does grow according to Eq. (1.11), then it must tend towards the mode with the largest wavelength. This would necessitate a finite width to the density transition layer, or shear in the magnetic field.

Ruderman (2017) studied the effect of compressibility on the RTI, with limited success. It was found that application of the derived results was questionable, with the inverse of the wavenumber of the most unstable mode not matching those found in observations.

Lastly, we look at the work of Berger et al. (2017b). Returning to Hinode/SOT observations no evidence was found of reconnection-led downflows (as suggested by Chae, 2010), though this may be on a case-by-case basis. The primary purpose of the study was the investigation of mixed KH/RT instabilities, and a strong shear force capable of generating the KHI greatly suppressed the RTI.

We will next look at the instruments and satellites used in this work (Chapter 2), their use in the 3D reconstruction of a prominence, and then the role of large-scale instabilities in a prominence eruption (Chapter 4), before returning to small-scale instabilities in Chapter 5

Chapter 2

Instrumentation

Thunderbirds are go!

Jeff Tracey, *Thunderbirds*

In order to study the kinematics of the kink and torus instabilities and their relation to the event, we use two satellites: the Solar Dynamics Observatory (SDO), and the Solar Terrestrial Relations Observatory (STEREO). Later, we will study the Rayleigh-Taylor and Kelvin-Helmholtz instabilities using the Swedish Solar Telescope (SST). The following sections will discuss the instruments we use aboard these satellites.

2.1 The Solar Dynamics Observatory (SDO)

The Solar Dynamics Observatory (Pesnell et al., 2012) was launched on 11th February 2010 as part of the Living with a Star programme. The goal of SDO is to understand the influence of the Sun on, and near, Earth by studying the solar atmosphere at high spatial and temporal resolution across multiple wavelengths. SDO carries three instruments, however we focus on the Atmospheric Imaging Array (AIA) (Lemen et al., 2012) and The Helioseismic and Magnetic Imager (HMI).

2.1.1 The Atmospheric Imaging Array (AIA)

As depicted in Fig. 1.1, AIA is capable of providing full disk images in seven extreme ultra-violet (EUV) wavelengths, of the Sun at 0.6"/pixel resolution every 12 seconds out to 1.5 solar radii using 4096×4096 CCDs.

These seven wavelengths allow a view of the Sun ranging in temperature from a few tens of thousands of degrees to a few tens of millions of degrees Kelvin. Each channel is dominated a different spectral line, and subsequently observes different aspects of the Sun's atmosphere. For the purpose of this work, we focus on the 304 and 171 Å channels. 304 Å observes plasma at emittance temperatures characteristic of the chromosphere and transition region. This makes it ideal for studying prominences, which appear strongly in emission at these temperatures. This line observes mostly the He II line at 303.8 Å, but also contains emission from the SI XI line at 303.4 Å, which may contribute up to 20% of the detected intensity. The Fe IX line at 171 Å is also capable of detecting a prominence in emission. There is some overlap between the response functions of 304 Å and 171 Å, as can be seen in Fig. 2.1, however 171 Å is dominated by plasmas at temperatures characteristic of the quiet corona and upper transition region. This makes it capable of studying prominences, or more specifically the PCTR. In Fig. 2.1 we include the wavelength and temperature response functions of both 171 and 304 Å.

2.1.2 The Helioseismic and Magnetic Imager (HMI)

HMI (Schou et al., 2012) is capable of full disk images of the continuum, line-of-sight magnetic fields, and the vector magnetic field of the photosphere centred at the Fe I absorption line at 6173 Å from which several data products such as Doppler shifts can be attained. Using two 4096×4096 CCDs HMI has a cadence

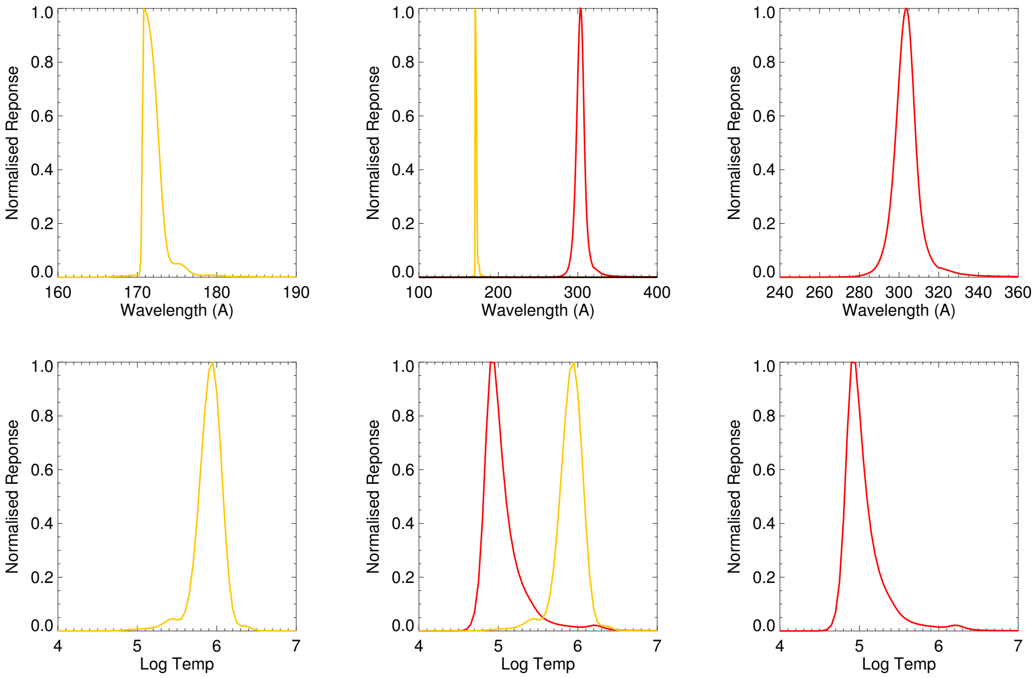

Figure 2.1: The top row shows the wavelength response functions of 171 (gold lines), and 304 (red lines) Å separately and combined. The bottom row shows the temperature response functions of 171 (gold lines), 304 (red lines) Å separately and combined.

of 45s for the Doppler shifts, continuum, and line-of-sight magnetic fields, with a slower cadence for the full vector magnetic fields. Here we use the line of sight magnetograms of the photosphere.

2.2 STEREO/EUVI-A

The Solar Terrestrial Relations Observatory (STEREO)(Kaiser et al., 2008) is a twin satellite mission in which one satellite orbits the sun ahead (A) and the other behind (B) Earth's own orbit. Launched on 26th October 2006 the satellites were designed to allow stereoscopic imaging of the Sun. Here we only consider the Extreme UltraViolet Imager (EUVI) (Wuelser et al., 2004) contained within

SECCHI onboard STEREO-A. EUVI-A is capable of providing full disk images in four wavelengths, 171 Å, 195 Å, 284 Å and 304 Å at 1.6"/pixel resolution out to 1.7 $R_\odot$. The cadence, however, varies with wavelength and the distance from Earth. In the case of the observations shown later the cadence for EUVI-A 304 Å is 10 minutes. Due to the 2 hour cadence of EUVI-A's 171 Å channel we do not include it for analysis here.

2.3 SST/CRISP

The Swedish 1-metre Solar Telescope (SST) is a vacuum tower solar telescope based at the Observatorio del Roque de los Muchachos on the island of La Palma. Its 1-metre aperture is supported by adaptive optics, and has been at full operation since 21st May 2002 (Scharmer et al., 2003). The SST has a spatial resolution of 0.14 arcsecs per pixel in Hα (6563 Å). Of primary interest is the CRisp Imaging SpectroPolarimeter (CRISP, Scharmer et al., 2008), which operates between 510 nm to 860 nm. Two of its three CCD cameras are narrow band, with a FWHM of 0.3 to 0.9 nm, with its third being wide-band. These tunable pre-filters utilise a dual Fabry-Pérot interferometer.

We now look at the use of SDO and STEREO as part of the investigation of ideal-MHD instabilities in a prominence eruption.

Chapter 3

The 3D Reconstruction of a Prominence Eruption

Slowly, slowly, slowly getting
faster

Count von Count
Sesame Street

Parts of this chapter form the basis of content of a paper entitled "2D and 3D Analysis of a Torus-Unstable Quiet-Sun Prominence Eruption" that has been submitted to The Astrophysical Journal in collaboration with my supervisors, Drs. E. Scullion and D.S. Bloomfield.

3.1 A Brief Overview

In the early hours of 27th February 2013 a quiet-sun prominence erupted from the south-western limb of the Sun, resulting in a CME[1]. Due to the location of the eruption, it was observed in the 304 Å wavelength channel of both SDO/AIA,

---

[1] `http://sidc.oma.be/cactus/catalog/LASCO/2_5_0/2013/02/CME0111/CME.html`

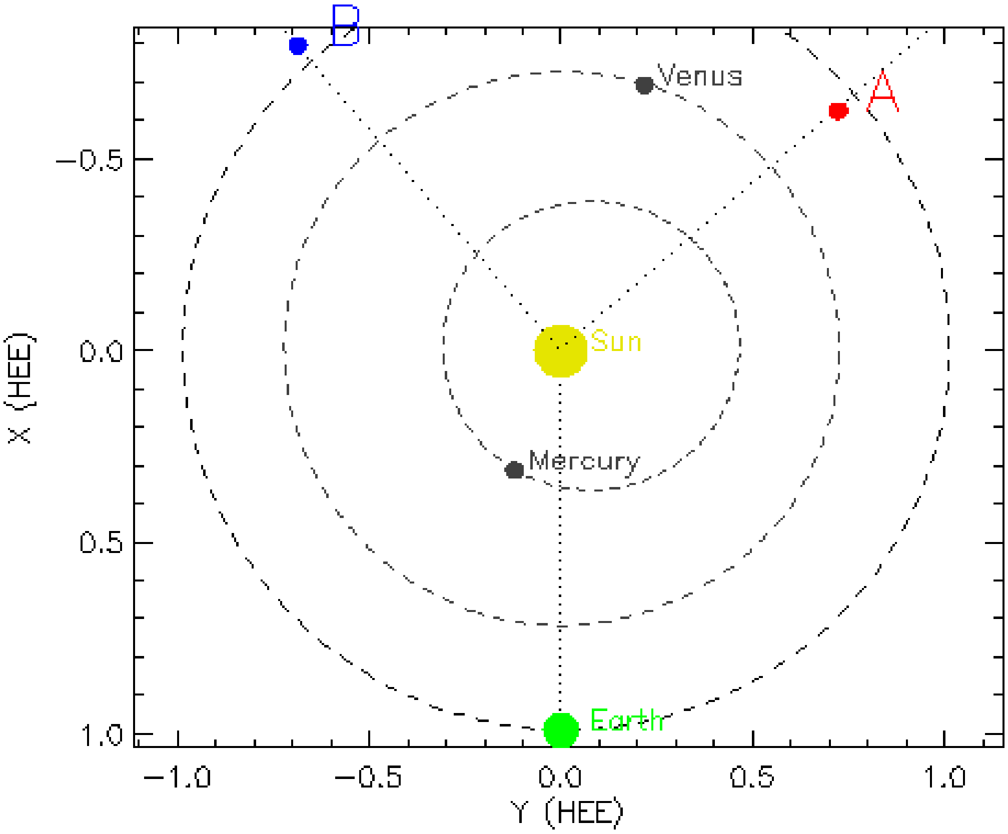

Figure 3.1: Relative positions of SDO (Earth), and STEREO-A (represented by A) at the time of the eruption.

and STEREO/EUVI-A, the relative positions of which may be seen in Fig. 3.1. As these two satellites were separated by 131° stereoscopic reconstruction can be performed. This method is illustrated in Fig. 3.5, and explained fully in Sec. 3.2.

3.1.1 X-Ray Time Series

Before we look at the possible ideal-MHD mechanisms of this eruption, we first rule out resistive mechanisms. Visual analysis provides no obvious reconnection sites (i.e. localised transient brightenings).To verify the lack of presence of reconnection as a driving force of the eruption, quick-look data from the RHESSI and GOES X-ray satellites were inspected. RHESSI and GOES provide full disk intensity profiles in various X-ray wavelengths. Thus, an increase in intensity in any channel in either instrument requires one to check the full disk using imaging instruments, such as AIA, for possible sources. As this eruption took place sometime between 00:00 to 05:00UTC any brightening over this period was checked. There is a brightening recorded by GOES around 00:30:00UTC (labelled ‘A’), as can be seen in Fig. 3.2, during RHESSI night time, but this is most likely due to a minor brightening event in an active region (NOAA 11681) near the north-eastern limb. Whilst a small brightening was found in the two lowest channels of RHESSI, 3-6 and 6-12 KeV (see Fig. 3.3 where it is labelled ‘B’), around 01:20:00UTC this is most likely due to small brightenings in the active region (NOAA 11682) nearest disc centre. There are also some brightening in these lowest channels and in GOES around 02:30:00 to 03:30:00UTC (labelled ‘C’). This again, is most likely due to activity in the AR near disc centre.

Therefore as there is no conclusive evidence that reconnection was the driving force behind the eruption, we assume that the eruption developed due entirely to magnetohydrodynamic processes.

3.2 3D Reconstruction

As coordinated observations are available from both SDO/AIA and STEREO/EUVI-A it is possible to use the SSWIDL routine scc_measure.pro to recreate the prominence in 3 dimensions. This works by having the user select a point in one image, which is then drawn as a line of possible points in the other image, which simultaneously observes the prominence at a different viewing angle. This is done through the conversion from the user selected helio-centric Cartesian co-ordinates to the helio-projective Cartesian. The user may then select the point along the line that they believe matches the original point. Once both have been chosen

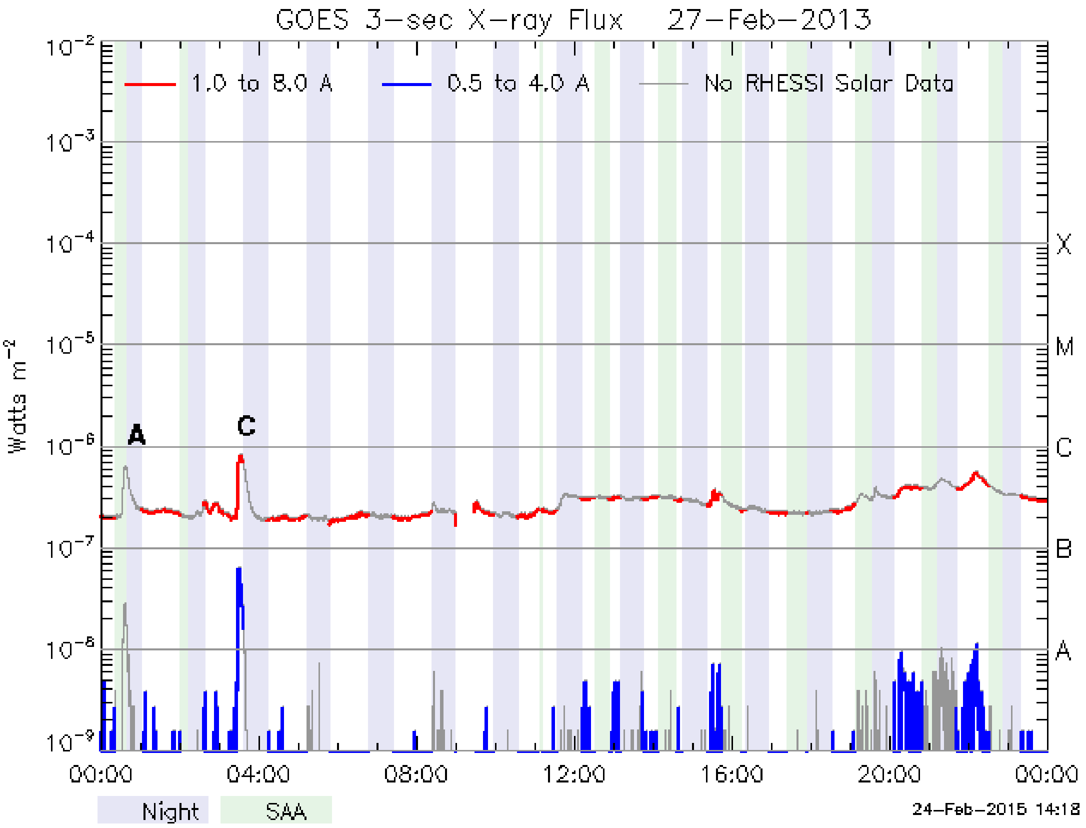

Figure 3.2: The GOES 3-sec X-ray Flux. The grey sections correspond to regions where the satellite enters 'Night' mode, and the light green sections show where the satellite enters the South Atlantic Anomaly (SAA). The red line shows the X-ray flux recorded between 1.0 and 8.0 Å, and the blue between 0.5 and 4.0 Å. The labels 'A' and 'C' refer to events discussed within the text.

the routine outputs the position information.

For an example, see Fig. 3.4. Here, when the user clicks on a point in the AIA FoV (left panel) the line appears in the EUVI-A FoV (right panel). When the user then clicks on the respective point in the STEREO FoV the stereoscopic 3D co-ordinate is then calculated and output. The scc_measure process was repeated three times. A different "consistent" feature of the prominence was chosen from the EUVI-A FoV each time for the same AIA points. In the first the northern-most edge of the prominence, in the second the centre (shown as the green line along the prominence in fig. 3.5), and in the third the southern-most edge. This process was repeated for each image-pair of AIA and EUVI-A 304 Å over the

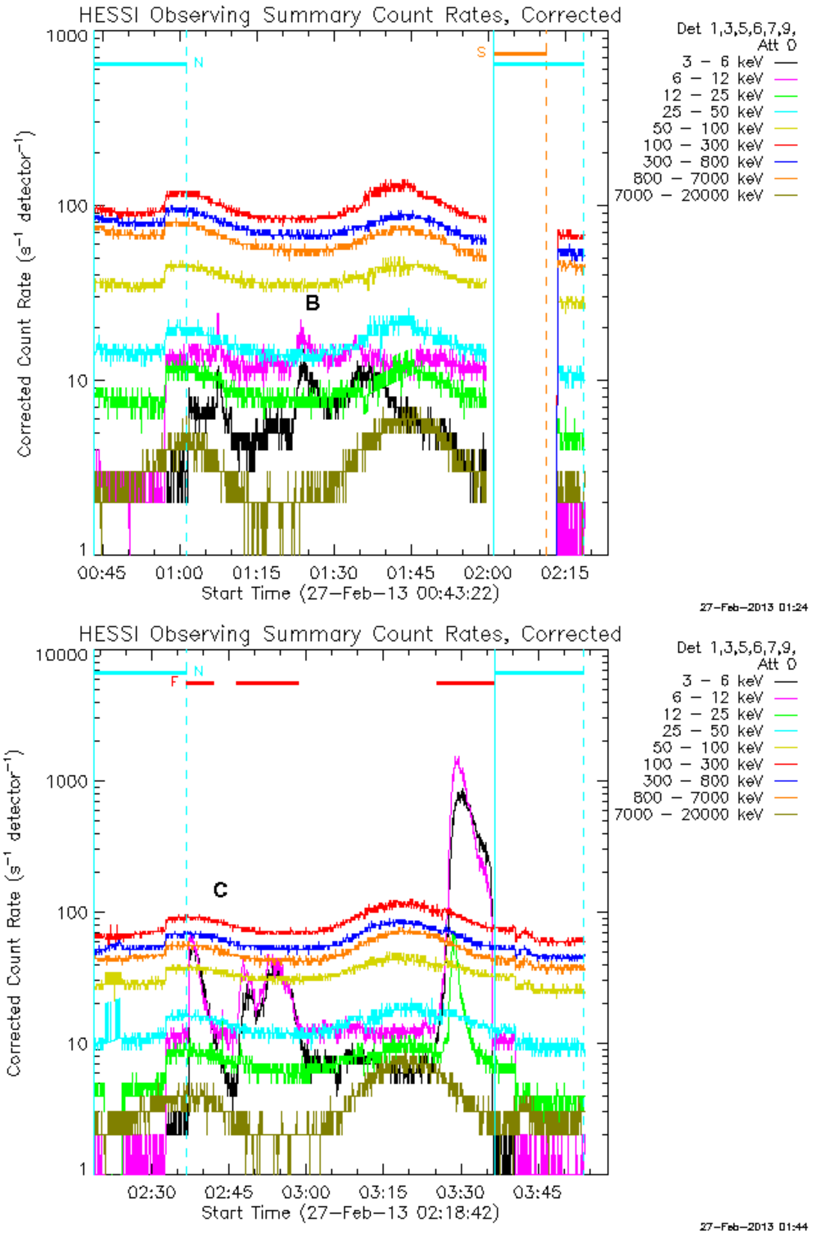

Figure 3.3: The RHESSI X-ray light curves from 00:45 to 03:45 UTC on 2013/02/27 showing the X-ray flux across the 9 channels. The labels ‘A’ and ‘B’ correspond to the same events shown in Fig. 3.2. The Light blue sections marked ‘N’ show when RHESSI enters ‘Night’ mode, the orange regions marked ‘S’ show entry into the SAA, and the red sections marked ‘F’ show the occurance of a flare.

time range. As such, this is limited to the STEREO cadence of 10 minutes. This will be discussed further in Sec. 4.2.2. As part of this, the apex of the prominence was calculated for each image-pair. We then used these co-ordinates

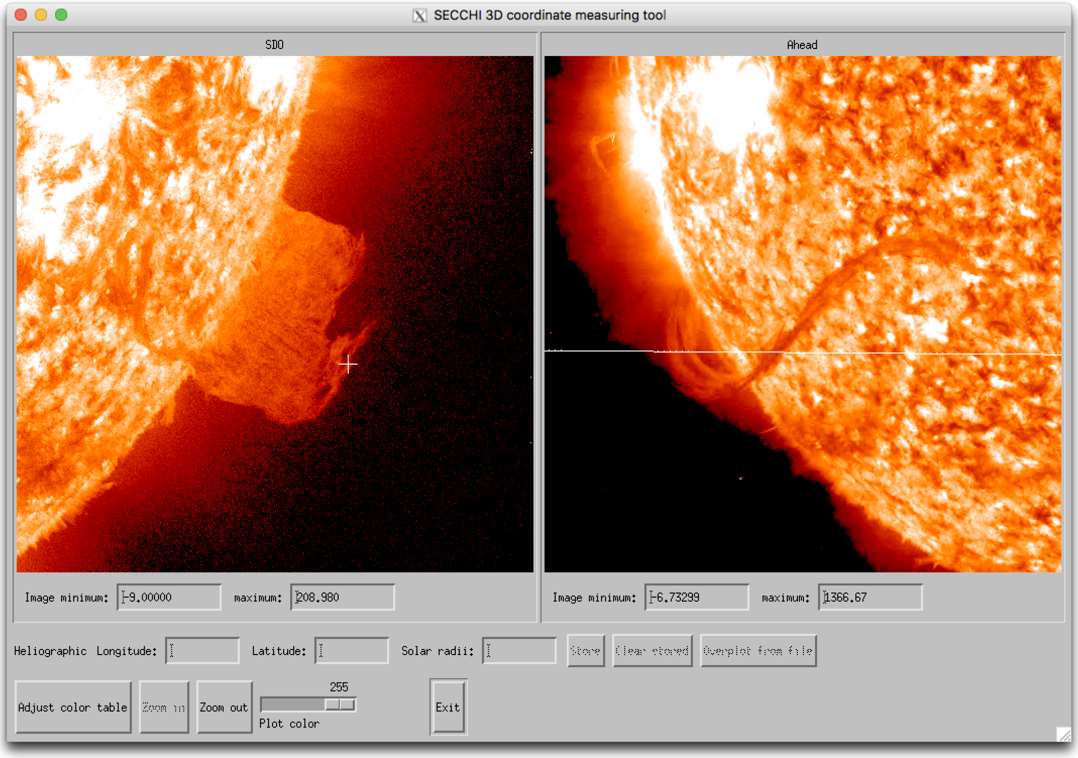

Image minimum: -9.00000 maximum: 208.980

Image minimum: -6.73299 maximum: 1366.67

Plot color: 255

Figure 3.4: The user interface for scc_measure with the clicked point in the AIA FoV (left), and the corresponding drawn line in the EUVI-A FoV (right).

for positioning a radial slit used to reproduce a height-time plot from which we calculate radial velocities by two different approaches. The data is then extracted from this slit to allow the construction of height-time plots. The reconstructed 3D co-ordinates (in latitude, longitude, and radial height) were converted from the World Co-ordinate System (WCS) to heliographic co-ordinates, using the standard WCS SSWIDL routines, as part of the pre-extraction preparation. Due to this we are also able to correct for solar rotation throughout the eruption as part of the height-time plot building. While this correction was small over the short time-span of this eruption, the functionality is present. The velocity due to the movement of the prominence as it moves around the Sun would correspond to an apparent height speed of approximately of 0.4 km s^{-1}.

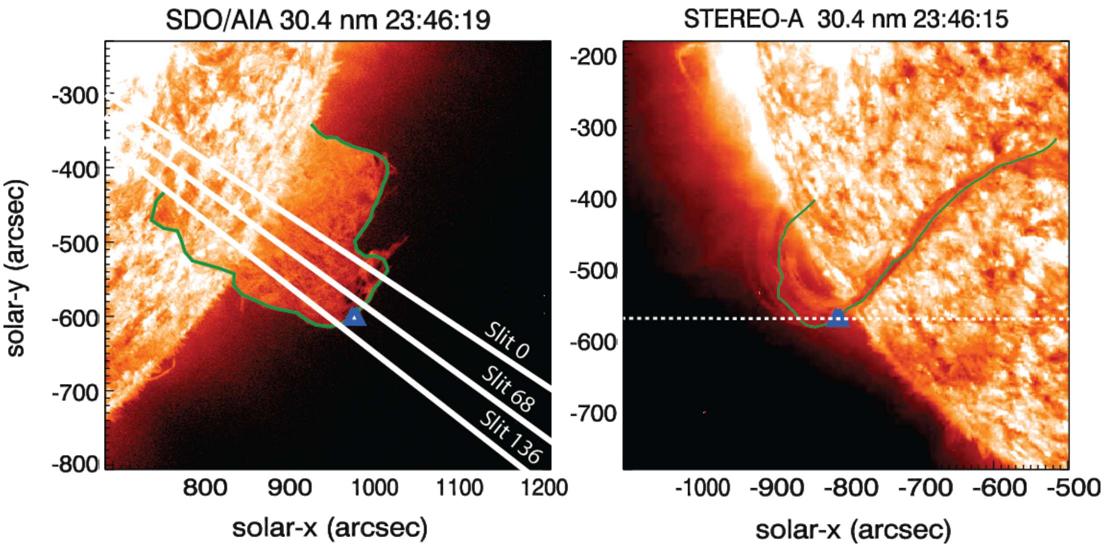

Figure 3.5: Co-temporal SDO/AIA 304 Å and STEREO-A/EUVI 304 Å intensity images of the prominence. The left AIA-panel shows the range of the 137 slits used for kinematic analysis. The blue triangle shows the position of the apex in both FoVs as recovered from the sterescopic reconstruction. The green line shows the position of the reconstructed edge along the spine of entire structure at the time shown.

As can be seen in the two right-most columns of Fig. 3.6 the apex of the structure slowly moves towards the centre of the prominence as it erupts. This is perhaps in part due to the asymmetric nature of the eruption, wherein the centre of the loop rises both the earliest and highest - this will be discussed in greater detail in Sec. 4.2.2. This may have something to do with the nearby southern coronal hole deflecting the erupting prominence as has been shown to be possible in Aulanier et al. (2010) and Zuccarello et al. (2012), but is not investigated further here.

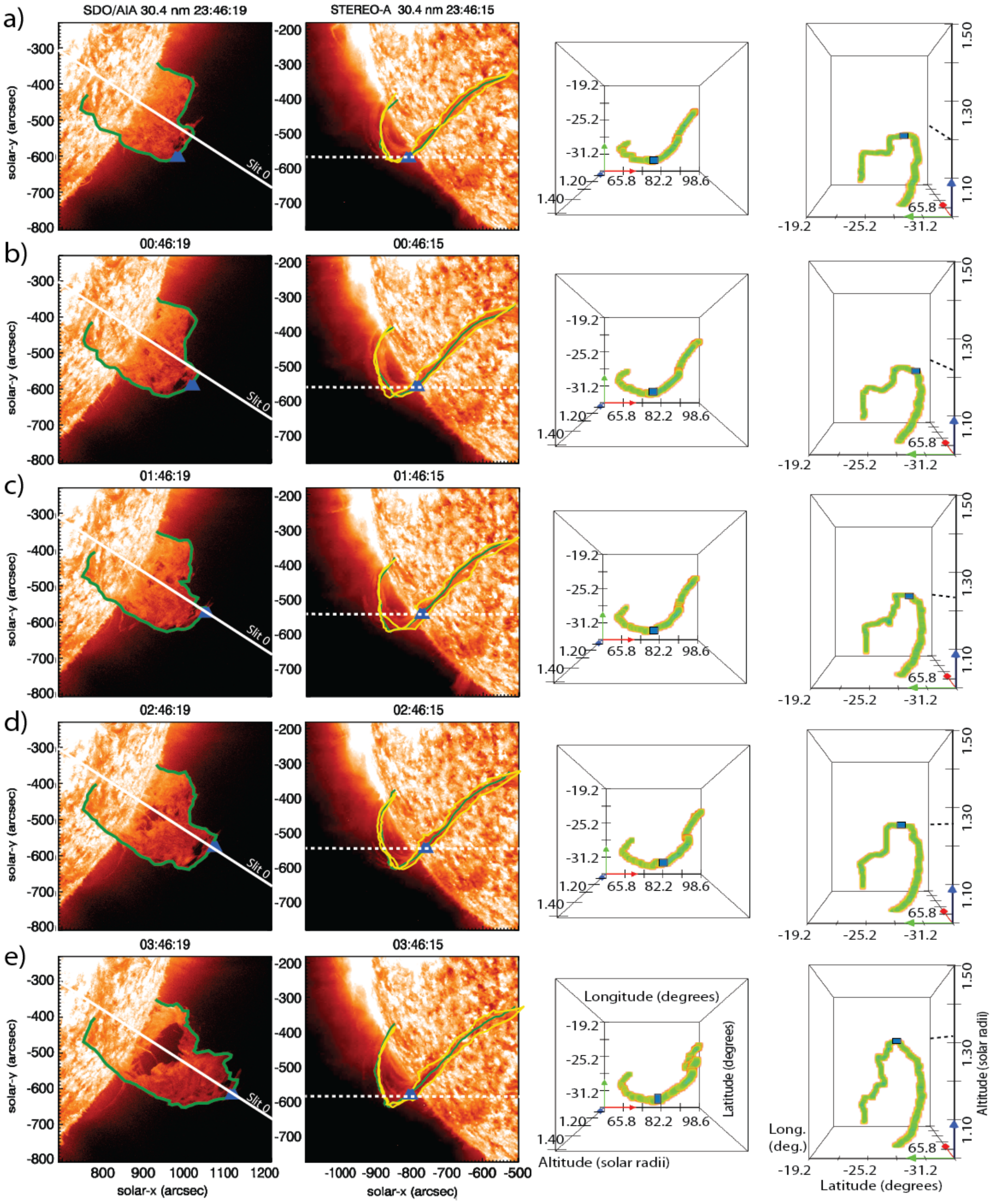

Figure 3.6: Results of the 3D prominence reconstructions. In all, the blue symbol marks the maximum height pixel for the detected edge. Rows a)-e): Hourly time steps of the eruption. First and Second column: Coincident images of the prominence eruption as observed at 304 Å with AIA and EUVI-A, respectively. The solid green line indicates the 3D reconstructed prominence leading edge deprojected onto the FOV. The solid yellow lines in EUVI-A are the northern- and southern-most 3D reconstructions of the prominence. The dashed white line represents the line-of-sight with respect to the maximum height pixel from the AIA image as it appears in the EUVI-A plane-of-sky. Third and fourth columns: Top-down and side-on perspectives, respectively, of the 3D leading edge incorporating the solid green/yellow line reconstructions, visualised in 3D with VAPOR (https://www.vapor.ucar.edu).

3.2.1 Geometric Analysis of the Prominence

Before we look at the kinematic analysis of this prominence (detailed in Sec. 3.3 and Chapter 4) we briefly analyse the geometry of the eruption through comparison to three curves: a circle, an ellipse, and a polynomial function. This allows us to demonstrate, and quantify, the difference between various simple models of a prominence compared to that of an actual observation of a prominence. For the sake of simplicity, we collapse the 3 dimensions of our reconstruction into the distance between points (in just latitude and longitude), which we plot against the height of each point as shown in Fig. 3.7. In Fig. 3.7 we show the evolution of the prominence through its eruption each hour from 22:46 (panel a) to 03:46 UTC (panel f).

A Circle In order to model a circle for each time-frame, we take the distance between footpoints of the prominence as the diameter, shown as the dot-dash black line in Fig. 3.7. We then compare this to the circle drawn this way for the first time-frame of the dataset at 22:06 UTC, shown as the solid black circle in all panels of Fig. 3.7. This shows little difference in the movement of the footpoints of the prominence over the course of the eruption, with the small fluctuations in part due to changes in the locations of the clicked points as part of the reconstruction.

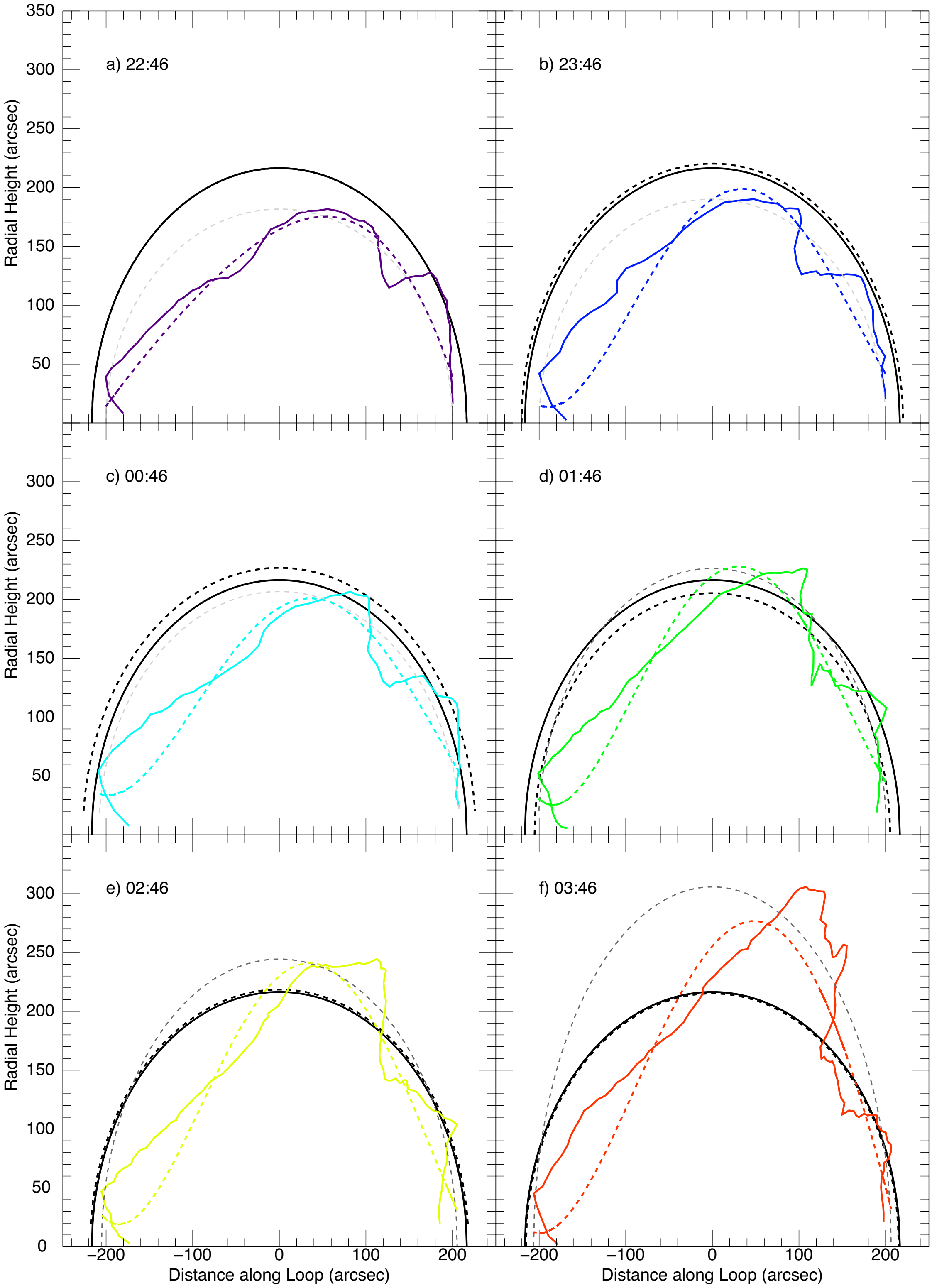

Figure 3.7: From left to right, top to bottom respectively we show the evolution of the prominence each hour from 22:46 to 03:46 UTC. In each panel, the solid black line is the circle that would be drawn from one footpoint to the other relative to the prominence at 22:06UTC, with the dot-dash black line representing a circle drawn from one footpoint to another at each time-frame. The dashed grey line represents the ellipse drawn with one axis being the distance between footpoints, and the other being the height of the prominence above the surface. The solid coloured line represents the distance between measured points along the prominence, with the dot-dash coloured line showing the best-fit of Eq. 3.3 to the prominence.

An Ellipse In addition to this we also compare the erupting prominence to an ellipse, modelled using the usual equation:

$$\frac{x^2}{a^2} + \frac{y^2}{b^2} = 1 \ , \tag{3.1}$$

where x and y are the distance along the prominence and height respectively, and a and b the semi-major and semi-minor axes of the ellipse respectively. Whether x or y is set against the semi-major axis, a, or the semi-minor axis, b, depends simply on which is appropriate for a given time-frame. We show these ellipses in Fig. 3.7 in light grey when the distance between footpoints is greater than the height, and in dark grey when the opposite is true.

We are also able to calculate the eccentricity of these ellipses using the equation:

$$e = \sqrt{1 - \frac{b^2}{a^2}} \ , \tag{3.2}$$

where e is the eccentricity. This is shown in Fig. 3.8 where we see the prominence firstly become less eccentric (i.e. more circular) as it begins to rise, and then more eccentric as it rises further. Note that the switch between which axes are defined as the semi-major and semi-minor happens at 01:06 UTC. Minor variations in the eccentricity from time-frame to time-frame are likely due to the difference in the points chosen as part of the 3D reconstruction. However this is now also sensitive to the points chosen along the leading edge of the prominence, unlike the circular models that were only sensitive to the locations chosen at the footpoints. In certain cases, such as 22:36 UTC in Fig. 3.8, the interaction of these points may cause a larger fluctuation.

A Polynomial Function The selection of a polynomial function to apply to this dataset may initially seem arbitrary, however there is a key piece of information that we must consider. Namely, that the prominence is asymmetric. This means that we must either choose an asymmetric function, or choose a piece-wise

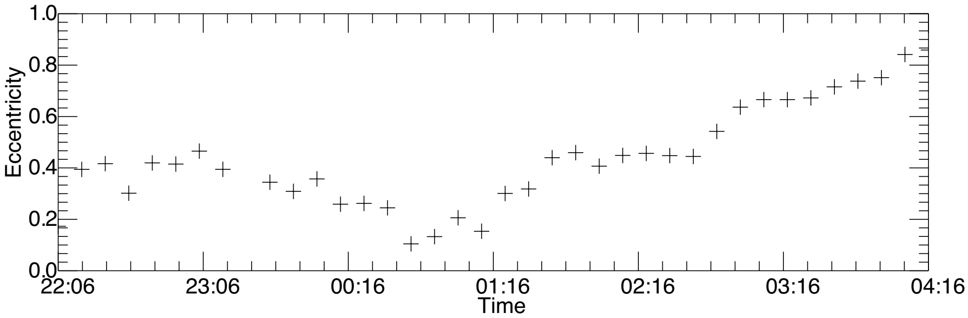

Figure 3.8: The eccentricity of the ellipse model of the prominence as calculated from Eq. 3.2 at each time over the dataset, where an eccentricity of 0 (i.e. a = b) represents a circle. Note that at 01:06, the semi-major and semi-minor axes of the ellipses switch.

function. Whilst a piece-wise solution would likely be the most physical solution, determining not only what number of sub-domains and where to place their boundaries but also their respective functions is beyond the scope of this study. Therefore we choose an asymmetric function. For the sake of simplicity we choose the lowest degree polynomial that can satisfy this requirement, i.e. one of the fourth degree which we define as:

$$y = a + bx + cx^2 + dx^3 + ex^4 \ , \tag{3.3}$$

where a, b, c, d, and e are the coefficients of their respective terms, and x and y maintain their previous meanings. In order to apply this to the prominence we use the IDL procedure MPFITEXPR, the output of which can be seen as the dot-dash colour lines in each panel of Fig. 3.7 As part of this procedure we must also supply an error on each height-point. As errors are not accounted for as part of the 3D reconstruction process (something we discuss further in Sec. 3.3, and Chapter 4) we instead choose to take the square root of the height of each point as its error for this process. This has the benefit of errors being smallest at the footpoints, where there is minimal movement over the course of the eruption (as can be seen in the solid colour lines of Fig. 3.7). This also allows the fitting procedure to account for greater deviations within the profile that occur as the eruption evolves in height. In order to determine the goodness of fit we use χ^2_{red}, given by $\chi^2_{\mathrm{red}} = \chi^2/\nu$ where ν is the number of degrees of freedom of the model as output by the fitting procedure. In Fig. 3.9 we present the χ^2_{red} of Eq. 3.3 when applied to the prominence at each time-frame.

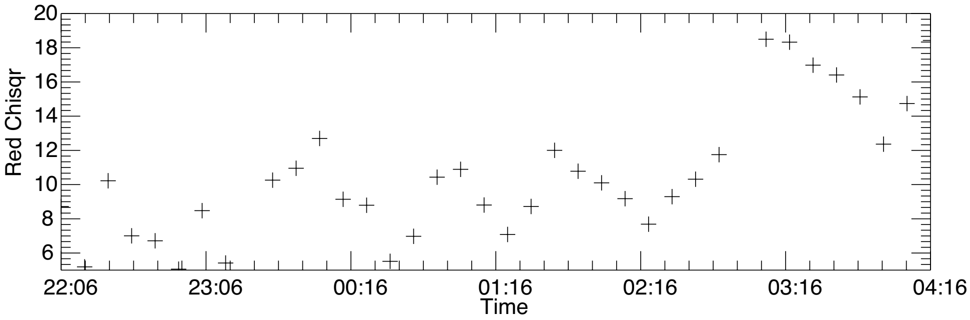

Figure 3.9: The χ^2_{red} of the best fit of the function to the prominence over time.

As can be seen in Fig. 3.9 the majority of fits have a χ^2_{red} of 12 or less, until around 03:00 UTC where there is a sudden jump to 18 where it remains generally higher. These values of χ^2_{red} are to be expected, as they are due to the deviations in the profile of the prominence away from the idealised profile of the function, especially as the eruption evolves. Something the model must take into account in all time-frames is the apparent change in direction of the prominence (See Fig. 3.7) at around 100-150 arcsecs along the prominence and at around 150 arcsecs in height. This can also be seen in the leftmost column of Fig. 3.6, just above the slit.

In Fig. 3.10 we show the returned values of each coefficient from a (top panel) to e (bottom) respectively with their respective errors as output by the fitting process. These errors are determined from the formal 1-sigma errors calculated from the covariance matrix of each parameter. For coefficient a we see the slow rise of the apex of the prominence from around 150 arcsecs at 22:06 to over 310 arcsecs at 04:16 UTC. For coefficient b, we see little change over the first few hours of the event, but can see a slowly increasing trend beginning somewhere between 01:16 and 02:16 UTC. This slow increase would correspond to the apex of the model slowly skewing to the top right of the panels in Fig. 3.7, i.e. increasing in both height and distance along the the prominence. Coefficient c, we see a slowly decreasing trend until around 02:16 UTC where it stalls and then remains. With coefficient d we see a mirror of b, with a generally static trend, until somewhere between 01:16 and 02:16 UTC when it begins to experience a net negative trend. For coefficient e we see no clear trend, but see most points distributed around $\pm 5 \times 10^{-8}$. The physical meaning of these coefficients is difficult to interpret in of themselves, but they do show an interesting change happening somewhere after 01:16 UTC. When viewed in conjunction with Figs 3.7, and 3.8 it suggests that the eruption began sometime between 01:16 to 02:16UTC. In order to more accurately determine the eruption time, we require significantly more detailed kinematic analysis which we detail in Sec. 3.3, and Chapter 4.

First however, we look at the writhe of this prominence.

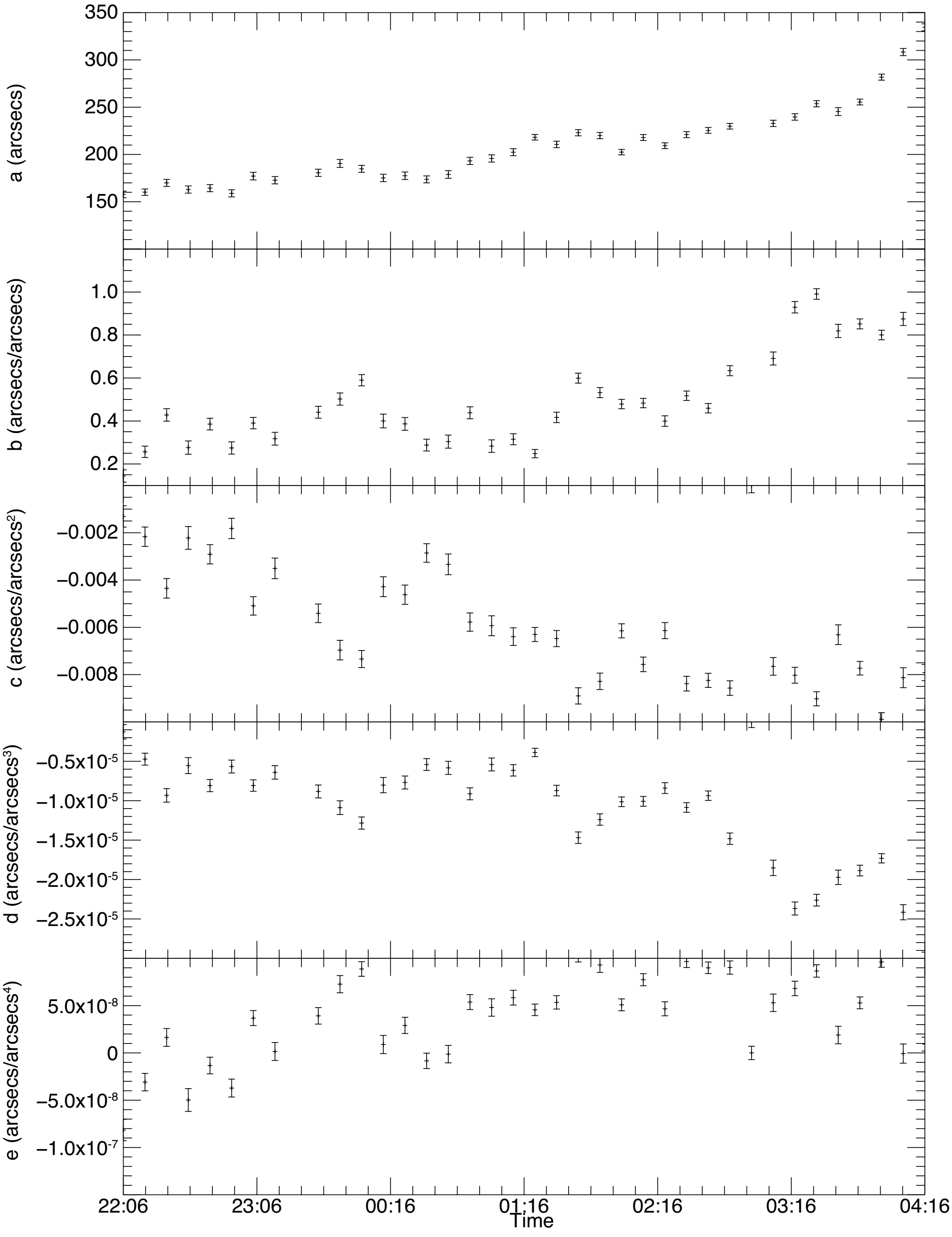

Figure 3.10: The coefficients of the polynomial from a to e from top to bottom respectively.

3.2.2 Writhe

One of the main goals with this reconstruction was to determine the role of the kink instability in the slow rise phase of the eruption. This would be done through the calculation of the writhe. To do this we use the method outlined in Berger & Prior (2006), and Török et al. (2010), wherein we take the sum of the local and non-local writhe of the prominence at each time frame.

In Fig. 3.11 we show the writhe as calculated for the central profile of the prominence (the green line in Figs. 3.5 and 3.6).

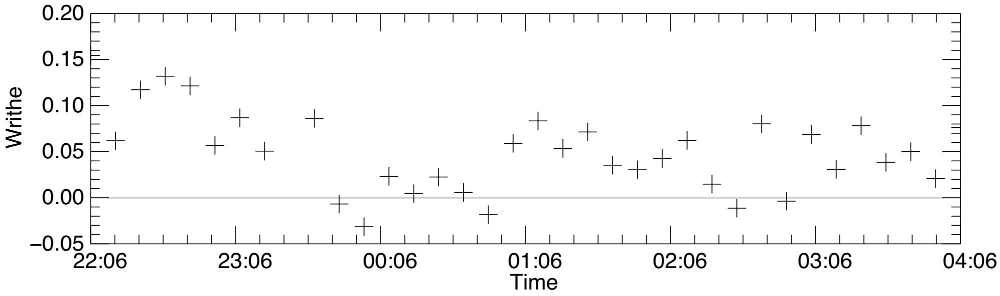

Figure 3.11: The writhe of the central profile of the prominence (see Fig. 3.6) over the time of the eruption with a grey line drawn at 0.

As can be seen in Fig. 3.11 there is no clear trend in writhe over the time of the eruption. There is perhaps a slight downwards trend between 22:26 and 00:56 UTC, but this too would likely become indeterminable once errors were introduced. This is perhaps unsurprising given that there is no obvious writhing in the structure through time as can been in Fig. 3.6.

We therefore conclude that the Kink Instability did not play a role in this eruption, and must therefore suppose that some other mechanism is responsible for the linear rise seen in this event.

3.3 Kinematic Analysis

3.3.1 Edge Detection and Height-Time Plots

3.3.1.1 Fully Automated Edge Detection

In order to assess the 3D kinematics of this eruption, we must accurately measure the leading edge of the prominence within the height-time reconstruction in a number of slits at all times. We therefore developed a novel dual-method edge detection program. This program utilises a threshold of the the background plus several sigma that is common to such analysis, and also includes a second edge detection method: the maximum negative derivative. This double approach allows for the robust assignment of error to all measurements of the returned location of the leading edge of the prominence, something not comprehensively addressed by other analyses, such as Schrijver et al. (2008).

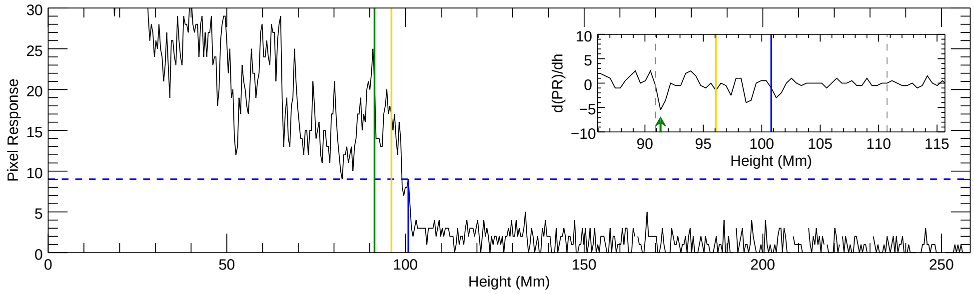

Figure 3.12: The position of the detected edges for an individual time-slice. As in the height-time plots shown in Sec. 4.1.1, the green line corresponds to the derivative threshold line, blue the background line, and yellow to their average. The inlaid panel is the derivative of the intensity profile along that slit, with the grey dashed lines showing the search range around the background detected pixel.

The step-by-step procedure behind this approach is illustrated in Fig. 3.12, and works as follows:

I The user defines several inputs: the section size for discrete time-averaged derivation of radial velocities, the wavelength (or which AIA channel), the desired 3D co-ordinates, and whether a transient filter is to be applied for removal of spurious edge perturbations and dynamics. A section corresponds to the number of time-slices over which linear fitting of the leading edge of the height-time profile take place.

II The height-time plot is built using radial slit data deduced from the 3D reconstruction.

III An empty part of the height-time plot from the slit with the greatest off-limb portion is used to calculate the image statistics for backgrounding. In this case, this corresponds to the southern-most slits, and can be seen as the dashed white boxes in Figs. 3.17, and 3.21. The background is defined as the mean+6σ of the chosen area, where σ is the standard deviation, and can be seen as the dashed blue horizontal line in Fig. 3.12. Any pixel found below this value was set to 0.

IV We then apply a transient filter to the background-filtered height-time plot. This filter removes any pixel that is not spatio-temporally related to the main body of the prominence. It preserves, however, any transient feature of the leading edge that is beyond a set size, or connected to the main body of the prominence as a potential deviation. A more detailed description of this filter is given in the next subsection, Sec. 3.3.1.2.

V The non-zero pixel that is greatest in height is then found for each time-slice. This pixel will become the upper boundary for the uncertainty of the measurement of the edge location along the time-slice. This can be seen as the short solid vertical blue line in Fig. 3.12.

VI The derivative along each time-slice's light-curve is calculated and the maximum negative derivative within a set range above and below the background pixel is then determined. For this analysis this search range is set to ±10 Mm (15.6 arcsec, or 26 pixels) and can be seen as the inlaid panel in Fig. 3.12. This range is to set to avoid detecting any lower-lying edges below the leading edge within the main body of the prominences. This is represented by the solid green line in Fig. 3.12.

VII The average of the background height and derivative height is then used as the detected edge location and can be seen as the gold line in Fig. 3.12, with the difference between the boundaries and average then used as the error. If the two boundaries have chosen the same pixel, the error is set to 1.

VIII The edge is then linearly fitted over the section using the IDL routine MPFITEXPR. The section is fit to minimise the χ^2 value. The sections are then moved one pixel to the right, and fit again, creating a sliding boxcar window that can measure radial velocities at the leading edge.

IX Velocity and acceleration are then calculated.

This can then be repeated for different section sizes, allowing any bias introduced by the section size to be accounted for. Effectively, different section sizes also allow us to account for plasma motion on different spatio-temporal scales enabling a characterisation of the different physical scales in the prominence. Tested section sizes correspond to 15, 20, and 25 minutes. Comparisons of the derived height and velocity profiles will be presented in the results section.

In total, applying this method to the 137 slits found in Sec. 3.3.3 takes around 40-45 minutes per section size, averaging around 20 seconds per slit after all data has been loaded. This method is currently optimised to take a minimal amount of time by loading all data before the height-time plots are constructed. The data has also been pre-cropped to the appropriate quadrant of the AIA FoV. This still requires a large amount of RAM (a little more than 60GB). This method could be run on significantly less RAM (less than a few hundred MB for the time range studied here) if instead the method loads each individual FITS file sequentially. However, doing so would significantly increase the amount of time required for the completion of all slits. This has been added and tested on a later version of the code, which is not used here.

3.3.1.2 The Transient Filter

Ideally, a height-time plot should have a continuous edge across all times. This would prevent erroneous velocities that would arise from the edge suddenly dropping to a lower edge, or rising to a higher one. To aid in this, a transient filter was designed and programmed to filter out small, relatively low intensity (i.e., "wispy") emission features that lie above the main body of the prominence after the background threshold mask has been applied. At its most simple, this works by checking small numbers of non-zero pixels in a given time-slice for non-zero pixels at a similar height in preceding and succeeding time-slices. When no pixels are found either before or after those being checked, they are set to zero. Because of this, the process is applied from $t = 1$ to $t = max - 1$ in both directions. This method will only remove pixels from the actual height-time plot that pass the checks in both forward (i.e., from $t = 1$ to $t = max - 1$) and backward ($t = max - 1$ to $t = 1$) operation. Therefore if a pixel is removed when going forwards in time but not going backwards, or vice-versa, it will not be removed from the resulting height-time plot. These checks are:

Check I The gap is less than a set number of pixels (10 in this case). This is shown by the range of grey pixels (i.e non-zero) bounded by the green pixels in Fig. 3.13. Wispy elements that are greater than a certain size must be manually examined to determine whether they are in fact part of the main body of the prominence. If they are not part of the main body, the filter gap size can be increased.

Check II The pixel has zeroes from below to above it in the time slice before plus or minus two pixels in the relevant direction. This is shown by the capped black dashed line in the preceding time-slice in Fig. 3.13.

These checks are applied upwards in height before moving onto the next time. If the pixels in the $n-1$ time slice are zeroes, the nth time-slice pixels will be set to zero before the algorithm moves to the $n+1$ time-slice. Therefore the feature will be eroded in the direction of time being considered.

An example of this method for a single time-slice is shown in Fig. 3.13. Here an element of plasma at t=3, represented by the grey pixels, in the range of 5 to 11 has passed its first check by being less than 10 pixels tall. This is represented by the green pixels set below and above the pixels at 4 and 12 respectively. These pixels at 4 and 12 are now used as the positions from which to perform the second check. Here the preceding time-slice is checked from over the height range of the bottom minus two (4-2=2), to the top (12+2=14), as shown by the capped black line in Fig. 3.13. As there is nothing in this range the pixels at t=2, the pixels in the column at t=3 will be set to zero.

We now show an example of the method applied across several iterations over the same time frames and in both directions in Fig. 3.14. The initial height-time plot, seen as the top left panel, is copied into separate forward (middle row) and backward (bottom row) arrays, which are operated on separately. Moving forwards in time, as can be seen on the middle row of Fig. 3.14, there are two regions to be checked. The lowest of the two is checked first. The gap between the zeroes marked by 4 and 9 is less than 10, and there is nothing in the preceding time-slice in the height-range of the the bottom-2, i.e 1, or the top+2, i.e 10.

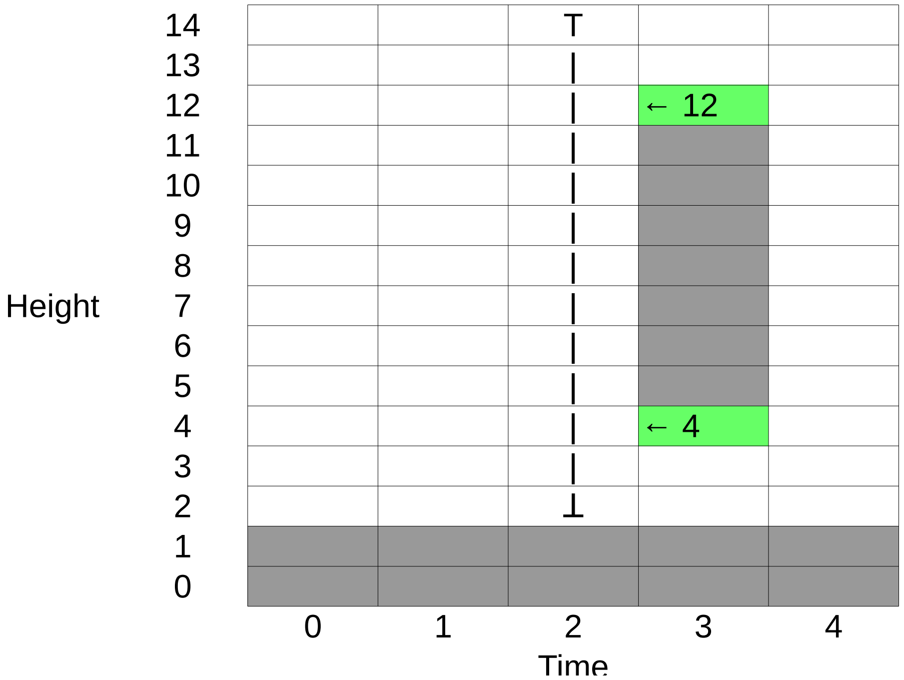

Figure 3.13: This cartoon shows an example of the checks being applied to a single time-slice of a height-time plot in "pixels", where white represents a value of zero and grey represents non-zero. Here there is an element of plasma (at t=3 over the height range 5 to 11) that is not connected to the main body (the lower two rows of pixels) in space or time. It is first checked for height and passes as it is only 8 pixels tall. The preceding time slice is then checked over the range (shown by the capped black dashed line) from the bottom (the pixel under the element) minus two pixels to the top (the pixel above the element) plus two shown the green pixels marked 4 and 12. As there is no plasma within the range searched over, this element will be set to zero.

Therefore these pixels will be zeroed. We now move to the next group of pixels to be checked at this time, i.e. those pixels bounded by the zeroes marked 14 and 18. The gap is less than 10, and there is nothing in the preceding time-slice's height range of 12 to 20. Therefore these pixels will be zeroed. The next time is then iterated through. Like before there is nothing in the range of the top+2, now 17, to the bottom-2, now 4. These pixels will therefore be zeroed. This is then repeated for the next time-slice in the third iteration. In the fourth iteration at t=5 there is a series of pixels to be checked that cover less than ten pixels. However, there is something in the search range so these pixels will not be removed.

The backwards array, shown as the bottom row in Fig. 3.14, is then iterated through in the reverse manner.

Once both have been iterated through, they are re-combined into the resultant height-time plot, shown in the top right panel of Fig. 3.14. As mentioned before if something fails either check in either direction, it will be kept in the resulting height-time plot.

However, all slits were subject to an unforeseen effect. It was assumed that the body of the prominence would consist a single continuous mass and move as such, aside from small scale transient effects. Instead, it appears that the prominence consists of a main body and a band of plasma above the main body. When this band disappears there is the undesired sudden drop in height of the apparent edge location. This reduces our ability to accurately derive the radial velocity profile of the prominence. In Fig. 3.15 below are two panels, the first is without the transient filter applied, allowing a continuous profile. The second is with the transient filter applied, removing a transient effect and causing the height to fall. Due to this drop in height, these features will be referred to as “drop-outs” in later sections (even when the plasma appears to “drop-in”). With regard to the transient filter, only transient edge features which are fully disconnected from the main body of the prominence are ignored. The slit shown in Fig. 3.15 is not used in the following kinematic analysis, but instead chosen as an extreme example of what the filter can do.

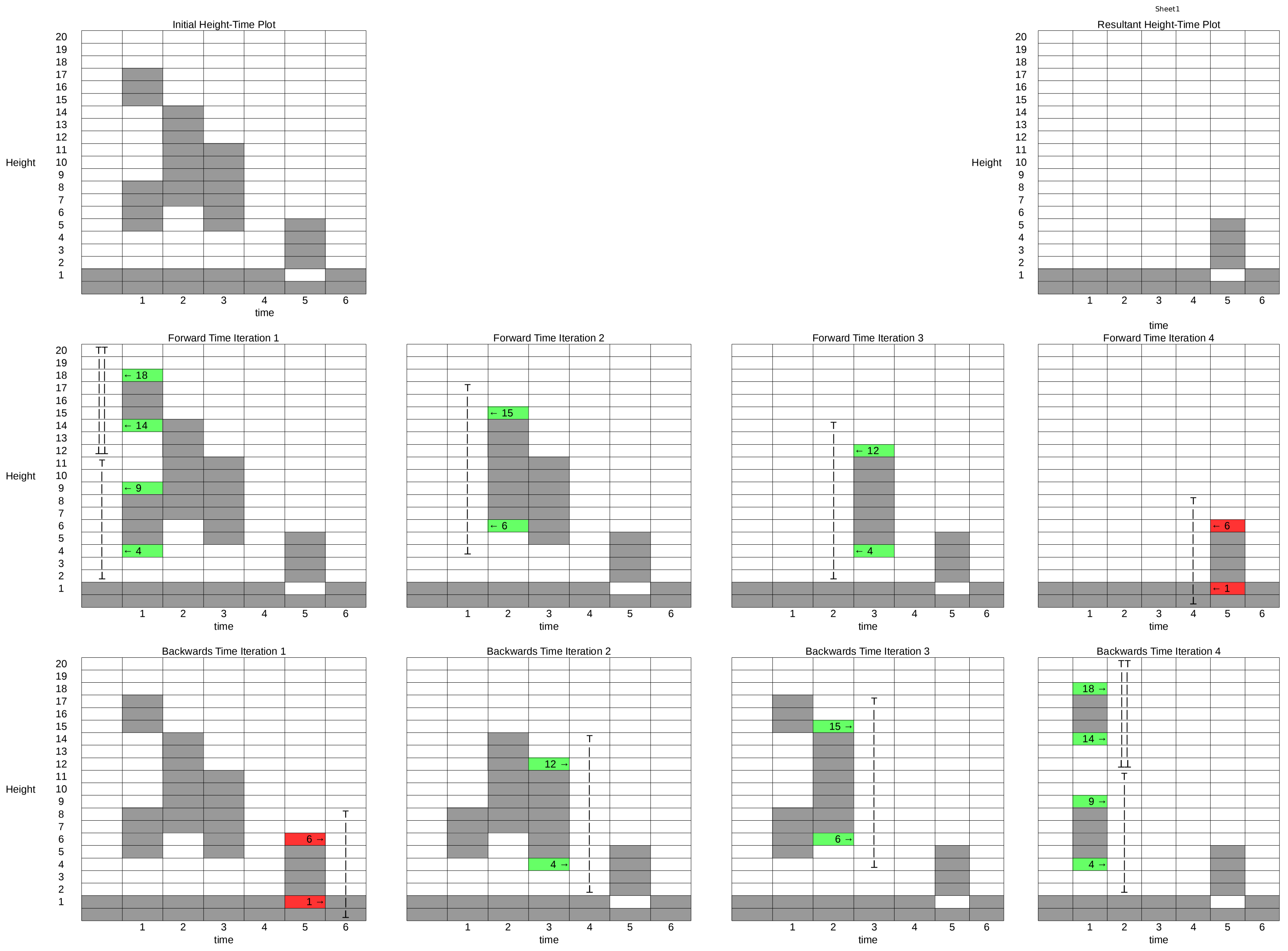

Figure 3.14: On the top left we show the pre-filter height-time plot. The four middle panels show the forward operation. The four bottom panels show the backward operation. On the top right is the resulting post-filtering height-time plot.

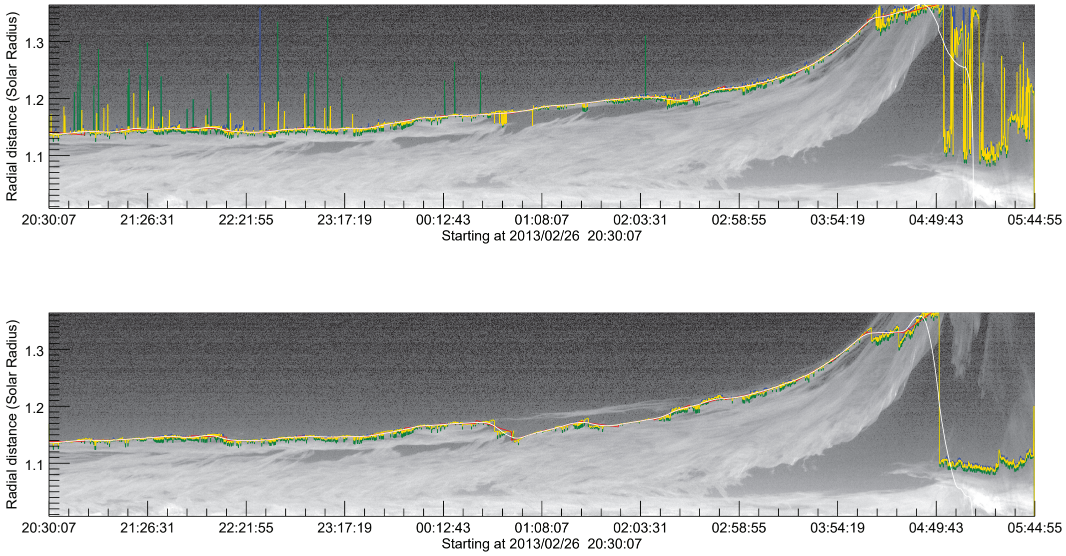

Figure 3.15: Top: The height-time plot without the transient filter applied. The spikes in blue, green, and yellow correspond to "hot" pixels, i.e. above background. Bottom: The height-time plot with the transient filter applied. The transient filter also helps to remove hot pixels. The ribbon can be seen as the part of the prominence that contains gaps between itself and the main body, and disappears around 00:30:00. As mentioned above, this is not an example of the slits studied, but instead chosen to clearly illustrate the possible effect of the filter.

In order to understand why the feature was removed one must carefully follow the detected edge in the top panel. It is possible to see that just before 01:08 the intensity dips, and thus the edge-detection finds a lower boundary, causing a disconnected jump when it returns to the feature just afterwards. One can also see a more gentle deviation just after 02:03 from the feature to a lower boundary. This means that the feature is disconnected from the main body of the prominence, and will thus be checked by the filter. As can be seen, it fails all checks and the feature is therefore removed. If the filter gap size was reduced this feature would remain. These two panels also demonstrate the filter's ability to remove other unconnected above-threshold pixels as can be seen from the random spikes that have also been removed between the panels of Fig. 3.14.

3.3.2 The Kinematics of the Entire Prominence

We first apply this method across the full length of the prominence. In order to do this we draw slits through the coordinates from the prominence at 22:16 UTC. In Fig. 3.16 we show the positions of the points through which the radial slits have been drawn, numbered accordingly from the northern most footpoint of the prominence towards the southernmost along the leading edge of the structure.

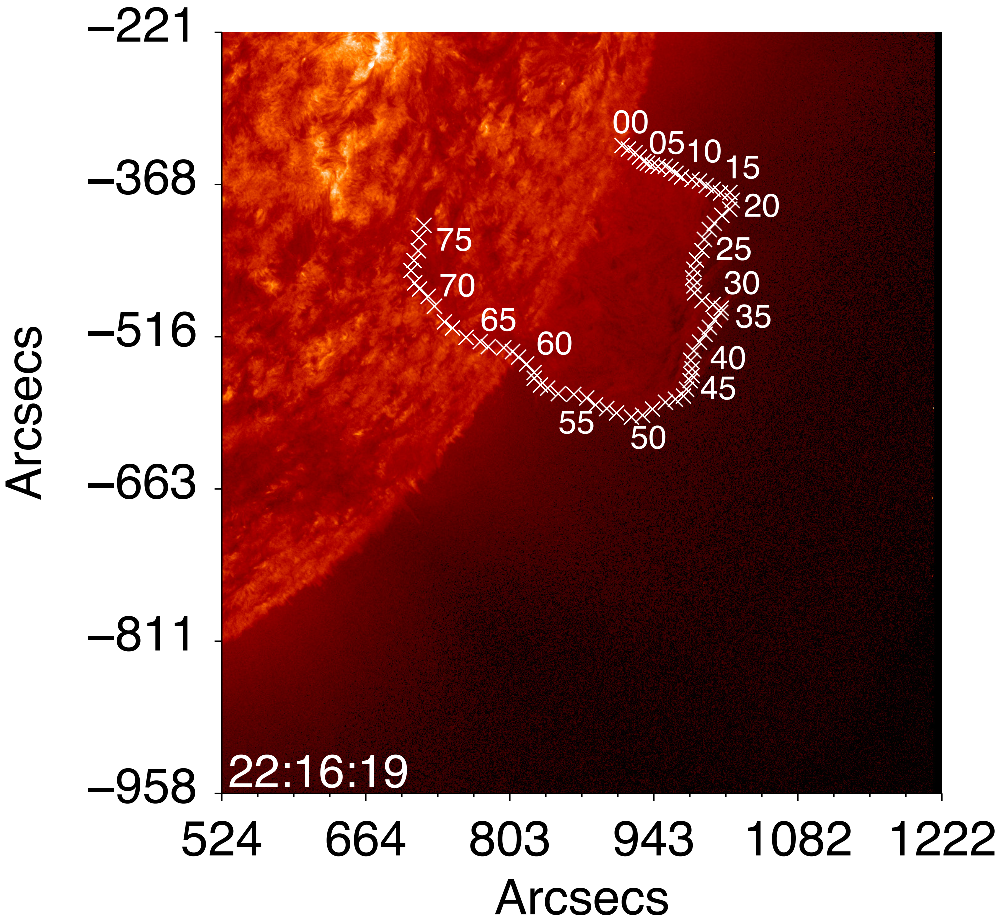

Figure 3.16: A snapshot of the prominence at 22:16UTC with the points clicked upon by the user as part of the 3D reconstruction method, and numbered accordingly.

As can be seen in Fig. 3.16 the prominence is well sampled in space at this time along the full length of the structure.

In Fig. 3.17 we present the results of this method applied to each 10th slit from slit 0 to slit 70 as seen in AIA 304 Å. In all of the following height-time plots the green line is the derivative threshold, the blue line is the background threshold, and the yellow line is the average of the two. In Slits 0, 10, and 60 we see the result of the method when applied to a slit in which the prominence appears only rarely over the course of the eruption. It instead picks up the lower corona emitting at the chromospheric temperatures that can be detected in the 304 Åpassband. This is detected due to this part of the solar atmosphere emitting above the background threshold that has been set. Whilst these slits are not ideal when trying to consider the kinematics across a prominence, they do still serve as a good example of the method. This is because they find a consistent height, showing that there are only minor variations in the plasma over this time range. In slits 10 and 60 we see the results of plasma appearing and disappearing from the height-time plot. In slit 10 we see a sudden influx of plasma at around 21:36 that causes a sudden jump in height, and thus an example of a drop-out. That this feature has not been removed by the transient filter suggests that it either is too significant in size to be removed or that it is connected to the prominence. A short while later at 22:21 UTC we see the feature disappear and the detected edge drop out more. However, careful inspection suggests that a small part of that feature may remain and be picked up again at 23:36. It should be noted at this point that the dynamic range of the background images in each height-time plot has been compressed to allow both the bright limb and comparatively dark prominence to appear clearly. Thus the thin piece of plasma that can be seen just prior to the jump in the detected edge 23:36 can actually be much less intense than it may initially seem. Nonetheless there is actually surprisingly little evidence of any eruption taking place in slits 0, 10, and 20, with only a small rise in slit 60 after 03:00 UTC.

Returning, briefly, to the transient filter one can also see examples of its work in slit 30 just before and after the short-lived rise between 22:36 and 23:21 UTC. These elements of plasma are clearly not connected to the main body of the prominence, like the later example at 02:51 UTC in the same slit. Thus the transient filter allows us to avoid large, unphysical jumps, and drops, in height and therefore in the velocity determined from these heights. However, it cannot remove all of these features especially when they are larger than the size threshold set.

We instead focus on the results from slits from points greater than 30. Though we must be careful to realise due to the shape of the prominence we may actually be re-sampling the prominence material found between slits 40 to 50 when we take slits through points after 50. In these slits we see a well defined, and consistent prominence edge that shows clear signs of an eruption beginning from around 02:36 UTC. It appears to erupt earliest in slits closest to the 3D apex of the structure, seen here in slits 40 and 70, and later when moving away from this point for instance in slits 30, 50, and 60.

We now present the velocity profiles that correspond to these height-time profiles. Ideally, we would have used the velocity profiles to help determine the onset time of the non-linear phase in each slit. Due to these drop-outs, however, this is not possible. Despite of this we present the velocity profiles, and directly demonstrate the effects of the drop-outs.

The hope was to use the last minima before monotonic increase began as an indicator of the start of the eruption. The major problem with this is that the last minima will always correspond to a drop-out if it takes place any where near the non-linear phase, as can be seen very easily in any of the velocity profiles in

Fig. 3.18.

As can be seen in Fig. 3.18 determining the eruption time is difficult in all but a few of these slits. As such, the time range for the eruption as found by this method across all slits is 1:00 - 03:30UTC for 304Å. As these limits are the limits of the search range, this means that the method is too sensitive to drop-outs to provide a meaningful time range. The velocity profiles of these slits can be used to colour height-time surfaces of the event, providing an immediate insight into larger-scale effects than can be detected with single slit height-time plots. Figure 3.19a shows the leading edge height-time profiles for all slits, stacked together and colour-coded by their running boxcar linear velocities. When comparing all slits for 304 Å the maximum outward velocity is 98.6 km s^{-1}, with all eruptive slits reaching at least 20 km s^{-1}. Fig. 3.19c shows the running boxcar linear velocity profiles averaged across all slits, highlighting a slow nearly linear rise of < 5 km s^{-1}. It is important to remember when viewing these plots that the slits diverge with height, which is why certain features both start and cease to exist in neighbouring slits. As mentioned, the height-time profiles and the corresponding velocity profiles are marred by the now distinctive colour patterns of the drop-outs. These manifest as dark streaks followed shortly by bright streaks, characterising the sudden rise and fall in the leading edge. For instance in Fig. 3.19 between 22:36UT and 01:06UT for slits 30-40. It is clear that velocity profiles in many of the eruptive slits depict some form of acceleration, with the possibility of the onset perhaps tending towards later times for slit numbers further away from the centre. Or, more explicitly, the onset of eruption starts nearer to the centre of the prominence structure and progressively gets later further along the edge. In order to study this further we must ‘zoom-in’ on a section of the prominence. Specifically we shall focus on the section of the prominence in which the apex of the structure can be found throughout the eruption.

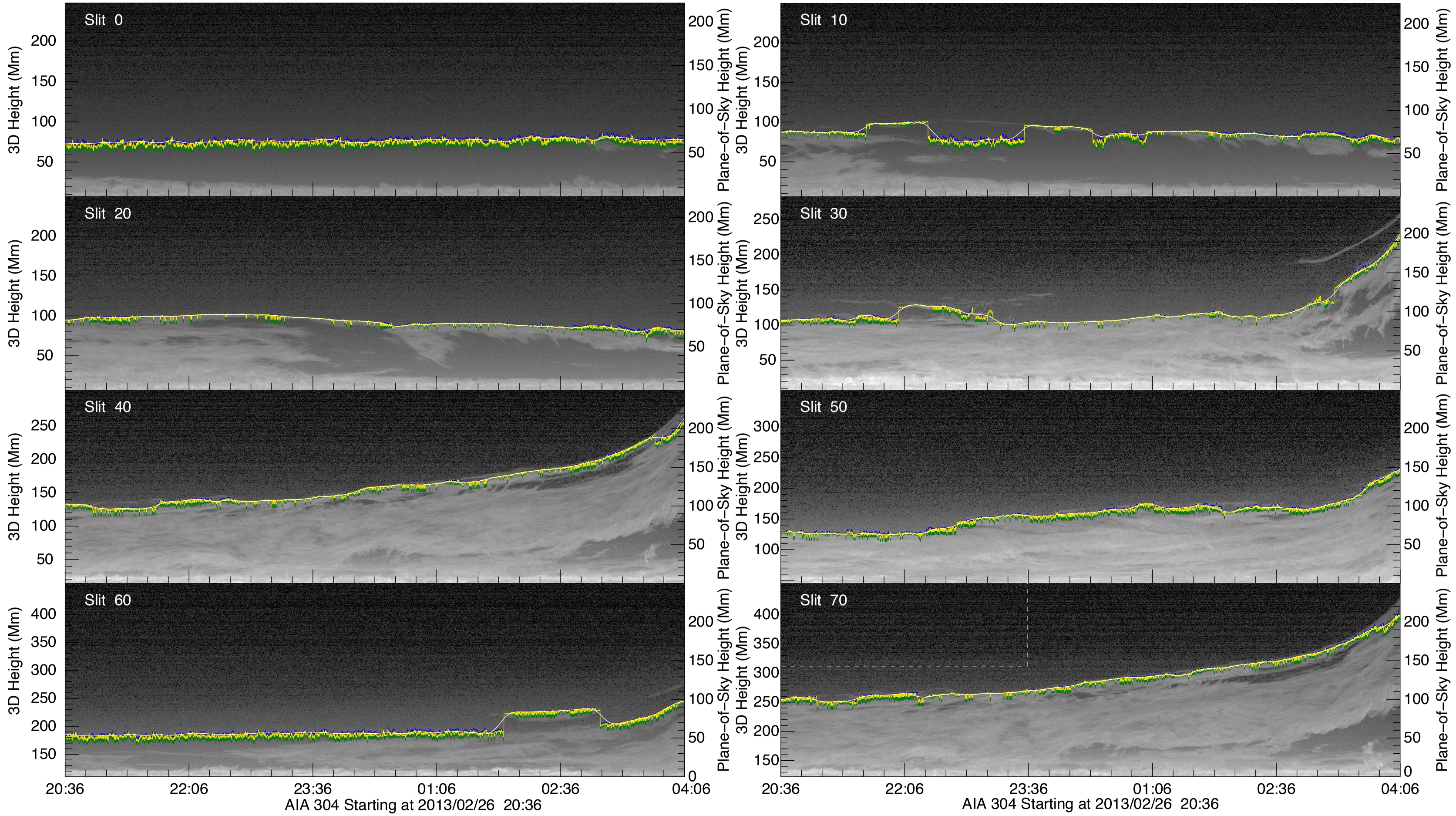

Figure 3.17: The Height-Time plots of every tenth slit from slit 0 to slit 70 (top to bottom respectively) along the prominence as can be seen in Fig. 3.16 between 20:36 to 04:06 UTC and 0 to 280 Mm above the limb in the plane-of-sky. Here the blue line is the background threshold, the green line the derivative threshold, and the yellow line the average of those two.

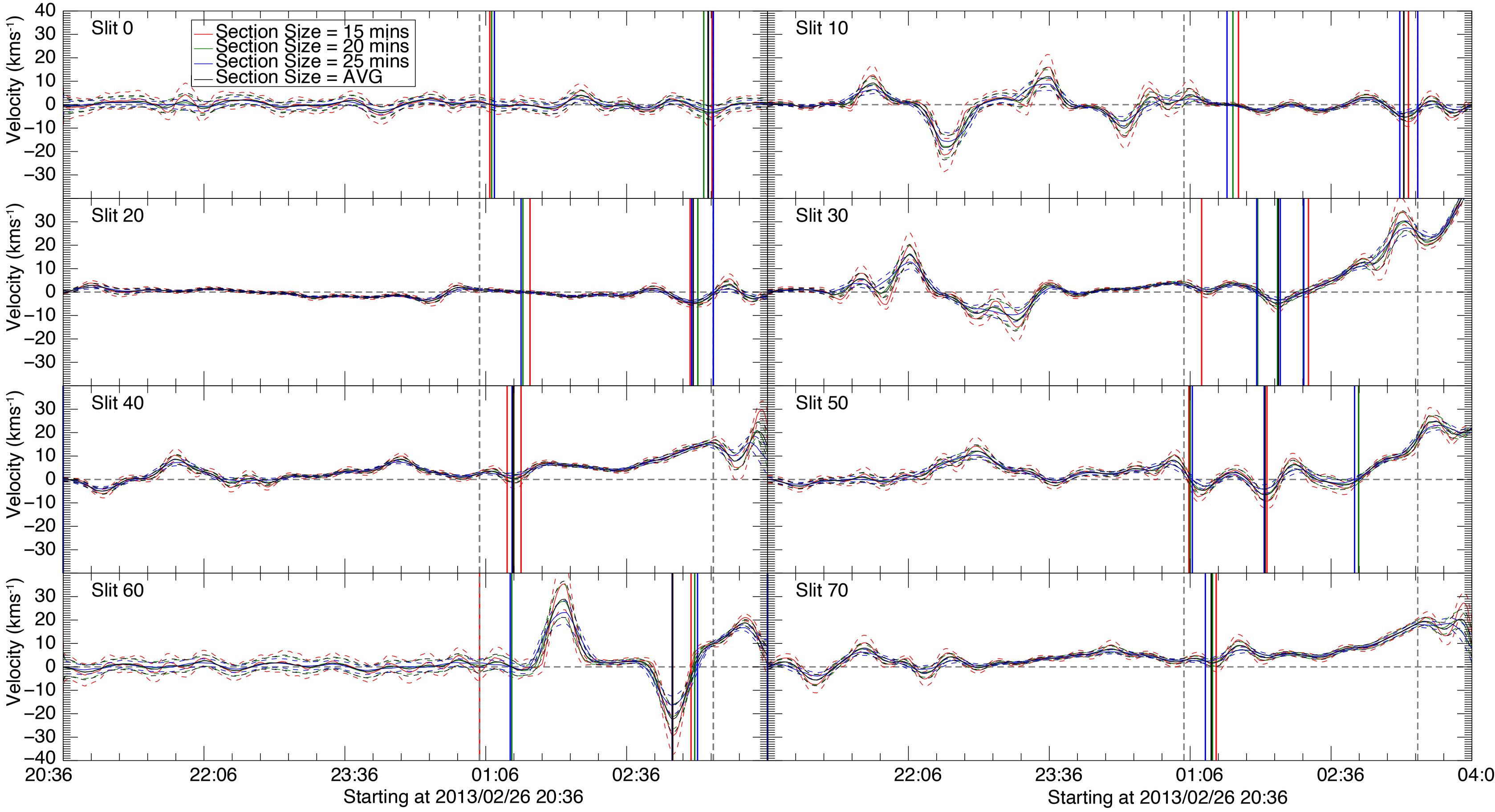

Figure 3.18: The velocity profile of the three slits shown for 304Å. The dashed gray horizontal line is at $0\mathrm{kms}^{-1}$. The horizontal gray bars indicate the search range. The solid coloured lines represent the velocity profiles. The vertical solid lines represent the automated detection of the velocity minima. The fainter, coloured, dashed lines represent the error on each line. Each colour represents a different section size: red=15 minutes, green=20 minutes, blue = 25 minutes

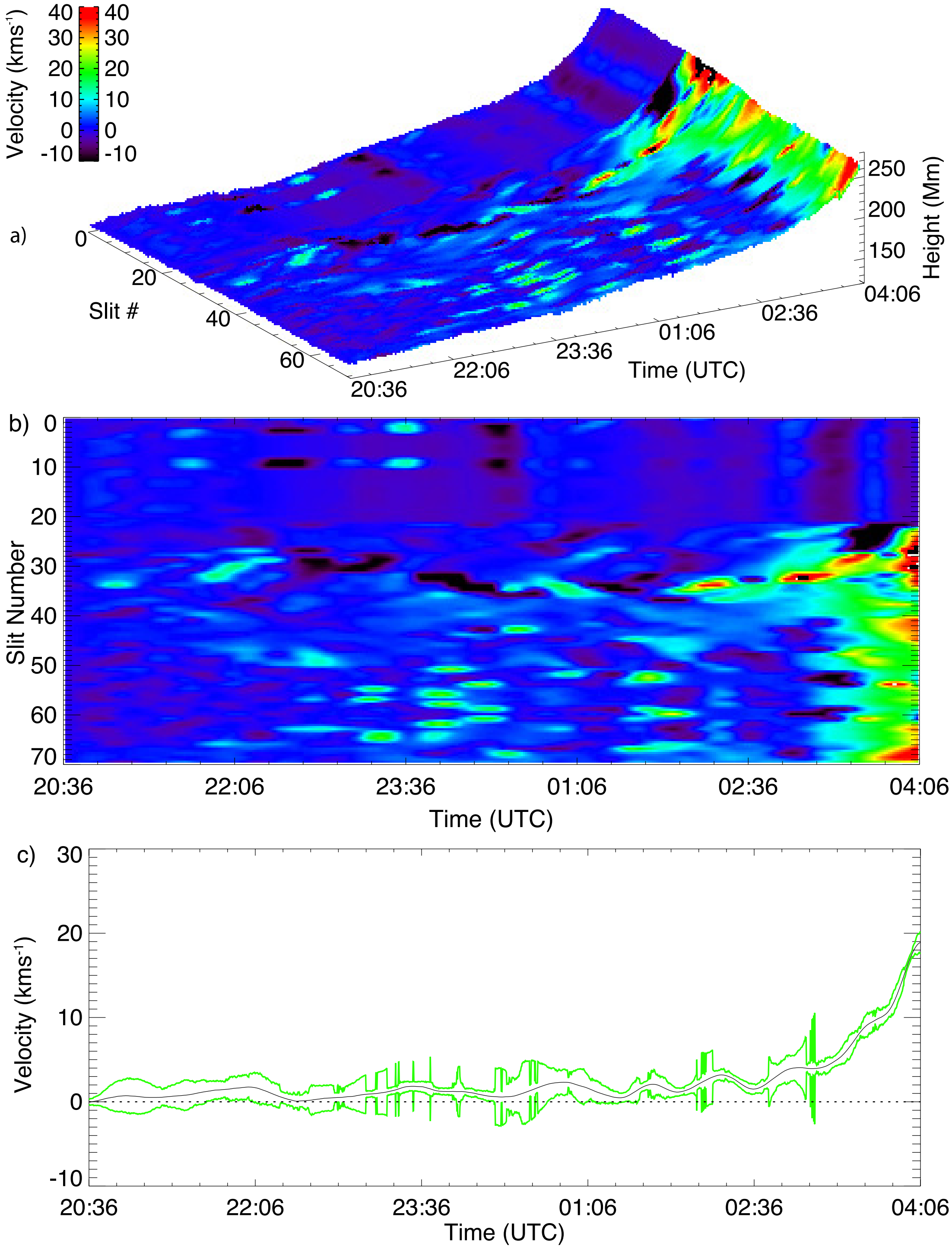

Figure 3.19: a) The side-on view of the surface plot of height for each slit number vs time. b) The top-down view of the same surface plot. In both, colour represents running boxcar linear velocity truncated here at -10 to 40 km s^{-1}. c) The running boxcar linear velocity averaged across all slits with the green lines representing the standard deviation of the velocity across all slits.

3.3.3 The Kinematics of a Section of the Prominence

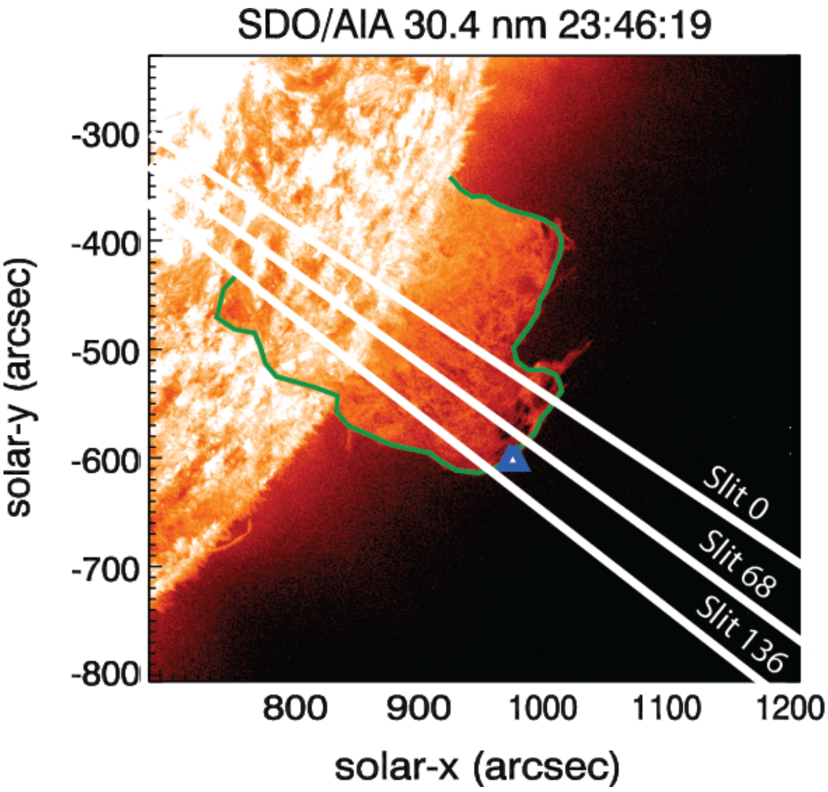

Figure 3.20: The left panel of Fig. 3.5 shown here again to clarify the range of slits used in this section.

We now focus on the range of the prominence as can be seen in Fig. 3.20. This is the range of the prominence over which the apex of the 3D structure can be found at all times. As such, it will allow us to determine the kinematics of the prominence over the section of the prominence in which the torus instability will be most likely to act.

Although the 3D reconstruction is based upon the use of 304 Å, we can also use the 171 Å channel in AIA through the same slits. Whilst this cannot be directly related to the results that come from 304 Å, they do allow us to determine something slightly different about the structure. This is due to 171 Å emitting from the PCTR, rather the prominence core as 304 Å does.

We now present the result of this method in Figs. 3.21, and 3.22. As before, in the following height time plots, the green line is the derivative threshold, the blue line is the background threshold, and the yellow is the average of the derivative and background thresholds, where all times are given in UTC. As there are 137 slits we will only present three, the northern-most (0), the middle (68), and the southern-most (136), the range of which can be seen in Fig. 3.20.

As can be seen in Fig. 3.21 the method performs extremely well at providing a consistent edge in time. A prime example of this consistency is found between 01:06 and 02:36 UT in slit 0 where there exists cavities in the prominence below the detected edge. However, there can still exist spurious drop-outs in structures at the leading edge over short intervals in time. For example in slit 68 at ∼03:20, shown as the central zoom-in, which will impact upon the accurate determination of kinematics at such time intervals. When comparing all three height-time profiles it is clear that the onset of eruption appears to happen earlier in lower slit numbers, i.e. closer to the centre of the prominence.

We now present the height-time profiles drawn through the same slits for 171 Å.

As with 304 Å, an extremely consistent edge has been found. Although the plasma seen is that of the much more weakly emitting PCTR the method still works perfectly. Due to the different properties of the plasma we are able to see a different part of the structure.

This difference is presented in Fig. 3.23, where we show the height-time profiles, and their errors, of both 171 and 304 Å overlaid. Here we see that the profiles are actually very similar, with the greatest (non-dropout) differences appearing earliest, when the prominence is lowest. This difference also increases with slit number, with little difference appearing in slit 0, but greater difference appearing in slit 136. Due to this we believe this discrepancy to be caused primarily by

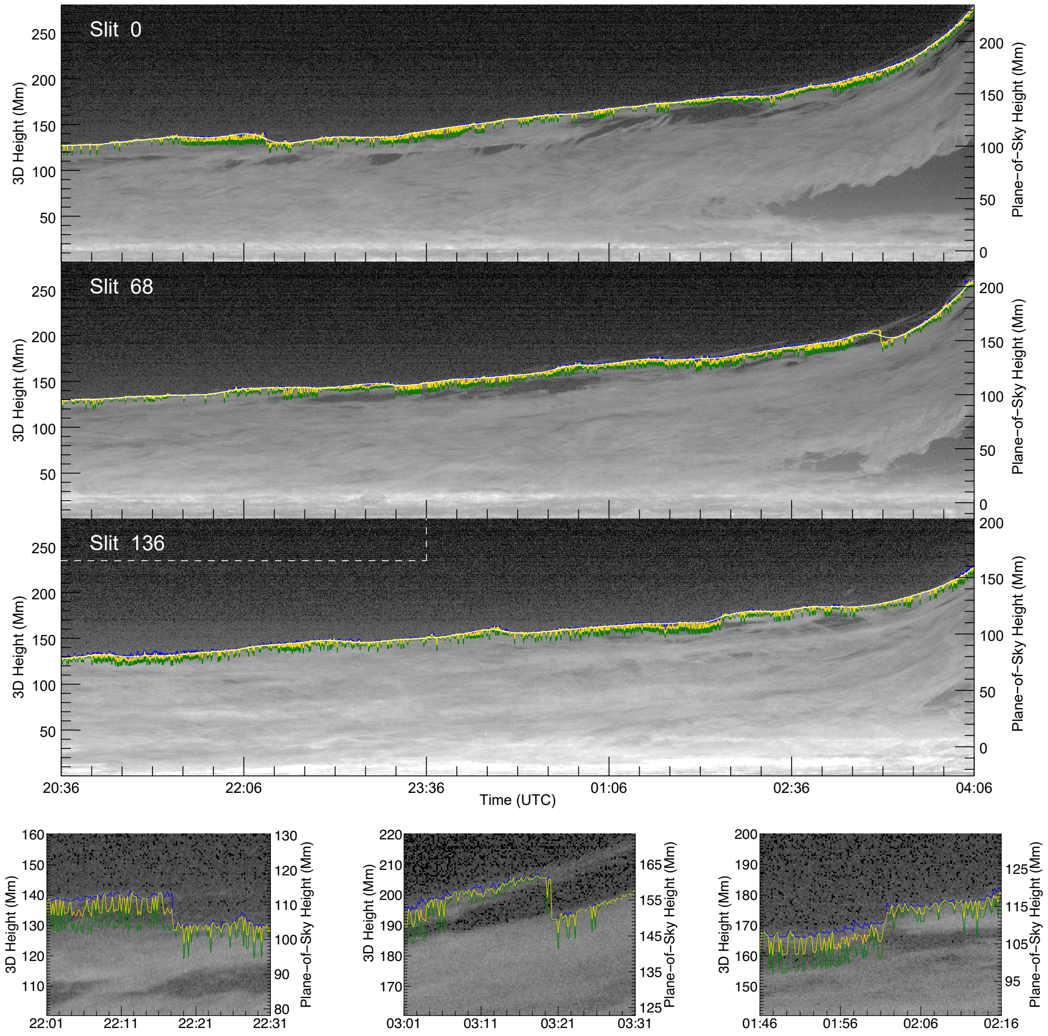

Figure 3.21: Height-time plots of AIA 304 Å for 3 radial slit positions. In all height-time plots, the green line is the derivative threshold, the blue line is the background threshold, the yellow is the average of the derivative and background thresholds, and the white line fit to the edge is the boxcar smoothed height line. The left y-axis shows the height measured above the 3D surface. The right y-axis shows the height measured above apparent the plane-of-sky surface (i.e. the limb). The dashed white lines in slit 136 show the extent of the backgrounded area within this smaller FoV. The bottom three zoomed-in panels show examples of discontinuities ('drop-outs') in each slit respectively

optical and radiative transfer effects, as any problem in alignment of the images themselves would likely lead to an constant difference across slit number. We will discuss this further in Sec. 3.4.1.3. This difference across slit number can be seen in Fig. 3.24 where we present the histogram of the difference between the profiles

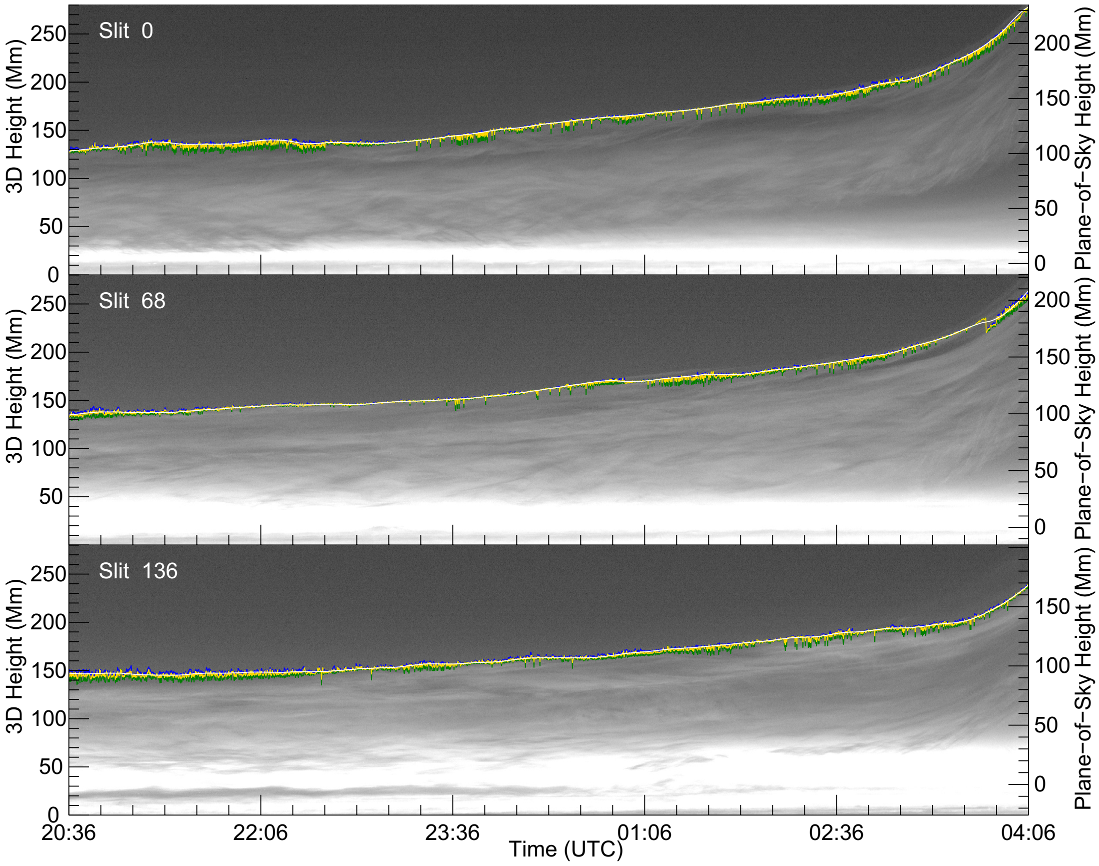

Figure 3.22: As for Fig. 3.21 but for 171 Å.

of each slit (i.e. the profile of 171 minus the profile of 304 Å.) We have applied no filtering to these profiles. As such, they contain the effects of drop-outs. This will be discussed further in Sec. 3.4.1.3. These profiles have been colour coded from black to blue to green to red corresponding to increasing slit number. As can be seen in Fig. 3.24 the peak of the histogram moves from around 0 Mm for the earliest (black/dark blue) slits, to around 6 Mm for later slits. This average profile peaks at 3.3 Mm. Of note here is that the profiles are positively skewed. This means that the height-time profiles of 171 are generally higher than those of 304 Å, with the majority of the reverse cases being on order of a few pixels. The context of these results will be discussed further in Sec. 3.4.1.3.

We now present the velocity profiles that correspond to these height-time

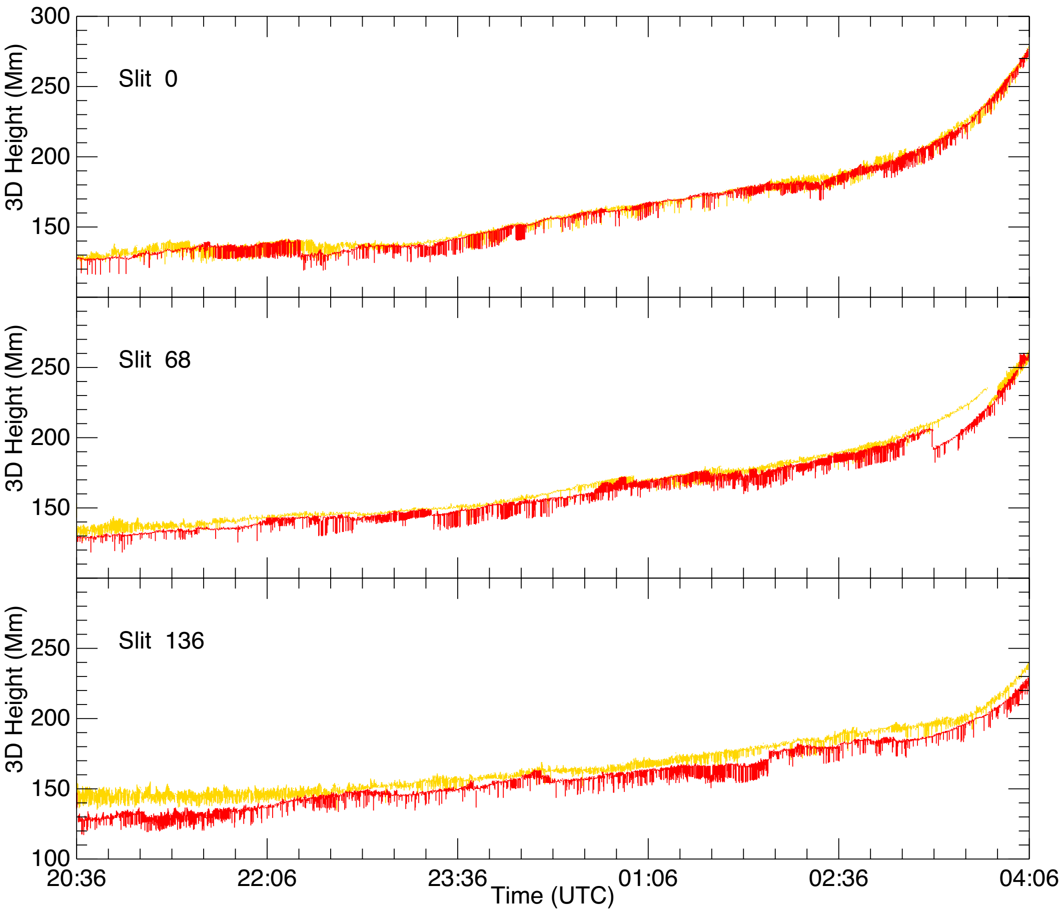

Figure 3.23: The combined detected edges and their errors of both 304 Å, and 171 Å in red and yellow respectively for slits 0, 68, and 136 in 3D height.

profiles. Ideally, we would have used the velocity profiles to help determine the onset time of the non-linear phase in each slit. Due to these drop-outs, however, this is not possible. Despite of this we present the velocity profiles, and directly demonstrate the effects of the drop-outs.

The hope was to use the last minima before monotonic increase began as an indicator of the start of the eruption. The major problem with this is that the last minima will always correspond to a drop-out if it takes place any where near the non-linear phase, as can be seen very easily in any of the velocity profiles in either of Figs. 3.25 and 3.26.

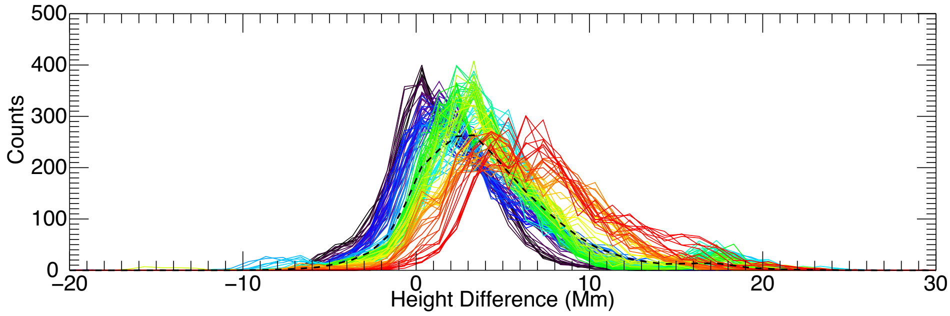

Figure 3.24: A histogram of the difference in height between the detected edge profiles of 171 Åand 304 Å for each slit, colour coded by slit-number from black (slit 0) to red (slit 136). The dashed black line represents the mean profile of all slits.

The current time ranges for both wavelengths of the eruption as found by this method are 1:00 - 03:30UTC for 304Å, and 01:00 - 03:31UTC for 171Å. As these limits are, once again, the limits of the search range, this means that the method remains too sensitive to drop-outs to provide a meaningful time range.

The velocity profiles of these slits are now used to colour height-time surfaces of the event as before. Figures 3.27a and 3.28a show the leading edge height-time profiles for all 137 slits, stacked together and colour-coded by their running boxcar linear velocities. When comparing all slits for 304 Å the maximum outward velocity is 48.6 km s^{-1}, with all slits reaching at least 30 km s^{-1}. For 171 Å the maximum outward velocity is 38.6 km s^{-1}, with all slits also reaching at least 30 km s^{-1}. Figs. 3.27c and 3.28c show the running boxcar linear velocity profiles averaged across all slits, highlighting a slow nearly linear rise of < 5 km s^{-1}. It is important to remember when viewing these plots that the slits diverge with height, which is why certain features both start and cease to exist in neighbouring slits. As mentioned, the height-time profiles and the corresponding velocity profiles are marred by the now distinctive colour patterns of the drop-outs. For instance in Fig. 3.27 between 00:36UT and 01:36UT for slits 50-70. Due to the

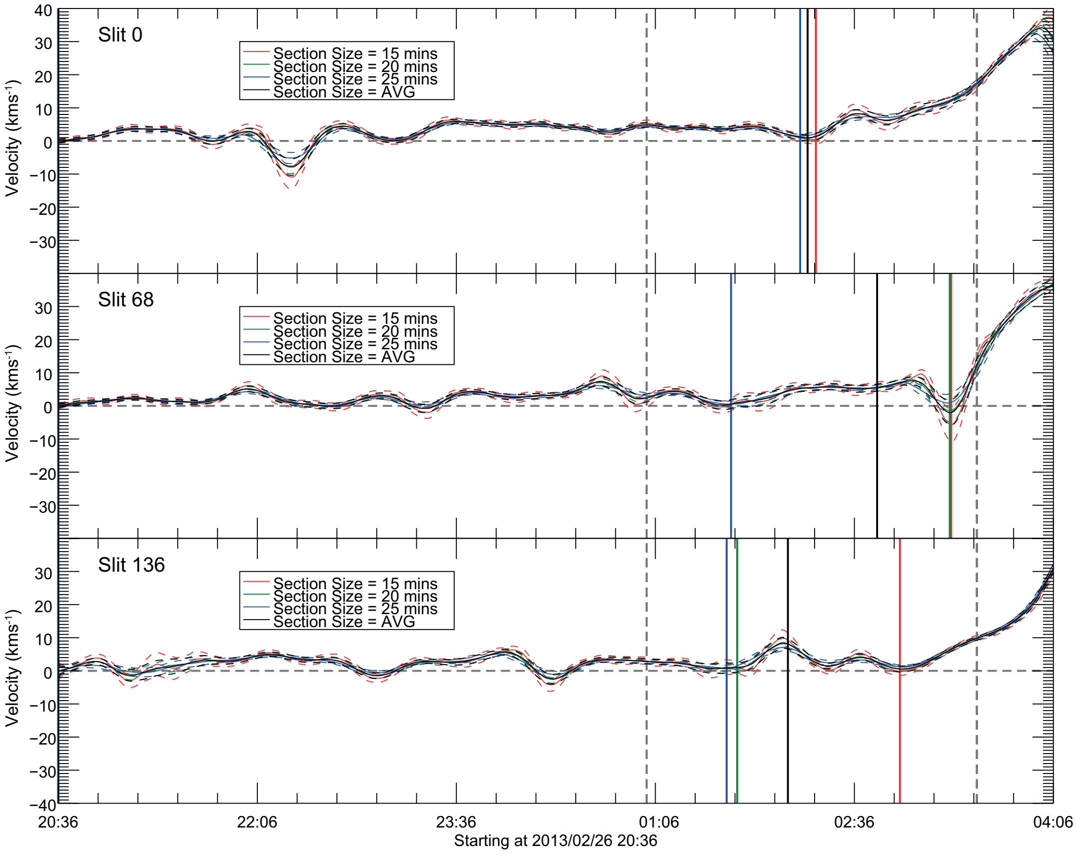

Figure 3.25: The velocity profile of the three slits shown for 304Å. The dashed gray horizontal line is at 0kms^{-1}. The horizontal gray bars indicate the search range. The solid coloured lines represent the velocity profiles. The vertical solid lines represent the automated detection of the velocity minima. The fainter, coloured, dashed lines represent the error on each line. Each colour represents a different section size: red=15 minutes, green=20 minutes, blue = 25 minutes

more focussed nature of these slits we can begin to see dropouts propagate through the structure. For instance, the dark streak starting around 22:06UT and lasting ~15 minutes in slits 0-30 and appearing progressively later in slits 30-80. It is now clear that velocity profiles in all slits, and both wavelengths, depict some form of acceleration with the onset tending towards later times for increasing slit numbers. Or, more explicitly, the onset of eruption starts nearer to the centre of the prominence structure and progressively gets later further along the edge. However, this may have something to do with the rather notable dropout masking the beginning of the acceleration phase, in particular with regards to slits 45-90

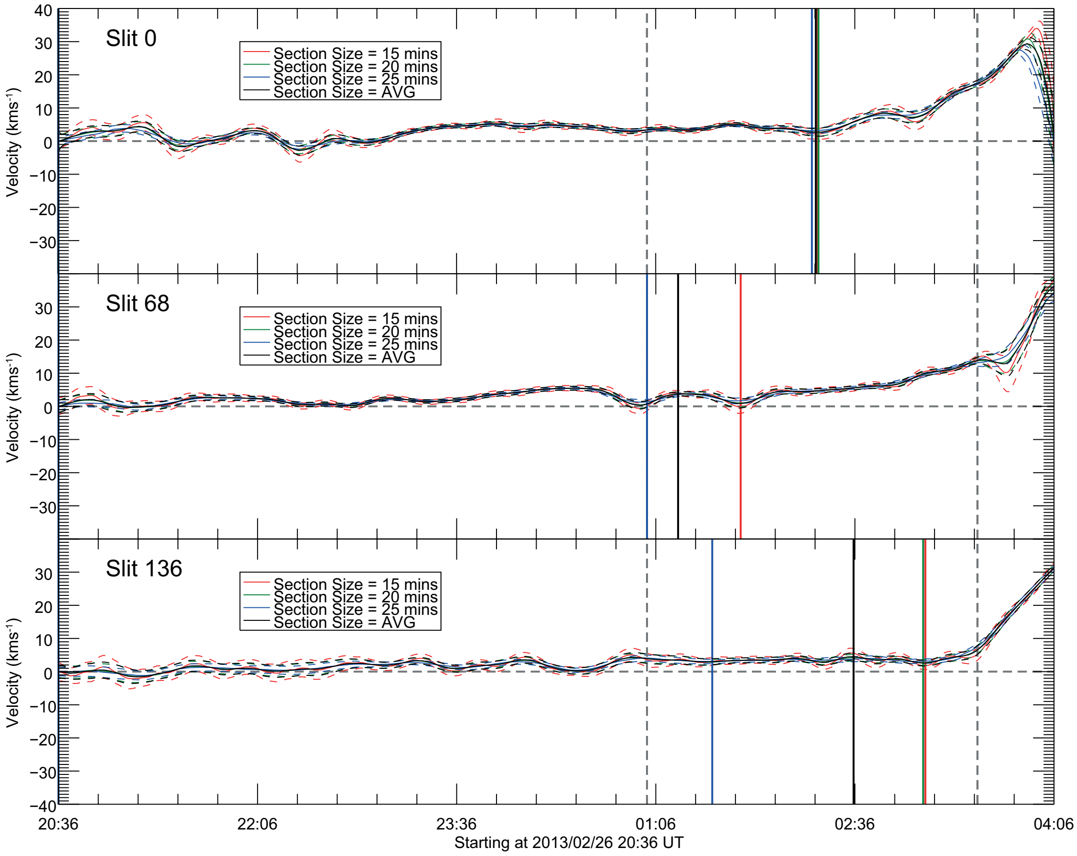

Figure 3.26: The velocity profile of the three slits shown for 171Å. The dashed gray horizontal line is at 0km/s. The horizontal gray bars indicate the search range. The solid coloured lines represent the velocity profiles. The vertical solid lines represent the velocity minima. The fainter, coloured, dashed lines represent the error on each line. Each colour represents a different section size: red=15 minutes, green=20 minutes, blue = 25 minutes

between 02:51 UT and 03:21UT.

3.4 Discussion and Conclusions

3.4.1 Discussion

The aim of this chapter is to begin to determine the role of ideal-MHD instabilities in a prominence eruption. We will now combine our results from geometrical modelling, writhe calculations, and kinematic analysis to further understand the evolution of this eruption, and in particular the linear rise phase.

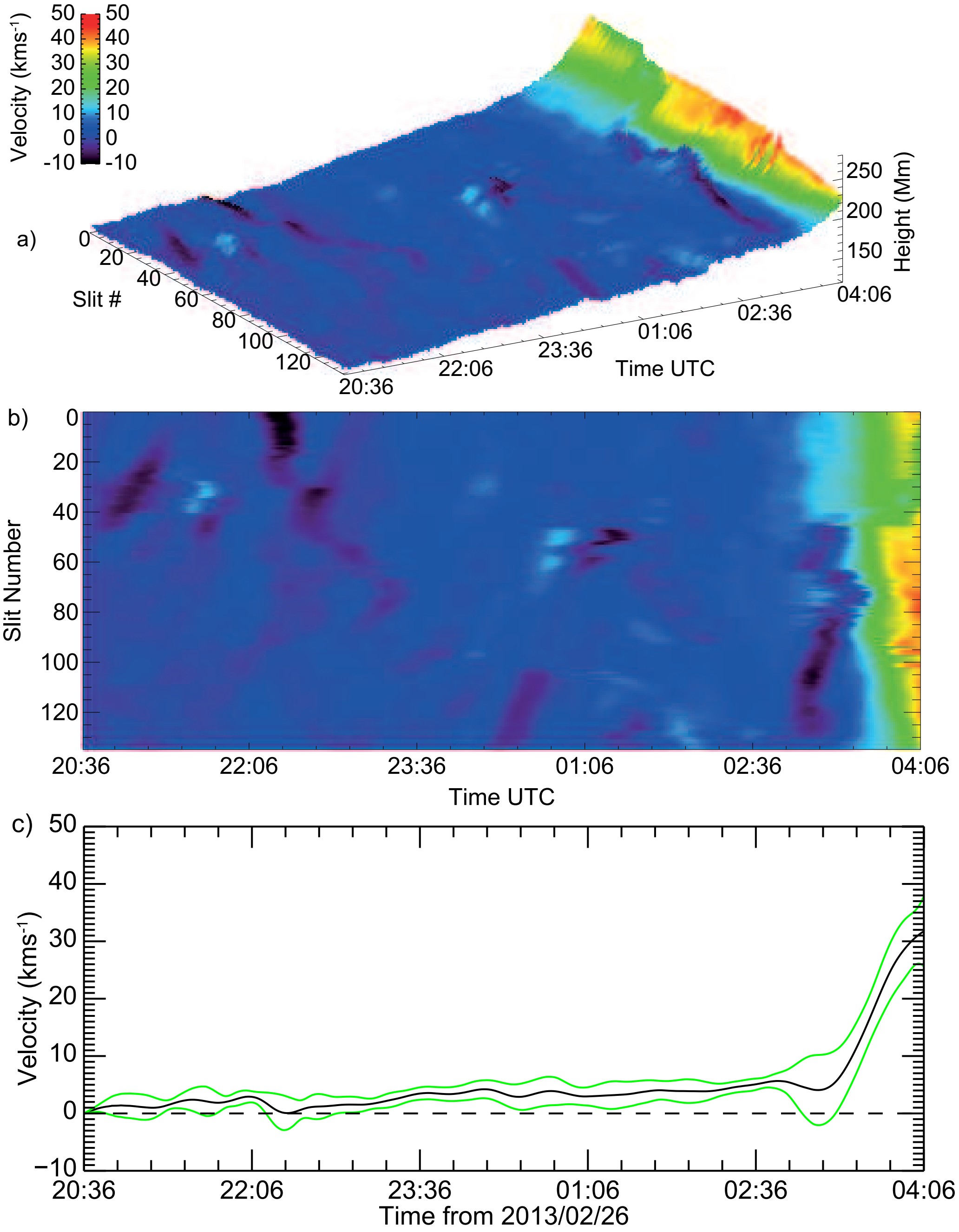

Figure 3.27: For 304 Å. a) The side-on view of the surface plot of height for each slit number vs time. b) The top-down view of the same surface plot. In both, colour represents running boxcar linear velocity. c) The running boxcar linear velocity averaged across all slits with the green lines representing the standard deviation of the velocity across all slits.

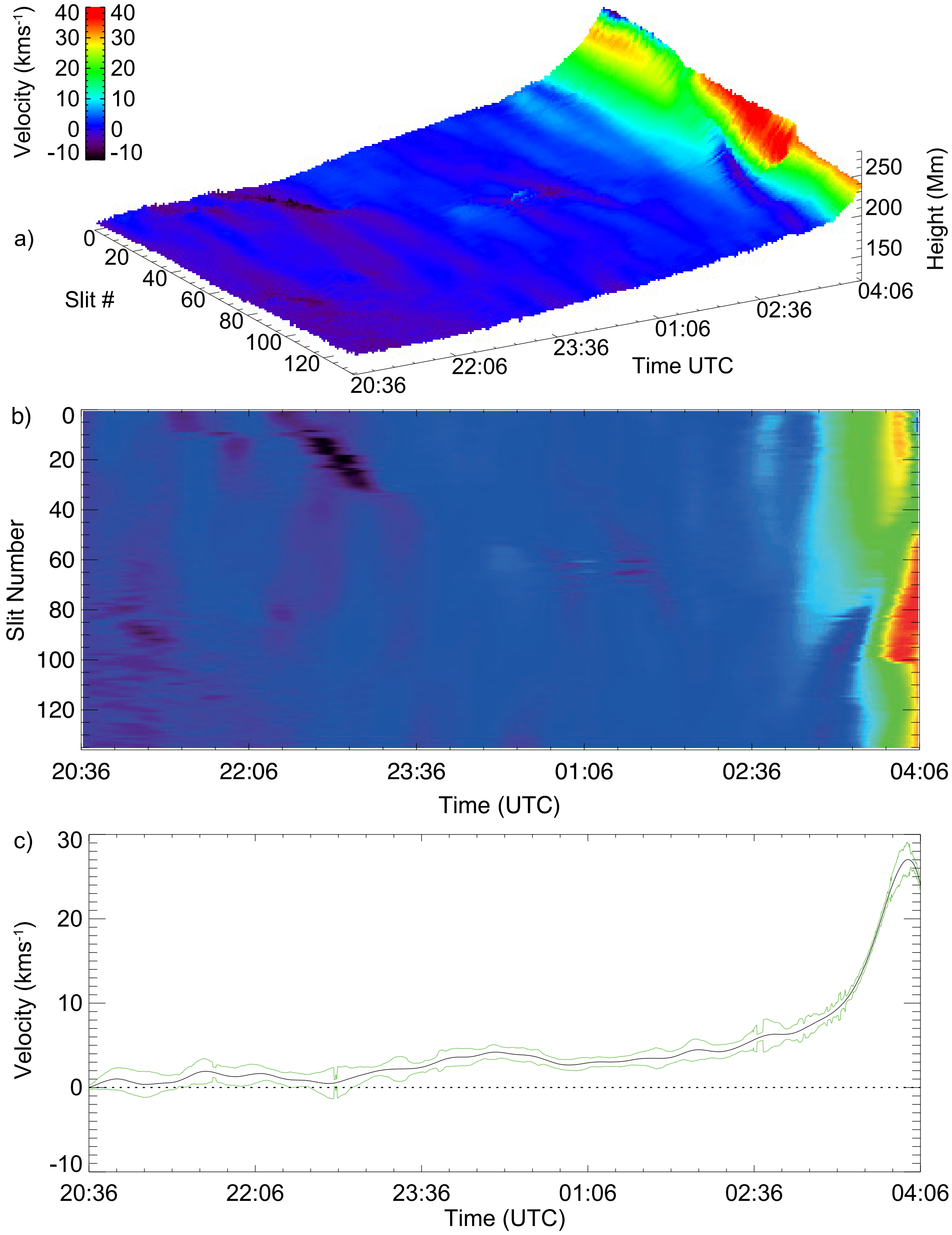

Figure 3.28: For 171 Å. a) The side-on view of the surface plot of height for each slit number vs time. b) The top-down view of the same surface plot. In both, colour represents running boxcar linear velocity. c) The running boxcar linear velocity averaged across all slits with the green lines representing the standard deviation of the velocity across all slits.

3.4.1.1 The Linear Rise Phase

We explored the possibility of whether or not the linear rise could be caused by the prominence undergoing the kink instability. As mentioned in Section 1.2.2.3 we would not expect to see the KI fully develop here. Furthermore, we would expect to see the development of writhe as the structure erupts. However, as shown in the third column of Fig. 3.6, we do not see any kinking of the structure from a top-down perspective. When measuring the writhe of the three independent 3D-reconstructions we found only noise, with no systematic changes for all times prior to the non-linear rise phase. For this reason we rule out the kink instability. The change we do see in Fig. 3.6 could correspond to a deflection away from the polar coronal hole to the south of the structure as has been suggested by Aulanier et al. (2010); Zuccarello et al. (2012).

Instead, we assume that the prominence was driven to eruption by some mechanism that first causes the linear rise phase. In regards to this, there is an aspect of this prominence we have not yet discussed – i.e., we have not explicitly considered the role of the prominence mass in this eruption. Although the mass of a MFR was originally included in early prominence models (Kuperus & Raadu, 1974), it was considered negligible and subsequently ignored by many later authors seeking insight into the TI. Recent work by Jenkins et al. (2018), Tsap et al. (2019), and Jenkins et al. (2019) highlights the importance of including mass and the impact of mass drainage. A loss of mass in the prominence channel could lead to a destabilisation of the magnetic structure resulting a force balance that could cause a buoyant uplift of the whole structure. There is perhaps some limited evidence of mass drainage ongoing in this event prior to eruption, sourced at the apex and flowing along the legs in 304 Å movies in both AIA and STEREO of the event. Further investigation of these flows will be part of a follow-up study.

3.4.1.2 Geometrical Modelling and Kinematic Analysis

Upon reconstructing the prominence we first performed some basic geometric modelling in three forms; that of a circle, an ellipse, and a polynomial function. Although these models were applied to a simplified form of the reconstruction we nonetheless gained some fascinating insights. Whilst the circular models tell us relatively little, they do at least confirm the lack of a large-scale restructuring at the footpoints. We gain greater insight from the elliptical model. From the lack of large scale motion of the footpoints, but with the ability of an ellipse to model the height of the prominence we gain an abstracted form of a height-time plot. Although interestingly there is no clear point at which the non-linear phase could be said to have begun as the eye-catching jump around 02:46 UTC is in reality no bigger than the changes around 00:36 UTC. This is perhaps due to the asymmetry of the prominence with the increase in height, and thus eccentricity, not lying solely in the mid point of the structure thus diminishing its effect. It is for this reason that we invoked a polynomial function with the capacity for asymmetry. As mentioned previously about this function, whilst a piece-wise function would almost certainly provide a more accurate description of the prominence there are considerations that exclude its use here. Instead this functions allows us to quickly assess some basic kinematics of the structure, including an early estimate of an onset of the non-linear phase at somewhere from 01:16 to 02:16 UTC from the b and d coefficients. Interestingly, this is earlier than can be seen in either the full prominence or the high-detail section slits. However, this must be viewed in the context of the χ^2_{red} of a number of these fits being quite high. Furthermore, the height-time plot of the apex created by coefficient a visually suggests a much later onset time of somewhere around 03:16 UTC. This roughly matches the onset time seen in the surface plots of both the full prominence and the smaller section, specifically in the slits closest to the actual apex of the structure (i.e mid slit numbers across the full prominence, but low slit numbers in the detailed analysis).

3.4.1.3 The PCTR and Radiative Transfer Effects

As shown in Figs. 3.23 and 3.24 we have potentially been able to recover the width of the PCTR by comparison of the prominence in 171 and 304 Å. Though many models of the PCTR exist (see Parenti (2014) and references therein), few mention the potential size of the structure, instead choosing to focus on other properties such as mass, density or temperature. It is therefore difficult to set our recovered width into context. However, our average width of 3.3 Mm is in very good agreement with that of 3.5 Mm recovered by Anzer & Heinzel (2008) when using an idealised model. As mentioned previously, we believe that the differences between the profiles found in 171 and 304 Å are primarily due to optical and radiative transfer effects. The first of these is an important difference between a 3D height and a plane-of-sky height. As the slits increase in number, they move further towards the disk in the plane-of-sky of AIA. This means that although the prominence starts at roughly similar 3D heights in slit 0 and 136 (see Fig. 3.21), it is at a lower height in the plane-of-sky. As such, the contribution from the lower solar atmosphere to the apparent emission of 171 Å in the prominence will become greater as it moves towards the disk. The second of these is the difference in optical thickness, with 171 Å being optically thin and 304Å being optically thick in the context of prominences. As such, in 304 Å the plasma itself will block any major contribution from behind the prominence. Therefore, we would expect that our detected edge in 304 to primarily that of the side of the structure closest to us. Whereas at our detected edge in 171 Å, whilst the prominence is the dominant source of emission we would not only expect to see contributions from both the closest and furthest side of the prominence but also potentially from the corona in front and behind it. This means that as the slits increase in number, and therefore move closer to the disk, there is a greater contribution from the solar atmosphere in 171Å. The third effect we believe to be making a major contribution is the solar atmosphere itself, or more specifically the height at which it continues to emit. As can be seen in some of the panels in Fig. 3.17 the atmosphere itself emits enough to be detected at around 60 Mm (in 3D) in 304 Å. Whereas, although not shown here for the sake of brevity, in 171 Å this occurs at heights at over 100 Mm (in 3D). Furthermore detection of minimal emission from the PCTR at the top of an off-limb prominence has been noted by Del Zanna et al. (2004), who note the importance of the contribution of the chromosphere-corona transition region in the detection of the PCTR.

3.4.2 Conclusions

The leading edge is clearly dynamic whilst the eruption ensues and a physical explanation on the nature of the dropouts is not investigated here. The purpose of this research is to accurately determine the onset time of acceleration in the eruption and it is clear that the plasma dropouts inject a strong influence on many height-time profiles. This prevents an accurate, effective, interpretation of the transitions in velocity (and more so acceleration) at critical times prior to the onset of acceleration in the eruption. The running boxcar linear velocity study provides a qualitative interpretation of the evolution of the leading edge prior to, and during, the eruption. To reach a quantitative assessment of this transition to acceleration we must apply a more interpretable forward fitting approach. This will take the form of a parametric study into the onset time of acceleration through examination of a two-component fit (consisting of a linear and non-linear terms) to all slit profiles. The details are further discussed in Section 4.1.2. A two-component forward fitting approach will be performed on the lower cadence stereoscopic results. This will allow the kinematic study of the eruption to be applied directly on the 3D-determined stereoscopic height-time profiles, which are a truer determination of heights in the eruption. Lower cadence observations also provide the added value of suppressing the impact of the dropouts in the time series. The running boxcar linear velocity results will be placed in context with this alternative forward fitting approach.

Chapter 4

The Parametric Analysis of Field Instabilities in a Prominence Eruption

A fo ben, bid bont

Branwen ferch Llŷr,
Pedair Cainc y Mabinogi

Parts of this chapter form the basis of content of a paper entitled "2D and 3D Analysis of a Torus-Unstable Quiet-Sun Prominence Eruption" that has been submitted to The Astrophysical Journal in collaboration with my supervisors, Drs. E. Scullion and D.S. Bloomfield.

4.1 An Alternative Kinematic Analysis Method

Continuing with the analysis performed in the previous chapter, only a subsection of the prominence has been selected for further kinematic analysis. This subsection, as can be seen in Fig. 3.20, comprises the range of the 137 slits at which the apex of the prominence is found at some point over all times. This was done due to the importance of the apex of the prominence in the torus instability (TI).

4.1.1 3D Height-Time Reconstruction

This second method differs in several ways from the method outlined in the previous chapter. Firstly, this method maintains the 3D radial heights found from the reconstruction. Due to this, it is limited to the STEREO cadence of 10 minutes. Secondly, although it also uses a background+σ threshold, it is taken from an empty nearby region of space due to there being no background data within the profile itself. As such, the threshold is the background+7σ, which results in a negligible difference in the actual values. Thirdly, the errors in this method are found by de-projecting the 3D co-ordinates into the AIA FoV, then by finding the difference between the clicked point and the pixel that is greatest in height above the threshold. Examples of this for each slit shown in Fig. 3.20 can be seen in Fig. 4.1.

This approach is limited in comparison with the first approach as it requires the starting location of the edge to be done by eye. This means it cannot be realistically applied to thousands of image sequences at the full AIA time resolution. Therefore the sampling of this approach being performed at the STEREO 10 minute resolution, results in 36 points for each height-time profile, rather than the 2275 time points for the automated method.

4.1.2 Parametric Fits

Once the 3D height time profile of the prominence has been derived we follow the lead of Schrijver et al. (2008) and perform linear+power-law fits of the leading edge in height-time profiles. This is done using a kinematic function of the form

$$h(t) = h_0 + v_0 t + \alpha \left(t - t_{\mathrm{nl}}\right)^{\beta} H \left(t - t_{\mathrm{nl}}\right). \tag{4.1}$$

In the above equation, $h(t)$ is the returned height at time t, t is the number of seconds since start of observation (2013-02-26 22:06:19UTC), h_0 is the height at time $t = 0$, v_0 is the linear velocity, t_{nl} is the time of onset of the non-linear or "acceleration" phase in the eruption, α is the acceleration-like multiplier, β is the acceleration-term power index and $H\left(t - t_{\mathrm{nl}}\right)$ is a Heaviside function that switches on at $t = t_{\mathrm{nl}}$. This is completed using the IDL routine MPFITFUN. This is done in a piece-wise fashion to allow the point at which the linear section joins the power-law section to be parameterised. Each parameter of the equation, i.e. h_0, v_0, α and t_{nl}, can be freely varied. This allows the fitting process to place the start time of the acceleration phase at the position that minimises the χ^2 value. The fitting process was repeated for each slit over a range of β values from $\beta = 1.5$ to 4.0 in increments of 0.1 therefore sampling the full range of power indices proposed to pertain for prominence eruptions as reported in Lynch et al. (2004); Schrijver et al. (2008). As part of MPFITFUN each parameter can have limits placed upon it. For instance, it is possible to ensure a positive linear velocity or a start time over the data range. However, placing any limit on the fit will affect the time at which the onset of the acceleration phase is placed. As this is what we are attempting to find, we place no limits. Thus it is possible that some models will contain parameter values that are unphysical, but this is necessary in order to more accurately find the eruption time in all slits. As part of the fitting process, initial estimates for each parameter are required. Here they are $h_0 = 120\,\mathrm{Mm}$, $v_0 = 0.5\,\mathrm{km\,s^{-1}}$, $\alpha = 1\,\mathrm{m\,s^{-\beta}}$, and $t_{\mathrm{nl}} = 15000\,\mathrm{s}$. Once the process has found the local minima of χ^2 for a given β the free parameters are output with their formal 1σ errors calculated the fit's covariance matrix. As in

Chapter 3, we compare the goodness-of-fit of each value of β using χ^2_{red}, given by $\chi^2_{\mathrm{red}} = \chi^2/\nu$ where ν is the number of degrees of freedom of the model.

The form of the kinematic function chosen here is a departure from what has been seen in recent works by other authors looking at similar events (see the "Obs" papers in Table 1.1, for instance (McCauley et al., 2015)) where an exponential form has been chosen. Specifically, many authors use the exponential form first presented by Cheng et al. (2013), $h(t) = c_0 e^{(t-t_0)/\tau} + c_1(t - t_0) + c_2$, where t_0 is time at $t = 0$, τ is a free parameter, and $t_{\mathrm{onset}} = \tau \ln(c_1\tau/c_0) + t_0$. We have tested both this form, and a form more similar to our own , i.e. $h(t) = h_0 + v_0 t + \alpha(e^{(t-t_0)/\tau} - 1)H\,(t - t_0)$. As will be discussed further in Sec. 4.2.2, neither of these provided adequate results and were thus discounted.

4.2 Results

4.2.1 Height-Time Plots

4.2.1.1 Semi-Automated Edge Detection Method

Height-time plots were generated at the STEREO cadence of ten minutes for 304Å using the same 137 slits. This allows us to compare our results for onset times using a separate method over the same data. These profiles are more suited for the parametric fitting that will be applied, due to their lower sensitivity to random plasma motion.

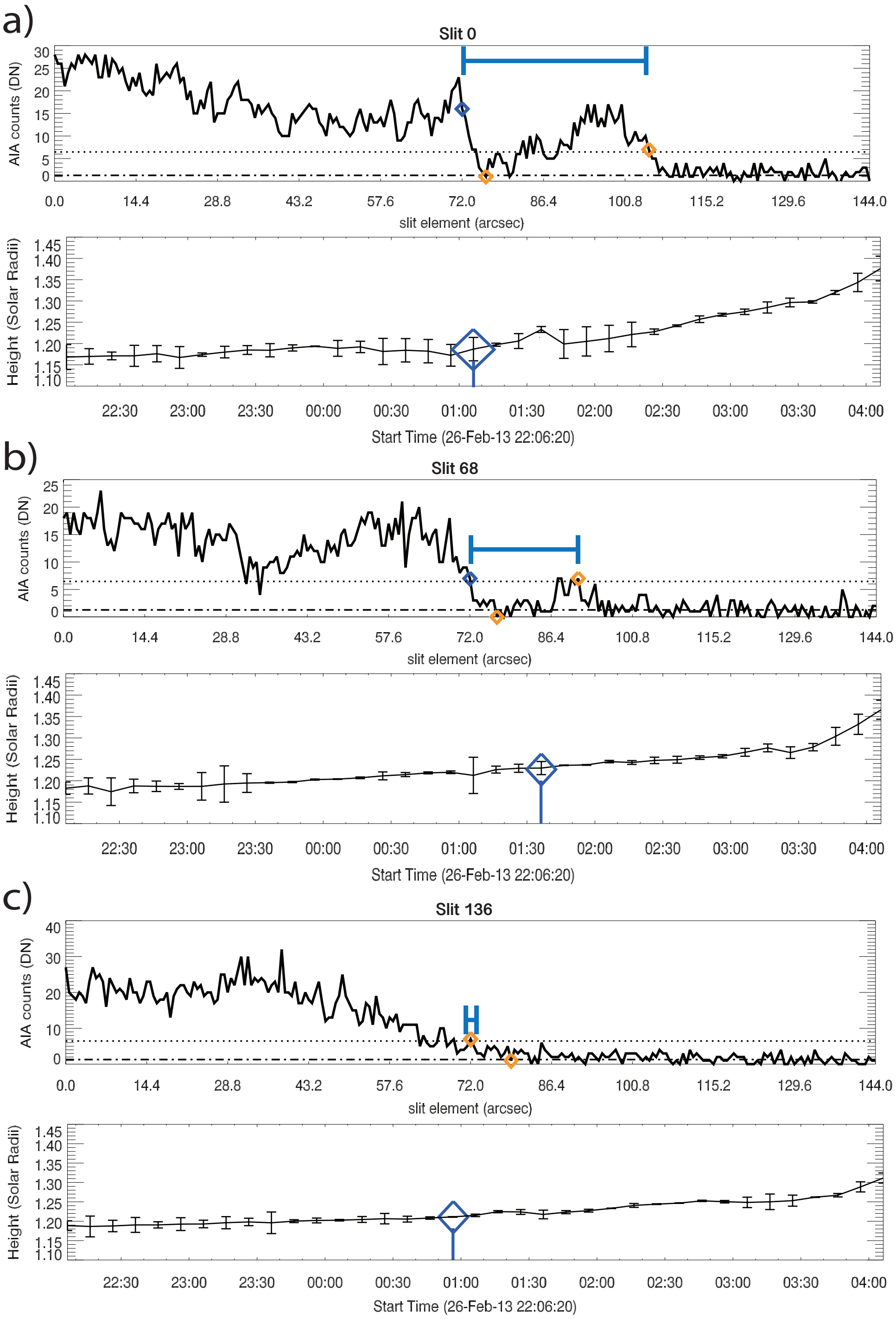

Figure 4.1: a)-c) The 304 Å AIA intensity profiles for 3D radial slits 0, 68, and 136, respectively, deprojected onto the AIA FOV. The manually-detected edge of the prominence is indicated with the blue symbol. The first detected background-level pixel (right-most orange symbol) and the first detected 7σ-above-background pixel (left-most orange symbol) along the slit are indicated. The horizontal blue error bar represents a measure of the uncertainty in height of the detected edge.

This method is less sensitive to drop-outs under certain conditions. Namely, if the user selects, for instance, the higher edge, but the threshold selects the lower, that point would have a large error bar. This allows the fitting process more freedom over the effected points. In contrast the first approach would likely maintain a very small error on the measured height, but is more sensitive to discontinuities as can be seen in Fig. 3.21.

4.2.2 Parametric Fits

For all best-fit parameter plots that follow in this sub-section, a specific colour is assigned to each β value from the IDL rainbow colour table 39 – i.e., black ($\beta = 1.5$), through purple ($\beta = 1.8$) to green ($\beta = 2.9$) to red ($\beta = 4.0$).

4.2.2.1 General Properties

In Fig. 4.2a we show the combination of the components in the fitting function (red dotted, blue dashed, and green solid lines) that combine as the best fit to the observations (black symbols with error bars). It is important to note that the linear velocity component, $v_0 t$, continues to contribute to the model after the onset of the acceleration (i.e., $t > t_{\rm nl}$). Figures 4.2b - 4.2g display the 1σ extent of the best-fit models for a selection of β. Of particular note in Fig. 4.2 is panel b) which shows a fit resulting from the initial guesses of the parameters. Whilst initially this may seem to be a very poor fit, one must remember that this is due to the unconstrained nature of each parameter. Improving this particular fit, which is a fairly common result for this value of β across all slits, would negatively impact the unconstrained nature of the other fits. As this would directly counter our goal to find the unconstrained $t_{\rm nl}$, no limits are set.

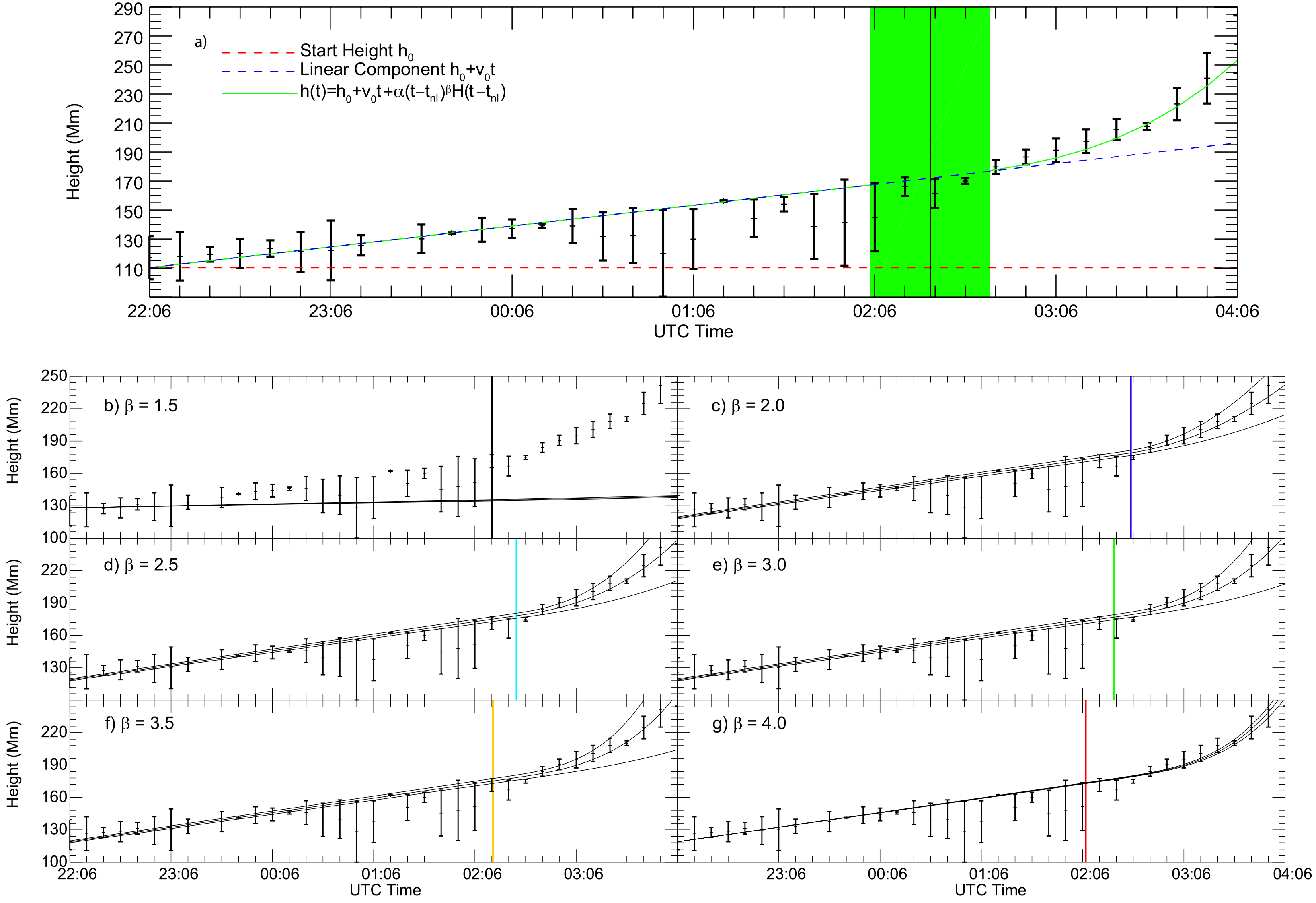

Figure 4.2: a) The height-time profile of slit 68 overlaid with combinations of the best-fit model components. The horizontal dotted red line shows the starting height h_0, the dashed blue line is the combined starting height h_0 plus the linear velocity v_0t term, while the solid green line is the combination of starting height plus linear velocity term plus the acceleration-like $\alpha\left(t-t_{\mathrm{nl}}\right)^{\beta}$ term. The green shaded box indicates the range of possible non-linear phase onset times in this example. b)-g) Best-fit height-time models as central curves that are bounded above and below by curves indicating their 1σ extent (based on the returned best-fit parameter errors), with vertical lines marking the resultant non-linear phase onset times coloured according to the value of β.

In Figure 4.3, for all values of β we show overlays of the best-fit models to the individual height-time plots of slits 0, 68, and 136. Notably, over the full range of slit numbers the majority show best-fit results with a pattern similar to that of slit 68 – higher values of β show earlier t_{nl} onset times (i.e., the general colour order of the vertical lines being red earliest to purple/black latest) – which is understandable based on the relationship between the model parameters α, β, and t_{nl}. Higher values of β increase the curvature in the modelled height-time profile, which the fitting process compensates for by decreasing the acceleration-like multiplier α (see Fig. 4.7) in order to achieve a good fit. In turn, smaller values of α cause the point of visible departure from the linear component to appear later, which the process compensates for by moving t_{nl} (see Fig. 4.8) to earlier in the fitting. This is clearly demonstrated in Figs. 4.2c-4.2g with the shift of t_{nl} (i.e., coloured vertical lines) to earlier times for increasing β. Aside from the typical fit behaviour exemplified by slit 68, in a small number of slits a greater degree of scatter is found in t_{nl} for $\beta < 1.9$ and $\beta > 3.6$. This is represented in Fig. 4.3 by slits 0 and 136, but it is worth noting that the intermediate portion of the β parameter space still generally results in a smooth variation of earlier t_{nl} with increasing β, e.g. between 02:56–03:26 for slit 0, and 02:16–02:36 for slit 136. Due to the relationship of parameters, one can see that in each panel of Fig. 4.3, the majority of the fits are similar despite their large range of acceleration onset time, t_{nl}, which will be discussed further in Sec. 4.3.1.1.

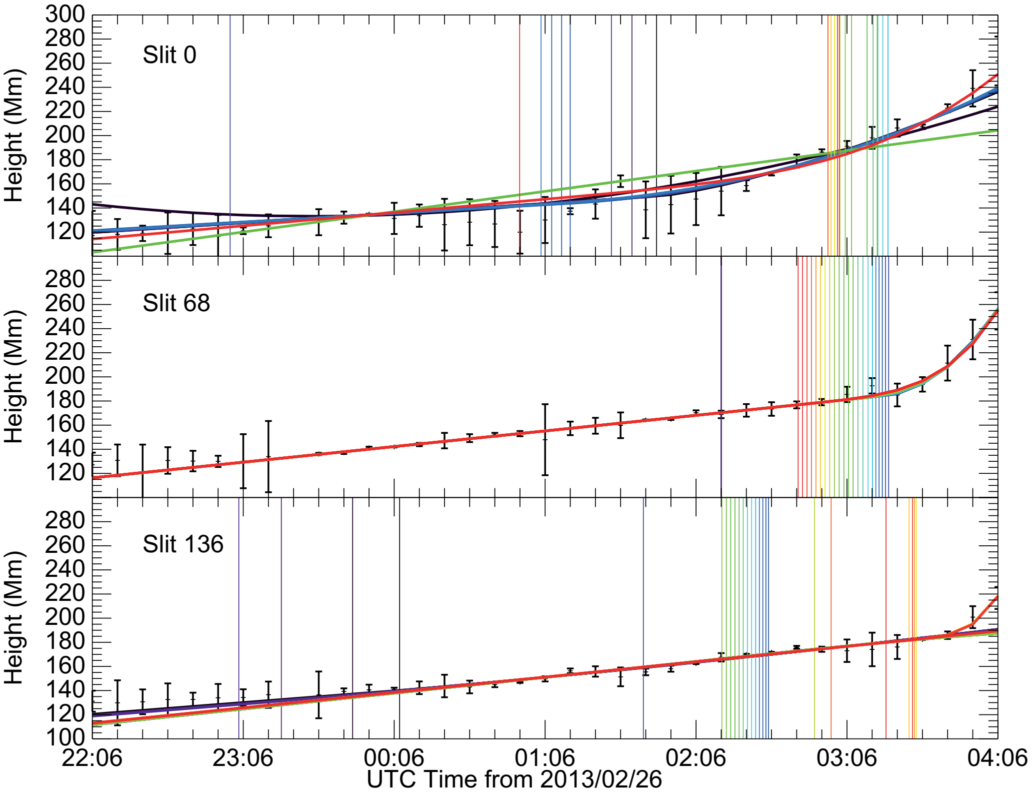

Figure 4.3: The best-fit models for all values of β are overlaid onto each height-time profile (represented as data points with vertical error bars) for slit 0 (top), slit 68 (middle), and slit 136 (bottom). Each model overlay is represented by a specific colour assigned to each β value, i.e., purple ($\beta = 1.5$) through green ($\beta = 2.7$) to red ($\beta = 4.0$).

4.2.2.2 Returned Parameter Values

The $\chi^2_{\rm red}$ is shown in Fig. 4.4 across all slits for increasing values of β (left to right, and top to bottom). The $\chi^2_{\rm red}$ of these fits will be considered in our interpretation of the $t_{\rm nl}$ results (see Fig. 4.8) in Sec 4.3.1.1.

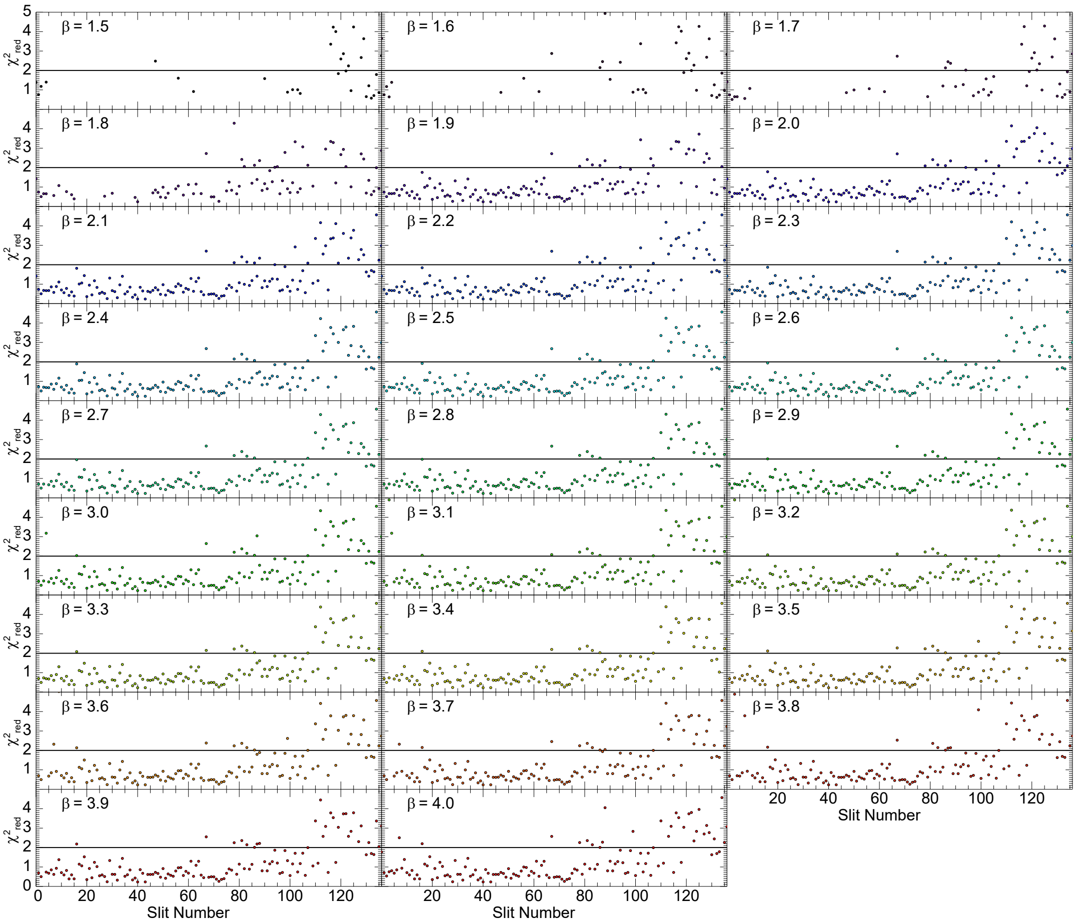

Figure 4.4: The χ^2_{red} versus slit number for all slits for a given β. A horizontal line is drawn at $\chi^2_{red} = 2$. Each panel displays the results for a specific value of β (i.e., increasing left to right and top to bottom) coloured accordingly.

As can be seen in Fig. 4.4 almost all fits possess a $\chi^2_{\mathrm{red}} < 5$, with the majority having a $\chi^2_{\mathrm{red}} < 2$. For $\beta < 1.8$ the fitting process fails. Shown below in Fig. 4.5 is the start height, h_0, for all slits across each value of β.

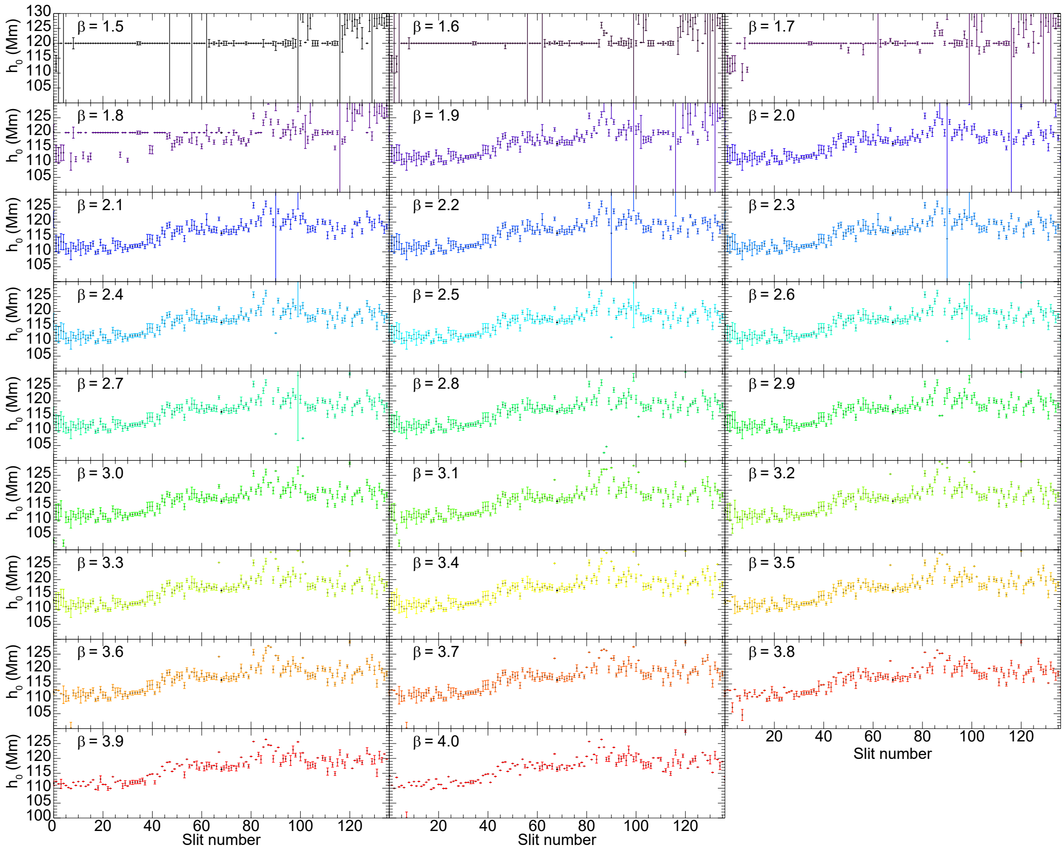

Figure 4.5: The start height, h_0, versus slit number for each value of β

As can be seen above, the start height, h_0, is lowest for the smallest slit numbers, and increases with slit number across all $\beta > 1.8$. Those below $\beta < 1.8$ that could not converge to a fit take the value of the starting estimate. To ensure clarity: this is the height of the prominence at the start of the data (i.e. the height at 22:06 UTC) not the height at the onset of $h(t_{\mathrm{nl}})$. As can be seen in Fig. 4.5 there is a slight upward trend with slit number across all values of β. This means that the slits nearest the footpoint, i.e. those towards slit 136, start at a greater height than those at the midpoint of the structure, as can also be seen in Figs. 3.21,and 3.22. The relevance of this will be discussed further in Sec. 4.3.1.3.

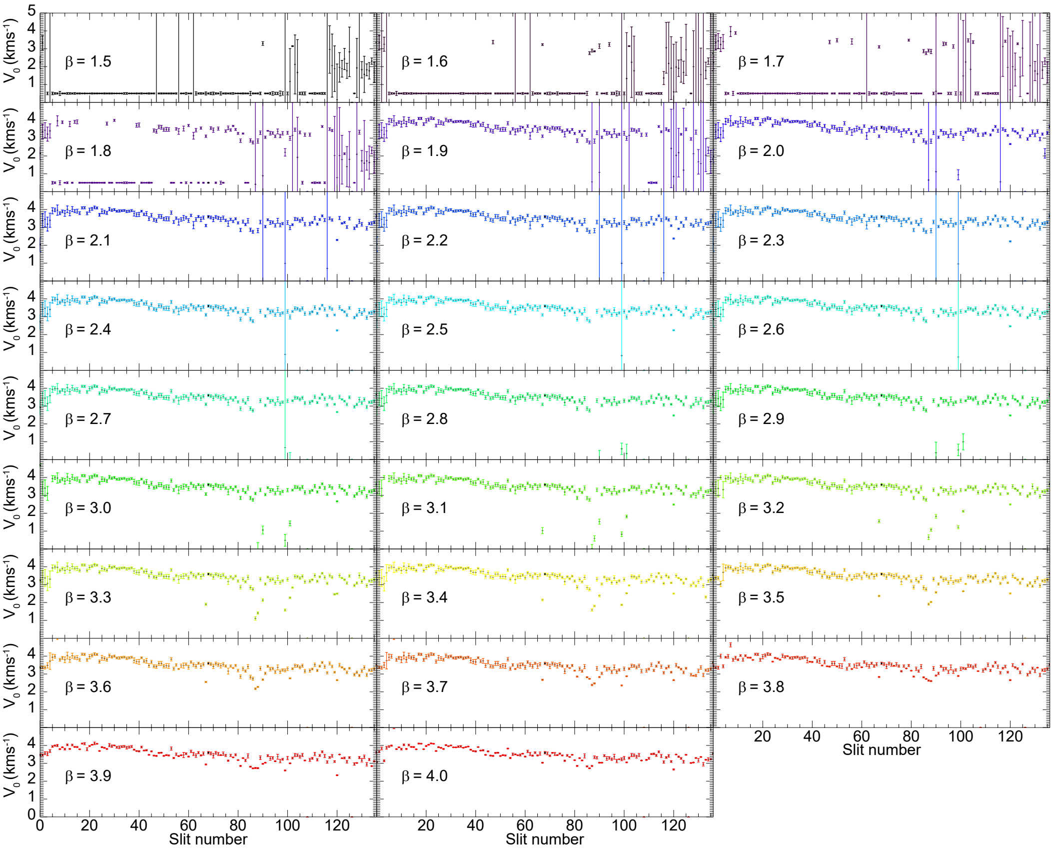

Figure 4.6: The linear velocity, v_0, versus slit number for a given β

Fig. 4.6 shows that the smallest slit numbers have the greatest linear velocity, v_0, for all $\beta > 1.8$. As for h_0, the majority of slits for $\beta < 1.8$ take the value of their initial estimate. Whilst the difference is small, it becomes significant over the several hours of the linear rise phase, as will be discussed further in Sec. 3.4.1.1.

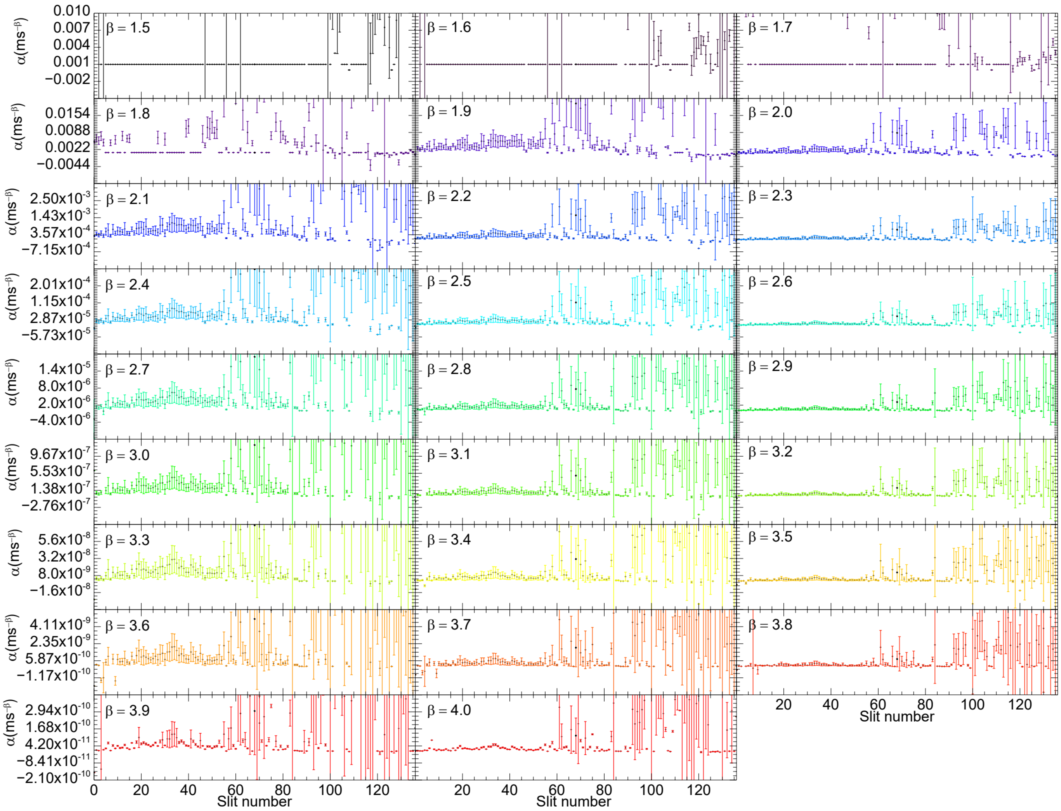

Figure 4.7: The acceleration multiplier, α, versus slit number for a given β. Note the changing y-axis values for each row, which is due to the multiplier actually being related to its value of β. Each multiplier is therefore in units of ms$^{-\beta}$, not ms^{-2}.

In Fig. 4.7 we show the acceleration multiplier, α, for each slit number and beta. For each value of β we see a trend of increasing α with slit number, with a trend of decreasing orders of magnitude with increasing β. It is important to notice the changing scale of the y-axis in figure 4.7. It is also important to notice the units on the y-axis. This is because the multiplier is actually related to its value of β. Thus each multiplier is in units of ms$^{-\beta}$, not ms^{-2}.

In Figure 4.8, we present the start times of the non-linear phase t_{nl}, as determined by the fitting process independently carried out for all slits, where each panel displays the results for a specific value of β (i.e., increasing left to right and top to bottom). It is clear that the fitting process fails across the vast majority of slits for $\beta \leqslant 1.8$. As stated previously, and demonstrated here, there is a trend of earlier t_{nl} with increasing β for most slits. Notably, at the earliest time of acceleration (corresponding to slit 0), we find that the maximum height location of the 3D reconstructed loop coincides with the intersection of slit 0 (as shown in Fig. 3.6: first-row panels). This is expected given that the eruption should start at the apex of the prominence structure according to the TI and, furthermore, this result addresses the second observational signature relating to the TI (as mentioned in Section 1.2.2.3). Overall, with regards to $\beta \geqslant 2.0$, a general trend is observed whereby t_{nl} consistently becomes later with increasing slit number indicating that the eruption is slowly (i.e. over more than an hour) propagating along the structure, rather than happening everywhere practically simultaneously. This will be discussed further and put into the context of the other parameter's results in Sec. 4.3.1.1.

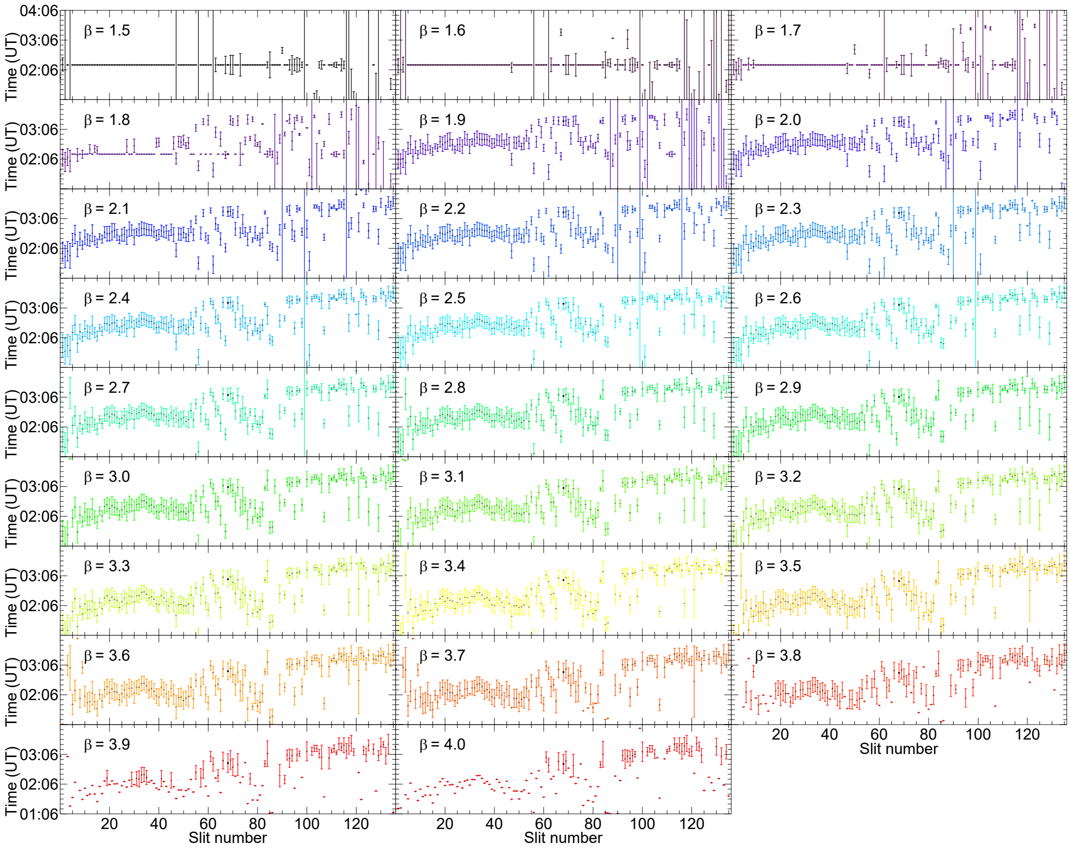

Figure 4.8: Time of onset of the non-linear ("acceleration") phase, t_{nl}.

In Figure 4.9, we present the height of the prominence at the time of acceleration, $h(t_{nl})$, as determined for each slit from the best fit parameters. These are not measurements of the height across the prominence structure at an instant in time, rather these are heights corresponding to the time of acceleration onset in a given slit. As before, we do not consider the results for $\beta \leqslant 1.8$ due to their poor fits. When considering a single slit number (across all β), there is a general progression to lower $h\left(t_{\mathrm{nl}}\right)$ with increasing β, which we expect given that we determine earlier t_{nl} with increasing β. When considering a single value of β (across all slit numbers), we observe a slight trend of increasing $h\left(t_{\mathrm{nl}}\right)$ with increasing slit number. As mentioned above, the use of slit-dependent t_{nl} values means that this result cannot be interpreted simply as an increase in height along the prominence structure, but instead that slightly greater heights are achieved for larger slit numbers at the later t_{nl} values recovered for those slits. Over all slits and all β we find values for $h\left(t_{\mathrm{nl}}\right)$ that are relatively consistent along the prominence structure, the implications of which will be discussed in Sec. 4.3.1.1.

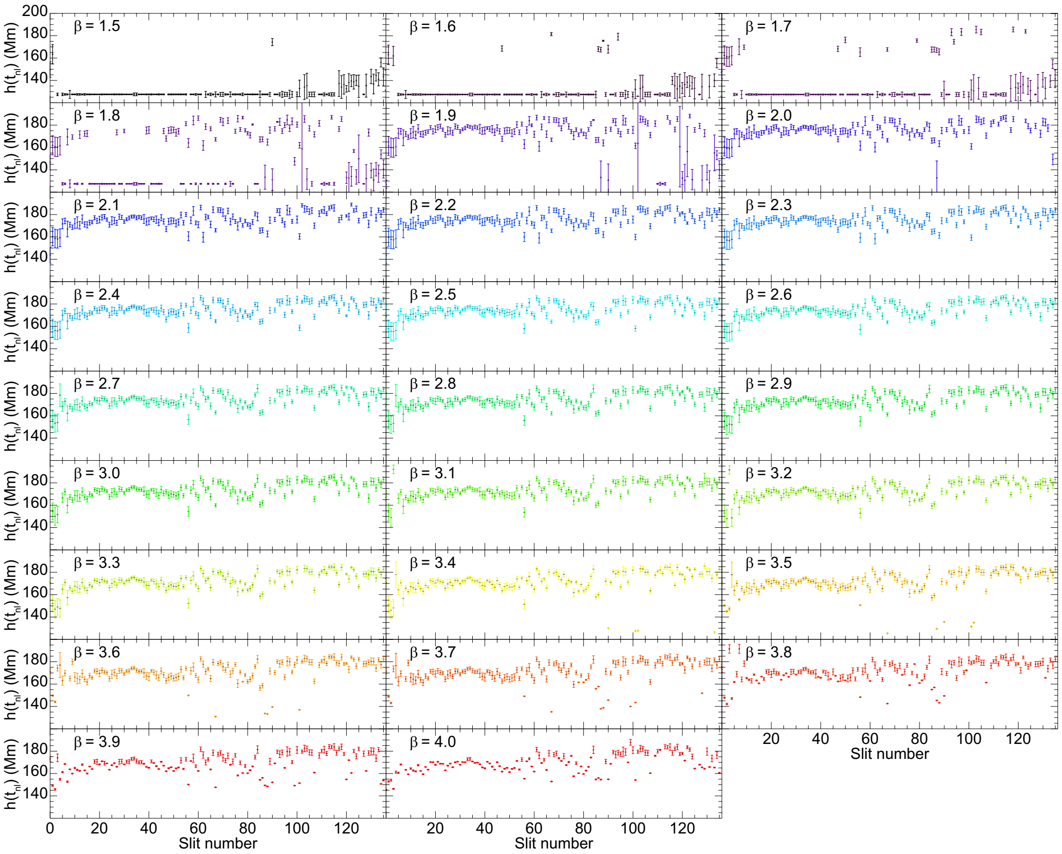

Figure 4.9: Height at the time of onset of the non-linear phase, $h(t_{\mathrm{nl}})$.

4.2.2.3 Testing α and β

As previously stated, we have fixed only our value of β as part of our parametric fitting. We now test the assumption we have made about our range of β being acceptable, and to ensure that there is not a preferred range or value of β. We do this by fitting only the non-linear section of our profiles, by modifying our kinematic function and height-time plots to remove the linear section, i.e. the contribution of terms $h_0 + v_0 t$. As we have modified the heights of each point in our new height-time plot according to our previous fits we have propagated the errors in the linear terms into the new heights. As defining the onset time has been a key part of this work, we use the onset time as output by the previous fitting for each value of β for each slit. As our onset time becomes our start time, we also remove the Heaviside function. To ensure clarity between fits from the fixed values of β, and fits that will result from free values of β, we shall refer to the new free β instead as B. We shall also refer to the new values of α as A This leaves us with a function of the form

$$h_{mod}(t) = A(t)^{B} \ , \tag{4.2}$$

where h_{mod} is the modified height, and A and B are now free parameters.

An alternative exponential form was tested, however due to some points lying beneath the initial height (and thus became negative when the linear section was removed) fitting became impossible when a logarithm of those height was taken.

As before, we use the IDL procedure MPFIT to minimise the $\chi^2_{\rm red}$ of each fit. This, along the formal 1 sigma errors calculated from the covariance matrix, are output by the fitting process. Thus we are able to fit the resultant profile of every single value of every single slit. As A remains dependent on its value of B, it is as difficult to interpret as α in Fig. 4.7, thus we omit it here for clarity. In Fig. 4.10 we present the resulting range of B found over all slits for three values of β, coloured coded as appropriate.

As can be seen in Fig. 4.10 we see the values of B and their associated errors output by the new fitting process for each slit. We now combine each fit found for each slit into a box and whisker plot, Fig. 4.11. These plots graphically represent the inter-quartile range (i.e., 25th to 75th percentile) by the vertical extent of the box, the median as the horizontal line within the box, and the minimum and

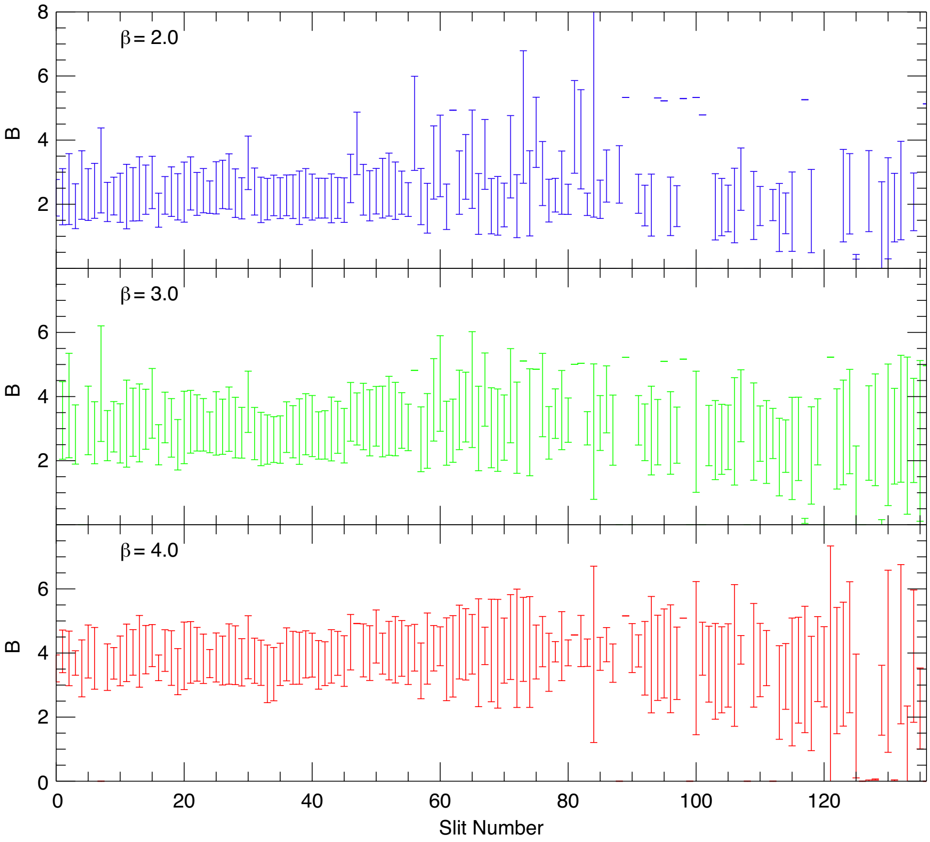

Figure 4.10: Range of acceptable B with increasing initial fit β.

maximum values as the lower and upper extrema of the whiskers, respectively. We include two distributions within this plot: i) in purple with uncapped dashed whiskers, the unfiltered distributions which include all previous fits, and ii) in gold with solid capped whiskers, only those new values of B for which the original fit had a $\chi^2_{\text{red}} < 2$.

As can be seen in from the filtered box and whiskers in Fig. 4.11 our chosen range of β covers slightly further than the range of acceptable B values over the majority of slits. We therefore conclude that our range of β values is acceptable, but displays no preferred value.

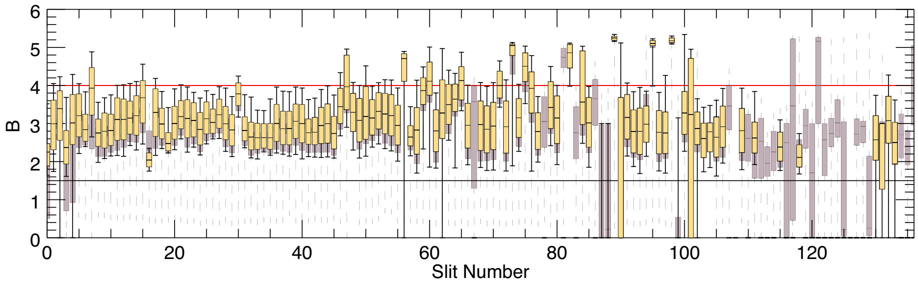

Figure 4.11: A filtered boxplot of the range of acceptable B values for each slit. The red and black lines represent the previous limits of β. Purple boxes with dashed semi-transparent uncapped whiskers represent unfiltered data. Gold boxes with solid capped whiskers represent filtered data whose original fits had a $\chi^2_{\mathrm{red}} < 2$.

4.2.3 Magnetic Field Decay Index

In regards to the first observational signature of the TI (see Section 1.2.2.3) it was stated that if the onset height, $h(t_{nl})$, can be determined, the decay index (Eq. (1.3)) should be smoothly varying if measured over its neighbouring points along the prominence. Now that we have established a relatively constant $h(t_{nl})$ across adjacent slits over a range of β, we next explore the variability of the decay index for this event. Note that the slits diverge as they increase in height, causing the horizontal separation between measured points along the prominence edge to increase as the prominence increases in height. In order to calculate the decay index using Equation (1.3), we first make the assumption that the prominence is dominated by potential fields. We make this assumption due to the area surrounding the prominence being that of the quiet Sun. We thus make use of a potential magnetic field model from the SSWIDL package PFSS (Schrijver & De Rosa, 2003). Ideally, we would like to use a PFSS field extrapolation resulting from the photospheric field closest to the time of eruption. However, given that the eruption occurs close to the Earth-viewed limb, we instead use a PFSS extrapolation from when the prominence was at disk centre (i.e., 2013-02-21 12:04 UT) as shown in Fig. 4.12b. Examining an extrapolation primarily based on disk-centre magnetogram observations minimises the impact of projection effects and ensures there is no contribution from the flux transport model that the PFSS method transitions to when approaching the Earth-viewed limb (i.e., keeping the extrapolation as data-constrained as possible). In order to test the assumption of potential field domination, we test a small region around the prominence using the IDL routine optimization_fff, which is capable of performing non-linear, and linear/potential force-free field extrapolations (NLFFF and LFFF respectively). We use a small region due to the input requirement of optimization_fff of a symmetric box . This region has Carrington co-ordinates of longitude 0° to 26° and latitude $-46°$ to $-20°$, and can be seen as the region from which field lines are drawn (according to PFSS) in Fig. 4.12c. This region was chosen to encompass the length of the prominence containing the slits, whilst avoiding the northerly active region, and the southerly coronal hole. Using the PFSS extrapolation, we calculate the transverse component of the field, $B_{\rm t}$, at each height step as,

$$B_{\rm t}(\phi,\theta) = \sqrt{B_{\phi}^{2}(\phi,\theta) + B_{\theta}^{2}(\phi,\theta)}\ , \tag{4.3}$$

where B_ϕ and B_θ are the longitudinal and latitudinal components of the magnetic field, respectively. This is assumed to be dominated by an external constraining field at higher altitudes (i.e., $B_{\rm t} \approx B_{\rm ex}$). In order to construct a decay index profile as a function of radial height for the prominence region, we first calculate the decay index n using Equation (1.3) for each latitude/longitude location in the FOV indicated by the relevant regions (panels a and b) in Figs. 4.12, 4.13, 4.14. At each height step, we then take the mean of n across all latitude/longitude locations, leading to the mean decay index profile. Fig. 4.12 shows the region where the mean decay index is calculated overplotted onto the prominence as observed by AIA 193Å, HMI, and the corresponding PFSS extrapolation.

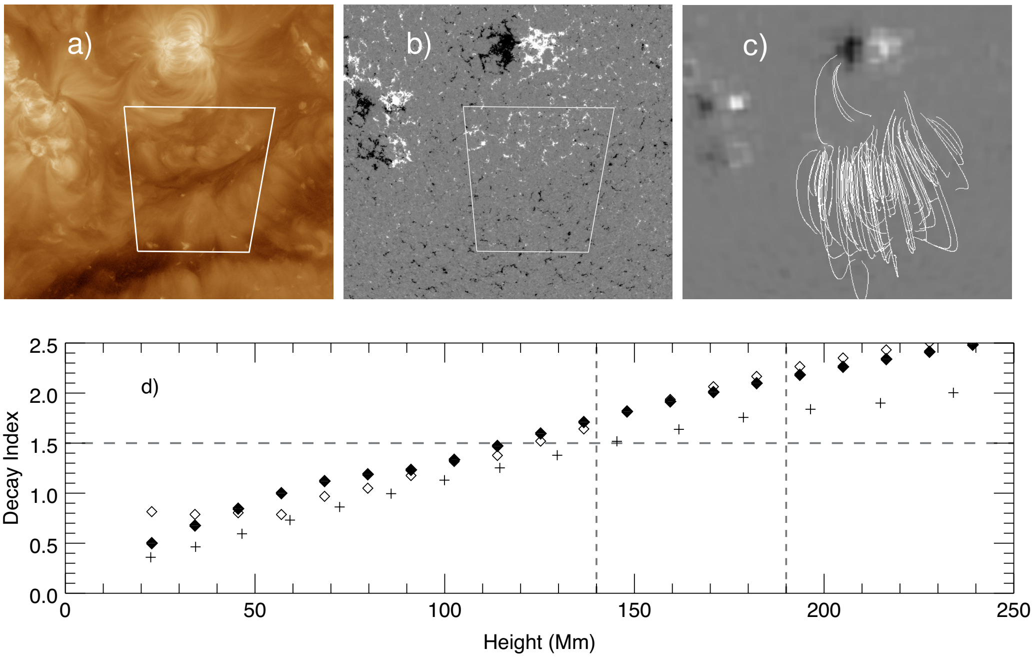

Figure 4.12: a) The region used for the PFSS extrapolation as seen in AIA 193 Å. b) The region as seen in HMI. Note the trapezoid shape comes from the projection of the box onto the solar surface. c) The PFSS extrapolation from the same time. d) The derived decay indices for the PFSS solution (pluses), the linear/potential solution (empty diamonds), and the non-linear solution (filled diamonds) for the region bounded by Carrington co-ordinates of longitude 0° to 26° and latitude −46° to −20°.

As can be seen in Fig. 4.12 the NLFFF solution closely matches that of the linear/potential solution output by the same code. Note that the input magnetogram into the PFSS calculation, as shown in Fig. 4.12c, is a smoothed and resampled version of that in Fig. 4.12b, which is at full resolution. The vertical dashed lines indicate the upper and lower limits of $h(t_{\mathrm{nl}})$ for all slits (i.e., $140 - 190\,\mathrm{Mm}$), as shown in Fig. 4.9. A horizontal dotted line is placed at the canonical value of $n_{\mathrm{crit}} = 1.5$. Within these limits all slits indicate a decay index value above 1.5 at the time of non-linear phase onset.

Though there is some discrepancy in heights less than 90 Mm, this does not have an impact as our prominence begins above this height. We find a difference of less than 4% throughout the area inside the vertical lines between the NLFFF and linear/potential solution of optimization_fff. This shows that our assumption that the region is dominated by potential fields is valid, despite a small amount of connection to the northerly active region in Fig. 4.12c.

Due to the differences in methods and domain sizes between PFSS and optimization_fff, we should not expect to see the potential solutions match each other. We do not ultimately use a solution that is able to include NLFFF deviations from potential fields due to the localised nature of such a solution. This is due to the solution changing if the size of the computational region over is changed, due not only to the inclusion of new flux, but also due to boundary conditions and effects. The PFSS extrapolation is global for a synoptic magnetogram, thus avoiding this problem.

We now look at how changing the area of a bounding region surrounding the prominence from which the decay index is taken changes the result. First, we look at how the decay index changes as a function of position along length of the spine of the prominence relevant to the slits studied here, again with its relative position shown in 193 Å, and HMI.

As shown in Fig. 4.13a and b, the full range of points shown here correspond to the range of slits used in the previous sections colour coded according to their slit number: starting from red (slit 0) in the top right, through green (slit 68), and ending with blue (slit 136). In Figure 4.13a, we show the prominence in absorption at this time as seen in 193 Å. The axis of the prominence channel is clearly coincident with the location of the PIL that separates the opposite polarity fields in the lower half of the native resolution SDO/HMI magnetogram of Fig. 4.13b, and the corresponding closed fields of the PFSS extrapolation in Fig. 4.12c. From the observations, comparing Fig. 4.13a with Fig. 3.5 from STEREO-A, it appears that the prominence experiences no significant evolution from when it exists at

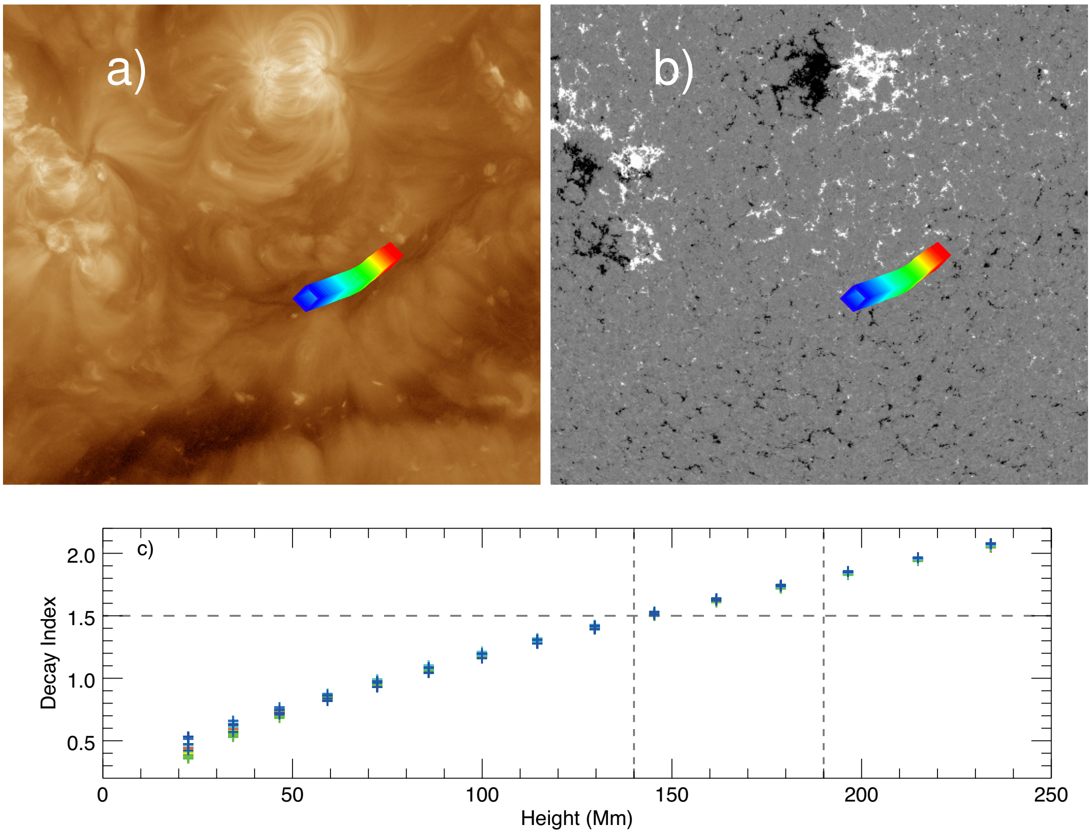

Figure 4.13: a) The location of the slit positions projected onto the AIA 193 Å FoV, with position colour coded from red (slit 0) through green (slit 68) to blue (slit 136). b) The colour-coded slit positions projected onto the full resolution HMI magnetogram. c) The decay index profile of all slit numbers. The dashed horizontal grey line is drawn at n=1.5, and the two vertical grey dashed lines show the extent of the majority of $h(t_{\mathrm{nl}})$.

disk centre until later at the limb prior to eruption. As can be seen in Fig. 4.13c there is very little deviation in the decay index measured across the points along the prominence at heights greater than 40 Mm. This suggests that the overlying field is uniform above at least this section of the prominence.

We now look at how the decay index varies when averaged over a broader area taken around the prominence. These areas are calculated as Gaussian masks applied to the data of incrementally increasing widths (0,1,2...5) centred on each longitude and latitude of each point.

As shown in Fig. 4.14 there is once again little deviation between decay index

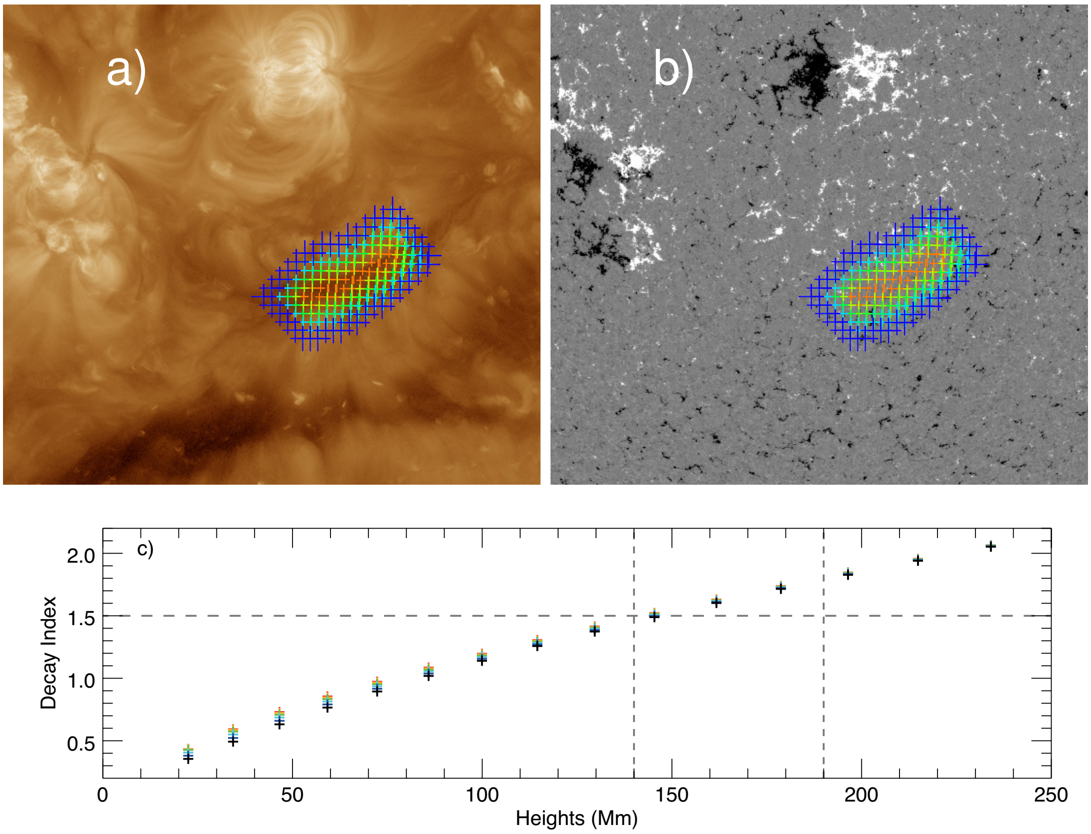

Figure 4.14: a)The locations of the contours of Gaussian masks of increasing size around the prominence colour coded from smallest (width=0, red) to largest (width=5, blue). b) The same contours projected onto the HMI magnetogram. c) Decay index as a function of mask width around the prominence spine. The dashed horizontal grey line is drawn at n=1.5, and the two vertical grey dashed lines show the extent of the majority of $h(t_{\rm nl})$.

profiles over the relevant height of 140-190 Mm. This is likely due to the nature of the quiet-sun magnetic field surrounding the prominence varying very little over the range studied here. This small variation is in part due to the inclusion of equal amounts of positive and negative flux surrounding the PIL that the prominence lies above as the width of the mask is increased. As there is very difference between the decay index profiles either as function of position along the slit, nor as a function of width surrounding the prominence we choose to take the profile of only the prominence itself. This would correspond to the innermost red symbols in Fig. 4.14a and b. Fig. 4.15 shows the resultant mean decay index profile, and the resulting distributions of $n(h(t_{\mathrm{nl}}))$, and $n(h_t)$. For comparison we again include the PFSS extrapolation.

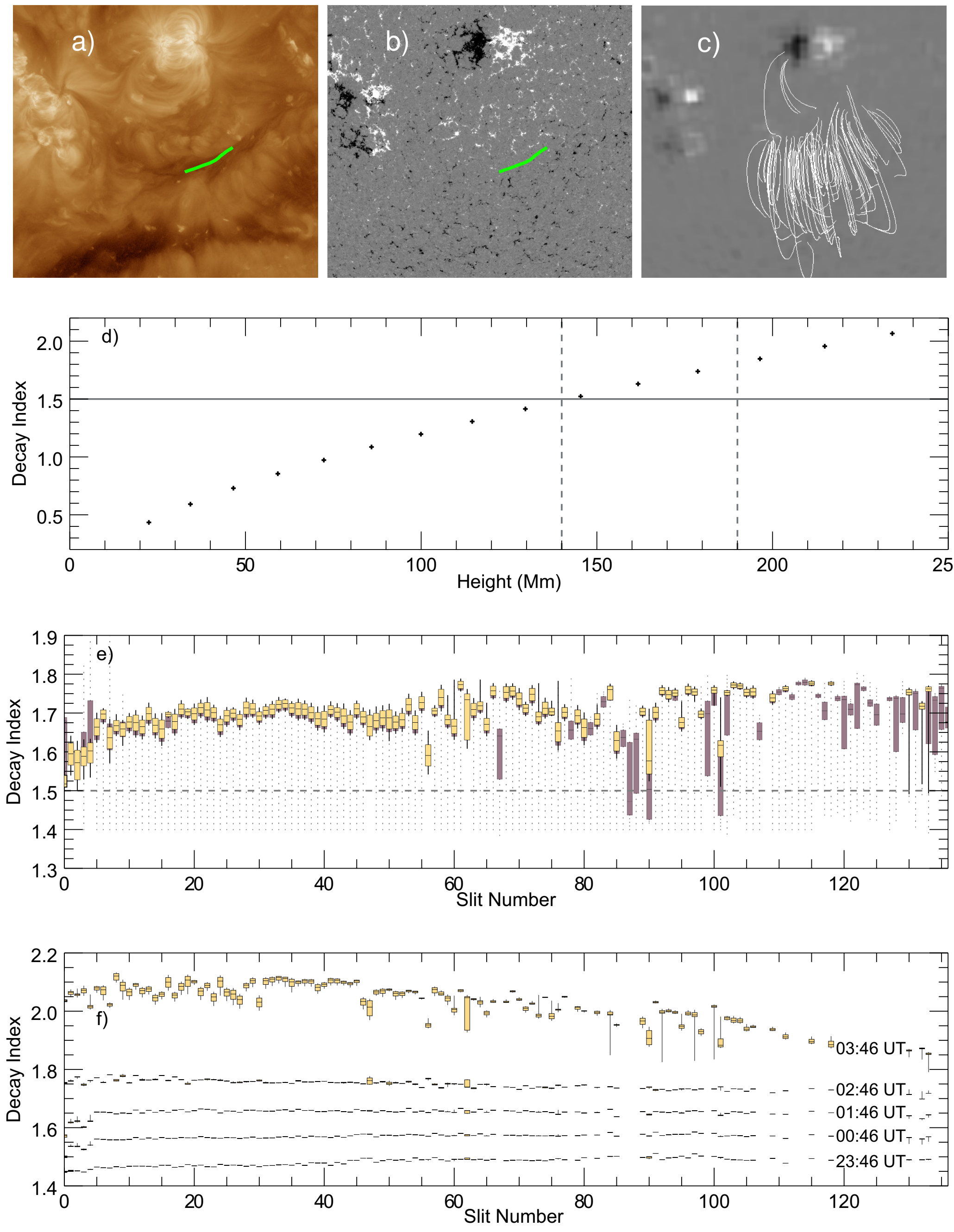

Figure 4.15: a) The prominence on 2013-02-21 12:04 UT as seen in AIA 193 Å. The green line shows the section of the prominence through which slits are drawn. b) The SDO/HMI magnetogram of the same region. c) The PFSS solution from the same time, with field lines drawn starting from the region bounded by Carrington longitude 0° to 26° and latitude $-46°$ to $-20°$. d) Mean decay index vs. height over the observed height range. e) Box and whisker plots showing the range of decay index values over all β. Individual box and whisker plots are displayed for each slit, using the non-linear phase onset times specifically found for that slit. Purple plots correspond to the results from all fits, while gold plots correspond to results from fits with $\chi^2_{\text{red}} < 2$. f) Box and whisker plots of the range of filtered decay index values across the structure at a sequence of specific times.

The mean decay index profile at the known PFSS heights is interpolated to the $h(t_{\mathrm{nl}})$ values (for each β in each slit) using the SSWIDL routine DSPLINE. In Figure 4.15e, we present box and whisker diagrams for each slit that characterise the derived decay index range for $h(t_{\mathrm{nl}})$ across β. Each box and whisker plot displays the characteristics of the distribution of decay index values over a range of β values for each slit. In this panel, we include two sets of box and whisker diagrams: i) purple boxes with dashed whiskers representing the unfiltered data (i.e., the distribution of decay index values over all values of β). Note the lower extrema in the dashed whiskers are limited to a lower decay index value of ∼1.35 in the majority of box plots. This is because the majority of slits have at least one power fit that does not iterate away from the starting height estimate of 120 Mm. ii) Gold boxes with solid whiskers represent data that has been filtered to remove the effects of bad parametric fits according to the χ^2_{red} statistic (displayed in Fig. 4.4). Decay index values calculated from fits with $\chi^2_{\mathrm{red}} \geqslant 2$ are discarded, retaining only those decay indices in each slit that correspond to very good fits. This removes 28.5% of decay index values. Over half of the removed decay indices are associated with slit numbers greater than 100, where the majority of fit results for all values of β return $\chi^2_{\mathrm{red}} \geqslant 2$. Note that box and whisker distributions can get removed completely if there are less than 5 fits remaining after filtering. This results in the removal of the decay index distributions of 21.5% slits entirely from further analysis, concentrated at larger slit numbers. Most of the remainder of the removed decay indices correspond to the lowest values of β (i.e., $1.5 - 1.8$) in slit numbers less than 100, again where $\chi^2_{\mathrm{red}} \geqslant 2$. This can be seen in Fig. 4.15e, with the majority of the solid lower whiskers being significantly reduced in length. This also causes a systematic change in the distributions of decay index in the filtered data, corresponding to a visible offset between gold and purple boxes, particularly evident for lower slit numbers.

An additional filtering of decay index values is applied, based upon our determination of when, in time, we are confident that the eruption has not yet started. We have chosen to rule out any fit with a t_{nl} that occurs before 2013-02-27 00:00 UT, based upon our interpretation of the image sequences of the event and Figs. 3.21, 3.27, 4.3, and 4.8. This removes a further 3.8% of decay index values, with the vast majority coming from a variety of β values in only a few large-numbered slits. We emphasise that is not indicative of the structure at any individual time. In constructing Fig. 4.15e we derive decay index distributions according to the heights achieved at the non-linear phase onset time, which varies across slit number. However, in Fig. 4.15f the derived decay index distributions correspond to the fitted model heights in each slit at the same fixed time(s), allowing for an interpretation of the structural evolution of the prominence leading edge in terms of decay index value.

In Fig. 4.15f we show the evolution of the distribution of the decay index across all slits in hourly time steps throughout the observation (i.e., 23:46:19-03:46:19 UT) – i.e., in accordance with the times shown in Fig. 3.6. There are three notable features in Fig. 4.15f.

I With regards to observational signatures of the TI, the decay index is expected to be approximately constant if measured over its neighbouring points along the prominence. There is evidence for this in each hourly time step in Fig 4.15f. Furthermore, the decay index varies slowly over the length of the prominence and over the course of the eruption (as proposed in the observational signatures of the TI in the introduction).

II There is an approximately equal spacing in decay index between the four earliest times. This results from a combination of the linearity of the decay index profile as a function of height, shown in Fig. 4.15d, together with the linear rise phase of the prominence as it increases in height across all slits during this time range.

III The earliest non-linear phase onset time occurs in lower slit numbers (as shown in Fig. 4.8). However, the decay index is lower in smaller slit numbers and greater in larger slit numbers at earliest times. Later, this trend reverses with greater decay indices in the smaller slit numbers compared with larger slit numbers. This is a result of the greater velocity found in the linear rise phase of the smaller slit numbers, causing this portion (i.e., the midpoint of the prominence) to overtake the larger slit numbers and become the highest point of the leading edge, hence reaching criticality first.

Next, we will discuss these results by placing them in the context of the overall evolution of this prominence eruption, and drawing conclusions concerning the conditions instabilities.

4.3 Discussion and Conclusions

4.3.1 Discussion

The aim of this chapter is to determine the role of ideal instabilities leading to a prominence eruption. We have established that the event can be characterised by a linear rise phase before undergoing a non-linear acceleration-like phase. In this section, we will first discuss the onset of the non-linear rise phase. We will follow this with an interpretation of the “critical” decay index is presented in the context of Table 1.1.

4.3.1.1 Onset of the Non-Linear Rise Phase

One of the benefits of the height-time fitting process that has been applied here is the exploration of different non-linear temporal dependencies through the $\alpha(t - t_{\mathrm{nl}})^{\beta}$ term that switches on at time t_{nl}. Our consideration of a range of β values was chosen to specifically avoid prescribing any particular form of temporal dependence (i.e., acceleration when $\beta = 2$ or jerk when $\beta = 3$). Interestingly, we find two main results. First, for most slits we find that larger values of β return fits with earlier non-linear onset times, t_{nl}. Although models with greater β should deviate more rapidly from the underlying linear rise profile, the fitting procedure compensates for this by decreasing the acceleration-like multiplier α with increasing β. Secondly, when we classify "good" fits as having $\chi^2_{\mathrm{red}} < 2$ we find a large range of acceptable values of β (i.e., $1.9 \leqslant \beta < 3.9$) across all slits.

put alpha beta stuff here

A similar kinematic analysis was performed by Schrijver et al. (2008) who found $\beta = 3.1 \pm 0.2$ by fitting $h_0 + \alpha(t - t_{\mathrm{nl}})^{\beta}$ to plane-of-sky height-time profiles of two filament eruptions. To further a point made by Schrijver et al., we emphasise that it is not appropriate to adopt a physical driving mechanism based solely upon an exponential fit or that of a power-law with an index from a single slit. Indeed, higher fidelity modelling is required to physically interpret the role of β in the eruption process in order to differentiate between physical mechanisms. However, we disagree that one cannot infer a governing physical mechanism based solely on observational height-time analysis. In Fig. 4.15e, we demonstrate that when taking into consideration not just one slit position along the prominence structure, but many slit positions, and not just one temporal power-index fitting function, but many (all with acceptable goodness-of-fit), then the underpinning driving mechanism can be revealed. What is more pertinent is that Fig. 4.15e is constructed from many acceptable fits resulting from polynomial fit functions of multiple temporal power indices, yet, the basic principle of the TI is preserved such that the onset of the non-linear rise phase happens at a consistent height across the structure. We will now discuss the relevance of this consistent non-linear onset height in terms of the "critical" decay index.

4.3.1.2 The "Critical" Decay Index

In terms of the non-linear rise phase, we have investigated the role of the TI whose eruptive mechanism relies on a critical value of the decay index being reached. As mentioned in Section 1.2.2.2 and shown in Table 1.1, some physical considerations can raise or lower the critical value, while the choice of where in the structure the critical value should be considered also has an effect (i.e., either at the leading edge of the prominence mass or at the axis of the MFR).

When we compare our decay indices to those that are measured at the prominence-mass leading edge in Table 1.1, we find that for most slits our "good"-fit filtered critical values at the non-linear onset time (approx. $n = 1.55 - 1.80$) are relatively large compared to those reported in other papers. Only Liu (2008) and Liu et al. (2010) report higher critical decay index values, but their critical values are determined from averages over the lower-altitude height range of $42 - 105\,\mathrm{Mm}$. Following those authors, Aggarwal et al. (2018) also report critical decay indices based upon an average value from $42 - 105\,\mathrm{Mm}$. Reporting an averaged critical decay index over such a broad range of heights is i) not useful given that the initial height of our event is already above this, and ii) not helpful given that the decay indices span approx. $0.5 - 1.2$ for this height range based on the PFSS potential field model. The required precise determination of the critical decay index requires a precise determination of the critical height at a precise time of eruption. With the exception of Zuccarello et al. (2014a,b) and Vasantharaju et al. (2019), all other critical indices reported in Table 1.1 do not use 3D reconstructions of the heights of the prominence-mass leading edge. Vasantharaju et al. (2019) recently pointed out that the reported values for critical decay index from multiple authors investigating prominence eruptions often involve errors induced by projection effects on the determination of prominence positions. For example, McCauley et al. (2015) use only the AIA plane-of-sky to recover prominence heights which is not the true 3D height. The observed difference between 3D and plane-of-sky heights could lead to a considerable offset in the recovered critical decay index value, even when considering slits placed only a few degrees of longitude away from the limb. This can be seen clearly when comparing the height axes shown the top three panels of Fig. 3.21 to the decay index profile in Fig. 4.15d. For example, when considering slit 136 (originating at 86° longitude), the decay index for the prominence edge 3D height of $\sim 150\,\mathrm{Mm}$ is ~ 1.5, whereas the equivalent plane-of-sky height is $\sim 100\,\mathrm{Mm}$ above the limb resulting in a significantly reduced decay index value of ~ 1.2. Therefore, there is a very high likelihood that when using a plane-of-sky height measurement the returned decay index will be consistently lower than the true value.

A precise determination of the height is also important with regards to understanding the offsets between different features within the overall magnetic structure of the prominence. Sarkar et al. (2019) shows that the offset between the leading edge of the observed prominence and the observed cavity centroid, taken as the assumed location of the FR axis, accounts for a difference in recovered decay index. These respective decay indices are verified in the simulation results of Zuccarello et al. (2016), who report a decay index of the FR axis (i.e., centre of the cavity) of 1.4 ± 0.1 while at the height of the prominence leading edge the value was 1.1 ± 0.1, for an active region eruption. As shown in Table 1.1, we have identified from numerous authors that when considering the flux rope axis one naturally expects to find higher decay index values compared with prominence-mass leading edges. Determining the exact separation of the mass and the FR axis in this event would require numerical modelling. Another structural feature that can cause the decay index to rise is introducing curvature to the flux rope axis. This was shown by Démoulin & Aulanier (2010), where simulating a straight current channel resulted in a decay index of 1.1, whereas a curved current channel resulted in a value of 1.3.

The work of Olmedo & Zhang (2010) outlines the properties of the Partial Torus Instability (PTI), which considers how changing the ratio of the arc length of the partial torus above the photosphere to the circumference of a circular torus of equal radius can change the critical value of the decay index. We trivially explored this ratio simply using our 3D coordinates in determination of the half-length separation of the prominence footpoints and the maximum height of the prominence closest to the mid-point of the structure at the time of eruption, resulting in a fractional number of 0.42. The interpretation of this number is restricted by the fact that there are other model parameters leading to a theoretical critical decay index that we cannot account for, such as the self-inductance of the torus. Furthermore, the 3D prominence structure is certainly not circular in our case and consists of large deviations in height close to the mid-point (as shown in Figs. 3.7, and 3.6). Hence, the PTI modelling requires further development for comparison to our work. Thus, while we expect that the PTI will modify our decay index value in at least some capacity, we are unable to quantify this.

We have shown in Fig. 4.12 that the PFSS assumption of a fully potential environment around the prominence is reasonable (at least above it), however, this is really only applicable at the start of the eruption. Once it begins, the evolution of the magnetic environment is undoubtedly going to challenge this assumption. This however is secondary to the errors introduced by the PFSS method itself (Schrijver & De Rosa, 2003), that we are also currently unable to quantify. We can however discuss, at least, the influences these may have on the result of our decay index profile. The first is that of the rebinning of the magnetogram from the extrapolation is performed (compare panels b and c of Fig. 4.15). As the decay index is dependent on the gradient of the magnetic field and not directly its strength, this will not necessarily greatly change the returned decay index profile. However, the rebinning will naturally effect the distribution of the field above it, which could cause some change in the decay index. As we have shown in Fig. 4.14 the distribution changes very little over a number of spatial distributions, so we therefore conclude that the effect is minimal for this event. The second is those of the extrapolation itself. The global assumption of a potential field is obviously unphysical, especially around highly non-linear concentrations of flux such as active regions. This will certainly cause large changes to the distribution of the field above the surface around those regions. Whether the active regions to the north of this prominence are close enough to cause an effect would have to be tested, though with careful choice of boundary conditions. Furthermore, the propagation of errors throughout the extrapolation could be enough to dwarf those of the kinematic analysis.

We do not observe any clear evidence of a cavity present in our AIA observations, but there is a textbook 3-part CME associated with the prominence eruption in SOHO/LASCO C2 quicklook movies, as can be seen in Fig. 1.6. According to CACTUS[1] (Computer aided CME tracking) the CME associated with this event was first detected at 04:36 UT and had a minimum plane-of-sky velocity of 244 $\mathrm{km\,s^{-1}}$ with a maximum of 710 $\mathrm{km\,s^{-1}}$. Xu et al. (2012) presented the decay index vs. CME speed for 38 CMEs associated with filament eruptions. They provide a third-order polynomial fit to that distribution identifying two distinct trends for the CME speed as a function of the decay index: i) below

---

[1] `http://sidc.oma.be/cactus/catalog/LASCO/2_5_0/2013/02/CME0111/CME.html`

$\sim$1000 km s^{-1} CME speeds increase steadily with decay index; ii) for CMEs with a speed above 1000 km s^{-1} the decay indices are almost constant at 2.2. Based upon our maximum CME velocity of 710 km s^{-1} we estimate an expected decay index value in the range of 1.8±0.1 from their fit, which is in good agreement with our results. However, as reported in Table 1.1, the five observed quiet-Sun eruptions investigated by Xu et al. (2012) exhibit critical decay indices ranging over $0.98 - 1.68$ and these are determined as a result of averaging over a large height range ($42 - 105$ Mm). Therefore, we hesitate to draw close association between the CME speed with their polynomial fit in regards to the decay index. Finally, knowing the precise time of eruption can impact upon the resultant critical decay index given that the prominence is continually going through the linear rise phase. This is clear from Fig. 4.15f where we show that over intervals of 1 hour the decay index across our slits can increase by anywhere from $\sim$0.1 to as much as $\sim$0.25. A key outcome of this work is that defining any single decay index as being "critical" for all events is not appropriate because there is no single canonical or critical value of decay index through which all eruptions must succeed.

4.3.1.3 The Evolution of the Erupting Prominence

We have not fully considered the effect of the prominence structure rising through the solar atmosphere on the magnetic field gradient and therefore on the decay index. Fig. 4.15e describes the decay index across the structure at the onset of the non-linear rise phase locally, and in determining the decay index we assume that the magnetic field environment above and below the structure is static. However, after onset of eruption the magnetic environment becomes dynamic and we do not have a suitable model on the timescales of the eruption to account for this in our determination of the decay index. For this reason, Fig. 4.15f tells the story of the change of structure in the prominence as it erupts through the static magnetic environment, in terms of the decay index, before and after the onset of the non-linear phase (i.e. we can only model the change in the structure, not in both the structure and the surrounding environment). This will now be contextualised in terms of the fit parameters and results as presented in figs. 4.5 (h_0), 4.6 (v_0), 4.7 (α), 4.8 ($t_{\rm nl}$), and 4.9 ($h(t_{\rm nl})$).

When discussing trends within the results, we will refer collectively only to the acceptable fits associated with powers in the range $1.9 \leqslant \beta < 3.9$, where the trends are very similar across slit number. In Fig. 4.5, we find the trend that the height, h_0, of the prominence structure (i.e., $\sim 110 - 115\,\mathrm{Mm}$) at the start of the observation (26-03-2013 22:06 UT, i.e. the start of the linear rise phase fit), increases with increasing slit number to $\sim 120 - 125\,\mathrm{Mm}$ at the prominence leg. However, the onset of the acceleration in the eruption in fact first occurs in the lowest slit numbers near the mid-point (at 27-03-2013 ~01:06 UT) and the time differential for the onset of acceleration is ~2 hours with increasing slit number, with acceleration occurring latest in the prominence leg as shown in Fig. 4.8. At first this appears contrary to the concept of the TI because we assume that the prominence must reach a critical height before onset of acceleration in the eruption and one would infer that this should take place first closer to the legs where the prominence is initially with a peak in height. The explanation for why the mid-point of the structure erupts first becomes clear when we inspect Fig. 4.6. The linear rise velocity is largest at the mid-point with a value of $\sim 4\,\mathrm{km\,s^{-1}}$ and it decreases linearly with increasing slit number towards the leg with a velocity of $\sim 3\,\mathrm{km\,s^{-1}}$. A velocity differential of $\sim 1\,\mathrm{km\,s^{-1}}$ across all slits spanning the structure, applied over a duration of 3 hours (22:06 – 01:06 UT) during the linear rise phase, is enough to cause the low slit number mid-point locations to catch-up and even surpass the prominence leg locations, with regards to their relative heights at earliest time of eruption. This means that the onset of eruption occurs first in the structure mid-points (low slit numbers) which first reach the height at which the eruption begins in line with what one expects for the TI.

More interestingly, even though the time differential for the onset of acceleration across slit number spans a broad time range (∼2 hours) the height at which the onset of acceleration, $h(t_{\mathrm{nl}})$, occurs with respect to slit number is remarkably consistent, as shown in Fig. 4.9. Here we note one of the strongest signatures of the TI where we find very little deviation in heights (∼10 Mm of variance about a height of ∼170 Mm) corresponding to the onset of acceleration, implying that regardless of how much time passes once the critical height is reached, eruption will ensue. The evolution of the prominence structure, where the eruption first occurs close to the mid-point, is apparent in Fig. 3.6 where the 3D reconstruction revealed the maximum height location shifting from the leg towards the mid-point as the observation progresses. The evolution with regards to the height profile is also evident from Fig. 4.15f, where we show decay indices being lower in the low slit numbers (corresponding to lower heights) compared with higher decay indices in higher slit numbers at 23:46 UT. Only after all prominence locations corresponding to all slits have erupted, corresponding to 03:46 UT, do we see the effect of acceleration on the height differential across the structure, such that the smallest slit numbers give substantially higher decay indices compared with largest slit numbers.

When interpreting the role of the TI in this event we are left with a number of pressing unanswered questions which calls for further studies of prominence eruptions from advanced numerical simulations. We detect that the height of the (near mid-point) structure at the first onset of acceleration has only just surpassed adjacent locations along the structure. This is due to the interplay of a lower starting height but greater linear rise velocity when compared with locations in higher slit numbers. This begs the question as to whether or not a) the eruption onset sourced to the mid-point is responsible for dragging the nearby locations into the critical regime in a sequential manner until the entire structure undergoes acceleration or b) the nearby locations are each independently entering the critical regime and accelerating without the aid of parts of the structure already undergoing eruption. This question can be addressed through considering the rate at which information is transferred along the magnetic structure of the prominence which should be dependent upon the local Alfvén speed. Given that the section of prominence sampled by the slits is 403 Mm in length, considering a delay in the onset of acceleration from slit 0 to slit 136 of ∼2 hours, then the speed at which information should travel in scenario-a) would be $55.97\,\mathrm{km\,s^{-1}}$. This is not unrealistic for the Alfvén speed in a prominence channel. Only advanced numerical modelling of prominence eruptions can explore the role of magnetic connectivity across the structure with regard to the impact of the drag effect in connection with the application of the TI across the whole structure or as a PTI.

4.3.1.4 Comparison to Other Work

Recently, work of a similar nature to this was published by Myshyakov & Tsvetkov (2020), in which the third eruptive prominence they analyse (EP III in their nomenclature) is the event studied here. We believe that work demonstrates perfectly why the approach laid out here is necessary. Their method is to draw a single plane-of-sky slit through the apex of the prominence. As we have shown, using a single slit cannot provide an adequate view of the structure in determining any eruption mechanism. Neither is it appropriate to define an apex without defining the time at which you are doing so as we have also shown that the apex moves. Furthermore, they show STEREO data but do not use it to perform a 3D reconstruction. This means that the apex they define is the 2D plane-of-sky apex.

In terms of their recovered height-time plot, it is constructed from irregularly separated points (with no explanation as to how the height is recovered at any point) that are then regularly gridded onto a 5 minute cadence. These heights are then averaged with its two adjacent neighbours for noise suppression before being used to construct a velocity profile. The last minima before the velocity reaches 10 km s^{-1} is then chosen as the onset time, with the height at this time chosen as the onset height. The value of 10 km s^{-1} is chosen based upon an event-specific magnetic reconnection paper (Sterling & Moore, 2004) that does not impose that value as an eruption criteria. As has been previously discussed here, and can be easily and immediately seen in Figs. 3.19, 3.27, and 3.28, using the velocity profile of this event for calculating the onset time is highly uncertain.

Similar to our study, they perform potential field extrapolations of the area. However, whereas we used PFSS extrapolations, they instead use a novel method that utilises Green's function solution of the Neumann boundary-value problem of a sphere applied to HMI magnetograms. They note the problems of using magnetograms at the limb. However, they then take data from the 25th, rather than the 21st as we do. Therefore we should expect to see some difference in the recovered decay index profile. Comparing their Fig. 5 to our decay index profile in Fig. 4.15d, we do indeed find that they are mostly similar. We would expect the minor variations to be the result of the play-off between the global (PFSS) solution versus their local solution. We would also expect some differences between our disk-centre observation of the photosphere versus theirs, which is temporally closer to the limb. Their ability to put minima and maxima on their decay index profiles is an improvement over the PFSS solution shown here. Fortunately, whilst they define the critical decay index at 1.5, they still show their actual value at ~ 1.6. This is remarkably close to our result, which is ~ 1.7 for most slits. Theirs is an underestimate, but this is to be expected as they define a onset time that is too early and thus when the prominence was lower. Their use of a plane-of-sky height rather than the true 3D height will also cause an artificial lowering of the decay index.

4.3.2 Conclusions

The TI, based upon the measure of the critical decay index, is the governing mechanism driving this prominence eruption. The results presented are established using two different edge detection algorithms to carefully determine the 3D kinematics and geometrical properties of the prominence leading edge. The criteria for the TI is reached at all 137 3D radial slit locations when the leading edge reaches approximately the same critical height, $h(t_{\rm nl})$, at all locations. The criteria for TI is typically established along a 1D radial path, whilst we find that the application of it is still preserved across the whole 3D structure. An analysis of the decay index is applied across the 3D prominence structure. However, an important outcome here is that defining any single decay index as being "critical" is not appropriate because there is no canonical or critical value of decay index through which all eruptions must succeed. An analysis such as this must be conducted on a case-by-case basis in order to reach what one may define as a critical value of decay index. This implies that either i) the criteria for the TI must be reached at all locations along the prominence structure in order for a successful eruption to take place or ii) the criteria for the TI can be reached on part of the structure and, given that all points along the structure are connected in the MFR, this will lead to a run away process through which neighbouring locations become dragged into the critical regime, leading to a slowly varying critical value from apex to lower heights in the prominence leg. Only numerical simulations can establish whether i) or ii) prevail. Advanced 3D numerical simulations are also required to provide clearer insight into the expected decay index values of the prominence-mass leading edge versus the outer-most edge of the MFR providing the critical decay index.

There is evidence that the linear rise velocity is greatest nearest to the prominence mid-point (where the onset of acceleration first occurs) and lowest nearest the prominence foot-points (where the onset of acceleration occurs last). The driving mechanism for this has not been established. We have ruled out the KI, however, we have not yet ruled out the important role that mass drainage may play in triggering a buoyant uplift of the MFR. There is tentative evidence for this in the observations. Exploration of this will be the subject of future observational work. Numerical simulations can also provide valuable insight into the effect of mass drainage on the evolution of a prominence undergoing eruption.

Chapter 5

The Observational and Numerical Analysis of Fluid Instabilities in a Hedgerow Prominence

I'm such a star
I take meteor showers

James Dunn,
Performance at Gwdihŵ

This work has been aided by the award of the RAS E.A Milne travel fellowship. This allowed me to visit both the Insituto de Astrofsica de Canarias (IAC) in Tenerife from the 4th to the 13th of June in 2017, and then subsequently the Swedish Solar Telescope at the Observatorio del Roque de los Muchachos on La Palma from the 13th to the 17th June. As part of the visit to the IAC, the code MANCHA that will be used in this chapter was installed upon the Northumbria University cluster "Oswald". This work will form part of a collaboration with Drs. Elena Khomenko, Angel di Vicentes, and potentially others at the IAC.

Having looked at the large-scale instabilities driving the eruption of prominences, the remainder of the work will focus on understanding the nature of small-scale instabilities governing the dynamics of the prominence sub-structure. In particular, we look at the Rayleigh-Taylor instability. Using observations from SST/CRISP and simulations from the numerical code MANCHA we hope to understand the formation of rising bubbles and falling plumes and how they can be used to derive important information about the nature of the internal magnetic field within the prominence itself.

5.1 Observational Methods and Results

Observations were taken from 08:50:11 to 09:50:11 UTC on 6th June 2014 using SST/CRISP (see Chapter. 2), focusing on the near-disk portion, and up to about 10 Mm off-limb, of a quiet-sun hedgerow prominence on the north-eastern limb. This 55x55 arcsec observation is centred around Hα (6563Å), and consists of 9 spectral points with equidistant sampling of 0.258Å in the range of ±1.03Å.

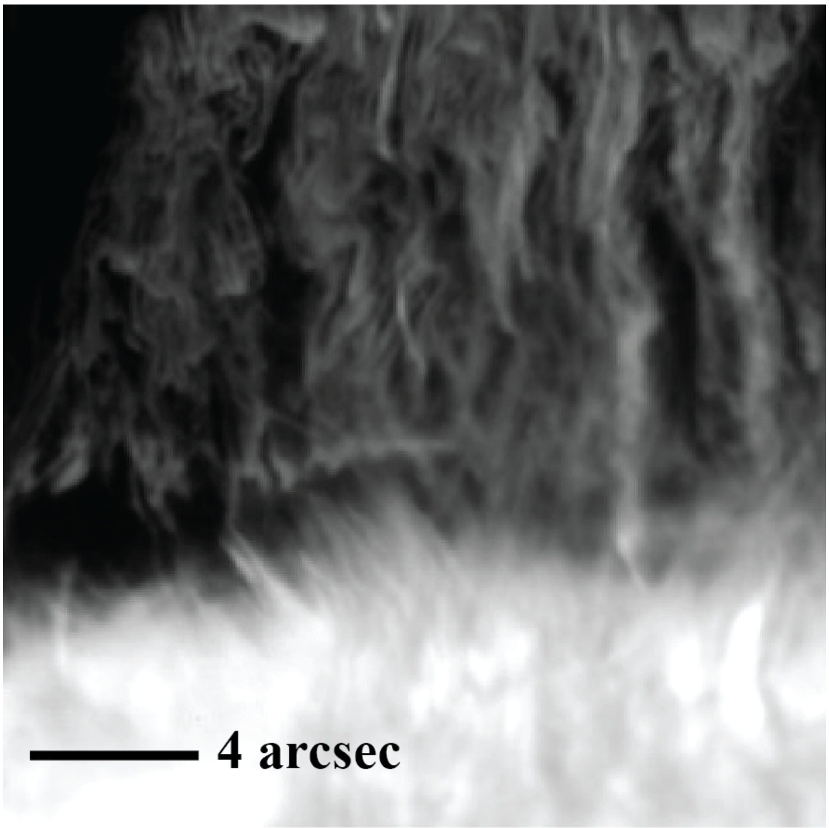

Figure 5.1: A cut-out of the observed region, with examples of the rising bubbles and falling plumes of the RTI.

The Hα scan was followed by a scan in the Ca II line (8542Å), which also had 9 spectral positions in the range of ±0.38Å, but is not considered further here due to time constraints. The calcium data will form part of future work, as discussed later in Chapter. 6.

The CRISP FOV is corrected for solar tilt and the bright points in the wide-band images are cross-correlated with those in SDO/AIA 1700Å for co-alignment, achieving a sub-AIA pixel accuracy in the CRISP pointing and establishing a heliocentric coordinate system for CRISP (seen as the first panel of Fig. 5.2). Sub-AIA pixel alignment of the CRISP pointing is achieved as a result of a cross-correlation of the most intense CRISP pixel within the AIA pixel space of 10 coincident bright points (initially identified by eye within a graphical user interface (GUI)). Then the CRISP pixel space, within the AIA bright point, is explored for each of the 10 bright points in order to maximise the correlation and a correction to the pointing information of CRISP is established. As a result, the CRISP observations are centred on $(x, y) = (-570.8'', -742'')$. Each pixel contains the 9-point spectral scan of Hα and this makes up the spectral data cube for investigation using the CRisp SPectral EXplorer (CRISPEX: Vissers & Rouppe van der Voort (2012)). The standard procedure for the reduction of CRISP is given by de la Cruz Rodríguez et al. (2015), and includes a correction for differential stretching. Post-processing was applied to the data sets using the image restoration technique Multi-Object Multi-Frame Blind Deconvolution (MOMFBD), as outlined by van Noort et al. (2005).

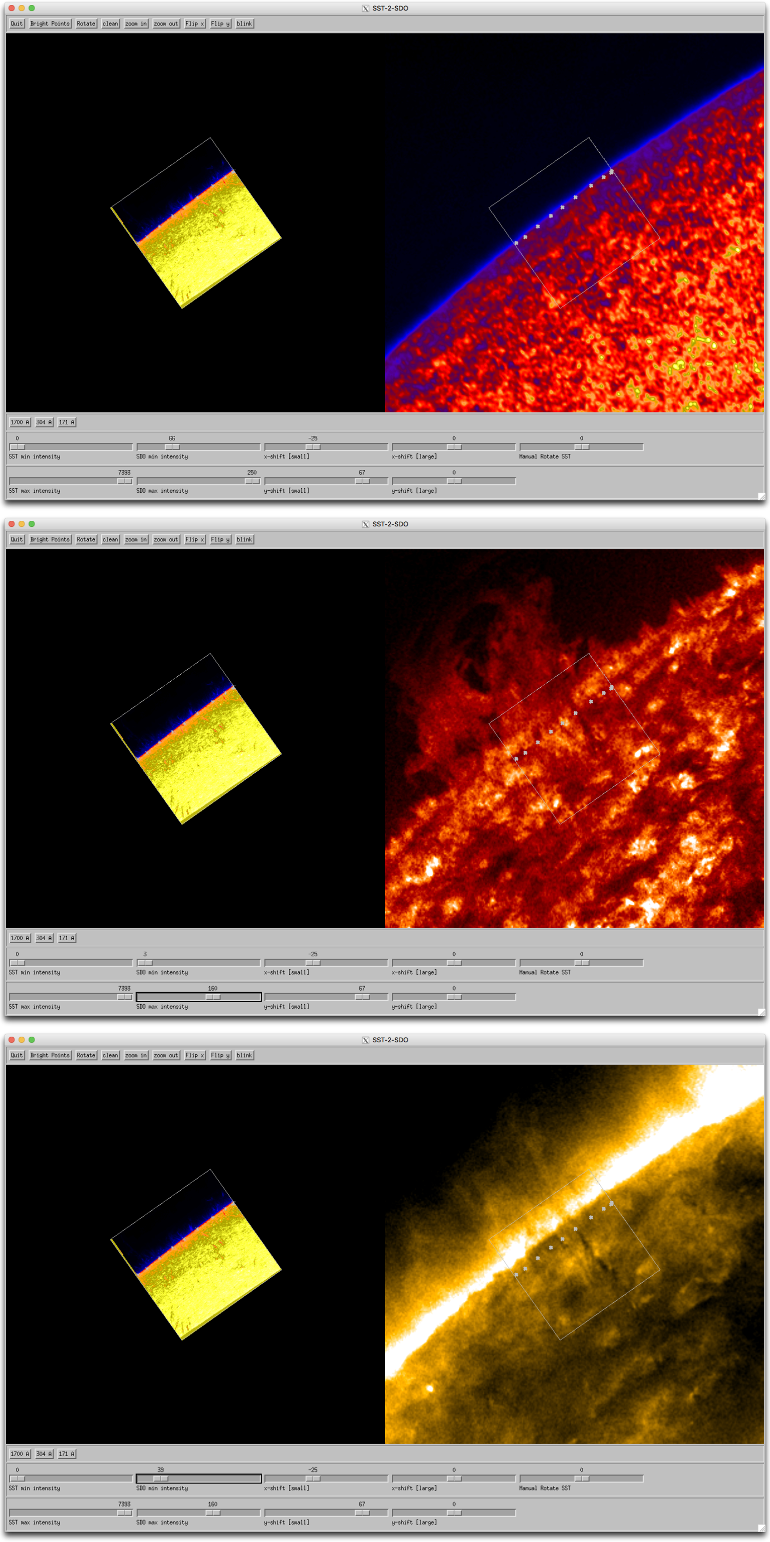

SST min intensity 0
SDO min intensity 66
x-shift [small] -25
x-shift [large] 0
Manual Rotate SST 0
SST max intensity 7393
SDO max intensity 250
y-shift [small] 67
y-shift [large] 0

SST min intensity 0
SDO min intensity 3
x-shift [small] -25
x-shift [large] 0
Manual Rotate SST 0
SST max intensity 7393
SDO max intensity 160
y-shift [small] 67
y-shift [large] 0

SST min intensity 0
SDO min intensity 39
x-shift [small] -25
x-shift [large] 0
Manual Rotate SST 0
SST max intensity 7393
SDO max intensity 160
y-shift [small] 67
y-shift [large] 0

Figure 5.2: Each panel shows the relative view points of SST versus an AIA wavelength (1700, 304, 171 Å, respectively).

We now present the aligned FoV of CRISP (here the line core) overlaid as a contour onto the AIA FoV. We highlight the region of interest within the SST CRISP FoV with a red box, i.e. the off-limb section.

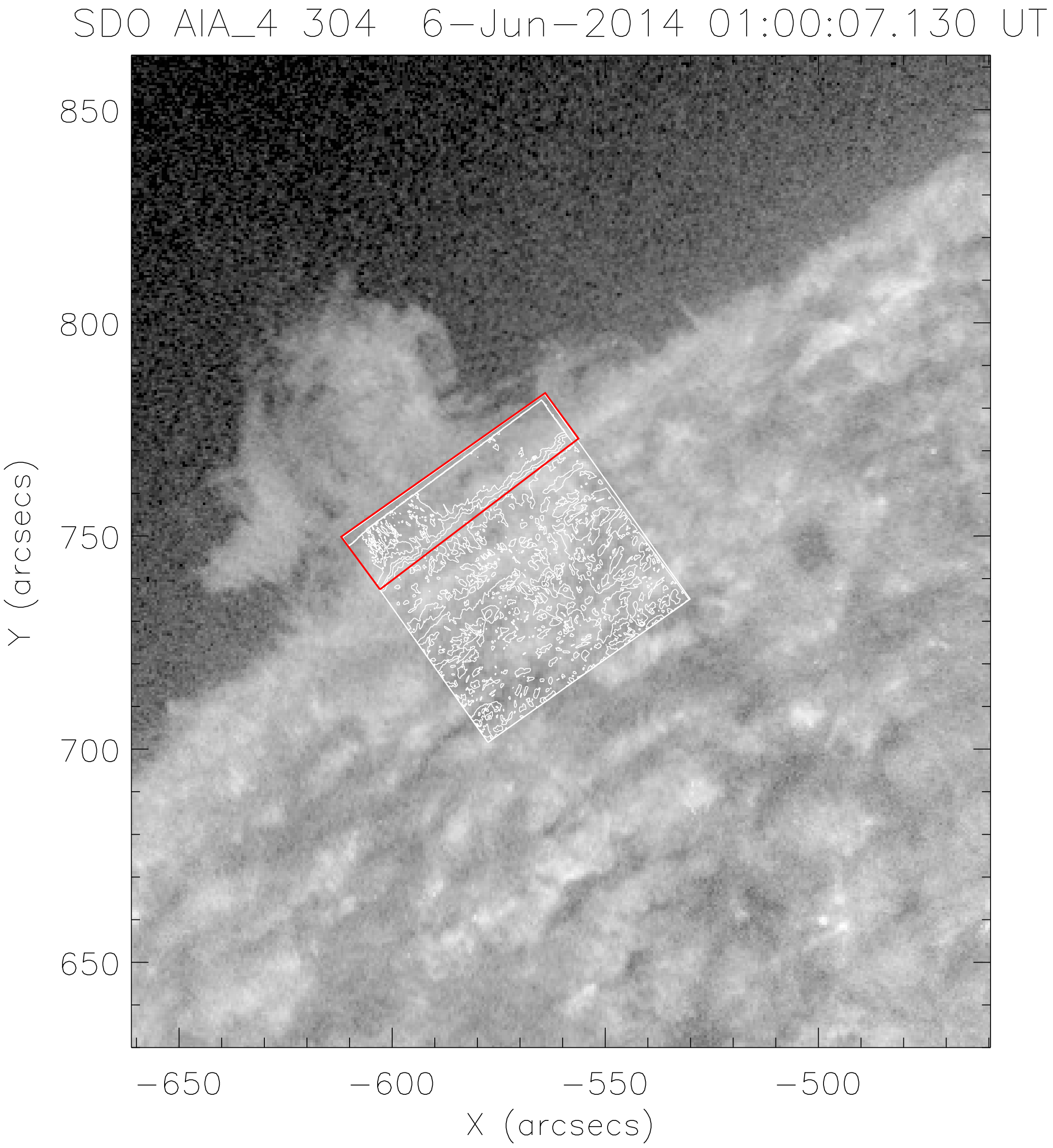

Figure 5.3: The SST line Hα line core intensity overlaid as a contour map onto the 304 Å FoV of AIA. The red box highlights the $\sim$ 10 Mm region of the observation that we are interested in, i.e. the off-limb portion.

As mentioned previously, the data consists of 9 spectral positions, which are shown below in Fig. 5.4 with the line core being the central panel.

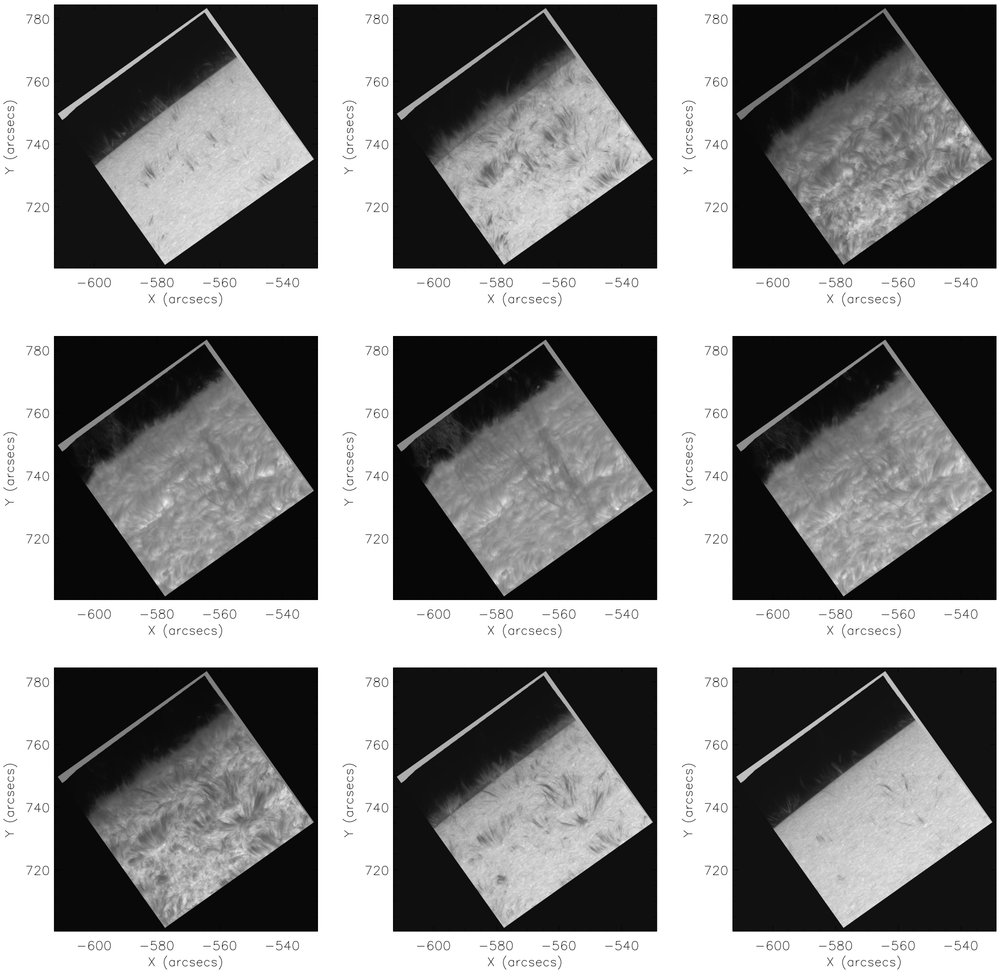

Figure 5.4: The nine spectral positions of Hα from the "blue" wing to the "red" wing, left to right, top to bottom, in CRISP. The central panel represents the line core.

As shown in Fig. 5.5, a radial slit is now drawn through each of the pixels along the top-left edge, though for clarity only every 20th of the 784 slits are drawn here. Slits 122 and 260 have been emphasised with red lines as they are used as examples later. This level of sampling was done to ensures that all plumes are caught in at least one slit.

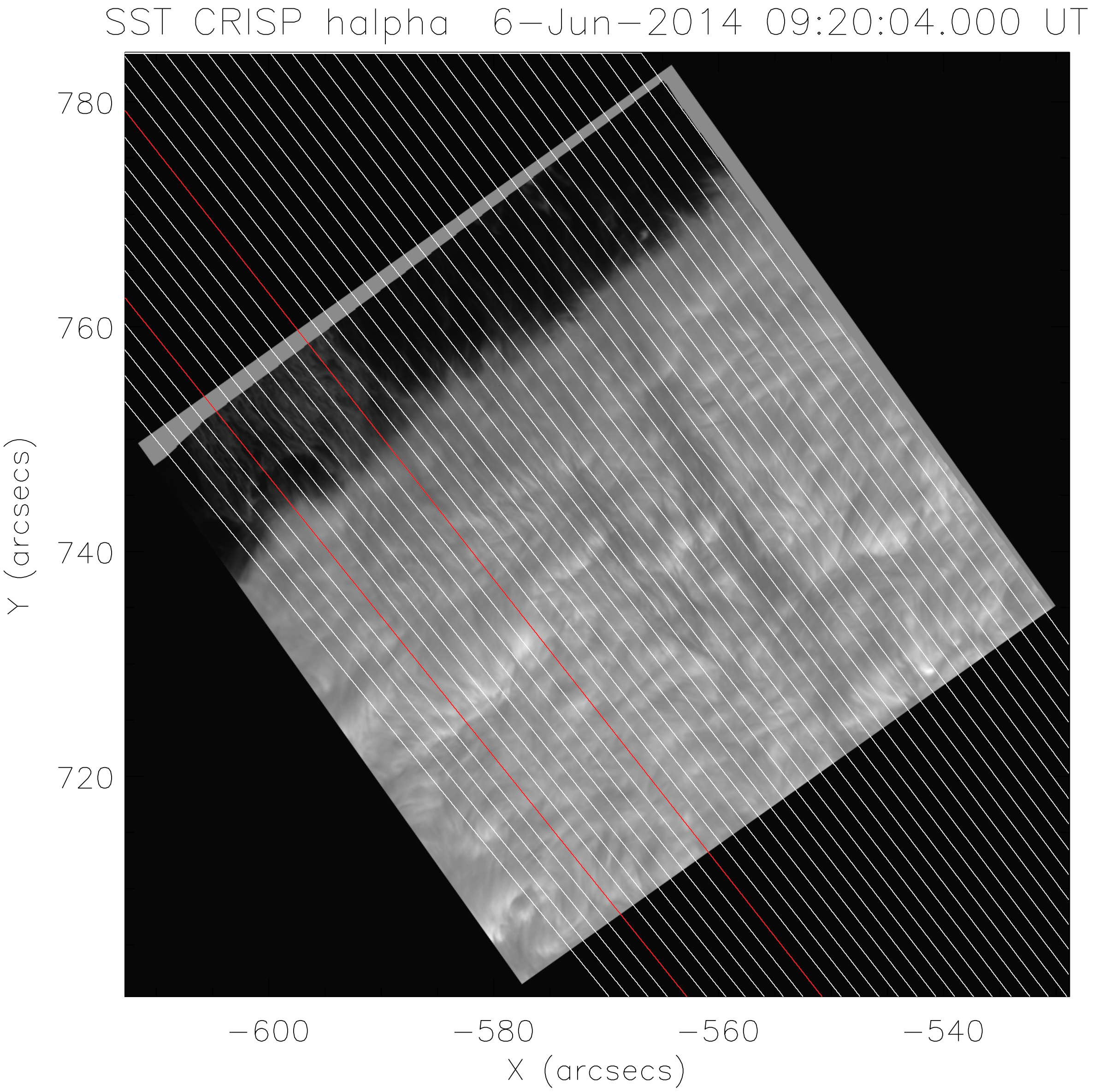

Figure 5.5: Location of every 20th slit of the 784 slits drawn through the image. The red slits correspond to slit 122, and slit 260, which are used as examples later.

Using these slits we create height-time plots and click along the distinct tracks of falling plumes (Fig. 5.6 top panel, clicked points represented by stars). By using height-time plots we are able to determine which parts of the structure are moving predominantly downwards over extended time periods. We now focus on the bulb of the plume, which we loosely define as the bright, dense leading part of the structure. Examples of these bulbs can be clearly seen in the middle panels of Figs. 5.6, and 5.7. In order to get the width of the plume bulb, we then draw a perpendicular line to the slit centred on the clicked point at its location in space and time, of width ±20 pixels (1.18", 888km), and find the point of maximum intensity within the bulb along the slit (Fig. 5.6 middle panels, one for each clicked point, and points of maximum intensity represented by diamonds). This is done due to likelihood that the bulb has not been clicked at its centre. As the bulb is likely to be densest at its centre, and the place of strongest emission, we instead estimate the plume width from this point. We then plot the intensity profile along the slit, and click the point at the edge of the bulb, or the point at which the bulb has faded out as much as possible (Fig. 5.6 bottom panels, one for each clicked point, and triangles representing the chosen position of bulb half-width). This half-width is then doubled to give the full width of the plume. This is a matter that requires some interpretation, as choosing either an inflection point or exactly where along the profile to choose if it is fading to background is difficult. In the case of inflection points we choose the nearest, deepest inflection point. If an inflection point is not available, or is instead a stationary point, the point at which the profile becomes horizontal (i.e. the gradient becomes zero) is chosen.

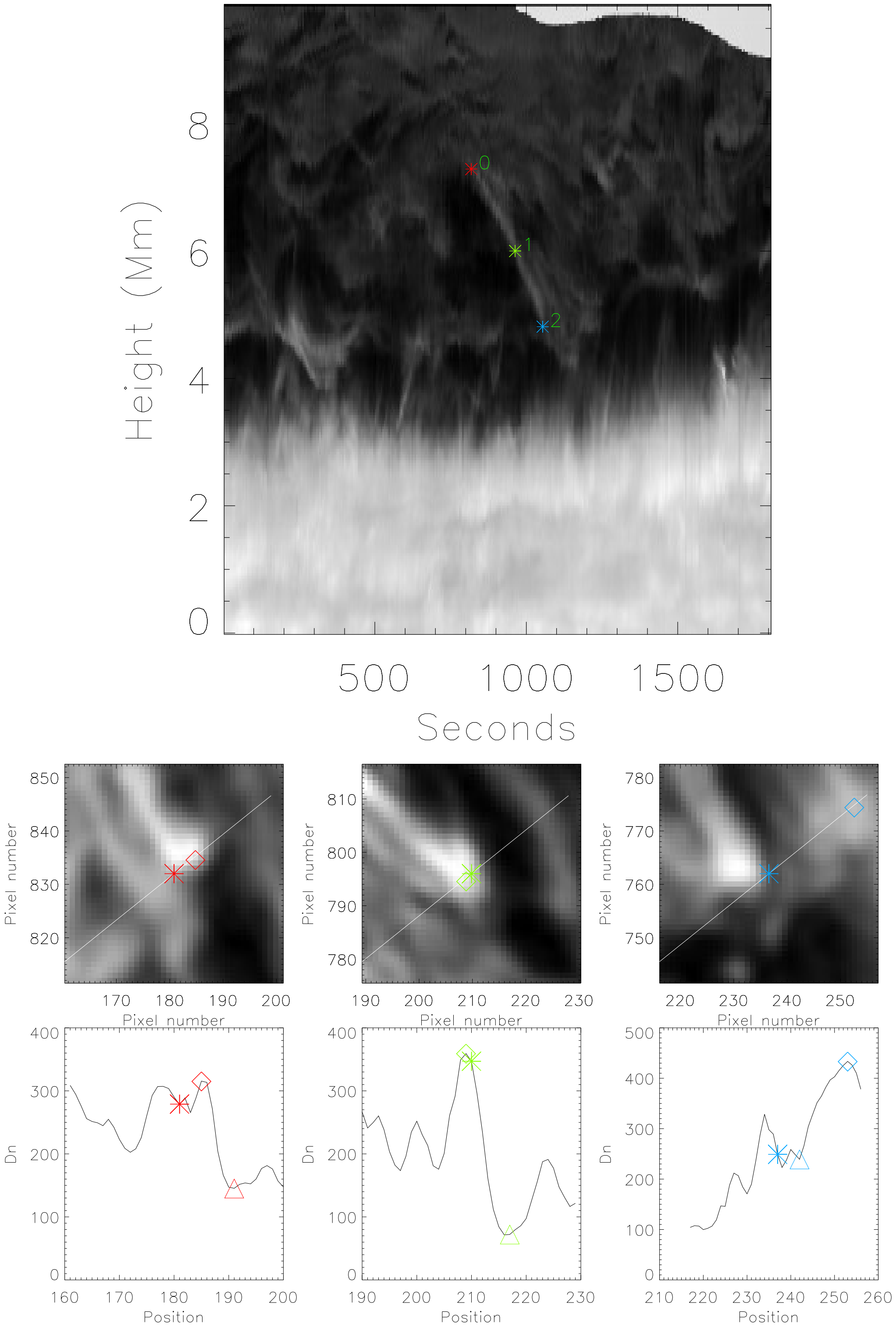

Figure 5.6: Top: The height-time plot and three colour-coded and numbered clicked positions (stars). Middle: The data cut-outs centred on each point, with the range of ±20 pixels in both directions of each respective clicked point and the point of maximum intensity (diamond) along the cut-out of the intensity line. The bottom three panels show the corresponding intensity plots with the clicked point, maximum intensity position, and the chosen position of the plume half-width (triangle).

As can be seen in the top panel of Fig. 5.6 the prominence is a highly dynamic medium full of turbulence, downflows, and upflows. At about 4.5 Mm one can see the discontinuity between the hot bubble and the cooler prominence material. In the middle panels of Fig. 5.6 we can see how closely we have clicked relative to the bulb. In all cases it is fairly close. Note that a line drawn perpendicular to a radial line will be at a constant height above the limb in the top panel, but varying in height in the middle panels. However, point 0 has a double peak of almost equal intensity. This could be due to several things, for instance this plume potentially recently merged with another, or is splitting. It could be due to a non-uniform mass distribution within the bulb, or simply that we are only grazing the leading edge of the plume in these two places. It is most likely due to these last two, i.e some combination of the mass distribution within the bulb, and where the slit is. This is because there is no guarantee nor need for the bulb to be uniform, and neither is there any guarantee of the slit being placed through the actual densest part of the bulb. Additionally, in the case of point 2 (rightmost, blue icons) we can see that a nearby feature has a greater intensity through the slit. This means that this profile can either represent the width of that bulb or can be aborted by the user.

When looking from left to right in the middle row we see the evolution of the bulb over the course of its lifetime, starting from newly formed, through where the classic mushroom cap is potentially formed on the higher side as it falls, ending as it collides with the bubble interface. Of note is the change in thickness of the tail from fairly thin in points 0 and 1, to thicker in point 2. This is perhaps due to the mass falling in the tail accumulating behind the bulb as it decelerates and stops.

Below in Fig. 5.7 we show the same method but applied to slit 260, away from the bubble, and with a much greater number of tracks. Note that we do not include every single data and intensity cut-out here for space, but instead show ones that occurred in the beginning, middle, and end of the time range, e.g. points 2 (red), 10 (cyan), and 17 (purple) respectively.

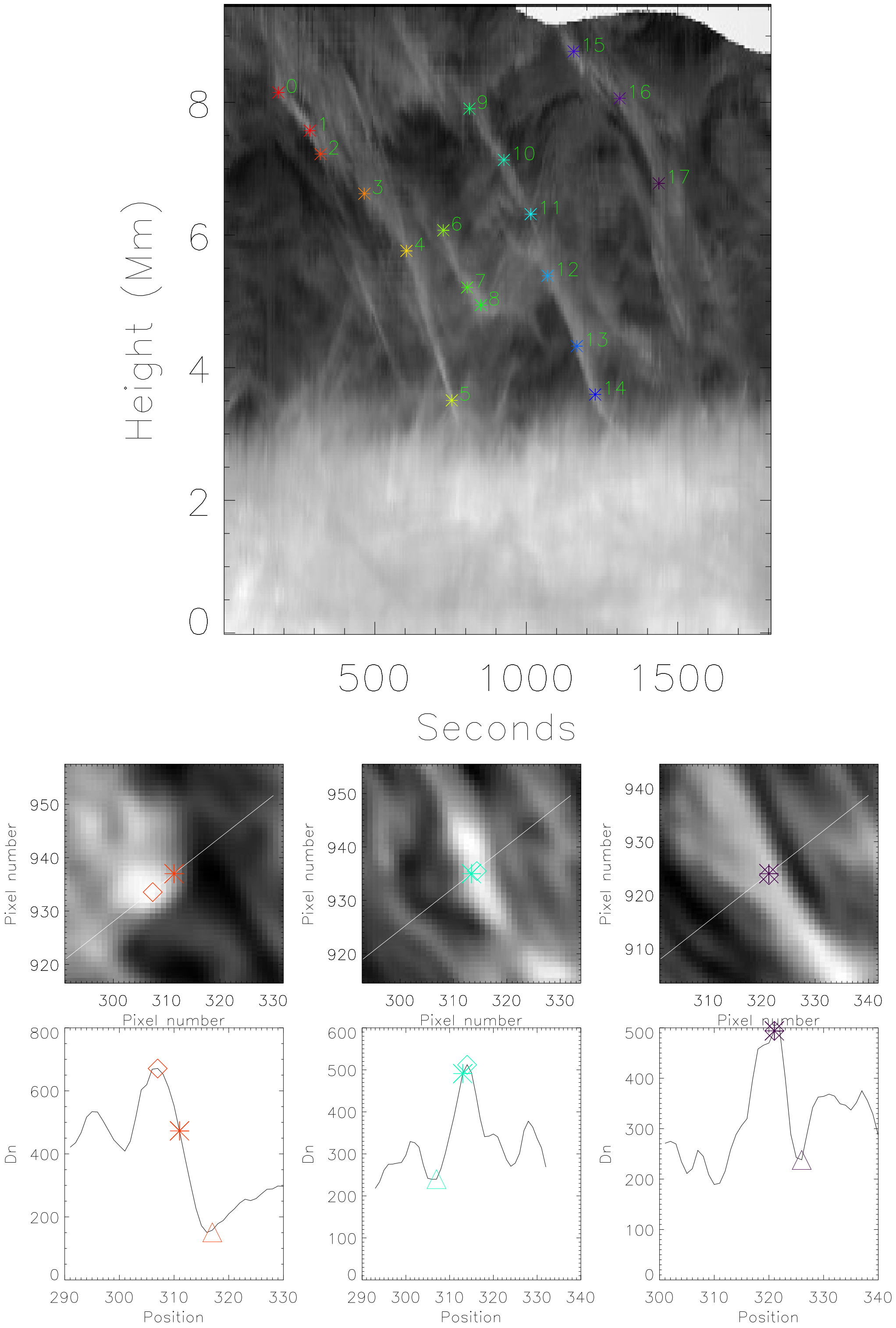

Figure 5.7: Top: The height-time plot and colour-coded clicked positions (stars) for slit 260. Middle: The data cut-outs centred on each point (2, 10, and 17 respectively), with the range of ±20 pixels in both directions of each respective clicked point and the point of maximum intensity (diamond) along the cut-out of the intensity line. Bottom: the corresponding intensity plots with the clicked point, maximum intensity position, and the chosen position of the plume half-width (triangle).

As can be seen in the top panel of Fig. 5.7, there are multiple bulbs that intersect this slit over the time range, not all of which have been registered by the user. This is possibly due to the 'droplet' formation method outlined in Haerendel & Berger (2011), wherein a distorted field creates the localised dip in the magnetic field in which mass can accumulate to form a droplet. This occurs after a droplet has disconnected, but before the restoring force has returned the distorted magnetic field to its un-perturbed position. It is also interesting to note that each plume seems to experience a slightly different velocity, perhaps due to local turbulent effects, as will be shown later in Fig. 5.9b. Of particular note is the question of whether the thin strand of plasma that connects point 11 to point 12 means that they actually form a much longer track, or whether it is just an off-shoot of a track that moves out of the slit and thus not a single continuous structure. In the middle panels of Fig. 5.7 we can once again check our accuracy. Unlike before, we cannot see the evolution of a single bulb, but instead we can see a few bulb configurations. Point 2 (leftmost, red) shows a spike seemingly about to fragment, with a broad bulb and no clearly defined tail. Point 10 (middle, cyan) presents a long, slender bulb, that is remarkably similar to the sketches presented in Haerendel & Berger (2011) of a forming droplet. Point 17 (rightmost, purple) seems instead to be the tail of a droplet, perhaps due to the user clicking too far to the right, and therefore into the tail passing through the slit instead of the bulb itself. The sudden acceleration in the rightmost track of the top panel is itself interesting, and perhaps related to the other motions one can see in the height-time plot around that time and place.

As we have now recovered the heights and times of several points, we can utilise Eq. 1.9 to recover the observational growth rate, σ_{obs}. In cases of more than two points representing a track, we determine instead the mean observational growth rate, $\hat{\sigma}_{obs}$. For instance the track in slit 122 (Fig. 5.6) we take the mean growth rate calculated between $h_1 = 0$, and $h_2 = 1, 2$, i.e 0 to 1, and 0 to 2. For slit 122 we find a mean of $\hat{\sigma}_{obs} = 5.44 \times 10^{-2}\ s^{-1}$, and for slit 260 (Fig. 5.7) we find a different growth rate for each plume, with the subscript denoting the h_1, and maximum point of the range of h_2 used in each case of each plume respectively. For instance, a subscript of 0:2 would mean that 0 has been used as h_1, and both points 1 and 2 have been used as h_2, whereas 3:4 means $h_1 = 3$, and $h_2 = 4$. $\hat{\sigma}_{obs,0:2} = 3.16 \times 10^{-2}\ s^{-1}$, $\sigma_{obs,3:4} = 3.93 \times 10^{-2}\ s^{-1}$, $\hat{\sigma}_{obs,6:8} = 6.98 \times 10^{-2}\ s^{-1}$, $\hat{\sigma}_{obs,9:11} = 4.02 \times 10^{-2}\ s^{-1}$, $\hat{\sigma}_{obs,12:14} = 9.15 \times 10^{-2}\ s^{-1}$, $\sigma_{obs,15:16} = 2.96 \times 10^{-2}\ s^{-1}$, With an overall average for slit 260 of $\hat{\sigma}_{obs} = 4.90 \times 10^{-3}\ s^{-1}$. These are higher than those found by Ryutova et al. (2010), but as this is sensitive to number of physical parameters, we do not expect to exactly match their numbers. This will be discussed later in the context of the results of the simulations in Sec. 5.3.

So far we have only presented 6 of the 1492 points we have attained using this method. All 1492 points are shown in Fig 5.8, with points in each slit being individually colour coded.

As can be seen in Fig. 5.8 the number of slits allows all plumes to be detected at all times. Using these points, we can determine the statistical properties of the falling plumes. Firstly, we look at the distribution of the bulb widths.

In Fig. 5.9a) we present a histogram of the widths of all plumes measured by this method. As can be seen, there is a strong peak at 400-600km, with the mean at 632km, and the median at 594km. These values are similar to those presented by Chae (2010). As can be seen from eq. (1.8), and will be shown later, the critical wavelength of the instability is proportional to the magnetic field strength and magnetic field direction, and thus the resultant width is an observational indicator of the magnetic field.

Next we look at the instantaneous downwards radial velocity, v_z, distribution of the plumes. Not all measurements that were used in determining plume widths

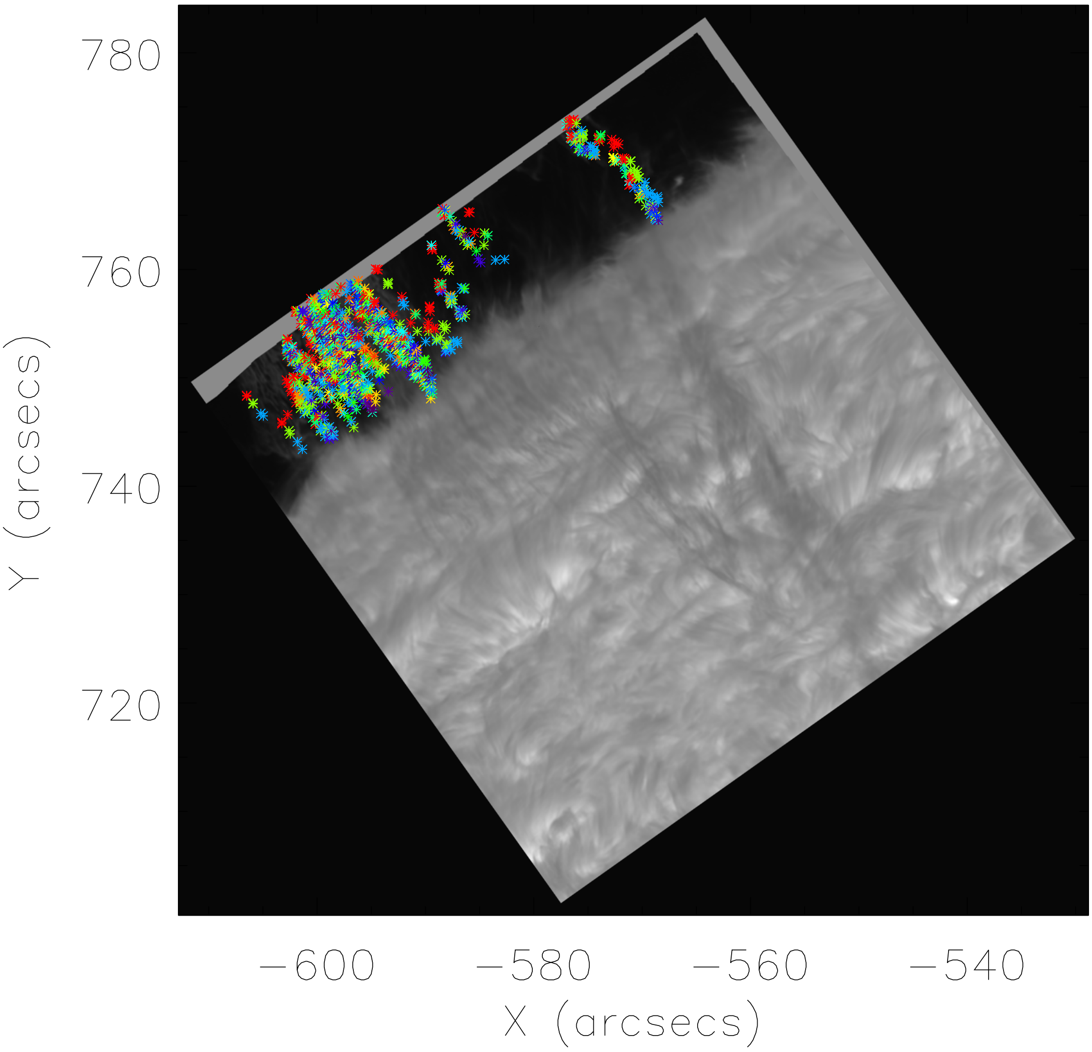

Figure 5.8: The positions of all clicked points for all slits, colour coded per slit.

can be used in determining velocities. This is due to some points (<10) being the only point to describe a track, as well as questions of connectivity between two points such as was discussed for Fig. 5.7. Nevertheless we are able to determine the instantaneous radial velocities of 896 pairs of data points, which we present in Fig. 5.9b.

As can be seen in Fig. 5.9b almost all velocity magnitudes are < 20 km s $^{-1}$, with a strong peak between -9 to -10 km s $^{-1}$, a mean of -9.8 km s $^{-1}$ and a median of -9.2 km s $^{-1}$. These velocities are lower in magnitude than are usually

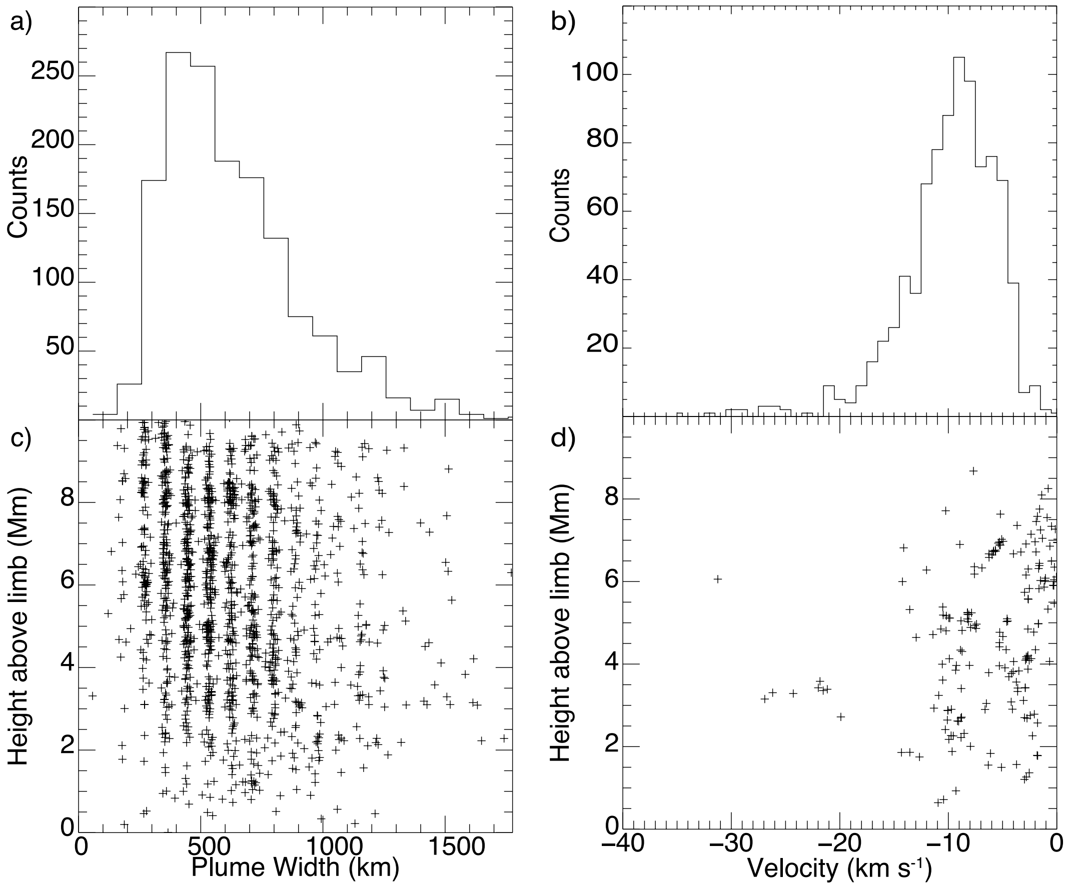

Figure 5.9: a) Bulb width distribution of the 1492 recorded events. Mean width = 632 km, median width = 594 km, and the most probable range = 400-600 km. b) Instaneous radial velocity, v_z, distribution of the 896 recorded event pairs from which velocities could be recovered. c) The disribution of plume width versus plume height above limb. d) The distribution of velocity versus averaged plume height above limb

reported by other authors, but this is likely due to several reasons. Firstly, there may be some inherent biases in the method that have previously been discussed in the explanations of Figs. 5.6, and 5.7. Secondly, other authors may only look at the fastest moving plumes, thereby actually showcasing the small number of faster moving plumes that we also recover in the range of -10 to -20 km s $^{-1}$. In our case, over 41.5% of the recovered values are over -10 km s $^{-1}$ in magnitude, with just over half of that number being in the range of -12 to -25 km s $^{-1}$. In Fig. 5.9c) we present the distribution of plume widths versus plume height. There is no clear trend between width and height suggesting that plumes can develop at a range of widths at all heights, but we see a strong preference for widths below 1000km at all heights. This is most likely due to a selection bias of the user, preferring smaller more obvious events that exist over a clear range in height. This is also effected by the way the current method does not necessarily interact with the thickest part of the plume. The apparent vertical lines present are due to the doubling of the chosen width effectively eliminating odd numbers. This bunching may in part be due to a over-sampling of events, as some plumes are represented in more than one height time plot. There may be evidence of the development of a single plume through small numbers of diagonal trends, as can be seen at around 2 Mm at 1000 km. This downward trend would suggest that as it falls to lower heights it becomes wider.

In Fig. 5.9d) we present the distribution of plume velocities versus plume height. Here, the height is the average of the two positions along the plume used to calculate the velocity. There is perhaps a slight trend for increased velocity with decreasing height as would be expected, but the majority of plumes fall at less 20 km^{-}1. This is perhaps due to the fact that the recovered velocities are only one component of a three-dimensional velocity. This is also a reflection of the chosen points, and the bias that will exist towards slow moving plumes that can be clicked multiple times within the same height-time plot, versus faster moving plumes that only exist for a short time within them.

Next we look at the local enhancement ratio of all plumes, calculated as the maximum intensity over the minimum intensity within the perpendicular search range.

As can be seen in Fig. 5.10a, the ratio peaks in the range of 2-3, with a mean

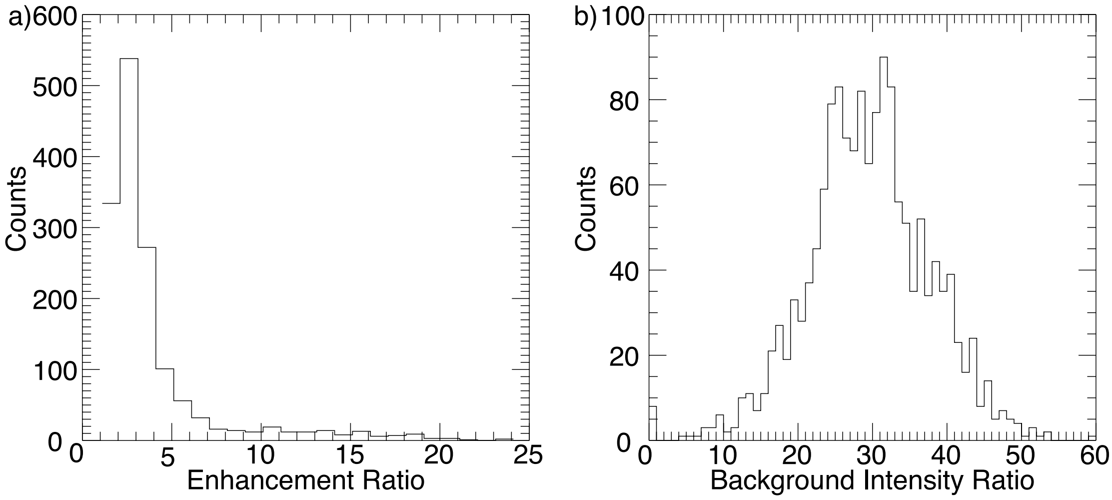

Figure 5.10: a) Local enhancement ratio distribution of the 1492 recorded events. b) Intensity ratio distribution of the 1492 recorded events.

of 3.96, and a median of 2.79. As mentioned above, this is a local enhancement ratio, rather than the ratio of the plume to a background. This means that the distribution shows that the plumes are usually 2-3 times brighter than the surrounding plasma.

We can also estimate the intensity ratio of the plumes to a background. This background is calculated as the peak of the histogram of the intensity of the data below the mean plume intensity value of 474 Dn, resulting in a background data value of 16 Dn. In Fig. 5.10b we show the distribution of the ratio of the maximum recorded intensity of the plumes to the background. Due to the background being coronal matter it is barely emitting in Hα, thus making the ratio significantly greater than that of the bulb to the surrounding prominence plasma. Taking the standard approximation of emission measure as $I \propto n_e^2$ we can estimate the density ratio of the plumes. As shown in Fig. 5.11 we find that the mean density ratio is 5.93, the median ratio is 5.43, and the peak range is 5.4-5.6.

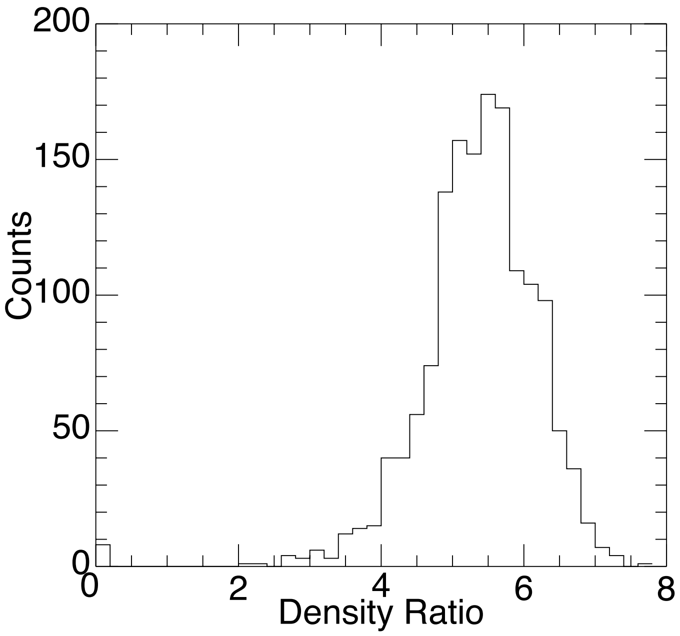

Figure 5.11: Density ratio distribution of the 1492 recorded events calculated as $n_e = \sqrt{I}$

5.2 Numerical Methods

To perform simulations of this event we use the MANCHA code (Khomenko et al., 2008; Felipe et al., 2010; Khomenko & Collados, 2012), specifically with its implementation in Khomenko et al. (2014, and references therein). MANCHA solves the non-linear equations for perturbations in ideal compressible MHD. Explicitly, these are the following:

For mass conservation:

$$\frac{\partial \rho}{\partial t} + \nabla \cdot (\rho \mathbf{u}) = 0 \ . \tag{5.1}$$

The conservation of momentum is given by

$$\rho \frac{D\mathbf{u}}{Dt} = \mathbf{J} \times \mathbf{B} + \rho \mathbf{g} - \nabla p \ . \tag{5.2}$$

The internal energy is

$$\frac{Dp}{Dt} = -\gamma p \nabla \mathbf{u} + (\gamma - 1)(\eta \mu_0 \mathbf{J}^2 + \eta_A \mu_0 \mathbf{J}_\perp^2) \ . \tag{5.3}$$

For the induction equation:

$$\frac{\partial \mathbf{B}}{\partial t} = \nabla \times [(\mathbf{u} \times \mathbf{B}) - \eta \mu_0 \mathbf{J} - \eta_A \mu_0 \mathbf{J}_\perp] \ , \tag{5.4}$$

where ρ (density) , and p (pressure) are summed over all plasma components, $\mathbf{J}$ is current density, $\mathbf{B}$ the magnetic field, μ_0 the magnetic permeability, α (neutrals [n],ions [i], and electrons[e]), $\mathbf{g}$ is equal to 274 m s^{-2}, and γ is the adiabatic constant and takes the value 5/3. The centre of mass velocity, $\mathbf{u}$, is averaged over the velocity of the individual species as

$$\mathbf{u} = \frac{\Sigma_\alpha \rho_\alpha \mathbf{u}_\alpha}{\rho} \ .$$

In Equations 5.3, 5.4, $\mathbf{J}_\perp$ is the component of current perpendicular to the magnetic field,

$$\mathbf{J}_\perp = -\frac{[\mathbf{J} \times \mathbf{B}] \times \mathbf{B}}{|B|^2} \ ,$$

and η and η_A are the Ohmic and ambipolar diffusion terms respectively,

$$\eta = \frac{m_\mathrm{e}(\nu_\mathrm{ei} + \nu_\mathrm{en})}{e^2 n_\mathrm{e} \mu_0} \ , \ \eta_A = \frac{(\rho_\mathrm{n}/\rho)^2 |B|^2}{(\rho_\mathrm{i} \nu_\mathrm{in} + \rho_\mathrm{e} \nu_\mathrm{en}) \mu_0} \ .$$

Here, ν_in, ν_en, ν_ei are the theoretical collisional frequencies and are given by

$$\nu_\mathrm{in} = n_\mathrm{n} \sqrt{\frac{8 k_B T}{\pi m_\mathrm{in}}} \sigma_\mathrm{in} \ , \ \nu_\mathrm{en} = n_\mathrm{n} \sqrt{\frac{8 k_B T}{\pi m_\mathrm{en}}} \sigma_\mathrm{en} \ , \ \nu_\mathrm{ei} = \frac{e^4 n_\mathrm{e} \Lambda}{3 \epsilon_0^2 m_\mathrm{e}^2} \left(\frac{m_\mathrm{e}}{2 \pi k_B T} \right)^{3/2} \ ,$$

where k_B is the Boltzmann constant, e is the electron charge, ϵ_0 is the permittivity of free space, n_e is the electron number density, and $m_\mathrm{in} = (m_\mathrm{i} m_\mathrm{n})/(m_\mathrm{i} + m_\mathrm{n})$, $m_\mathrm{en} = (m_\mathrm{e} m_\mathrm{n})/(m_\mathrm{e} + m_\mathrm{n})$. The cross-section of each respective frequency are $\sigma_\mathrm{in} = 5 \times 10^{-19}$ m^2, and $\sigma_\mathrm{en} = 10^{-19}$ m^2. Here Λ represents the Coulomb logarithm for T<600,000K,

$$\Lambda = 23.4 - 1.15 \log_{10} n_\mathrm{e} + 3.45 \log_{10} T \ .$$

The electron number density n_e is evolved through time using the instantaneous Saha equation. MANCHA explicitly does not assume magneto-static equilibrium. It utilises a 4th order central difference scheme in space and a 4th order Runge-Kutta scheme in time, and is stabilised against numerical instabilities through the use of hyper-diffusivity. It also utilises a perfectly matched layer for boundary absorption conditions, and the OPAL (OPacity Libraries) equations of state (Iglesias & Rogers, 1991). This code uses periodic boundaries on the left and right boundaries, meaning that plasma that flows through the left will appear on the right, with fixed on top and bottom, meaning that flows that attempt to pass through them are instead set to zero velocity. We now show the results of this code.

5.3 Numerical Results

We run MANCHA in 2.5D (i.e. solving for 3D magnetic field vectors and 2D velocity field vector), in order to investigate the development of the magnetic Rayleigh Taylor instability (MRTI) at the lower boundary of a prominence channel. Primarily, We will investigate the development of falling plumes formed due to MRTI into the coronal environment under a) different initial magnetic field environments and b) for different critical wavelengths under which the MRTI grows. In the simulations performed in this work, the x-axis corresponds to width, the y-axis to depth, and the z-axis to height. A parametric numerical study of these two properties will allow us to examine the evolution of a wide range of plume structures as they fall through the coronal atmosphere. This is achieved through an homogeneous horizontal (i.e in the XY-plane) magnetic field with strength B_0 in both the prominence and corona. As part of this study we vary the orientation of the magnetic field B_0 relative to the x-axis (I.e. the XZ-plane) from a minimum of $\theta = 76.53°$ (for $\lambda = 500\ km$, and $B_0 = 1\ G$) to $\theta = 89.70°$ (for $\lambda = 100\ km$, and $B_0 = 20\ G$). In total, 30 simulations are run sampling B_0 from 1 - 20 G, and λ from 100 - 500 km. We can then identify a narrow parameter range in which the simulated plumes best reproduce the kinematic and geometric properties of the observed plumes.

The x- and z-components of B_0 are set initially to zero. B_y is imposed uniformly throughout the domain (i.e. there is no magnetic stratification). The orientation of the magnetic field with respect to the density discontinuity interface can be seen in Fig. 1.7, wherein the instability and prominence develop in the XZ-plane. The full extent of the atmosphere in the z-direction is 10.5 Mm in physical units (spanning the full height of the observations) with 1500 grid cells corresponding to 7 km per grid cell. The x-direction spans 3.5 Mm in physical units, again, with 7 km per grid cell resulting in 500 grid cells. In order to initiate the MRTI instability we first impose a 1D atmospheric profile along the z-dimension and at all x grid cells in the domain. As shown in fig. 5.12, at $z =$ 6.3 Mm we impose a steep density discontinuity with a profile in the x-direction that exhibits a random distribution of density perturbations with varying frequencies and amplitudes. This random distribution consists of a multi-mode interface that is established over a narrow, smoothed transition region of 7 grid cells between the prominence and the corona and follows the implementation of Eq. 9 in Jun et al. (1995), as shown in the cutout panel of fig. 5.12.

In Fig. 5.13 we present an illustrative example of the 2.5D simulation in the x and z dimensions. The density profile at the interface is reproduced throughout the y-direction with the potential for a varying B_y component in the magnetic field. The density contours indicate the strong density contrast that exists within the leading edge of the plume.

In the top left panel of Fig. 5.14, we present the mass density (ρ) pro-

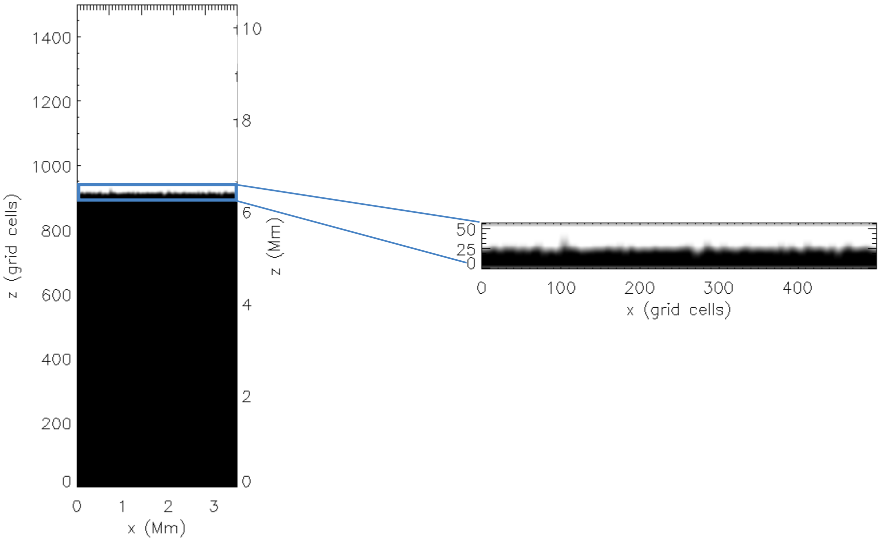

Figure 5.12: Initial grid configuration as seen in density, with the discontinuity shown in the zoom-in box.

file for the atmosphere, as a function of the z-dimension. A coronal density profile of $\sim 5.2\times 10^{-15}$ kg/cm^3 from z=0 to z=6.1 Mm is imposed. Between z=6.1 and z=6.5 Mm a steep mass density increase to prominence levels of $\sim 3.4\times 10^{-13}$ kg/cm^3 is imposed. The mass density profile then gradually decreases for heights greater than 6.3 Mm in the z-dimension. In this panel, we also represent the mass density profile, required to maintain a magnetohydrostatic equilibrium (no-flows) initially, given an initially uniform magnetic field everywhere in the domain. This magnetohydrostatic equilibrium is calculated by setting the temperatures of the prominence and corona at 10^4 K and 10^6 K respectively with a smooth transition, as mentioned previously. From this temperature profile, a scale height is calculated which is then used with the magnetic scale height to determine an effective scale height. From these we calculate the stratification of the background plasma pressure and magnetic pressure. The mass

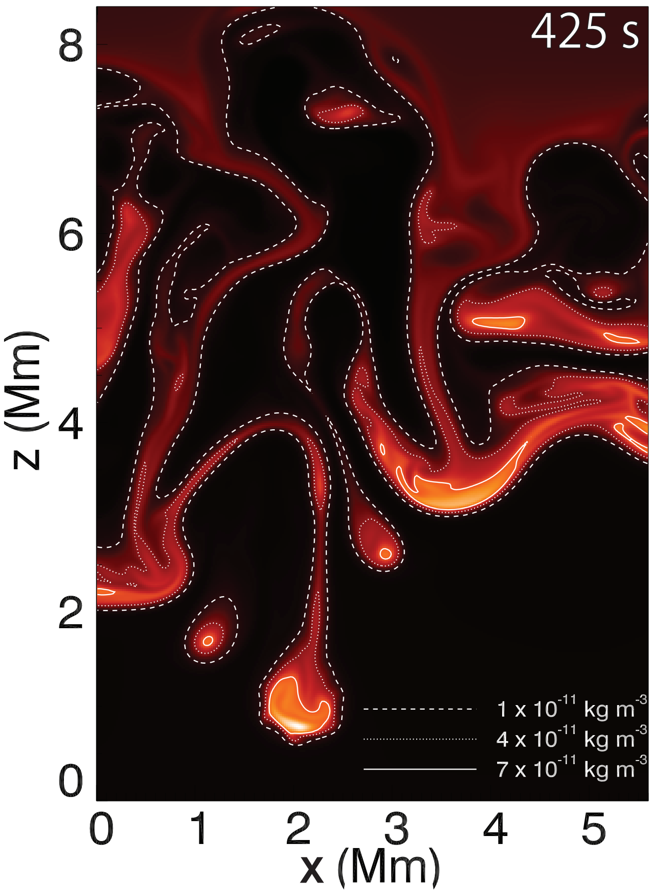

Figure 5.13: The mass density distribution ρ after 425 s in the x-z plane for a simulation with B_0 initial magnetic field strength of 10 G with an imposed critical wavelength of 50 km, resulting in an θ of 89.57° of B_y away from the vertical. Note the individual nature of each falling plume.

density profile can then be established from the set temperature profile and the calculated pressure profile determined from solving the equation of state for an ideal gas. The solid black line corresponds to an atmospheric profile associated with magnetic pressures resulting from the imposition of a 5 G B_y-component of the magnetic field uniformly everywhere through the simulation domain.

As shown in the top left panel of Fig. 5.14 the effect of increasing the field from 5 G to 6 G and then 7 G (solid, dotted, and dashed lines respectively) leads to marginally larger mass densities particularly at greater heights. This increase in mass density gives rise to increases in plasma pressure at greater heights (top right panel), offsetting the net increase in magnetic pressure given the slightly larger field strengths initialised uniformly at all heights. Over the height range of 6.3-10.5 Mm the resulting values of mass densities do not deviate significantly with larger values of B_y and remain within typical values of prominence material. Likewise, the resultant temperature values remain within those typical for prominences.

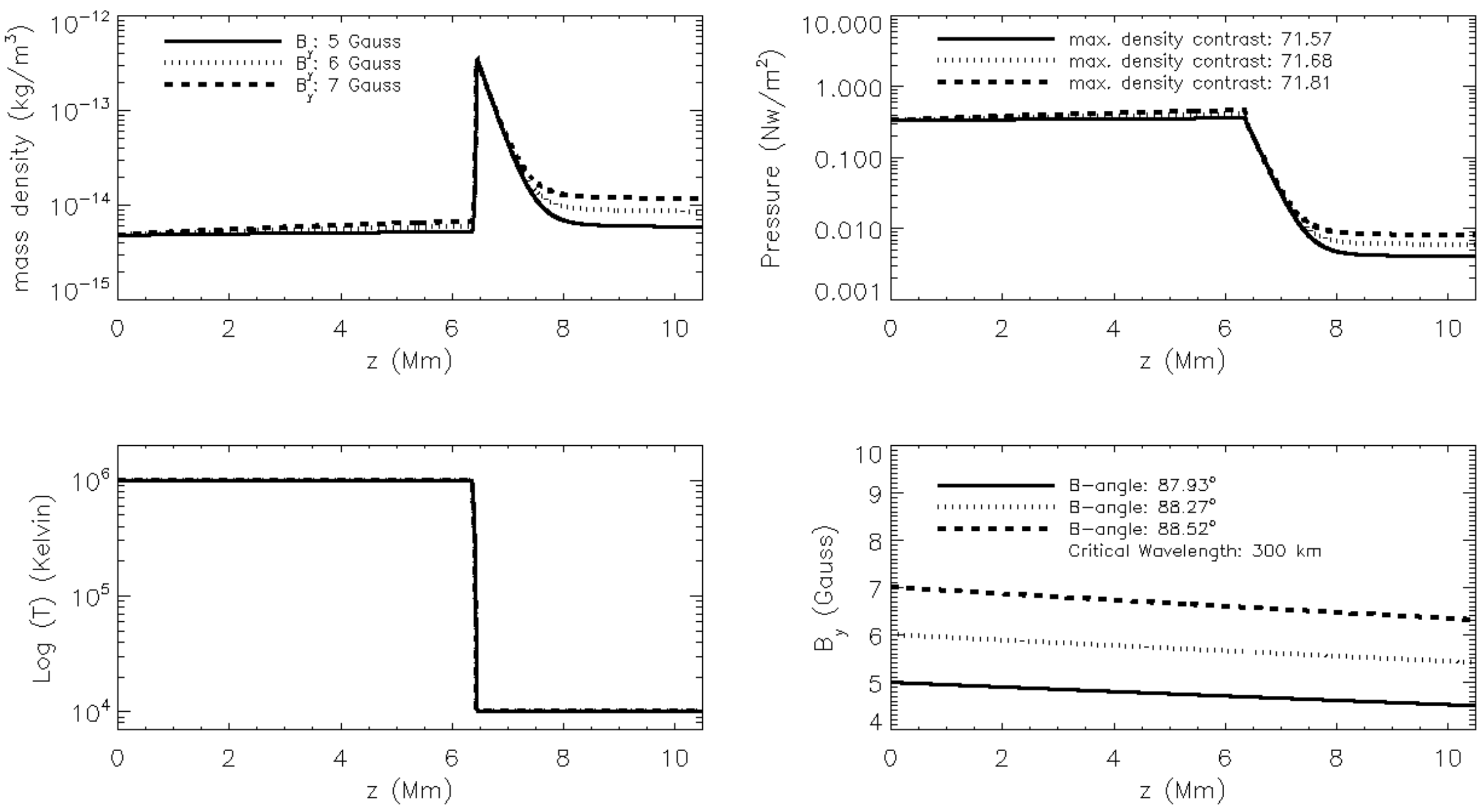

Figure 5.14: Top left: Mass density vs Height (z) for B_y =5, 6, and 7G (Solid, dotted, dashed respectively). Top right: Pressure vs Height for the same B_y. Bottom Left: Log (T) vs Height for the three B_y. Bottom Right: B_y v height for the three B_y.

We seek to investigate the role of the critical wavelength, λ_c (see Eq. (1.8)), and its effect on the development of the plumes. Explicitly, we wish to understand whether there are coherent structural properties and kinematics that manifest according to specific values of λ_c. λ_c and B_0 are parametrised, thus allowing MANCHA to find an initial equilibrium by varying ρ_h, ρ_l, and θ (see Sec. 1.3.2 for definitions). For a given B_0, MANCHA keeps ρ_h and ρ_l constant, varying θ to accommodate changes in λ_c. This change in θ is on the order of a degree or so for the values of λ chosen here. The pressure contrast for the 5 G, 6 G and 7 G atmospheric profiles is presented in the top right panel of Fig. 5.14.

The result of changing B_0 on θ is roughly an increase of half a degree for each unit increase in Gauss, as can be seen in the legend of the bottom right panel of Fig. 5.14. More importantly, imposing these angles for θ in the initial magnetic field B_0 as a function of z, can effectively allow us to explore the dynamics of falling plumes under the MRTI for specific values critical wavelengths and field strengths B_0.

Firstly, we investigated the evolution of plumes for $B_0 = 10$ G, and λ_c=50 km, which is below the resolution of CRISP, with the corresponding θ=89.57°. The mass density distribution in the falling plumes at 425 s is presented in fig. 5.13. In general, for this value of λ_c across other B_0 values, the evolving plumes are always highly non-uniform in their evolution. The plumes are not at all uniformly structured, and there is clearly no consistent downward motion in the falling plume trajectory which should be expected from the observations. As this value of λ_c cannot reproduce the observations, we discount it. Instead, we explore the plume properties associated with λ_c of 100 km, 300 km and 500 km across the B_0 range of 2 to 20 G. A snapshot at 400 s (satisfying the typical lifetime of the observed plumes from our observations), of the mass density distribution in all of the simulations exploring this parameter space, are presented in Fig. 5.15.

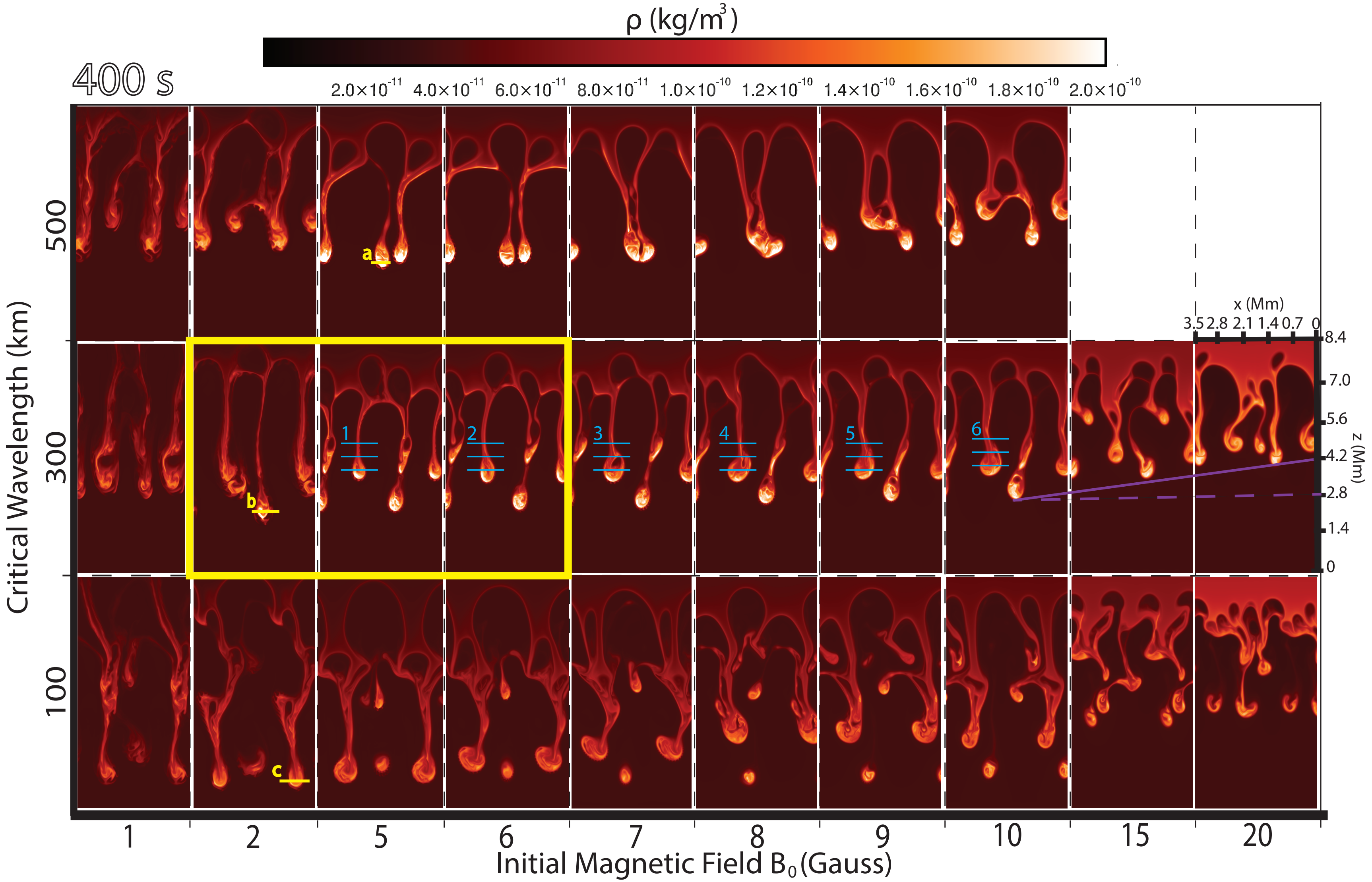

Figure 5.15: The mass density ρ in the x-z plane for all simulation runs, captured at 400 s, having parameterized the critical wavelength λ_c (y-axis) and the initial magnetic field strength B_0 (x-axis) acting in the B_y-component. The horizontal solid blue lines labelled 1-6 represent 3 slits used to determine plume widths for a coincident plume represented in all simulations, as a function of increasing B_0. The horizontal solid yellow lines labelled a-c represent 3 slits used to determine plume intensity ratios and V_z-component of velocity, as a function of λ_c. The yellow box represents a space within the parameter ranges that we identify as being the best at characterising most of the observable properties for the majority of plumes observed with the SST. The gaps are due to a lack of time to run those simulations.

Figure 5.15 provides an opportunity to explore the wide range of structural changes in plume formation, as a result of the interplay between λ_c and B_0 in the development of the MRTI. Continuing from the previous discussion, when we explore the structure of the plumes formed with λ_c=100 km, as a function of B_0, we find that there is still a significant amount of apparent deviation in the plumes away from the vertical. There exists disconnected plume bulbs from stems in $B_0 \geq 8$ G. At large initial magnetic field strengths there are a lot of incoherent structures that appear quite turbulent in nature. A notable and visible characteristic of λ_c is that for larger values, i.e. 300 km, we start to see a distinctly more coherent and continuous structure in the plumes. They are more clearly associated with their origins and more uniform in their dynamics. At λ_c=300 km they appear more similar to the long, coherent structures observed by the SST, when compared with λ_c=100 km and especially with λ_c=50 km for equal B_0. Note, the axis on the right-most panel in the λ_c=300 km row of Fig. 5.15 is zeroed on the location of the discontinuity at the start of the simulation on the z-axis. The physical effect of strong magnetic fields clearly has a role in suppressing the downward motion of the plumes. This is to be expected since the plume perturbation interface is almost perfectly perpendicular to the magnetic field plane, and as the plumes proceed to fall downwards the magnetic pressure gradient will counteract this motion. Due to the frozen-in flux condition the magnetic field is carried downwards by the plasma motion causing an increase of magnetic flux at the leading edge of the plume over time. This increase in flux causes an increase in an upwardly directed magnetic pressure force, resisting the downwards motion of the plasma, and therfore resulting in the deceleration of the plume as it nears the bottom boundary. Thus, for stronger initial fields we find (linearly) greater resistance to downward motion and the plumes of 20 G initial fields do not travel as far downwards as those at 15 G or 10 G after 400 s. This linear behaviour is demonstrated in Fig. 5.15 with the purple solid and dashed lines marking the leading edge of the plumes in 10 G, 15 G and 20 G simulations. A linear trend in the suppression of downward motion is to be expected given that the initial fields are uniform across the whole domain. Since the initial magnetic field strength constrains the downward velocities of the plumes, we can therefore impose limits on the B_0 parameter space given that we know the radial (downward) velocity distribution of the plumes.

When we consider the λ_c=500 km simulations, we find that the plume structures appear even more coherent and continuous. However, these plumes appear to have merged at some point along their evolution, given how their stems and bulbs appear connected. It is not unexpected that larger λ_c should give rise to larger plume structures, as this is inherent in the overall scalability of the MRTI and in its growth rate function. However, we can determine just how far in λ_c parameter space we need to explore by setting limits based upon the known size of plume structures from the observations, including what we should expect from mergers. We now identify the left-most plume that appears to manifest in all simulations at λ_c =100 km. We extract widths and size information for this plume, marked with blue horizontal slits and numbered 1-6 in fig. 5.15, as a function of B_0.

There also appears to be a consistent trend with regards to the mass density of the plume bulbs when comparing λ_c=100 km, 300 km and 500 km. The plume bulbs are significantly more dense at λ_c=500 km when compared with 300 km, and even more so comparing with 100 km. Later, we will explore the relationship between the mass density ratios (i.e. ratio of mass density at the location of the plume bulb vs. background) and the local V_z-components in the velocity field, using the yellow horizontal slits labelled a-c.

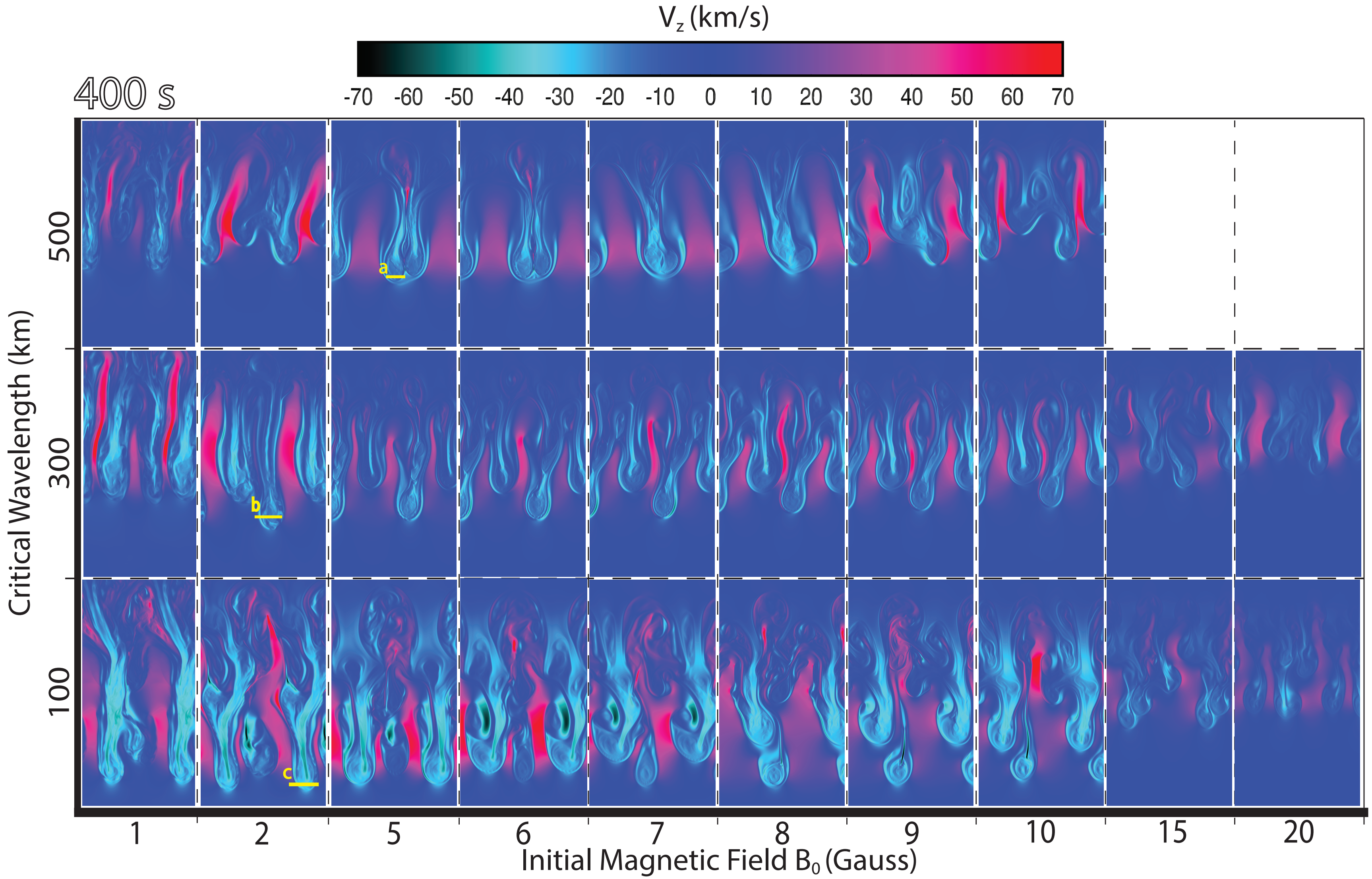

Figure 5.16: As for Fig. 5.15 but for the downward velocity vector V_z. The same yellow horizontal slits labelled a-c are over-plotted for comparison with those slits overlaid in fig. 5.15.

Figure 5.16 presents snapshots of the the same simulation (taken at 400 s) spanning the same parameter space but each panel now shows the distribution of the downward velocity, V_z, in the x-z-plane. Previously, it was shown that multiple falling plumes combine into a single plume structure, at λ_c=500 km. This unified nature of the structure becomes even more apparent in the velocity distributions corresponding to λ_c=500 km. Here we can see, for B_0=6 G there is clearly one combined downward moving structure, within which we can detect the presence of the previously separate plume bulbs (more easily seen in the mass density plots). So what appears potentially as two adjacent structures at λ_c=500 km is one large combined structure. In contrast with the V_z distributions at λ_c=300 km we find many more, narrower, and independently evolving structures in plumes, matching those clearly evident plumes in the associated mass density distributions. So λ_c=500 km may be leading to more coherent and continuous structures that are too large, whereas, λ_c=100 km is closer with regards to plume size and shape in comparison with the observations. Another interesting feature of fig. 5.16 is the relative magnitudes of the V_z-component of velocity. The fastest evolving plumes are the weakest with regards to initial field strengths (i.e. see 2 G) and with the smallest λ_c values of 100 km. There is a visibly more turquoise colouring, representative of downward velocities in the range of 30-40 km s^{-1}. Just as larger initial fields give rise to slower falling plumes, the weakest fields give rise to plumes that are too fast relative to the observations. We can match our measurements with the observed distributions to find a good comparison with regards to field strengths and critical wavelengths. Finally, when we consider only the largest plume structures at λ_c=500 km we find a trend in the upwards velocity of V_z for larger B_0. At 10 G we can detect exceptionally strong upflows (red) even as high as 60-70 km s^{-1} (twice that of the fastest downward plumes). These strong upflows also tend to be co-located with the dark voids / bubbles above the height of the discontinuity. This is likely due to the conservation of flow, with the plumes creating pressure gradients between them that drive mass upwards into the bubbles rising towards the top boundary. Dark rising bubbles have also been explored with Hinode/SOT observations (also referred to as plumes) which appear to be strongly linked with the formation of falling plumes.

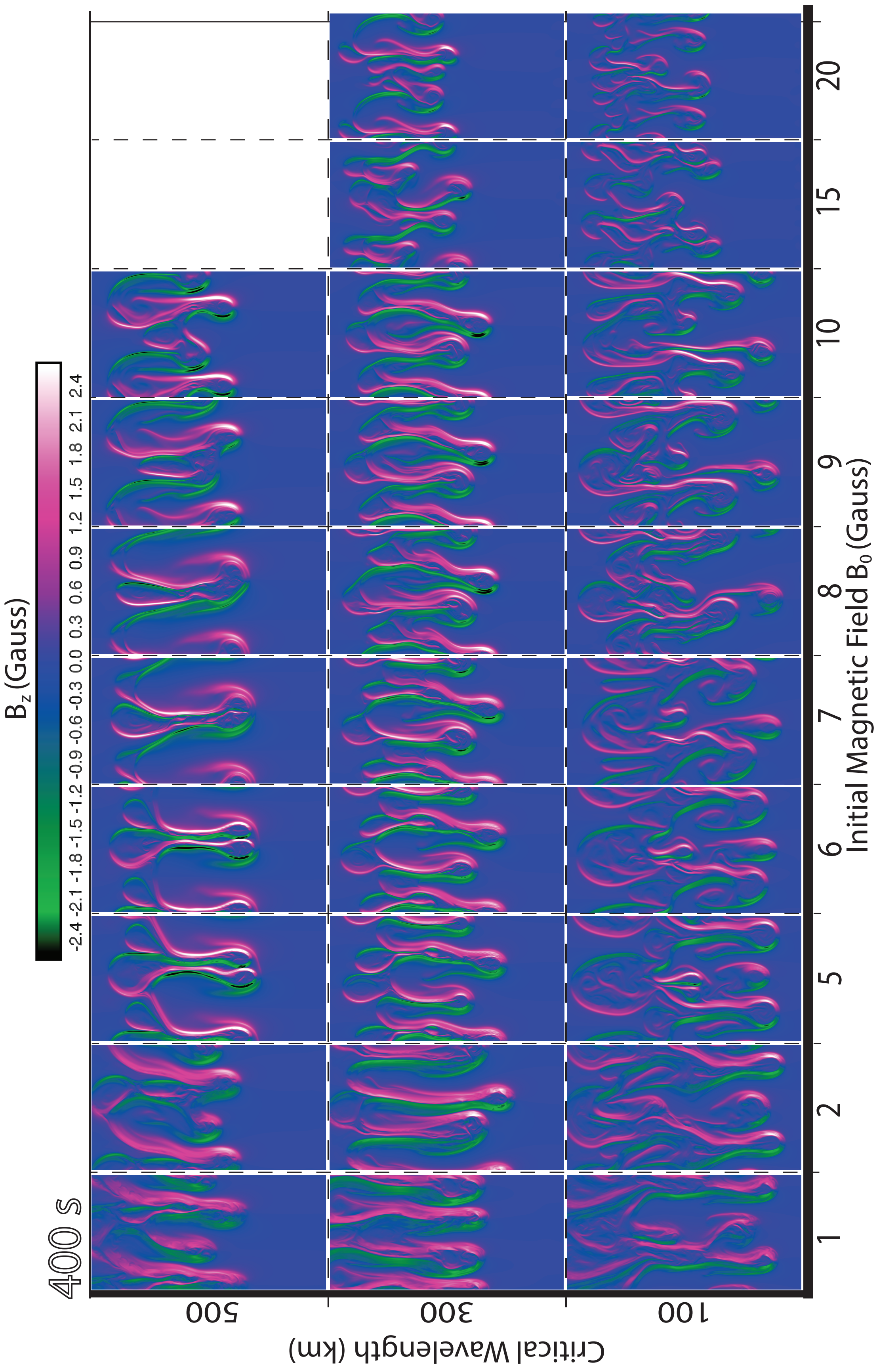

Figure 5.17: As fig. 5.15 but for downward magnetic field vector B_z distribution.

Figure 5.17 presents the same parameter space, showing the distributions of B_z. Green values of B_z denotes downward field vectors and pink values of B_z denote upward direction of fields in the x-z-plane. Initially, there is only a magnetic field perpendicular to the perturbation interface. As plumes develop they fall into the perpendicular fields, compress them, and drag them through the momentum of the downward motion. As a result the magnetic field interface deforms with the falling plume and forms a surrounding sheath. This is present in all plumes in all simulations.

The extent of the B_z component appears to be notably weaker in magnitude for the largest initial field strengths in B_0. This is due to a strong B reducing flows within the plasma due to the frozen-in effect.

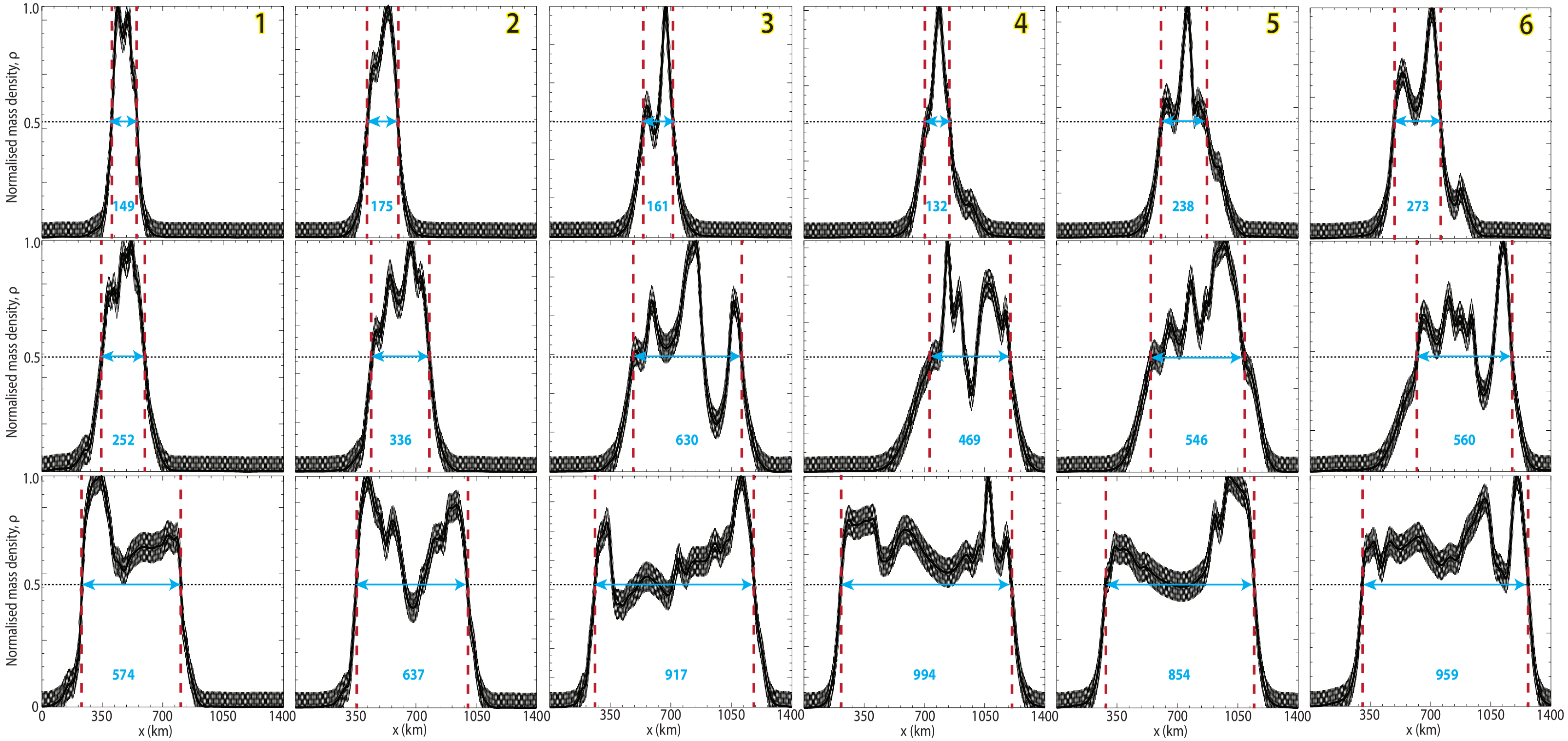

Figure 5.18: Each column labelled 1-6 consists of 3 panels representing mass density ρ (normalised to the maximum mass density) extracted from the blue horizontal slits labelled 1-6 of fig. 5.15. Vertial red dashed lines represent the boundaries of the plume cross-section set to the FWHM of the slit profile, i.e. at a normalised mass density of 0.5. The respective widths of each slit (km) are incorporated in blue into each panel.

In order to constrain the parameter space explored here in numerous simulations, we first examine the variations in size scale and plume widths, across plumes labelled 1-6 in fig. 5.15. The properties of each of the 3 slits (cross-cuts) associated with plumes 1-6, with respect to mass density ρ, are presented in fig. 5.18. Here each column, labelled 1-6, profiles the normalised mass density (ρ) cross-cuts of associated horizontal blue slits from fig. 5.15. Within each column of fig. 5.18, the 3 slit panels reveal changes to the widths of the plume structure at different locations along the plume length at 400 s, associated with simulations initiated with a B_0 of 5G - 10G. There was a consistent choice for the 3 slit intersections of the plume such that: the bottom slit panel in each column corresponds to the maximum width within the plume bulb at 400 s, the middle slit panel corresponds to the location of the neck of the plume (where the plume stem meets the bulb), the top slit panel corresponds to a location further upstream in the plume structure(i.e. at a location which is twice the separation distance between the locations of the middle and bottom slits). As shown in fig. 5.18, the plume structure generally broadens in width from top to bottom along the structure for each column(i.e. for progressively larger B_0). Considering the top panels for each column, there is a tendency to increase in the width of the plume stem for increasing B_0, i.e. spanning 149 km in column 1 at 400 s for the 5G simulation to 273 km in column 6 at 400 s for the 20G simulation. There is a slight discrepancy, however, for column 4 where the width recorded is at a minimum of 132 km. This is due to the large mass density and the FWHM of the plume boundary location missing the shoulder in density just to the right of the right-most red dashed line. The right most boundary is more likely to be 100-200 km further to the right if this shoulder was considered. A similar shoulder in the density profile is evident also for columns 5 and 6 meaning they too are under-estimates. The main point here is that there is a relationship between increasing plume widths along the stem for increasing initial magnetic field strengths. A similar trend holds for the middle panel slit cross-sections corresponding to the neck location of the plumes. However, there is a discrepancy with column 3 in this trend. The middle panel of column 4 could be explained by the fact that there are potentially two suitable locations which correspond to the FWHM for the right-side boundary. The significant drop in mass density within the cross-cut reveals the presence of a highly structured plume but reveals the challenge in determining where the true boundary lies. With regards to the bottom panels in each column, corresponding to the plume bulb maximum width, we again find a tendency towards increasing width (within each column) for larger initial magnetic field strengths. In this analysis, we compare the plume width data for the bottom panel slits in the different simulations, with the observations of the bright/intense plume bulb widths, in order to identify the best match. From the distribution of the 1492 observed plume bulb widths of fig. 5.9a) we reported a mean of 632 km and median of 593 km. The significantly drops after 825 km (i.e. with more than 80% of the recorded events having widths of less than 900 km). For this reason we prioritise plumes generated in columns 1 and 2 which exhibit bulb widths of 574 km in the 5G simulations at 400 s and 637 km in the 6G simulations at 400 s. Columns 3-6, associated with stronger magnetic field strengths, all record plume widths greater than 850 km which indeed exist within the observed events, but are not representative of the vast majority of events within the observable prominence. Based upon this deduction on plume widths, the 2-6 G simulations of fig. 5.15 associate best with the observed plumes.

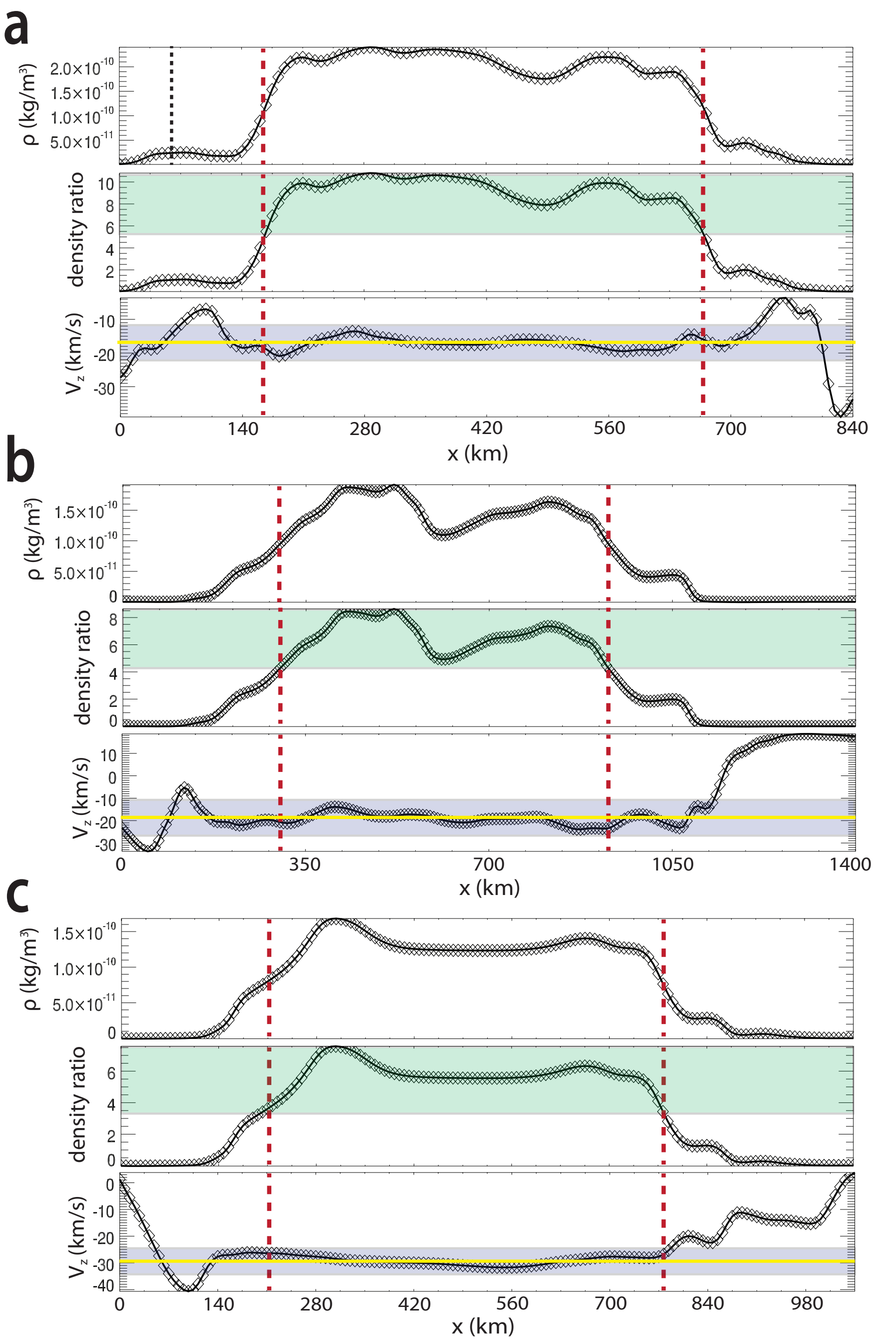

Figure 5.19: Panels a-c top: the mass density across the yellow slits labelled a-c in fig. 5.15. Panels a-c middle: the mass density ratio of the mass density profile in each simulation divided by the background density taken as the mass density at 70 km along the slit (marked by the vertical black dashed line). Panels a-c bottom: the V_z component of velocity for the slit cross-cut. The red vertical dashed lines mark the boundaries of the plume bulb corresponding to the FWHM. The green shaded box indicates a range of density ratio values that satisfy locations along the slit (limited to the boundary locations) where the mass density is greater than the FWHM density level. The purple shaded box indicates a range of V_z-component velocities that also satisfy the locations along the slit where the mass density is greater than the FWHM density level. The horizontal yellow line represents an average velocity within the purple shaded boxes.

The horizontal yellow cross-cuts of figs. 5.15- 5.16 are shown in detail fig. 5.19. In panel-a, we present the slit cross-cut mass densities for a plume bulb in the 5G simulation with $\lambda_c = 500$ km (labelled a in fig. 5.15). Likewise in panel-b and panel-c we present equivalent data from the slit cross-cuts for a plume in the 2G simulation at $\lambda_c = 300$ km and a plume in the 2G simulation at $\lambda_c = 100$ km, respectively. The purpose of fig. 5.19 is to explore the effect of an increasing critical wavelength (at approximately the same initial magnetic field strength) on the density contrast in the plume bulbs, for comparison with the intensity ratio's determined for the observed plume bulbs. For the largest critical wavelength of 500 km we find the largest density ratio in the plume bulb is in the range of 5.5-10.5. In the 2G simulation with critical wavelength of 300 km we find a smaller density ratio ranging from 4-8.5 and for the 2G simulation with critical wavelength of 100 km we find an even smaller density ratio range of 3.5-7. A prominence is an optically thick plasma, which makes it challenging to understand the interplay between plasma mass density and resulting emission measure / intensity. Given that we are observing spectral intensities at the limb in emission we can only approximate the relationship between the observed distribution of the intensity ratio with the simulated mass density ratio. We observe a strong peak in the intensity ratio distribution of 1492 events (see fig. 5.10b), in the range of 20-40, which favours critical wavelengths in the range of 100-300 km which, together, span a mass density ratio in the lower range of 3.5-8.5. The exact relationship between intensity ratio and mass density ratio is not clear and requires further investigation.

Considering the relative changes to the V_z-component of velocity in the plumes for panels a-c, the largest critical wavelength of 500 km (at a time stamp of 400 s) the V_z-component lies in the range of -12 km s^{-1} to -22 km s^{-1} with an average of -17 km s^{-1} in the downward z-direction. For the critical wavelength of 300 km (at a time stamp of 400 s) the V_z-component lies in the range of -10 km s^{-1} to -27 km s^{-1} with an average of -19 km s^{-1}. For the critical wavelength simulations of 100 km the downflow velocities within the plume bulb are again progressively larger in the range of -24 km s^{-1} to -35 km s^{-1} with an average of -29 km s^{-1}. The observed downward radial velocity distribution for the observed plume bulbs in fig. 5.9b, has a peak of -9 km s^{-1}, and spans a relatively broad distribution of -1 km s^{-1} to -21 km s^{-1}. Upon comparison with the observations, this distribution indicates a preference for critical wavelengths in the range of 300 km to 500 km and rules out $\lambda_c = 100$ km given that they are too fast.

In this analysis, we have established a criteria of: a) plumes with continuous structure and overall lengths of 7-8 Mm with lifetimes greater than 400 s, agreeing with the observations; b) plume widths that match the observed plume bulb width distributions c) plume velocities that best match the observed plume velocity distributions and d) plume density ratios that best match the observed plume intensity ratio distributions. Overall, the best agreement within the parameter space is found within the 2-6G initial magnetic field range (B_0) and around 300 km in terms of critical wavelength. This preferential parameter space has been highlighted with a yellow box in fig. 5.15. Most interesting is that if the most appropriate critical wavelength is indeed 300 km then, given that the resolution of the SST observations is 100 km in the Hα wideband, we can claim that we are fully resolving these falling plume structures adding further credibility to this comparison. Within this space we have selected the 5G B_0 at critical wavelength $\lambda_c = 300$ km to further investigate the evolution properties of these plumes.

In Figure 5.20, we show the temporal evolution of the mass density in the B_0=5G at λ_c= 300 km simulations. To interpret the kinematics of the fastest plume we placed a slit along the z-direction at 3.5 Mm along the x-axis. The

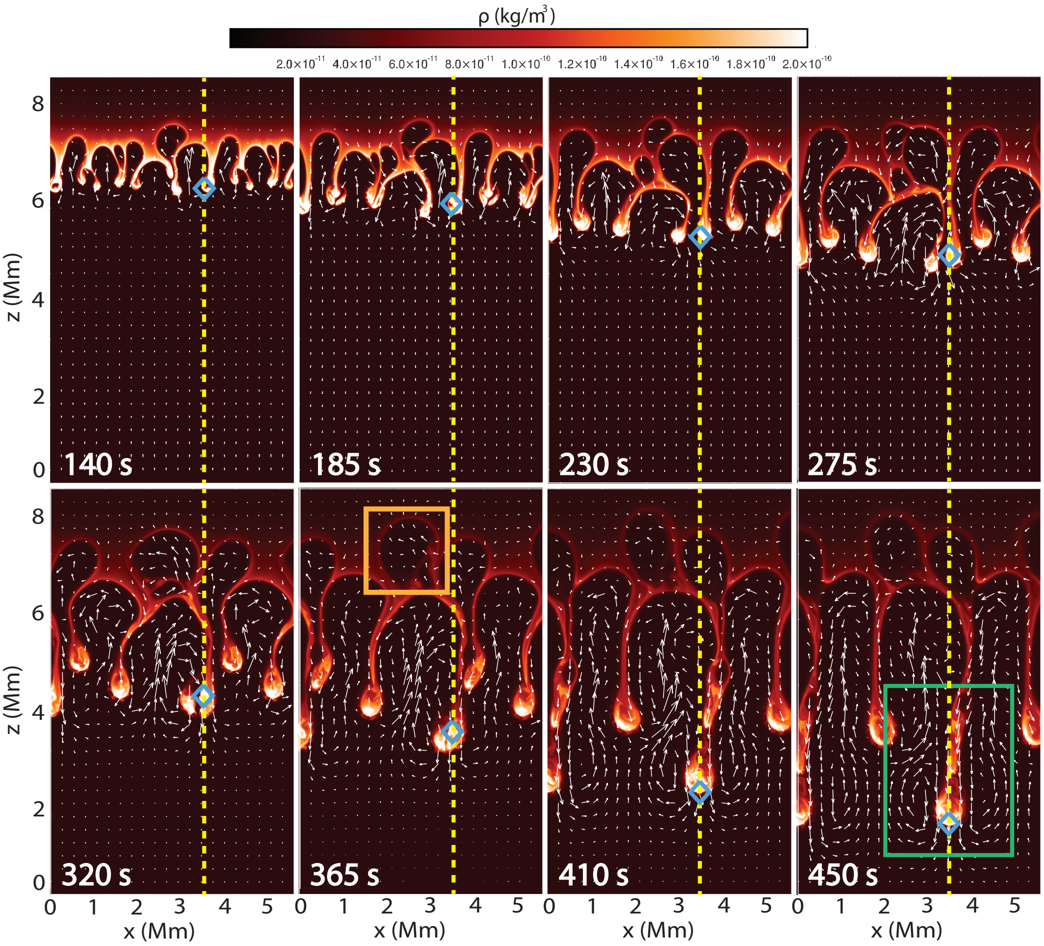

Figure 5.20: The time series of the mass density, ρ, in the B_0=5G at λ_c= 300 km simulation, evolving from top-left to bottom-right. The mass density images are overlaid with the V_x and V_z velocity vectors for the x-z plane, as white arrows. The lengths of the arrows correspond to the relative strength of the velocity vectors in the range of ± 30 km s^{-1}. The vertical yellow dashed line marks the location, along the x-dimension, of a slit from which we track the properties of the longest plume along the z-dimension to evolve after 450 s. The blue symbol marks the location of the maximum mass density ρ along the slit in time. The green box indicates a region of interest in the flow field of the falling plume towards the end of its lifetime (as it approaches the bottom boundary). The orange box marks another region of interest in the simulation corresponding to the location of a dark void within the mass density distribution.

plume follows a primarily straight trajectory in evolution and the slit can track the location of maximum mass density (marked with a blue symbol) which exists within the plume bulb. Following the location of the blue symbol in time we can see that the plume accelerates throughout its evolution. Furthermore, the mass density can be shown to be largely uniform along the stem and bulb of the plumes early on in its formation (until t=185 s). However, as the plume extends, unbroken in length (by 450 s), the mass within the stem continues to drain into the bulb where the mass concentrates. The more freely flowing plasma within the stem drains into the bulb given that there is much less resistance to flow given that there is no horizontal / perpendicular magnetic fields within the stem itself (i.e. the magnetic fields remain vertical within the XZ-plane of the stem as shown in fig. 5.17). This aspect of the plume flow dynamics will be discussed again later in the context of Fig. 5.21. The dynamics of the flow field around the plume structure and within the dark (under-dense) plasma voids is interesting. We highlight two regions of interest: the green and orange boxes of fig. 5.20. Within the green box we detect eddy-like currents in the flow-field around the plume as it passes through the corona environment to lower values of z. There appears oppositely directed vortices on either side of the plume as it passes through the otherwise stationary corona environment leading to strong shear flows between the plume structure and the ambient surrounding atmosphere. This environment experiences a conservation of angular momentum and vortices appear to trail alongside the plume. Such vortices appear to play an important role with regards to driving up-flows adjacent to the plumes back into the dark plasma voids. As previously shown in fig. 5.16 the up-flows in the voids can be substantial, i.e. on the order of 40-50 km $^{-1}$. The rising plumes can then extend further upwards, above the original height of the plasma discontinuity leading to the MRTI, manifesting as a rising under-dense bubble of hot corona plasma. Within the orange box, we explore the properties of these voids further. At 365 s within the hot rising plasma void we detect some rising flows in the arrow velocity vector field. What makes this structure particularly interesting is the nature of the magnetic vector field in the x-z plane in this region, as presented in fig. 5.21.

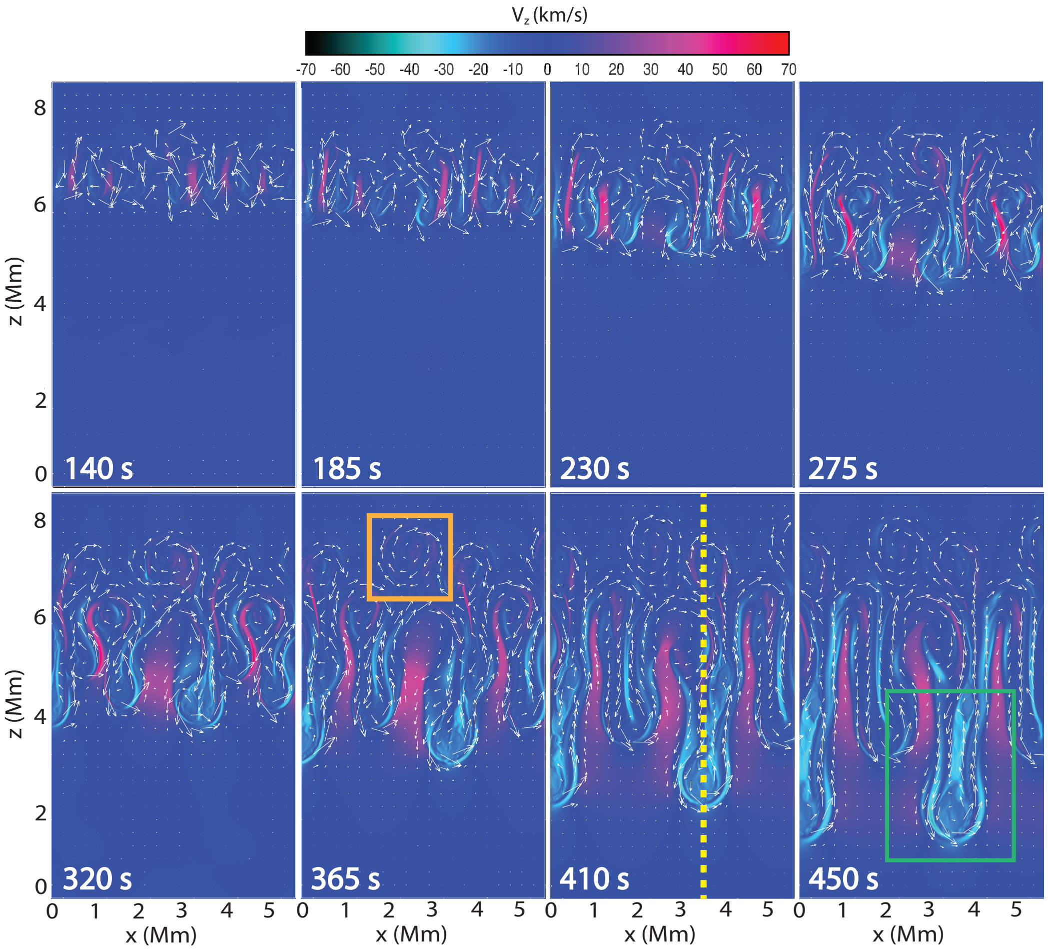

Figure 5.21: As shown in fig. 5.20, but for the V_z-component of the velocity distribution in the B_0=5G at λ_c= 300 km simulation.

In Figure 5.21, we investigate the temporal evolution of the mass density in the B_0=5G at λ_c= 300 km simulation. There is clear evidence evidence for an acceleration within the plasma flows of the plume stem throughout its evolution, with progressively higher velocities at later times (in particular after 410 s), which is coincident with vertically aligned magnetic field vectors. The flows are particularly prominent along the longest plumes where we expect the unimpeded downwards flows to naturally accelerate for longer thereby leading to larger and larger velocity flows. In fig. 5.21, for context, we have now overlaid the magnetic vector field as white arrows in the x-z plane. Considering again the orange box of interest, where we found a hot plasma void within the mass density maps in fig. 5.20, here we can reveal the corresponding behaviour of the magnetic field vectors. Interestingly, we find that within the dark and hot plasma voids, there exists a poloidal-like ring of magnetic field vectors within which we might expect currents to form (i.e. coming into and out of the x-z image plane). These rings of magnetic field appear to coincide with all of the other rising hot plasma voids. This manifestation of the magnetic field in the voids is likely to be connected to the eddy-vortices generated by the plumes that pass through the corona environment below the prominence transition layer. Those vortices spiral upwards with the red-coloured flow field within the voids adjacent to the plumes in the V_z maps in fig. 5.21, and the source of the induced vorticity in the magnetic field vectors must come from these rising plasma vortices. Beneath the prominence in the observations we also detect rising plumes adjacent to the falling plumes. Presumably, the plume-field extends further into the plane of the FOV and if so it is not clear what influence these ring-like magnetic vortices may have within the ensuing dynamics of the main body of the prominence channel. Plume formation may lead to the generation of flux-rope-like poloidal magnetic fields giving rise to additional line currents. This process may accumulate over time and play a role in the large-scale flux balance within the prominence channel and stability of the overall structure.

We place 5 consecutive vertical slits separated by 1 x-grid cell around $x =$ 3.5 Mm in the mass density field of fig. 5.20. Having tracked the location of the plasma bulb as the point of maximum mass density represented with blue symbols along each slit, in fig. 5.22 we explore the changes of vertical velocity in this plume, as a function of position in its evolution along the slit path. Fig. 5.22, shows that there is indeed an acceleration profile in the V_z component of the plume bulb as a function of time (throughout the full duration of the observa-

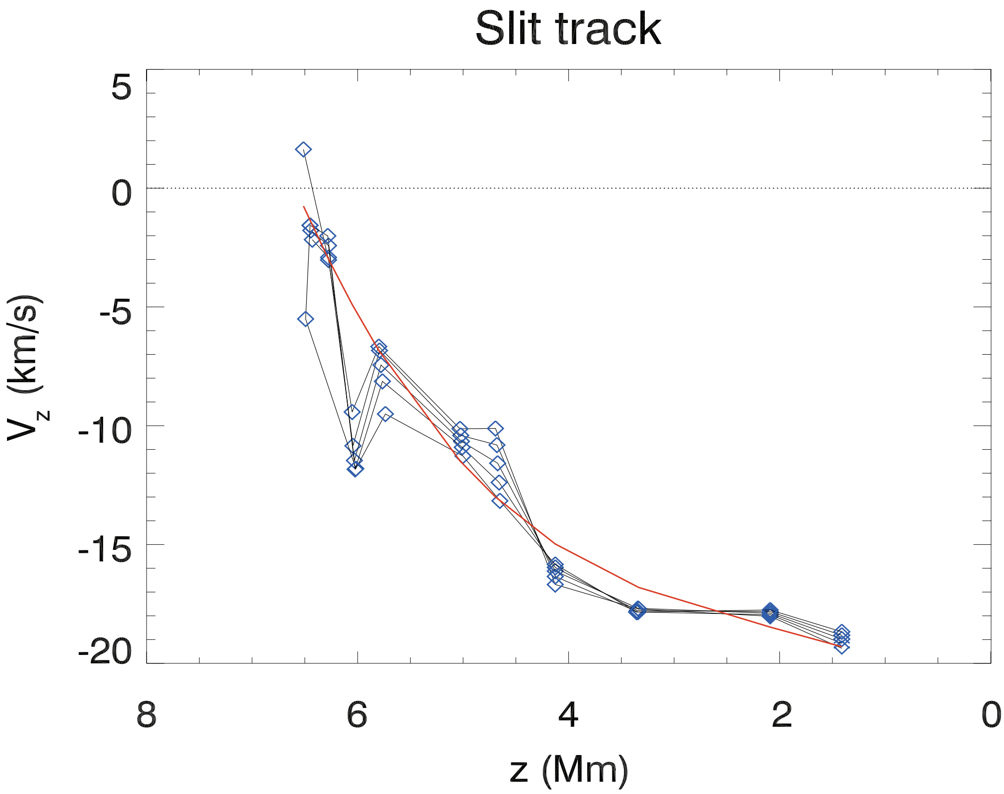

Figure 5.22: The evolution of the V_z-component of velocity in the simulated plume bulb at the location of the blue symbols, tracked along the vertical slit shown in fig. 5.20, is presented for the duration of the B_0= 5G and λ_c= 300 km simulation. There are a number of V_z measurements at respective heights along the z-axis of the structure because there are 5 consecutive slits overlaid, sampling 5 pixels along the x-dimension centered on the $x = 3.5$ Mm coordinate. The distribution of V_z profiles along the slit are fit with a 3^{rd} order polynomial, as a solid orange line to characterise the overall trend.

tion) as it propagates along the slit in the z-direction. We calculate an average propagation velocity in the plume bulb, over 450 s, of -12 km s^{-1} which is in good agreement with the mean in the observed velocity distribution. However, what is clear from fig. 5.22 is that the plume bulb can exhibit a wide range of velocities throughout its lifetime reaching as high as -19 km s^{-1} after 450 s. This velocity distribution is in good agreement with the observed range, as shown in fig. 5.9b, thus this observation of plume formation may be well represented by a B_0= 5G and λ_c= 300 km MRTI simulation. In fig. 5.22, there is a noticable decrease in the rate of change of acceleration. As the curve flattens with increasing z, there may be a maximum velocity that can be reached in the plume, indicative of properties of the atmosphere through which the plume passes. A terminal velocity is being reached as the plume bulb falls under gravity through the coronal environment which may account for it being sub-sonic (where the coronal sound speed is ≈200 km s^{-1} for a 1.5 MK plasma, Aschwanden, 2005), given the ambient medium of the corona. This may be related to the magnetic drag coefficient suggested by Haerendel & Berger (2011) which leads to a steady downward velocity due to the excitation of Alfvén waves which carry away momentum and energy.

5.4 Discussion and Future Work

We report in detail high resolution observations of extensive prominence plume formation, as observed by the 1-m SST / CRISP instrument on 6^{th} June 2014. With CRISP, we observed a forest of falling plumes with a high cadence spectral scan sequence in the chromospheric Hα line emission. Through 1419 radial slits we detected the appearance of bright plume tracks in the subsequent height-time plots. We developed a novel semi-automated detection algorithm that allows the user to select any pixel along any track within the height-time plots for any slit and manually extract important information about the widths, intensity ratio and kinematic properties of the plume bulbs. We produced histograms of falling plume bulb widths and detected a mean width of 632 km, mean downward velocities of -9 km s^{-1} and density ratios (derived from observed intensity ratios) in the range of 5-6.

With this observed information at hand, we explored plume formation using advanced 3D ideal MHD simulations with MANCHA. Through parametrisation of the equation for the critical wavelength we explored a range of fixed critical wavelengths λ_c (50 km, 100 km, 300 km and 500 km) and initial magnetic field strengths B_0 (2, 5-10, 15, 20 Gauss) in the plane perpendicular to the perturbation interface. The perturbation interface was established in a 2.5D simulation whereby the density above (ρ_h) corresponded to that of a prominence mass with prominence (chromospheric) densities, temperatures and pressures. The atmosphere below the density discontinuity characterised that of a solar corona, i.e. of lower mass density (ρ_l) and at higher temperatures and pressures. At the discontinuity the MRTI takes effect and plume formation ensues. The parameter survey was designed to identify a specific configuration giving rise to plume formation that most closely matched the falling plume observations. We investigated a) the physical origins of the plume formation and b) the properties of the observations that we could not otherwise determine such as the the magnetic field orientation and strengths. We have found that magnetic field strengths in the range of 2-6 Gauss pointing into the plane of the observations, with a critical wavelength in the MRTI preferably at or close to 300 km, is best at representing the observed plume statistical properties.

Given this result, we can now further verify our interpretation of the physical origins of the falling plumes, through considering the MRTI theoretical growth rate, σ_{th}. The growth rate was originally defined in Eq. (1.10). The theoretical growth rate contains directly measurable parameters, primarily the critical wavelength λ_c, which we take as being 300 km for best matching the observations. For our simulated atmosphere, with an initially uniform magnetic field strength of 5 G in B_0, the condition for magnetohydrostatic equilibrium resulted in density contrast (between ρ_h and ρ_l) of 71.57 whereby ρ_h = 3.44×10^{-10} kg m^3 and ρ_l = 5.21×10^{-12} kg m^{-3}. With these mass densities we calculate an Atwood (A) number of 0.97.

Given Eq. (1.8) for a λ_c of 300 km, with the determined variables, we calculate a critical angle θ in the horizontal component of the magnetic field of 87.93 degrees. With these values we calculate a theoretical growth rate of 7.46×10^{-2} s^{-1}. The measurements of the growth rate are straight-forward and reliable, allowing for a comparison with the observed growth rate, σ_{obs}. The observed growth rate was found to exist in the range of 3-9 $\times$ 10^{-2} s^{-1}. This agreement further supports the argument that a B_0 of 5G and λ_c of 300 km very well define the MRTI to reproduce the observed plume properties.

In Figure 5.23 we present a zoomed in view of a single plume from the simulation with B_0=5 G and λ_c=500 km and its temporal evolution. Most interesting is the formation of plasma protrusions at the lower boundary of the plume bulb which appear to grow in extent over the course of the plume's development. The protrusions are likely the continued manifestation of the MRTI at small scales on top of an MRTI developed plume, i.e. an instability on top of an instability - highlighting the multi-scale nature of the MRTI.

In Figure 5.24, we present synthetic observations of the falling plume seen in Fig. 5.23 at a time when it has fully formed and 50 s prior to it reaching the lower boundary of the numerical domain. This plume mass density image at each time step is synthesised into an observable intensity corresponding to a white light (broadband) emission. The image is then degraded upon convolution with a Point Spread Function (PSF) and a Lorentz profile according to the desired telescope aperture / pupil size and straylight contribution. The PSF image should be constructed in such a way that it has the same size of the image that one wishes to degrade to (this image is shown for both a 1-m and 4-m diameter aperture). The PSF is constructed by taking the module square of the Fourier transform of the pupil of the 4-m Daniel K. Inouye Solar Telescope (DKIST). This is rather straight-forward for a telescope like DKIST, since the pupil is just a circle, so the PSF is simply the Airy function. In addition, we convolved the ideal PSF

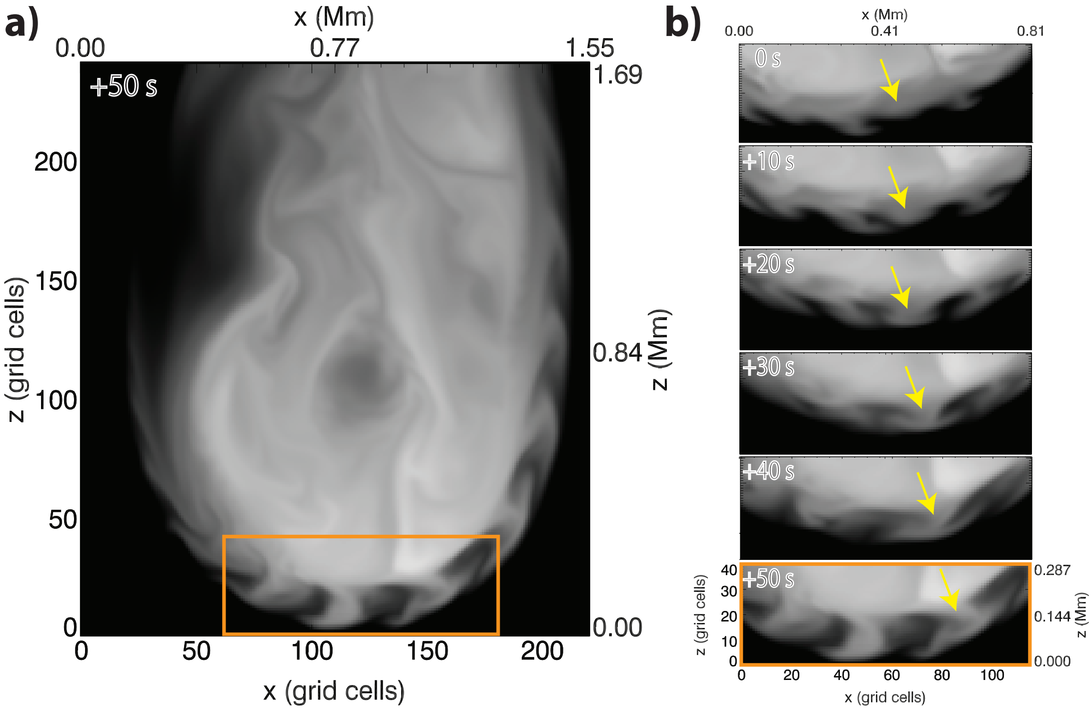

Figure 5.23: a) A zoomed in view of a simulated plume at 50s with B=5 G, and λ_c=500 km. The orange box highlights the part of leading edge chosen to show temporal development. b) The temporal evolution of the edge of the plume from 0 to 50 s. The yellow arrow highlights the position of the growth of further instability at the leading edge of a plume.

with a Lorentz profile, which was taken from the telescope model for the light path to the DKIST Visible Broadband Imager (VBI) instrument (upon private communication with the DKIST/VBI PI). This qualitatively accounts for stray light contribution to the image degradation. For DKIST images the pixel size in the blue channel (highest achievable resolution) will be 7 km. This matches the grid cell of the simulations. In the left column of fig. 5.24, we see the evolution of the DKIST synthesised images. The middle column shows the equivalent image sequence corresponding to the 1-m SST synthetic observation. With the 1-m we clearly see significant degradation of the observable structure, appearing much more blurred that with the DKIST synthesis. Furthermore, the SST image is rebinned to that of the 1k×1k CCD for SST, therefore, the SST synthesis has a pixel size corresponding to 43 km, leading to the apparent pixelated image

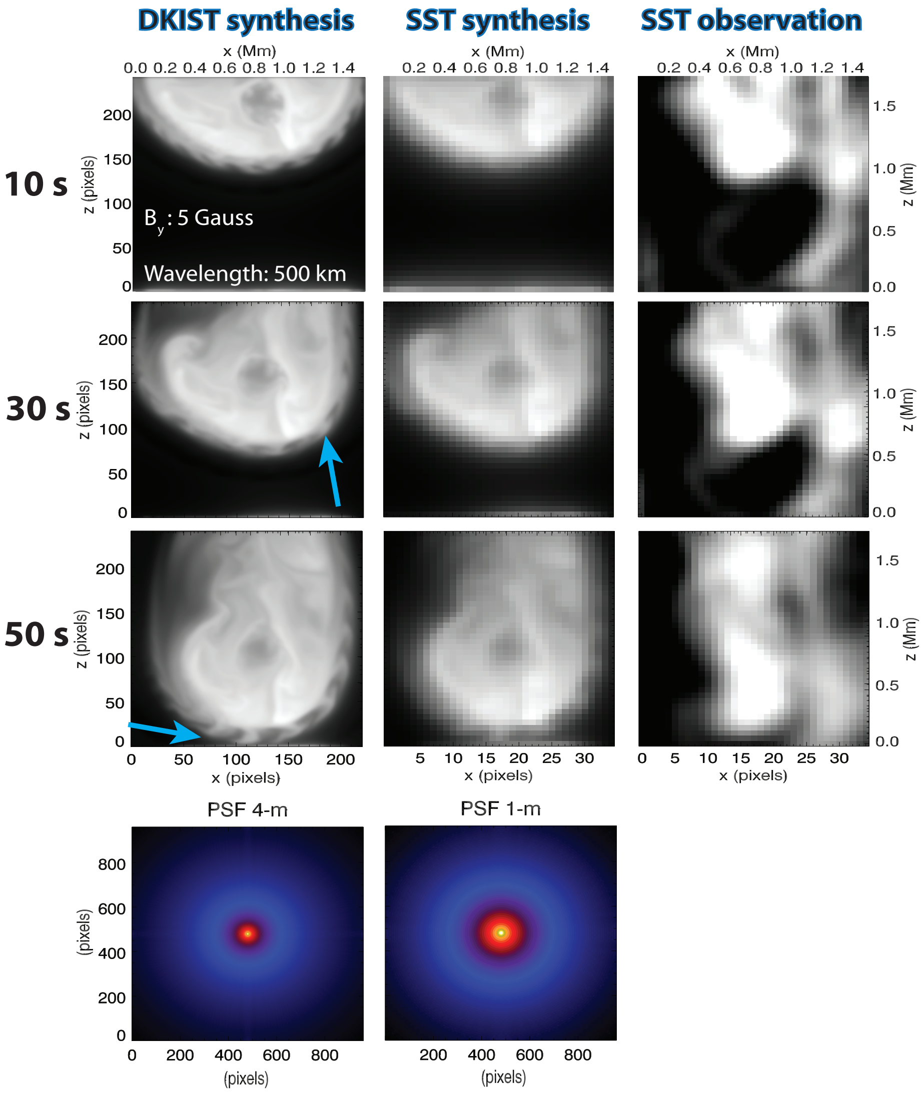

Figure 5.24: *Left:* We present a zoomed-in, synthetic, 4-m class, DKIST white-light observation binned at the DKIST blue channel pixel size of 7 km, of a large plume bulb that propagates towards the bottom boundary of the B_0= 5 G with λ_c= 500 km simulation. With blue arrows we highlight the notable development of small-scale plasma protrusions at the leading edge of the plume bulb which grow significantly within the 50 s time interval. The synthetic observation is convolved with the PSF for a 4-m aperture telescope as shown in the bottom row. *Middle:* An equivalent synthetic observation for a 1-m class telescope, rebinned to the SST blue channel pixel size of 43 km. The synthetic observation is convolved with the PSF for a 1-m aperture telescope as shown in the bottom row. *Right:* A observation of a falling plume bulb from SST and aligned vertically for comparison.

sequence.

For context, on the right column of fig. 5.24 there is an observation of one of the detected plumes from the SST. This plume is significantly narrower in width compared with the simulations, although the simulation used here was the B_0= 5G and λ_c= 500 km model, where we detect substantially larger plume structures given the large critical wavelength. These small-scale protrusions are not detectable currently with existing 1-m class solar telescopes. We provide this result as a prediction for DKIST which will commence full operations in mid 2020.

Chapter 6

Magnetohydrodynamic Instabilities in Solar Prominences

6.1 A Brief Summary, and Synthesis

Over the course of this work we have looked at both large and small scale instabilities in solar prominences. Whilst looking at the large scale evolution of an erupting prominence we used kinematic analysis on a 3D reconstruction of an event to determine the role of the torus instability. To do this, we had to develop a new automated edge-detection method, and utilise parametric fitting to recover the key kinematic properties of the event to find the onset time, onset height, and ultimately the decay index. By comparing the decay index from one slit to its 136 neighbours we were able to gain novel insight into its effect on the larger structure.

We now turn a small part of this analysis towards the prominence in which we studied the small-scale instabilities. By performing 3D reconstruction of this prominence, as can be seen in figs. 6.1 and 6.2, this time using STEREO-B instead, using the same methods as outlined in Sec. 3.2, we were able to attain its 3D height.

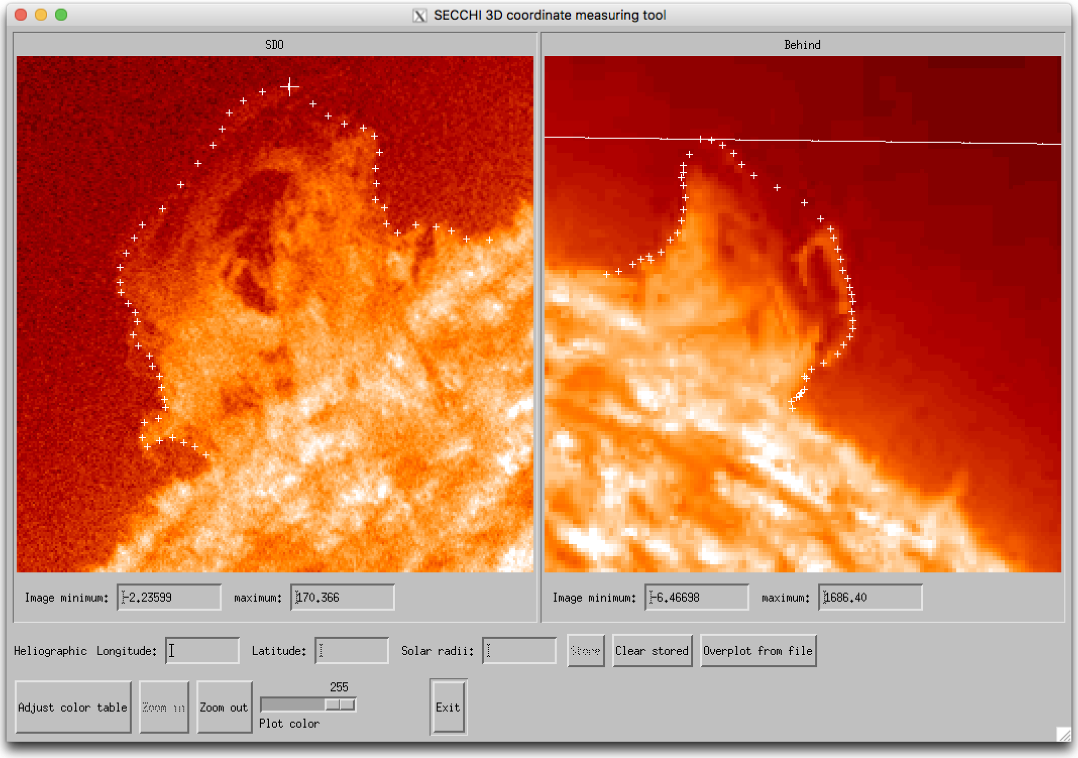

Image minimum: -2.23599 maximum: 170.366

Image minimum: -6.46698 maximum: 1686.40

Figure 6.1: The 3D Reconstruction of the Chapter. 5 prominence.

We perform this for only a single time here, as it is not undergoing eruption. Instead, something curious happens to this prominence; it simply fades away about a day after the observation. Nevertheless, we find that at its apex this prominence reached 65 Mm in true 3D height. This is just over half of the starting height of the prominence from Chapter 4. As it fades away before it can get to disk centre, we cannot determine the true magnetic field that this prominence experienced. However, we still use PFSS to find the magnetic field that the prominence would experience had it rotated to disk centre. Using this, we thus determine the decay index of the region that the prominence once occupied. Based upon both SDO and STEREO-B there is nothing but quiet-Sun surrounding this prominence at all times, so do not feel that this is entirely unreasonable.

As can be seen in Fig. 6.3 we present the decay index of the non-eruptive prominence. The apex at 65 Mm would correspond to $n = 0.19$. As should

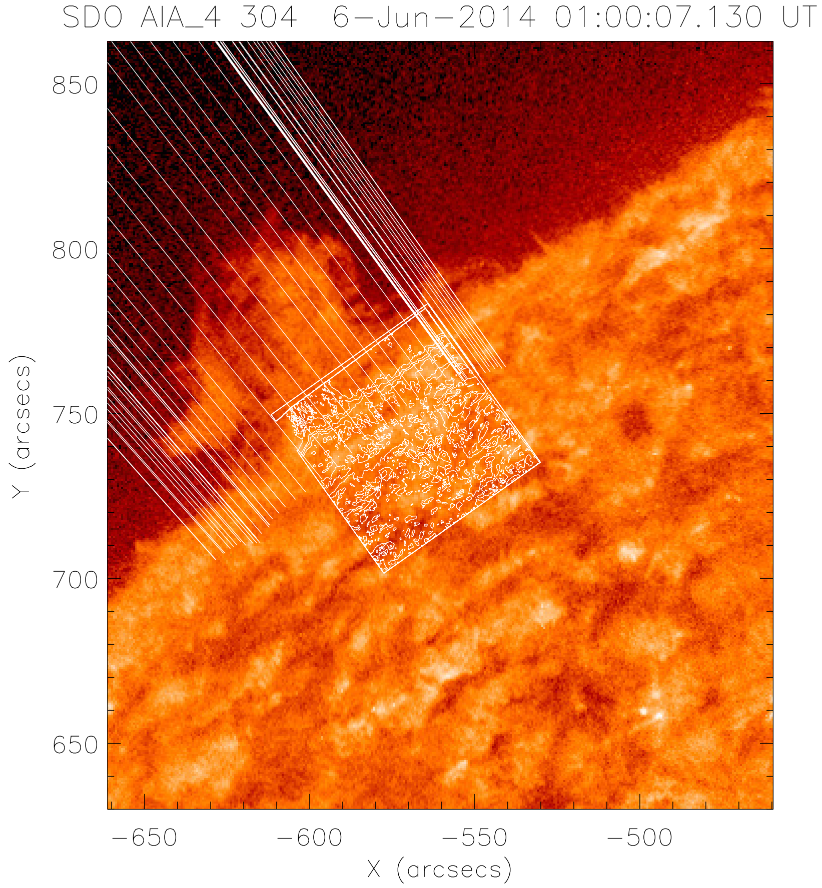

Figure 6.2: Slits drawn through the 55 points selected as the 3D height coordinates of the leading edge of this prominence, with the SST FoV overlaid as a contours.

be obvious, this is far from any sort of critical threshold. Though the torus instability is unable to take credit for the demise of this prominence, we instead wonder about the role of mass draining. As was alluded to in Chapter 4 we speculated that mass draining may in some way have been related to the linear rise phase, though it was outside the scope of the study. In this case however, we have direct observational evidence of mass draining out of the prominence. We

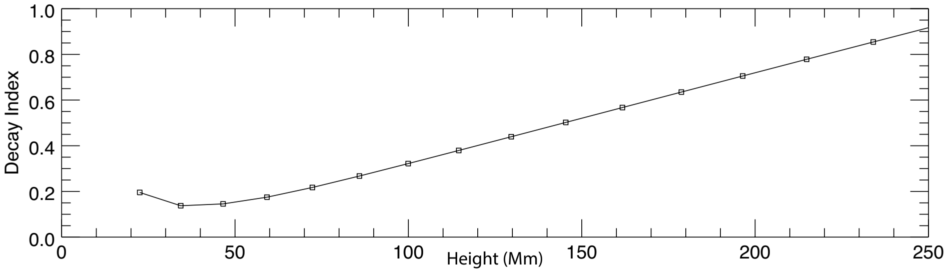

Figure 6.3: The decay index versus height (Mm) from the region that the Chapter. 5 prominence would have occupied.

must therefore wonder how it is related to the fading-out of this prominence. Is the RTI just a symptom of a larger process that is slowly draining the prominence of its material, or is it just a part of the convective cycle that keeps prominences filled with mass? Whichever it might be, our observations of the RTI using CRISP have been aided by the simulations performed in MANCHA. By selecting 1492 events we are able to confidently determine the statistical properties of the plumes of this event. Through matching our observations to B_0, and λ_c we have been able to constrain the range of possible magnetic environments actually experienced by the plumes.

6.2 Conclusions and Future Work

6.2.1 The Torus Instability

6.2.1.1 Further Application and Development of Techniques

Several of the techniques we have developed here are novel, such as the transient filter and automated edge detection, and iterations on previous techniques, such as the parametric fitting process, have been developed to allow the analysis performed here.

Firstly, we hope to eventually allow the calculation of error from the FLCT method. This will allow quantitative analysis of flows within prominences, potentially giving insight into how these change over the course of an eruption.

The transient filter, will be generalised to allow its use on other data sources, as it is currently written specifically as part of the automated edge-detection program. Its use as a post-backgrounding filter means it is ideal to remove pixels, small clusters, or faint features that are otherwise very difficult to remove using purely statistical procedures.

The automated edge-detection, is currently to off-limb data of any emitting feature at any cadence. Further development will be its application for absorption features, i.e. enabling to work on prominences in hotter channels, and on-disk. Whilst much of the automated analysis is aimed towards kinematic goals, the reality is that the techniques will work on a much more diverse range of phenomena.

The primary draw-back to the height-time method used from Sec. 4.2.2 is the manual nature of the 3D reconstruction (see Sec. 3.2). Ideally, this would also be automated to allow significantly faster analysis. This will not be an easy feat due to the subjective nature of the process, but it should ultimately be possible.

For the parametric fitting process, one of the current problems faced is the small number of available points to fit in the non-linear regime. Ideally, maximising the number of points in each slit would provide greater insight.

6.2.1.2 A Statistical Study

This work is solely based on one event. Applying the techniques described here to other events is a natural progression. that will allow greater insight into the underlying physics that guides prominence eruptions. In the future, the automation of 3D reconstruction of would also allow faster, and more meaningful analysis than that based solely in the plane-of-sky as done in other statistical studies such as McCauley et al. (2015).

6.2.1.3 Determining the Cause of the Linear Rise Phase

Determining the cause of the linear rise phase will be a further natural progression to this work. The recent work on mass drainage as a part of an eruption makes that a logical place to start.

6.2.2 The Rayleigh-Taylor Instability

By matching unique high resolution observations from SST/CRISP with supporting advanced 2.5D ideal-MHD simulations we were able to constrain the key parameters that define the development of the RTI as a governing mechanism. In future we would like to further develop the observational methods, and apply them to other events, especially eruptive ones.

Thank you for reading.

Bibliography

Aggarwal, A., Schanche, N., Reeves, K. K., Kempton, D., & Angryk, R. 2018, Prediction of Solar Eruptions Using Filament Metadata, Astrophysical Journal, Supplement, 236, 15

Alzate, N. & Morgan, H. 2017, Identification of Low Coronal Sources of "Stealth" Coronal Mass Ejections Using New Image Processing Techniques, Astrophysical Journal, 840, 103

Antiochos, S. K. 1998, The Magnetic Topology of Solar Eruptions, Astrophysical Journal, Letters, 502, L181

Antiochos, S. K., Dahlburg, R. B., & Klimchuk, J. A. 1994, The Magnetic Field of Solar Prominences, Astrophysical Journal, Letters, 420, L41

Anzer, U. & Heinzel, P. 2008, Prominence modelling: from observed emission measures to temperature profiles, Astronomy and Astrophysics, 480, 537

Aschwanden, M. J. 2005, Physics of the Solar Corona. An Introduction with Problems and Solutions (2nd edition)

Aulanier, G. 2014, in IAU Symposium, Vol. 300, Nature of Prominences and their Role in Space Weather, ed. B. Schmieder, J.-M. Malherbe, & S. T. Wu, 184–196

Aulanier, G. & Demoulin, P. 1998, 3-D magnetic configurations supporting prominences. I. The natural presence of lateral feet, Astronomy and Astrophysics, 329, 1125

Aulanier, G., Démoulin, P., Mein, N., et al. 1999, 3-D magnetic configurations supporting prominences. III. Evolution of fine structures observed in a filament channel, Astronomy and Astrophysics, 342, 867

Aulanier, G., Demoulin, P., van Driel-Gesztelyi, L., Mein, P., & Deforest, C. 1998, 3-D magnetic configurations supporting prominences. II. The lateral feet as a perturbation of a twisted flux-tube, Astronomy and Astrophysics, 335, 309

Aulanier, G., Török, T., Démoulin, P., & DeLuca, E. E. 2010, Formation of Torus-Unstable Flux Ropes and Electric Currents in Erupting Sigmoids, Astrophysical Journal, 708, 314

Bateman, G. 1978, MHD Instabilities (Cambridge, Mass., MIT Press, 1978. 270 p.)

Baudin, F., Ibarra, E., Avrett, E. H., et al. 2007, A Contribution to the Understanding of Chromospheric Oscillations, Solar Physics, 241, 39

Berger, M. A. & Prior, C. 2006, The writhe of open and closed curves, Journal of Physics A Mathematical General, 39, 8321

Berger, T., Hillier, A., & Liu, W. 2017a, Quiescent prominence dynamics observed with the Hinode Solar Optical Telescope . II. Prominence Bubble Boundary Layer Characteristics and the Onset of a Coupled Kelvin-Helmholtz Rayleigh-Taylor Instability, ArXiv e-prints

Berger, T., Hillier, A., & Liu, W. 2017b, Quiescent Prominence Dynamics Observed with the Hinode Solar Optical Telescope. II. Prominence Bubble

Boundary Layer Characteristics and the Onset of a Coupled Kelvin-Helmholtz Rayleigh-Taylor Instability, Astrophysical Journal, 850, 60

Berger, T. E., Shine, R. A., Slater, G. L., et al. 2008, Hinode SOT Observations of Solar Quiescent Prominence Dynamics, Astrophysical Journal, Letters, 676, L89

Berger, T. E., Slater, G., Hurlburt, N., et al. 2010, Quiescent Prominence Dynamics Observed with the Hinode Solar Optical Telescope. I. Turbulent Upflow Plumes, Astrophysical Journal, 716, 1288

Bernasconi, P. N., Rust, D. M., & Hakim, D. 2005, Advanced Automated Solar Filament Detection And Characterization Code: Description, Performance, And Results, Solar Physics, 228, 97

Bommier, V., Leroy, J. L., & Sahal-Brechot, S. 1986, The Linear Polarization of Hydrogen H-Beta Radiation and the Joint Diagnostic of Magnetic Field Vector and Electron Density in Quiescent Prominences - Part Two - the Electron Density, Astronomy and Astrophysics, 156, 90

Calugareanu, G. 1959, Lintégrale de Gauss et lanalyse des nœuds tridimensionnels, Rev. Math. pures appl, 4

Chae, J. 2010, Dynamics of Vertical Threads and Descending Knots in a Hedgerow Prominence, Astrophysical Journal, 714, 618

Chae, J., Ahn, K., Lim, E.-K., Choe, G. S., & Sakurai, T. 2008, Persistent Horizontal Flows and Magnetic Support of Vertical Threads in a Quiescent Prominence, Astrophysical Journal, Letters, 689, L73

Chandrasekhar, S. 1961, Hydrodynamic and hydromagnetic stability

Cheng, X., Zhang, J., Ding, M. D., et al. 2013, Investigating Two Successive Flux Rope Eruptions in a Solar Active Region, Astrophysical Journal, Letters, 769, L25

de la Cruz Rodríguez, J., Löfdahl, M. G., Sütterlin, P., Hillberg, T., & Rouppe van der Voort, L. 2015, CRISPRED: A data pipeline for the CRISP imaging spectropolarimeter, Astronomy and Astrophysics, 573, A40

de Toma, G., Casini, R., Burkepile, J. T., & Low, B. C. 2008, Rise of a Dark Bubble through a Quiescent Prominence, Astrophysical Journal, Letters, 687, L123

Del Zanna, G., Chiuderi Drago, F., & Parenti, S. 2004, SOHO CDS and SUMER observations of quiescent filaments and their interpretation, Astronomy and Astrophysics, 420, 307

Démoulin, P. & Aulanier, G. 2010, Criteria for Flux Rope Eruption: Non-equilibrium Versus Torus Instability, Astrophysical Journal, 718, 1388

Díaz, A. J., Soler, R., & Ballester, J. L. 2012, Rayleigh-Taylor Instability in Partially Ionized Compressible Plasmas, Astrophysical Journal, 754, 41

Druckmüller, M., Habbal, S. R., & Morgan, H. 2014, Discovery of a New Class of Coronal Structures in White Light Eclipse Images, Astrophysical Journal, 785, 14

Engvold, O. 2015, in Astrophysics and Space Science Library, Vol. 415, Solar Prominences, ed. J.-C. Vial & O. Engvold, 31

Fan, Y. 2017, MHD Simulations of the Eruption of Coronal Flux Ropes under Coronal Streamers, Astrophysical Journal, 844, 26

Fan, Y., Gibson, S., & Tomczyk, S. 2018, The eruption of a prominence carrying coronal flux rope: forward synthesis of the magnetic field strength measurement by the COronal Solar Magnetism Observatory Large Coronagraph, ArXiv e-prints

Fan, Y. & Gibson, S. E. 2007, Onset of Coronal Mass Ejections Due to Loss of Confinement of Coronal Flux Ropes, Astrophysical Journal, 668, 1232

Felipe, T., Khomenko, E., & Collados, M. 2010, Magneto-acoustic Waves in Sunspots: First Results From a New Three-dimensional Nonlinear Magnetohydrodynamic Code, Astrophysical Journal, 719, 357

Foullon, C., Verwichte, E., Nakariakov, V. M., Nykyri, K., & Farrugia, C. J. 2011, Magnetic Kelvin-Helmholtz Instability at the Sun, Astrophysical Journal, Letters, 729, L8

Gaizauskas, V. 1998, Astronomical Society of the Pacific Conference Series, Vol. 150, Filament Channels: Essential Ingredients for Filament Formation (Review), ed. D. F. Webb, B. Schmieder, & D. M. Rust, 257

Galsgaard, K. & Nordlund, Å. 1997, Heating and activity of the solar corona. 2. Kink instability in a flux tube, Journal of Geophysics Research, 102, 219

Garren, D. A. & Chen, J. 1994, Lorentz self-forces on curved current loops, Physics of Plasmas, 1, 3425

Gibson, S. E. 2018, Solar prominences: theory and models. Fleshing out the magnetic skeleton, Living Reviews in Solar Physics, 15, 7

Gopalswamy, N., Shimojo, M., Lu, W., et al. 2003, Prominence Eruptions and Coronal Mass Ejection: A Statistical Study Using Microwave Observations, Astrophysical Journal, 586, 562

Haerendel, G. & Berger, T. 2011, A Droplet Model of Quiescent Prominence Downflows, Astrophysical Journal, 731, 82

Heasley, J. N. & Milkey, R. W. 1976, Structure and spectrum of quiescent prominences. II. Hydrogen and helium spectra., Astrophysical Journal, 210, 827

Heinzel, P., Anzer, U., & Gunár, S. 2010, Solar quiescent prominences. Filamentary structure and energetics, Mem. Societa Astronomica Italiana, 81, 654

Hillier, A., Berger, T., Isobe, H., & Shibata, K. 2012, Numerical Simulations of the Magnetic Rayleigh-Taylor Instability in the Kippenhahn-Schlüter Prominence Model. I. Formation of Upflows, Astrophysical Journal, 746, 120

Hillier, A., Isobe, H., Shibata, K., & Berger, T. 2011, Numerical Simulations of the Magnetic Rayleigh-Taylor Instability in the Kippenhahn-Schlüter Prominence Model, Astrophysical Journal, Letters, 736, L1

Hillier, A. S. 2016, On the nature of the magnetic Rayleigh-Taylor instability in astrophysical plasma: the case of uniform magnetic field strength, Monthly Notices of the Royal Astronomical Society, 462, 2256

Hood, A. W., Archontis, V., Galsgaard, K., & Moreno-Insertis, F. 2009, The emergence of toroidal flux tubes from beneath the solar photosphere, Astronomy and Astrophysics, 503, 999

Hood, A. W. & Priest, E. R. 1979, Kink Instability of Solar Coronal Loops as the Cause of Solar Flares, Solar Physics, 64, 303

House, L. L., Wagner, W. J., Hildner, E., Sawyer, C., & Schmidt, H. U. 1981, Studies of the corona with the Solar Maximum Mission coronagraph/polarimeter, Astrophysical Journal, Letters, 244, L117

Hutton, J. & Morgan, H. 2015, Erupting Filaments with Large Enclosing Flux Tubes as Sources of High-mass Three-part CMEs, and Erupting Filaments in the Absence of Enclosing Flux Tubes as Sources of Low-mass Unstructured CMEs, Astrophysical Journal, 813, 35

Iglesias, C. A. & Rogers, F. J. 1991, Opacities for the Solar Radiative Interior, Astrophysical Journal, 371, 408

Illing, R. M. E. & Hundhausen, A. J. 1985, Observation of a coronal transient from 1.2 to 6 solar radii, Journal of Geophysics Research, 90, 275

Inglis, D. R. & Teller, E. 1939, Ionic Depression of Series Limits in One-Electron Spectra., Astrophysical Journal, 90, 439

Isobe, H., Miyagoshi, T., Shibata, K., & Yokoyama, T. 2005, Filamentary structure on the Sun from the magnetic Rayleigh-Taylor instability, Nature, 434, 478

Jejčič, S. & Heinzel, P. 2009, Electron Densities in Quiescent Prominences Derived from Eclipse Observations, Solar Physics, 254, 89

Jenkins, J. M., Hopwood, M., Démoulin, P., et al. 2019, Modeling the Effect of Mass-draining on Prominence Eruptions, Astrophysical Journal, 873, 49

Jenkins, J. M., Long, D. M., van Driel-Gesztelyi, L., & Carlyle, J. 2018, Understanding the Role of Mass-Unloading in a Filament Eruption, Solar Physics, 293, 7

Jiang, C.-W., Wu, S.-T., Feng, X.-S., & Hu, Q. 2016, A comparison study of a solar active-region eruptive filament and a neighboring non-eruptive filament, Research in Astronomy and Astrophysics, 16, 18

Jing, J., Liu, C., Lee, J., et al. 2018, Statistical Analysis of Torus and Kink Instabilities in Solar Eruptions, Astrophysical Journal, 864, 138

Jun, B.-I., Norman, M. L., & Stone, J. M. 1995, A Numerical Study of Rayleigh-Taylor Instability in Magnetic Fluids, Astrophysical Journal, 453, 332

Kaiser, M. L., Kucera, T. A., Davila, J. M., et al. 2008, The STEREO Mission: An Introduction, Space Science Reviews, 136, 5

Karpen, J. T., Antiochos, S. K., Hohensee, M., Klimchuk, J. A., & MacNeice, P. J. 2001, Are Magnetic Dips Necessary for Prominence Formation?, Astrophysical Journal, Letters, 553, L85

Keppens, R., Xia, C., & Porth, O. 2015, Solar Prominences: "Double, Double... Boil and Bubble", Astrophysical Journal, Letters, 806, L13

Khomenko, E. 2017, On the effects of ion-neutral interactions in solar plasmas, Plasma Physics and Controlled Fusion, 59, 014038

Khomenko, E. & Collados, M. 2012, Heating of the Magnetized Solar Chromosphere by Partial Ionization Effects, Astrophysical Journal, 747, 87

Khomenko, E., Collados, M., & Felipe, T. 2008, Nonlinear Numerical Simulations of Magneto-Acoustic Wave Propagation in Small-Scale Flux Tubes, Solar Physics, 251, 589

Khomenko, E., Díaz, A., de Vicente, A., Collados, M., & Luna, M. 2014, Rayleigh-Taylor instability in prominences from numerical simulations including partial ionization effects, Astronomy and Astrophysics, 565, A45

Kliem, B., Su, Y. N., van Ballegooijen, A. A., & DeLuca, E. E. 2013, Magnetohydrodynamic Modeling of the Solar Eruption on 2010 April 8, Astrophysical Journal, 779, 129

Kliem, B. & Török, T. 2006, Torus Instability, Physical Review Letters, 96, 255002

Kliem, B., Török, T., & Thompson, W. T. 2012, A Parametric Study of Erupting Flux Rope Rotation. Modeling the “Cartwheel CME” on 9 April 2008, Solar Physics, 281, 137

Kuperus, M. & Raadu, M. A. 1974, The Support of Prominences Formed in Neutral Sheets, Astronomy and Astrophysics, 31, 189

Labrosse, N., Heinzel, P., Vial, J. C., et al. 2010, Physics of Solar Prominences: I—Spectral Diagnostics and Non-LTE Modelling, Space Science Reviews, 151, 243

Lee, J., Liu, C., Jing, J., & Chae, J. 2016, Solar Eruption and Local Magnetic Parameters, Astrophysical Journal, Letters, 831, L18

Lemen, J. R., Title, A. M., Akin, D. J., et al. 2012, The Atmospheric Imaging Assembly (AIA) on the Solar Dynamics Observatory (SDO), Solar Physics, 275, 17

Lin, Y., Martin, S. F., & Engvold, O. 2008, Astronomical Society of the Pacific Conference Series, Vol. 383, Filament Substructures and their Interrelation, ed. R. Howe, R. W. Komm, K. S. Balasubramaniam, & G. J. D. Petrie, 235

Liu, C., Lee, J., Jing, J., et al. 2010, Motions of Hard X-ray Sources During an Asymmetric Eruption, Astrophysical Journal, Letters, 721, L193

Liu, R., Alexander, D., & Gilbert, H. R. 2009, Asymmetric Eruptive Filaments, Astrophysical Journal, 691, 1079

Liu, Y. 2008, Magnetic Field Overlying Solar Eruption Regions and Kink and Torus Instabilities, Astrophysical Journal, Letters, 679, L151

Lynch, B. J., Antiochos, S. K., DeVore, C. R., Luhmann, J. G., & Zurbuchen, T. H. 2008, Topological Evolution of a Fast Magnetic Breakout CME in Three Dimensions, Astrophysical Journal, 683, 1192

Lynch, B. J., Antiochos, S. K., MacNeice, P. J., Zurbuchen, T. H., & Fisk, L. A. 2004, Observable Properties of the Breakout Model for Coronal Mass Ejections, Astrophysical Journal, 617, 589

Martin, S. F. 1998, Astronomical Society of the Pacific Conference Series, Vol. 150, Filament Chirality: A Link Between Fine-Scale and Global Patterns (Review), ed. D. F. Webb, B. Schmieder, & D. M. Rust, 419

Martin, S. F., Marquette, W. H., & Bilimoria, R. 1992, Astronomical Society of the Pacific Conference Series, Vol. 27, The Solar Cycle Pattern in the Direction of the Magnetic Field along the Long Axes of Polar Filaments, ed. K. L. Harvey, 53

Martínez-Gómez, D., Soler, R., & Terradas, J. 2015, Onset of the Kelvin-Helmholtz instability in partially ionized magnetic flux tubes, Astronomy and Astrophysics, 578, A104

McCauley, P. I., Su, Y. N., Schanche, N., et al. 2015, Prominence and Filament Eruptions Observed by the Solar Dynamics Observatory: Statistical Properties, Kinematics, and Online Catalog, Solar Physics, 290, 1703

Moore, R. L., Sterling, A. C., Hudson, H. S., & Lemen, J. R. 2001, Onset of the Magnetic Explosion in Solar Flares and Coronal Mass Ejections, Astrophysical Journal, 552, 833

Möstl, U. V., Temmer, M., & Veronig, A. M. 2013, The Kelvin-Helmholtz Instability at Coronal Mass Ejection Boundaries in the Solar Corona: Observations and 2.5D MHD Simulations, Astrophysical Journal, Letters, 766, L12

Munro, R. H., Gosling, J. T., Hildner, E., et al. 1979, The association of coronal mass ejection transients with other forms of solar activity., Solar Physics, 61, 201

Myshyakov, I. & Tsvetkov, T. 2020, Comparison of Kinematics of Solar Eruptive Prominences and Spatial Distribution of the Magnetic Decay Index, The Astrophysical Journal, 889, 28

Olmedo, O. & Zhang, J. 2010, Partial Torus Instability, Astrophysical Journal, 718, 433

Olmedo, O., Zhang, J., & Kunkel, V. 2013, Lorentz Self-force of an Ellipse Current Loop Model, Astrophysical Journal, 771, 125

Parenti, S. 2014, Solar Prominences: Observations, Living Reviews in Solar Physics, 11, 1

Pesnell, W. D., Thompson, B. J., & Chamberlin, P. C. 2012, The Solar Dynamics Observatory (SDO), Solar Physics, 275, 3

Ruderman, M. S. 2017, Compressibility Effect on the Rayleigh-Taylor Instability with Sheared Magnetic Fields, Solar Physics, 292, 47

Ryutova, M., Berger, T., Frank, Z., Tarbell, T., & Title, A. 2010, Observation of Plasma Instabilities in Quiescent Prominences, Solar Physics, 267, 75

Sakurai, T. 1976, Magnetohydrodynamic interpretation of the motion of prominences., Publications of the ASJ, 28, 177

Sarkar, R., Srivastava, N., Mierla, M., West, M. J., & D'Huys, E. 2019, Evolution of the Coronal Cavity From the Quiescent to Eruptive Phase Associated with Coronal Mass Ejection, Astrophysical Journal, 875, 101

Scharmer, G. B., Kiselman, D., Löfdahl, M. G., & Rouppe van der Voort, L. 2003, in Solar Polarization, Vol. 307, 3

Scharmer, G. B., Narayan, G., Hillberg, T., et al. 2008, CRISP Spectropolarimetric Imaging of Penumbral Fine Structure, Astrophysical Journal, Letters, 689, L69

Schou, J., Scherrer, P. H., Bush, R. I., et al. 2012, Design and Ground Calibration of the Helioseismic and Magnetic Imager (HMI) Instrument on the Solar Dynamics Observatory (SDO), Solar Physics, 275, 229

Schrijver, C. J. & De Rosa, M. L. 2003, Photospheric and heliospheric magnetic fields, Solar Physics, 212, 165

Schrijver, C. J., Elmore, C., Kliem, B., Török, T., & Title, A. M. 2008, Observations and Modeling of the Early Acceleration Phase of Erupting Filaments Involved in Coronal Mass Ejections, Astrophysical Journal, 674, 586

Shafranov, V. D. 1966, Plasma Equilibrium in a Magnetic Field, Reviews of Plasma Physics, 2, 103

Stellmacher, G. & Wiehr, E. 1973, Observatino of an Instability in a “Quiescent” Prominence, Astronomy and Astrophysics, 24, 321

Sterling, A. C. & Moore, R. L. 2004, Evidence for Gradual External Reconnection before Explosive Eruption of a Solar Filament, Astrophysical Journal, 602, 1024

Terradas, J., Oliver, R., & Ballester, J. L. 2012, The role of Rayleigh-Taylor instabilities in filament threads, Astronomy and Astrophysics, 541, A102

Török, T., Berger, M. A., & Kliem, B. 2010, The writhe of helical structures in the solar corona, Astronomy and Astrophysics, 516, A49

Török, T. & Kliem, B. 2005, Confined and Ejective Eruptions of Kink-unstable Flux Ropes, Astrophysical Journal, Letters, 630, L97

Török, T., Kliem, B., Berger, M. A., et al. 2014, The evolution of writhe in kink-unstable flux ropes and erupting filaments, Plasma Physics and Controlled Fusion, 56, 064012

Török, T., Kliem, B., & Titov, V. S. 2004, Ideal kink instability of a magnetic loop equilibrium, Astronomy and Astrophysics, 413, L27

Tripathi, D., Isobe, H., & Mason, H. E. 2006, On the propagation of brightening after filament/prominence eruptions, as seen by SoHO-EIT, Astronomy and Astrophysics, 453, 1111

Tsap, Y. T., Filippov, B. P., & Kopylova, Y. G. 2019, Eruptive Instability of the Magnetic-Flux Rope: Gravitational Force and Mass-Unloading, Solar Physics, 294, 35

van Ballegooijen, A. A. & Cranmer, S. R. 2010, Tangled Magnetic Fields in Solar Prominences, Astrophysical Journal, 711, 164

van Noort, M., Rouppe van der Voort, L., & Löfdahl, M. G. 2005, Solar Image Restoration By Use Of Multi-frame Blind De-convolution With Multiple Objects And Phase Diversity, Solar Physics, 228, 191

Vasantharaju, N., Vemareddy, P., Ravindra, B., & Doddamani, V. H. 2019, Finding the Critical Decay Index in Solar Prominence Eruptions, Astrophysical Journal, 885, 89

Vissers, G. & Rouppe van der Voort, L. 2012, Flocculent Flows in the Chromospheric Canopy of a Sunspot, Astrophysical Journal, 750, 22

Wang, Y., Cao, H., Chen, J., et al. 2010, Solar Limb Prominence Catcher and Tracker (SLIPCAT): An Automated System and its Preliminary Statistical Results, Astrophysical Journal, 717, 973

Webb, D. F. & Howard, T. A. 2012, Coronal Mass Ejections: Observations, Living Reviews in Solar Physics, 9, 3

Wuelser, J.-P., Lemen, J. R., Tarbell, T. D., et al. 2004, in Proceedings of the SPIE, Vol. 5171, Telescopes and Instrumentation for Solar Astrophysics, ed. S. Fineschi & M. A. Gummin, 111–122

Xia, C. & Keppens, R. 2016, Internal Dynamics of a Twin-layer Solar Prominence, Astrophysical Journal, Letters, 825, L29

Xu, Y., Liu, C., Jing, J., & Wang, H. 2012, On the Relationship between the Coronal Magnetic Decay Index and Coronal Mass Ejection Speed, Astrophysical Journal, 761, 52

Zaqarashvili, T. V., Zhelyazkov, I., & Ofman, L. 2015, Stability of Rotating Magnetized Jets in the Solar Atmosphere. I. Kelvin-Helmholtz Instability, Astrophysical Journal, 813, 123

Zuccarello, F. P., Aulanier, G., & Gilchrist, S. A. 2016, The Apparent Critical Decay Index at the Onset of Solar Prominence Eruptions, Astrophysical Journal, Letters, 821, L23

Zuccarello, F. P., Bemporad, A., Jacobs, C., et al. 2012, The Role of Streamers in the Deflection of Coronal Mass Ejections: Comparison between STEREO Three-dimensional Reconstructions and Numerical Simulations, Astrophysical Journal, 744, 66

Zuccarello, F. P., Seaton, D. B., Filippov, B., et al. 2014a, Erratum: "Observational Evidence of Torus Instability as Trigger Mechanism for Coronal Mass Ejections: The 2011 August 4 Filament Eruption", Astrophysical Journal, 795, 175

Zuccarello, F. P., Seaton, D. B., Mierla, M., et al. 2014b, Observational Evidence of Torus Instability as Trigger Mechanism for Coronal Mass Ejections: The 2011 August 4 Filament Eruption, Astrophysical Journal, 785, 88